

Nonlinear Acoustics and an Inverse Scattering Problem

by

John Schofield

A thesis submitted to

University of East Anglia

for the degree of

Doctor of Philosophy

April 9, 2016

Abstract

This Ph.D is concerned with wave propagation problems. The main focus is on nonlinear acoustics, looking at sonic boom propagation in a physically realistic atmosphere, whilst a secondary part will look at the problem of landmine detection and how to improve the target detection rates.

The work on nonlinear acoustics emerged as a desire to model the behaviour of the sonic booms formed by supersonic aircraft in the atmosphere to see what environmental impact they would have on people and animals on the ground, in terms of the form of the sound waves once they reach the ground.

The work on landmine detection originated from a Knowledge Transfer Partnership between the University of East Anglia (UEA) and Cobham Technical Services (CTS) organised through the Knowledge Transfer Network (KTN). This partnership took the form of a six month internship with work undertaken afterwards to publish the findings of the internship.

Dedication

This thesis is dedicated to the memory of my father, Peter John Schofield. Thank you for showing me the kind of person I should aspire to be and for countless summer holidays and chess games together.

Acknowledgement

First of all, I must thank my supervisor, Dr. Paul Hammerton, for his countless good advice, endless patience and always being there for an impromptu meeting.

Also thanks must go Martin Walters and Julian Thompson for making the office an enjoyable working atmosphere and always being there for a most welcome distraction. I would also like to thank Fiona Marjoribanks for all your patience and delicious baking to help me write up this thesis. Lastly thanks must go to my mother, Carolyn Schofield, for your constant support, encouragement and your small proverbs of wisdom.

Contents

A	Nonlinear Acoustics	12
1	Introduction	12
2	Introduction to Nonlinear Partial Differential Equations	18
2.1	Method of Characteristics	18
2.2	Shock Formation	21
2.3	Jump Condition	23
3	Burgers' Equation	27
3.1	Derivation of Burgers' Equation	27
3.2	Exact solution to the plane case	30
4	Asymptotic Analysis	33
4.1	Weak Shock Theory	34
5	Numerical Schemes	42
5.1	Implicit Predictor-Corrector Scheme with a Variable Mesh	43
6	Asymptotic Breakdowns	50

6.1	Plane Waves	51
6.2	Cylindrical Waves	55
6.3	Spherical Waves	59
6.4	Further Analysis	63
6.5	Results	69
6.5.1	Plane Case	70
6.5.2	Cylindrical Case	71
6.5.3	Spherical Case	71
7	Solving for Long Time Asymptotics	82
7.1	Planar Case	85
7.2	Cylindrical Case	86
7.3	Spherical Case	87
8	Including the effects of relaxation	89
8.1	Introduction	89
8.2	Numerical Method	90
9	Understanding the effects of relaxation	92
9.1	Finding an analytic form for U_1	92

9.2 The effect of the relaxation term upon the waveform when $\tau_1 = O(1)$. . . 99

10 Full Atmospheric Model **110**

10.1 Introduction 110

10.2 Constants varying with Altitude 116

10.2.1 Temperature 116

10.2.2 Gravity 117

10.2.3 Speed of Sound 117

10.2.4 Ambient Pressure 118

10.2.5 Humidity 118

10.2.6 Density 119

10.2.7 Diffusivity of Sound 119

10.2.8 Relaxation Terms 120

10.3 Ray Tubes 121

10.3.1 Introduction and Ray Paths 121

10.3.2 General Ray Tube Theory 123

10.3.3 Ray Tubes in an atmosphere with a linear sound speed profile . . . 128

10.3.4 Sonic Boom Carpet 133

10.4 Numerical Model	137
10.5 Numerical Results	141
10.5.1 Test Case	141
10.6 Comparison with Experimental Results	144
11 Conclusion	145
11.1 Concluding Remarks	145
11.2 Future Work	146
11.2.1 Experimental Comparisons	146
11.2.2 The sonic boom strength from the centre of the sonic boom carpet .	146
11.2.3 The effect of varying weather conditions	146
11.2.4 Sub-shocks	147
B Inverse Scattering	148
12 Introduction	148
12.1 Historical Background	149
12.2 Technical Background	151
13 Literature Review	157

13.1	Deconvolution	157
13.1.1	Introduction and Basic Idea of Deconvolution	157
13.1.2	1-D Deconvolution using Stochastic Mutation	160
13.1.3	A Short Comparison of other Deconvolution Techniques	161
13.1.4	Blind Deconvolution	162
13.1.5	Deconvolution versus Blind Deconvolution	164
13.2	Feature Extraction Methods	165
13.2.1	Introduction and Basic Idea	165
13.3	Diffraction Tomography for Ground Penetrating Radar Imaging	166
13.3.1	Introduction and Basic Idea	166
13.3.2	Method	167
13.3.3	Forward Model	167
13.3.4	Inversion	169
13.3.5	Algorithm	170
13.3.6	Summary of Results	171
13.3.7	Strengths and Weaknesses	172
13.4	A Matched Filter	172
13.4.1	Introduction and Basic Idea	172

13.4.2	Method	172
13.4.3	Algorithm	174
13.4.4	Strengths and Weaknesses	174
13.5	Reverse Time Migration	175
13.5.1	Introduction and Basic Idea	175
13.5.2	Method	176
13.5.3	Algorithm	176
13.5.4	Summary of Results	177
13.5.5	Strengths and Weaknesses	179
13.6	Summary of Methods	179

14 Reverse Time Migration - A Multiple Migration and Stacking Algorithm 181

14.1	Aims	181
14.2	Full Reverse Time Migration	181
14.3	Plain Migration	182
14.4	Full Reverse Time Migration versus Plain Migration	183
14.5	Mathematical Modelling	184
14.6	Real Data Modelling	186

14.7 The Algorithm	192
15 Statistical Testing	194
15.1 Introduction	194
15.2 Norm of each A-Scan	195
15.3 Target Recognition	196
15.4 Results	197
16 Conclusion	200
16.1 Summary	200
16.2 Future Work	200
16.2.1 Short Time Fourier Transforms	200
16.2.2 Anti-Personnel Mines	201
16.2.3 C-Scans	201
16.2.4 Oblique Targets	202
16.2.5 Improvement to Metrics	202
16.2.6 Improvement to Target Detection	202
16.3 Acknowledgement	203
A Finite Difference Time Domain	204

Part A

Nonlinear Acoustics

1 Introduction

When considering most acoustical problems, we are typically only concerned with small amplitude disturbances where we can ignore any nonlinear effects. Problems concerning linear acoustics have been extensively solved in the 19th Century. However, in the case of large amplitude disturbances, the small nonlinear effects can no longer safely be ignored. The nonlinear effects slowly cause the wave to steepen which, in certain cases, can lead to the generation of shock waves.

Any aircraft or projectile travelling at supersonic speeds creates an acoustical disturbance formed by the superposition of the sound waves, called a sonic boom which invariably leads to a shock wave. There is a great amount of interest in the formation and propagation of these shock waves as they can have considerable impact on certain animals (e.g. bats) and cause annoyance for people hearing them. This means that any overland supersonic route would need to have minimal impact, in terms of the final wave reaching the ground. There are two key factors which determine the impact of a shock wave to people or animals on the ground. One is the shock wave's amplitude, while the other is the shock wave's thickness or rise time, that is how long it takes for the shock wave to rise from 10 per cent to 90 per cent of its maximum value. This provides the motivation for this Ph.D where the primary focus is to consider the case of a supersonic object travelling

in the atmosphere and predict what waves will reach the ground.

In this thesis we aim to investigate the behaviour and structure of sonic booms using a combination of asymptotic analysis and numerical solutions. Particular focus will be on the paths that sonic booms take to the ground from any supersonic objects flying ahead. There will be discussions on the pre-existing literature on sonic booms and the general techniques of solving nonlinear partial differential equations (PDEs).

This introductory chapter will offer a brief framework of what approach will be taken in each chapter and the motivation behind the work. The majority of the work on nonlinear acoustics is based on the work undertaken by David Crighton in the late seventies. The two papers of particular note are the ‘Model Equations of Nonlinear Acoustics’, [12] and the ‘Asymptotic Solutions of Model Equations in Nonlinear Acoustics’, [13]. In this thesis I shall follow the methods discussed in these papers and attempt to build upon their work. Alongside their asymptotic work, I shall also generate numerical solutions to ascertain how shocks can form and propagate under various external conditions.

While the work undertaken by Crighton and Scott does take into account the effect of thermoviscosity, it neglects other effects such as molecular relaxation and the varying parameters of the atmosphere associated with changes in altitude. Molecular relaxation is associated with the internal vibration of polyatomic molecules and has been discussed by Clarke and McChesney,[8]. Whereas another factor to be considered is the effect a realistic atmosphere has on the waveform. One effect is that the wave no longer travel in straight lines (due to the change in sound speed with altitude). Hence, more work must be done to predict their location and propagate the sound wave through this ray path as discussed by Taylor and Cleveland [9, 53].

Following this introductory chapter, the second chapter will present an introduction of nonlinear PDEs, along with various methods which have been used to obtain solutions and see where, if at all, a discontinuity will form. This work follows some of what is discussed in ‘An Introduction to Nonlinear Partial Differential Equations’ [39].

Chapter 3 will focus on deriving Burgers’ equation from the linearised equations of motion for a thermally and calorically perfect gas in the plane, cylindrically and spherically symmetric cases, see Crighton [12]. Burgers’ equation will form the basis of the PDEs used to model the propagation of the sonic booms in the atmosphere. Chapter 2 will also contain the well known Cole-Hopf solution (see [28, 10]) to solve Burgers equation in one dimension which will later be used to validate any numerical method developed.

In chapter 4, analysis will be performed of the shock structure to obtain an asymptotic solution (weak-shock theory) in the case where our diffusion effects are minimal (representing the conditions in the atmosphere). This chapter presents a new change of variables which keeps the shocks fixed at leading order allowing for more efficient numerical analysis and better clarity on any subtle changes in the shock structure during the wave propagation.

Chapter 5 will present the numerical scheme used throughout this thesis to propagate the numerical solution forward in time. This numerical scheme was originally developed by Chong [7] and makes use of an implicit, variable mesh, finite difference scheme to propagate the solution forwards in time whilst maintaining a high degree of accuracy on the shock to gain in depth results of the shock structure.

Having developed an asymptotic analysis of the shock structure in chapter 4 and a numerical scheme in chapter 5, chapter 6 will contain numerical solutions to illustrate

the breakdown from the asymptotic solution will take place for the plane, cylindrical and spherical cases. Particular focus will be on what form this breakdown takes and at what time this breakdown occurs and how this compares to what is predicted from the asymptotic solution. This work also appears in Schofield and Hammerton [49].

Chapter 7 will look at the old-age behaviour of the shock. Here we will look long past the breakdown of the asymptotic solution and consider the form the shock in its old-age once most of the energy has been diffused from the wave. Determining the general form is relatively simple, whereas more effort is required to determine the constant multiplier of the old-age solution. Here, this constant must be determined separately for the plane, cylindrical and spherical case. This chapter also features in Schofield and Hammerton [49].

Having analysed the basic Burgers' equation in the plane, cylindrical and spherical cases, chapter 8 will begin the process of adding additional effects to Burgers' equation to better model the atmosphere. Here, relaxation effects will be considered whereby the diatomic molecules (mainly Nitrogen and Oxygen) in the atmosphere can absorb the energy from a sonic boom which can produce a variety of effects.

In chapter 9, the relaxation effects will be further investigated in order to determine what effect it will have on the waveform of a standard shock wave. This will involve finding an analytic form for the relaxation effects and comparing the asymptotically predicted effect of the waveform with the numerical solutions of the waveform to validate the numerical model and asymptotic predictions.

Having included relaxation effects in chapters 8 and 9, in chapter 10 a full atmospheric model will be developed which will take into account all the effects of sonic boom prop-

agation in the atmosphere. A key part of this will be looking at ray tubes, which are the paths the sonic booms will take as they propagate through the atmosphere. In this section we also consider how various atmospheric quantities, such as temperature, vary with altitude. This results in the numerical model having to be extended to allow for the governing parameters to be changed in-between steps. This will allow us to run a test case for a supersonic aircraft travelling at Mach 2 at 8,000m and observe what wave the numerical models predicts will be heard on the ground (ignoring effects such as wind and turbulence).

Following on from this, chapter 11 will contain a few concluding remarks summarising the work undertaken and what new research has been taken in the field of sonic boom propagation along with a description of what future work can be taken based upon this work.

Having concluded the the work on nonlinear acoustics, the remaining work will focus on the problem of landmine detection and what methods can be used to improve the target detection rate. Therefore, chapter 12 will contain the introduction for the work to be undertaken on landmine detection. Here, the problem will be set out, along with a historical and technical background outlining the motivation behind the work. The main aim of this work is to improve the target detection rate (the rate of successful detections to false alarms) of landmine detectors using ground penetrating radar. The work presented in chapters 14-16 also appears in Schofield et al. [48].

In chapter 13, a literature review will be presented on the pre-existing methods which could potentially improve the target rate of landmine detection. Each method will be assessed in terms of its strengths and weaknesses to the particular problem of having it

working in real time with a detector.

Having analysed all these methods, reverse time migration was chosen to be investigated further. The development of this method is detailed in chapter 14, along with various changes to improve its performance and reliability.

In chapter 15, a large data set of results will be gathered which then need to be impartially tested to see what improvement the reverse time migration algorithm offers compared to the currently received signal.

Finally, in chapter 16, there will be a brief conclusion of the work on landmine detection, summarising the developments in the previous chapters and outlining areas of future work.

2 Introduction to Nonlinear Partial Differential Equations

Linear PDEs have the property that if y_1 and y_2 are solutions to a PDE then so is $a_1y_1 + a_2y_2$, where a_1 and a_2 are arbitrary constants. This forms a strong basis for solving linear PDEs. However, for nonlinear PDEs this is not the case. This means that, in general, nonlinear PDEs require a lot more effort to solve. This first section will deal with a general method for solving some types of nonlinear PDEs. The key methods and techniques used in this Chapter have been discussed in numerous papers and books. The key book which has been consulted here is ‘An introduction to nonlinear partial differential equations’ by J. David Logan [39].

2.1 Method of Characteristics

Consider a linear PDE of the form

$$u_t + cu_x = 0, \quad u(x, 0) = u_0(x), \quad (2.1)$$

where c is a constant. From the chain rule it can be seen that

$$\frac{d}{dt}u(x(t), t) = u_t(x(t), t) + u_x(x(t), t)\frac{dx}{dt}.$$

Comparing this with (2.1), it can be seen that $\frac{du}{dt} = 0$ along the curves defined by $\frac{dx}{dt} = c$. This is equivalent to saying u is a constant on lines where $x - ct = \zeta$, where ζ is a constant and represents what is called the characteristic curves. So, by plotting lines of constant

values of u (the characteristic curves) it can be seen that $u(x, t) = u(\zeta, 0) = u_0(\zeta) = u_0(x - ct)$ as is demonstrated in Figure 1. This idea can be extended to nonlinear PDEs of the form

$$u_t + c(u)u_x = 0, \quad (2.2)$$

with initial conditions $u(x, 0) = u_0(x)$. By defining characteristic curves in the same way, $\frac{dx}{dt} = c(u)$, We arrive at

$$\frac{du}{dt} = u_t + \frac{dx}{dt}u_x = u_t + c(u)u_x = 0, \quad (2.3)$$

and hence u is constant along the characteristic curves. Furthermore, it can be found that the characteristic curves are straight lines because

$$\frac{d^2x}{dt^2} = \frac{dc(u)}{dt} = c'(u)\frac{du}{dt} = 0, \quad (2.4)$$

which implies x is of the form $x = At + B$, for arbitrary constants A and B . Hence a similar characteristic diagram as in Figure 1 can be obtained. In cases where ζ , the characteristic curve, is not properly defined, a graphical solution can still be obtained using characteristics. For example, consider the problem

$$u_t + uu_x = 0, \quad (2.5)$$

with initial conditions

$$u(x, 0) = \begin{cases} 0 & x \leq 0 \\ e^{-\frac{1}{x}} & x > 0 \end{cases} \quad (2.6)$$

which represents a wave travelling at the speed of its amplitude and is shown in Figure 2.

By using the method of characteristics it can be seen that the solution is given by

$$u(x, t) = \begin{cases} 0 & x \leq 0 \\ e^{-\frac{1}{\zeta}} & x > 0 \end{cases} \quad (2.7)$$

where ζ is defined implicitly by $x - e^{\frac{-1}{\zeta}} t = \zeta$ for $x > 0$. Even though ζ is not explicitly defined, the behaviour of the solution can be found by considering the lines of constant u as is shown in Figure 3. Recalling that the wave travels at the speed given by its amplitude we can generate the following characteristic diagram, as shown in Figure 3. It can be seen that the wave spreads out over time giving us a rarefaction wave as is shown in Figure 4.

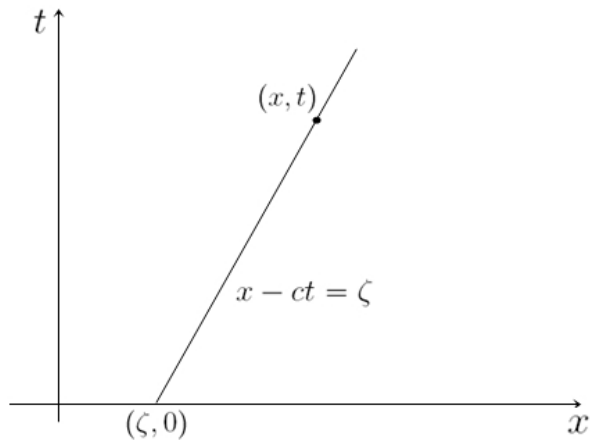


Figure 1: How to find the value of u at an arbitrary point (x, t) .

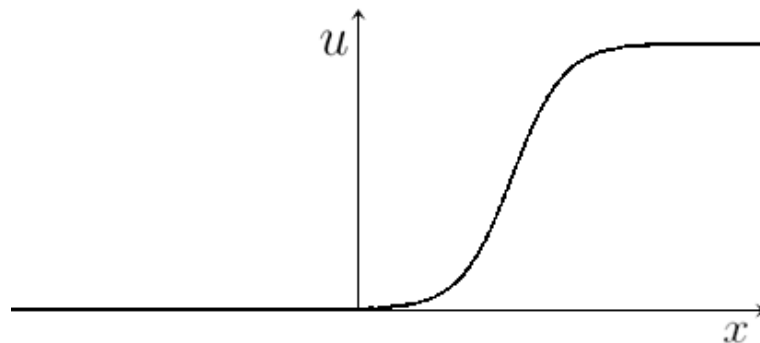


Figure 2: The initial condition defined in (2.6).

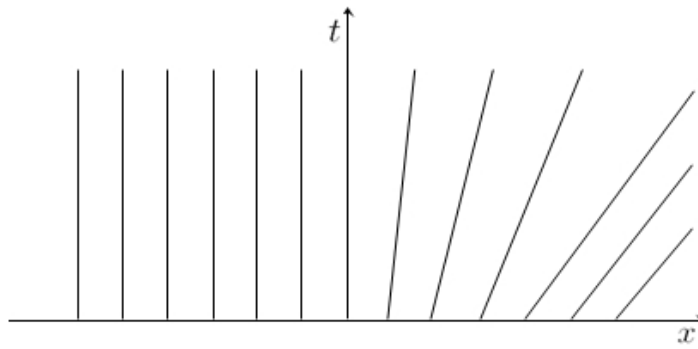


Figure 3: The associated characteristic diagram of (2.5) with initial conditions described in (2.6).

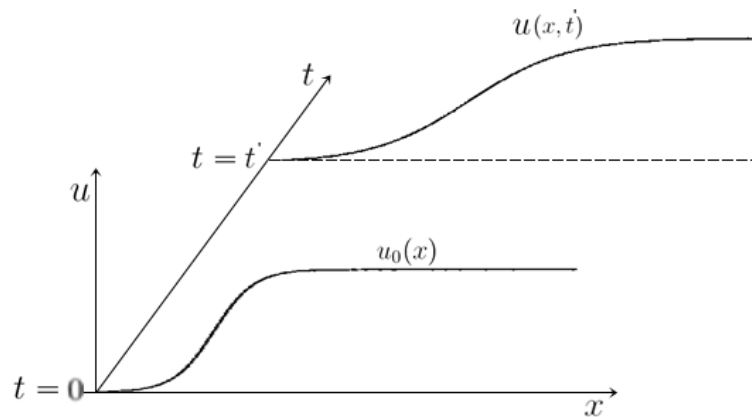


Figure 4: The general solution of (2.5) with initial condition given in (2.6).

2.2 Shock Formation

When dealing with nonlinear PDEs, there is a chance that a discontinuity will appear and it is typically of great interest to find out the position of the discontinuity and its magnitude. So here we shall discuss when, if at all, a discontinuity (or shock) will form. For example, let us re-consider (2.2)

$$u_t + c(u)u_x = 0, \quad \text{where} \quad u(x, 0) = u_0(x).$$

By using the method of characteristics, it can be deduced that u equals a constant on the lines defined by $\frac{dx}{dt} = c(u)$. We want to find out when, if ever, these characteristics will meet and form a shock as illustrated in Figure 5. If two characteristics cross in the (x, t) plane, this implies that there are two different values of u at this point which is equivalent to a shock or discontinuity. In order to determine the breaking time (the time at which

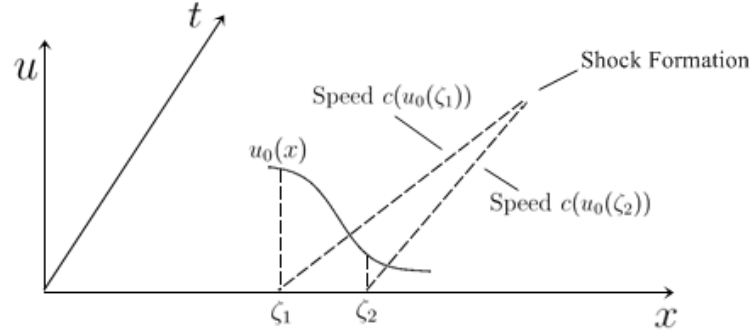


Figure 5: This diagram shows how two distinct parts of the wave can meet at a specific point due to the fact they are travelling at different speeds, leading to a discontinuity in the solution.

a shock or discontinuity occurs), we calculate u_x along a characteristic with the equation $x - \zeta = c(u_0(\zeta))t$. This is because a discontinuity forming is equivalent to the gradient becoming infinite at some point. Now, by letting $g(t) = u_x$ and considering the following the two equations we can arrive at an expression for u_x to determine whether or not a shock will form.

$$0 = \frac{\partial}{\partial x}(u_t + c(u)u_x) = u_{tx} + c(u)u_{xx} + c'(u)u_x^2, \quad (2.8)$$

and

$$\frac{dg}{dt} = g_t + \frac{dx}{dt}g_x = u_{tx} + c(u)u_{xx}. \quad (2.9)$$

By combining (2.8) and (2.9) it can be seen that $-\frac{dg}{dt} = c'(u)g^2$. This can be integrated with respect to t to obtain

$$\int -\frac{dg}{g^2} = \int c'(u)dt \quad \text{which leads to} \quad \frac{1}{g} = c'(u)t + A. \quad (2.10)$$

Now, by applying the initial condition that at $t = 0$, $u_x(x(t), t) = u'_0(\zeta)$, A can be found to obtain the following expression for u_x

$$u_x = \frac{u'_0(\zeta)}{1 + u'_0(\zeta)c'(u_0(\zeta))t}. \quad (2.11)$$

For a shock to occur, we require u_x to be infinite for some finite t . This is equivalent to having $u'_0(\zeta)c'(u_0(\zeta))t = -1$ for some finite t . From here, it can be seen that a shock wave will occur if and only if u'_0 and c' have opposite signs. In this case we can determine the times when a shock first forms to be given by

$$t = \min_{\zeta} \left[-\frac{1}{u'_0(\zeta)c'(u_0(\zeta))} \right]. \quad (2.12)$$

As an example of this consider equation (2.5) with an initial condition of a standard waveform as shown in Figure 6. We can determine when a shock will form by plotting its characteristic diagram which is shown in Figure 7 and as can be seen a shock will form after approximately 0.33 seconds.

2.3 Jump Condition

Having determined if and when a shock will form, it is of interest to know how the shock will behave once it has formed. In order to accomplish this a jump condition needs to be

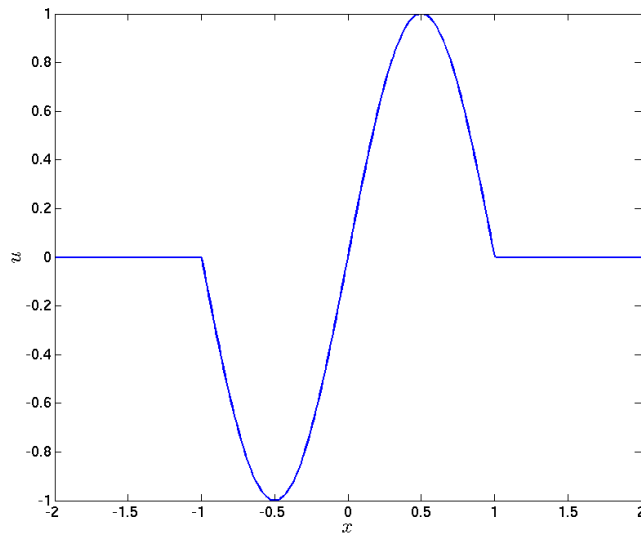


Figure 6: A typical waveform formed by a complete sine wave from -1 to 1 .

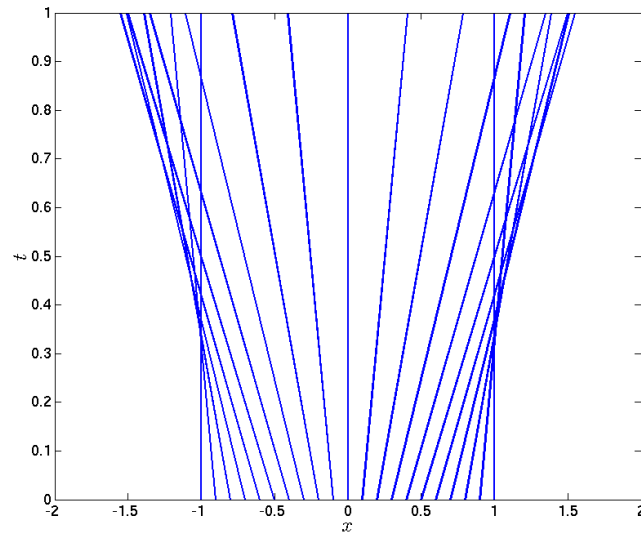


Figure 7: The characteristic diagram for the waveform shown in Figure 6.

developed. We start by observing the integral conservation law which states that in an interval between a and b we have

$$\frac{d}{dt} \int_a^b u(x, t) dx = \phi(a, t) - \phi(b, t), \quad (2.13)$$

where $\phi(x, t)$ is the flux of the particles passing through point x at time t where $u(x, t)$ is the corresponding flow speed. If the functions are suitably smooth, (2.13) is equivalent to

$$u_t + \phi_x = 0. \quad (2.14)$$

Now we consider a shock path at $x = s(t)$, a smooth curve in the x, t plane in which a discontinuity occurs between a and b as shown in Figure 8. From (2.13) we have

$$\frac{d}{dt} \int_a^{s(t)} u(x, t) dx + \frac{d}{dt} \int_{s(t)}^b u(x, t) dx = \phi(a, t) - \phi(b, t). \quad (2.15)$$

Now, applying Leibenz's rule [39] we obtain

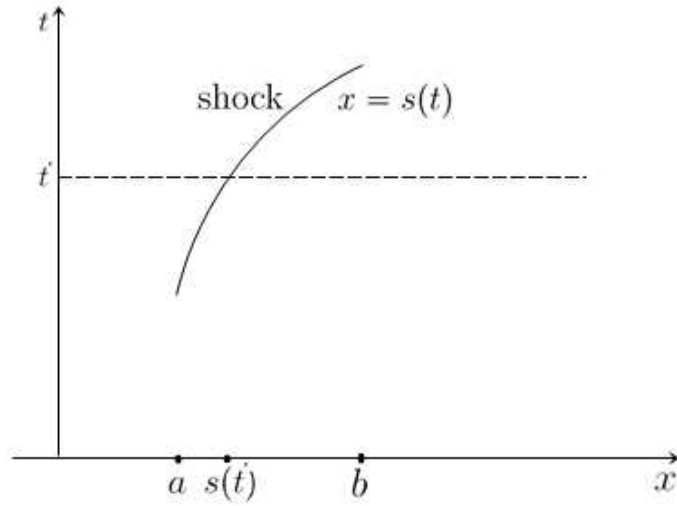


Figure 8: A shock path which propagates a discontinuity between a and b , where $s(t)^-$ represents the value under the shock and $s(t)^+$ represents the value above the shock.

$$\int_a^{s(t)} u_t(x, t) dx + \int_{s(t)}^b u_t(x, t) dx + u(s(t)^-, t) s' - u(s(t)^+, t) s' = \phi(a, t) - \phi(b, t), \quad (2.16)$$

where s' denotes $\frac{ds}{dt}$. Now we let $a \rightarrow s(t)^-$ and $b \rightarrow s(t)^+$ to obtain the jump condition

$$-s'[u] + [\phi(u)] = 0, \quad (2.17)$$

where $[u]$ represents $u(s^+, t) - u(s^-, t)$ and $[\phi(u)]$ is similarly defined. As an example, we can rewrite (2.5) as

$$u_t + uu_x = u_t + \left(\frac{u^2}{2}\right)_x = 0. \quad (2.18)$$

By comparing (2.18) to (2.14), it can be determined that $\phi = \frac{u^2}{2}$. Hence, the jump condition becomes $-s'[u] + \left[\frac{u^2}{2}\right] = 0$ which simplifies to

$$s' = \frac{1}{2}(u^- + u^+). \quad (2.19)$$

So the speed of the shock is the average of the values of u just ahead of and behind of the shock.

3 Burgers' Equation

3.1 Derivation of Burgers' Equation

Having looked at how shocks can form from nonlinear equations such as (2.5), it is of interest to develop equations for sound being propagated through the atmosphere. The key equation for modelling the behaviour of sound waves through the atmosphere is known as Burgers' equations and can be found by following Crighton's derivation of Burgers' equation in his paper 'Model Equations of Nonlinear Acoustics' [12]. Starting from the linearised non-dissipative forms of the equations of motion for a thermally and calorically perfect gas along with equations for conservation of energy and an adiabatic relation between pressure (p) and density (ρ), we have the following equations

$$\frac{\partial \rho}{\partial t} + \rho_0 \nabla \cdot \bar{\mathbf{u}} = 0, \quad (3.1)$$

$$\rho_0 \frac{\partial \bar{u}_i}{\partial t} + \left(\frac{dp}{d\rho} \right)_0 \frac{\partial \rho}{\partial x_i} = 0 \quad \text{and} \quad \frac{p}{p_0} = \left(\frac{\rho}{\rho_0} \right)^\gamma, \quad (3.2)$$

where $\bar{\mathbf{u}}$ is average velocity of the particles, ρ_0 is the initial or background density, p is the pressure and γ is the adiabatic exponent or ratio of specific heats. These equations imply that

$$\left(\frac{\partial^2}{\partial t^2} - a_0^2 \nabla^2 \right) \rho = 0 \quad \text{with} \quad a_0^2 = \frac{\gamma p_0}{\rho_0}, \quad (3.3)$$

which is the standard 1-D wave equation, describing the leading order behaviour of the density. We now consider the correction due to the nonlinear and dissipative effects. It is convenient to work with scalar and vector potentials ϕ and \mathbf{A} , where $\bar{\mathbf{u}} = \nabla \phi + \text{curl} \mathbf{A}$. It can be shown the flow is irrotational which is equivalent to \mathbf{A} being a constant. Hence,

we arrive at the following equation for ϕ

$$-a_0^2 \nu \text{Pr}^{-1} \nabla^4 \phi + \left(2 + \frac{\mu'}{\mu} + \frac{\gamma}{\text{Pr}}\right) \nu \nabla^2 \frac{\partial^2 \phi}{\partial t^2} + \frac{\partial}{\partial t} \left(a_0^2 \nabla^2 \phi - \frac{\partial^2 \phi}{\partial t^2} \right) = \frac{\partial}{\partial t} \left(2 \nabla \phi \cdot \nabla \frac{\partial \phi}{\partial t} + (\gamma - 1) \frac{\partial \phi}{\partial t} \nabla^2 \phi \right) \quad (3.4)$$

where Pr is the Prandtl number, $\nu = \frac{\mu}{\rho_0}$ is the kinematic viscosity and μ is the viscosity.

Using our first order relation we know that $\left(\frac{\partial^2}{\partial t^2} - a_0^2 \nabla^2\right) \phi = 0$ and assuming that the temperature boundary conditions are unimportant we may simplify (3.4) to

$$a_0^2 \nabla^2 \phi - \frac{\partial^2 \phi}{\partial t^2} + \delta \nabla^2 \frac{\partial \phi}{\partial t} = 2 \nabla \phi \cdot \nabla \frac{\partial \phi}{\partial t} + (\gamma - 1) \frac{\partial \phi}{\partial t} \nabla^2 \phi, \quad (3.5)$$

where $\delta = \left(2 + \frac{\mu'}{\mu} + \frac{\gamma-1}{\text{Pr}}\right) \nu$ is known as the diffusivity of sound. Now we proceed to seek solutions for plane, cylindrically symmetric and spherically symmetric cases (solutions will be extended to arbitrary areas later in §10.3). Firstly we note that $\nabla^2 \phi \equiv \phi_{rr} + \frac{j\phi_r}{r}$ where r is the radial distance and $j = 0, 1, 2$ for the plane case, cylindrically and spherically symmetric cases respectively. We also apply a far field condition of the form $k_0 r \gg 1$ where $k_0 = \omega/a_0$ is the acoustic wave number, with ω being the frequency. This ensures that the waves travelling outwards are of the form $F(r - a_0 t)$. By assuming only outgoing waves, we use our first order solution, (3.3), to make the following substitution

$$a_0 \phi_r \approx -\phi_t. \quad (3.6)$$

This substitution allows us to rearrange (3.5) into the form

$$a_0^2 \left(\phi_{rr} + \frac{j\phi_r}{r} \right) - \phi_{tt} + \delta \left(\phi_{trr} + \frac{j\phi_{tr}}{r} \right) = (\gamma + 1) \phi_t \left(\phi_{rr} + \frac{j\phi_r}{r} \right), \quad (3.7)$$

where $j = 0, 1, 2$ corresponds to plane, cylindrically and spherically symmetric cases respectively. Now applying the far field condition, $k_0 r \gg 1$, we can reduce (3.7) to

$$a_0^2 \left(\phi_{rr} + \frac{j\phi_r}{r} \right) - \phi_{tt} + \delta\phi_{trr} = (\gamma + 1)\phi_r\phi_{rt}. \quad (3.8)$$

Now we use the fact that $a_0^2\phi_{rr} - \phi_{tt} = (a_0\frac{\partial}{\partial r} - \frac{\partial}{\partial t})(a_0\frac{\partial}{\partial r} + \frac{\partial}{\partial t})\phi \approx -2(a_0\frac{\partial}{\partial r} + \frac{\partial}{\partial t})\phi_t$ by (3.6) and we can similarly re-express $a_0^2\frac{j\phi_r}{r}$ as $-a_0\frac{j\phi_t}{r}$ giving

$$2 \left(a_0 \frac{\partial}{\partial r} + \frac{\partial}{\partial t} \right) \phi_t + (\gamma + 1)\phi_r\phi_{rt} + \frac{ja_0}{r}\phi_t = \delta\phi_{trr}. \quad (3.9)$$

Now integrating with respect to t and then differentiating with respect to r (recalling that \mathbf{A} is a constant) we arrive at the following expression for \bar{u}

$$\bar{u}_t + a_0\bar{u}_r + \frac{\gamma + 1}{2}\bar{u}\bar{u}_r + \frac{ja_0}{2r}\bar{u} = \frac{\delta}{2}\bar{u}_{rr}. \quad (3.10)$$

This can be simplified further by introducing the following new variables, $\tau = t - \frac{r-r_0}{a_0}$ where τ is the retarded time and $\hat{r} = a_0 t$. This reduces (3.10) to

$$\bar{u}_{\hat{r}} - \frac{\gamma + 1}{2a_0^2}\bar{u}\bar{u}_{\tau} + \frac{j}{2r}\bar{u} = \frac{\delta}{2a_0^3}\bar{u}_{\tau\tau}. \quad (3.11)$$

This equation is now in a form suitable for solving wave propagation problems with an initial value specified. However, we can make more progress with this equation by non-dimensionalising the equation with the following dimensionless variables

$$X = -\omega\tau, \quad R = k_0\hat{r}, \quad \bar{U} = \frac{\gamma + 1}{2a_0}\bar{u}, \quad \epsilon = \frac{\delta\omega}{2a_0^2},$$

where ω is the frequency and k_0 is the acoustic wave number as previously defined. This transforms (3.11) into

$$\bar{U}_R + \bar{U}\bar{U}_X + \frac{j}{2R}\bar{U} = \epsilon\bar{U}_{XX}. \quad (3.12)$$

Now, applying the following transformations

$$\begin{aligned} U &= \bar{U}, & T &= R, & (j &= 0), \\ U &= R^{\frac{1}{2}}\bar{U}, & T &= 2R^{\frac{1}{2}}, & (j &= 1), \\ U &= R\bar{U}, & T &= \ln R, & (j &= 2). \end{aligned}$$

We can express (3.12) in the form

$$U_T + UU_X = \epsilon g(T)U_{XX}. \quad (3.13)$$

where

$$g(t) = \begin{cases} 1 & j = 0 \\ \frac{1}{2}(T + T_0 - 1) & j = 1 \\ \exp\left(\frac{T}{T_0}\right) & j = 2 \end{cases} \quad (3.14)$$

This result corresponds to equation (31) in [12] and now gives us an equation to be solved in the following sections.

3.2 Exact solution to the plane case

In the plane case (where $g(T) = 1$) we can find an exact solution to (3.13) by using the well known Cole-Hopf transformation [28, 10]. If we let $U = \psi_X$ and integrate with respect to X , (3.13) becomes

$$\psi_T + \frac{1}{2}\psi_X^2 = \epsilon\psi_{XX}. \quad (3.15)$$

Now, by letting $\psi = -2\epsilon \ln \varphi$ so that $U = -2\epsilon \frac{\psi_X}{\varphi}$, we arrive at

$$\frac{\partial}{\partial T}(-2\epsilon \ln \varphi) + \frac{1}{2} \left(\frac{\partial}{\partial X}(-2\epsilon \ln \varphi) \right)^2 = \epsilon \frac{\partial^2}{\partial X^2}(-2\epsilon \ln \varphi), \quad (3.16)$$

$$-2\epsilon \frac{\varphi_T}{\varphi} + 2\epsilon^2 \left(\frac{\varphi_X}{\varphi} \right)^2 = -2\epsilon^2 \left(\frac{\varphi_{XX}}{\varphi} - \frac{\varphi_X^2}{\varphi^2} \right), \quad (3.17)$$

$$\varphi_T = \epsilon \varphi_{XX}. \quad (3.18)$$

Equation (3.18) is the heat equation for which a general solution is known of the form

$$\varphi(X, T) = \frac{1}{\sqrt{4\pi\epsilon T}} \int_{-\infty}^{\infty} \exp \left[\frac{-(X-Y)^2}{4\epsilon T} \right] f(Y) dY, \quad (3.19)$$

where $\varphi(X, 0) = f(X)$. Finally, we can arrive at an analytical expression for U by using that $U = -2\epsilon \frac{\psi_X}{\varphi}$. We already have an expression for φ and one for φ_X can be found by simply differentiating (3.19) with respect to X . From the initial condition $U(X, 0) = U_0(X)$, it can be seen that

$$\varphi(X, 0) = \varphi_0(X) = \exp \left(\frac{-1}{2\epsilon} \int_0^X U_0(Y) dY \right). \quad (3.20)$$

Now, recalling that $U = -2\epsilon \frac{\psi_X}{\varphi}$ we arrive at

$$U(X, T) = \frac{\int_{-\infty}^{\infty} \varphi_0(Y) \left(\frac{X-Y}{T} \right) \exp \left(\frac{-(X-Y)^2}{4\epsilon T} \right) dY}{\int_{-\infty}^{\infty} \varphi_0(Y) \exp \left(\frac{-(X-Y)^2}{4\epsilon T} \right) dy}. \quad (3.21)$$

This exact solution in the plane case will later be used as a method of validating the numerical method developed to solve Burgers' equation. Once the numerical method has been validated, it can be used in more advanced cases where an exact solution is not available. Cases considered later in this thesis include cylindrical and spherical spreading

and other cases where we include further effects (e.g. density stratification and molecular relaxation).

4 Asymptotic Analysis

Having previously seen that sine wave disturbance will lead to the formation of a shock in the presence of nonlinear effects (see Figures 6 and 7). We can extend this to say that any sound wave will eventually form, what is called an N-wave shock as is shown in Figure 9. Eventually a balance will form between the nonlinear terms and the diffusive terms keeping the N-wave in balance for a considerable length of time. This N-wave is of great interest and is the focus of this section.

We consider the governing equation for $U(X, T)$ in the form

$$\frac{\partial U}{\partial T} + U \frac{\partial U}{\partial X} = \epsilon G(T) \frac{\partial^2 U}{\partial X^2}, \quad (4.1)$$

where $G(T)$ is given by (3.14), with T_0 is taken to be 1 in the cylindrical and spherical cases (T_0 is a representation of the initial conditions of the sonic boom's formation and for the cases of a sonic boom being propagated in the atmosphere by an aircraft we typically have that $\epsilon \ll 1$ and $T_0 = O(1)$). For the plane case, an exact solution for arbitrary initial conditions is available via the Cole-Hopf transform as shown in §3.2, while for the cylindrical and spherical cases no general solutions are available. However, for many practical purposes, such as the propagation of sonic booms through the atmosphere, we have $\epsilon \ll 1$ which then allows us to perform asymptotic analysis. For an initial disturbance, $U(X, 1)$, which is an odd function of X with $U \rightarrow 0$ as $|X| \rightarrow \infty$, nonlinear wave steepening leads to the appearance of shocks at some finite time and then weak shock theory predicts that the disturbance takes on the form of an N-wave at later times. Of prime importance is the range of validity of the N-wave with embedded shock and the particular shock structure. This is the main purpose of this chapter.

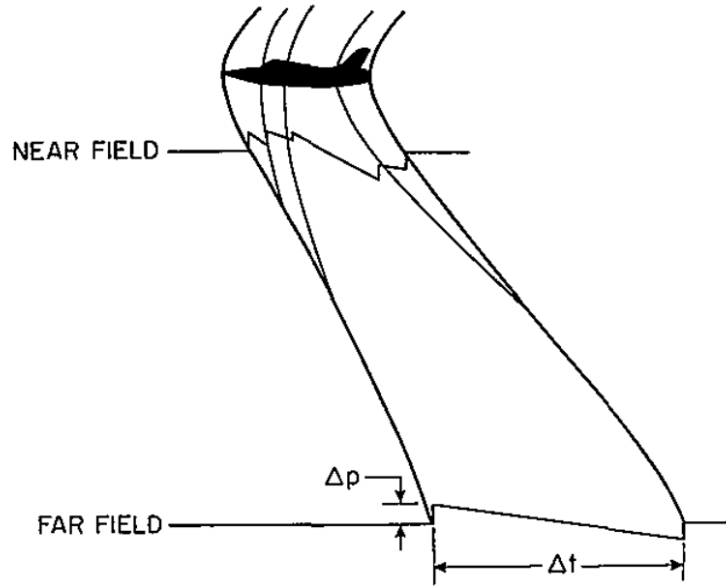


Figure 9: An example showing the waveform close to, and far from, a supersonic aircraft. Taken from Figure 17, [15].

Rather than using the method of characteristics to analyse the evolution of the solution up to the formation of the N-wave, we choose to take a unit N-wave as the initial condition

$$U(X, 1) = \begin{cases} X, & \text{if } |X| < 1, \\ 0, & \text{otherwise,} \end{cases} \quad (4.2)$$

and then ignore the small embryo shock region in which the discontinuity is resolved into a viscosity controlled shock.

4.1 Weak Shock Theory

In order to get an idea of the general behaviour of the shock with $\epsilon \ll 1$, we use weak shock theory. Here we consider the behaviour of the wave with $\epsilon = 0$. Solving (4.1), subject to

initial condition (4.2) for $\epsilon = 0$, gives us a solution of

$$U(X, 1) = \begin{cases} X/T, & \text{if } |X| < T^{\frac{1}{2}}, \\ 0, & \text{otherwise,} \end{cases} \quad (4.3)$$

This corresponds to weak shock theory predicting an N-wave with shocks located at $X = \pm T^{1/2}$ with corresponding amplitudes $\pm T^{-1/2}$. However, this solution is only valid when U_{XX} is not large. It can be seen that U_{XX} is large around the shocks so we need an inner solution around $x = \pm 1$, along with the outer solution of 4.3. These embedded shocks are controlled by thermoviscosity and the structure of these shocks can be obtained directly from the asymptotic analysis of Crighton & Scott [13]. However, rather than reproducing these results, we choose to present a condensed analysis in terms of the new variables,

$$x = T^{-\frac{1}{2}}X, \quad u = T^{\frac{1}{2}}U, \quad t = \ln T.$$

This rescaling results in weak shock theory predicting a static, unit N-wave which will highlight any small changes of the shock structure, therefore making analysis of the shock simpler. The change of time variable is of lesser importance and chosen merely to simplify the governing equation to be solved numerically.

In terms of these new variables, the generalised Burgers equation (4.1) reduces to

$$u_t = \frac{u}{2} + \left(\frac{x}{2} - u\right) u_x + \epsilon g(t) u_{xx}, \quad g(t) = \begin{cases} 1, & \text{Plane,} \\ \frac{1}{2} \exp(t), & \text{Cylindrical,} \\ \exp(\exp(t)), & \text{Spherical.} \end{cases} \quad (4.4)$$

This equation will now be referred to as the modified general Burgers' equation. Taking

an initial condition of a unit N-wave as before, the outer solution then becomes

$$u(x, t) = \begin{cases} x, & \text{if } |x| < 1, \\ 0, & \text{otherwise.} \end{cases} \quad (4.5)$$

Having developed an outer solution of $u = x$ for $|x| < 1$, we will now develop an inner solution. Considering the shock at $x = 1$, we introduce a change of variables of the form of $x = 1 + \epsilon \hat{x}$. In order to match the inner and outer solutions together we require the boundary conditions that $u \rightarrow 0$ as $\hat{x} \rightarrow \infty$ and $u \rightarrow 1$ as $\hat{x} \rightarrow -\infty$. Making this change of variable converts (4.4) into

$$u_T = \frac{1}{\epsilon} \frac{\partial}{\partial \hat{x}} \left[\frac{1}{2}((1 + \epsilon \hat{x})u - u^2) + g(t)u_{\hat{x}} \right] = \frac{1}{\epsilon} \frac{\partial}{\partial \hat{x}} \left[\frac{1}{2}(u - u^2) + g(t)u_{\hat{x}} + \frac{1}{2}\epsilon \hat{x}u \right]. \quad (4.6)$$

It is now assumed that $\epsilon \ll 1$ and an expression for the leading order behaviour of $u = \hat{u} + \epsilon \hat{v}$ can be found by considering the terms of order ϵ^{-1} giving

$$\frac{\partial}{\partial \hat{x}} \left[\frac{1}{2}(\hat{u} - \hat{u}^2) + g(t)\hat{u}_{\hat{x}} \right] = 0. \quad (4.7)$$

Now, integrating with respect to \hat{x} gives

$$\frac{1}{2}(\hat{u} - \hat{u}^2) + g(t)\hat{u}_{\hat{x}} = a(t), \quad (4.8)$$

which gives a solution of the form $u = A(t) \tanh(B(t)(\hat{x} + f(t))) + D(t)$. By applying the boundary conditions that as $\hat{x} \rightarrow \infty$, $u \rightarrow 0$ and as $\hat{x} \rightarrow -\infty$, $u \rightarrow 1$ it can be obtained

that $A(t) = -\frac{1}{2}$ and $D(t) = \frac{1}{2}$. Inserting this solution for \hat{u} into equation (4.8) gives

$$\frac{1}{2} \left[\frac{1}{4} - \frac{1}{4} \tanh^2(B(t)(\hat{x} + f(t))) \right] - \frac{g(t)B}{2} (1 - \tanh(B(t)(\hat{x} + f(t)))) = a(t). \quad (4.9)$$

Taking the limit as $\hat{x} \rightarrow \infty$ it can be obtained that $a(t) = 0$ and by simple matching it can also be found that $\frac{1}{8} - \frac{g(t)B}{2} = 0$ which gives $B = \frac{1}{4g(t)}$. This leads us to the expression for the leading order behaviour of u , \hat{u}

$$\hat{u} = \frac{1}{2} \left[1 - \tanh \left(\frac{\hat{x} + f(t)}{4g(t)} \right) \right], \quad (4.10)$$

or in terms of x

$$\hat{u} = \frac{1}{2} \left[1 - \tanh \left(\frac{x - 1 + \epsilon f(t)}{4\epsilon g(t)} \right) \right], \quad (4.11)$$

where (4.8) can also be solved using the method of separation of variables.

Now, in order to find $f(t)$ it is necessary to set $\theta = \frac{\hat{x} + f(t)}{4g(t)}$ based on equation (4.10). This will have the effect of simplifying (4.6) when trying to find the leading order asymptotic terms of $u = \hat{u} + \epsilon \hat{v}$. Making the substitution $\theta = \frac{\hat{x} + f(t)}{4g(t)}$ changes the boundary conditions to

$$\lim_{\theta \rightarrow \infty} u = 0 \quad (4.12)$$

$$\lim_{\theta \rightarrow -\infty} u = 1. \quad (4.13)$$

Now, by applying the chain rule, expressions for $\frac{\partial}{\partial t}$ and $\frac{\partial}{\partial \hat{x}}$ can be found in terms of θ and

t as is shown below

$$\begin{aligned}\frac{\partial}{\partial t} &= \frac{\partial}{\partial \theta} \frac{\partial \theta}{\partial t} + \frac{\partial}{\partial t} \frac{\partial t}{\partial t} = \left(\frac{f'}{4g} - \frac{\theta g'}{g} \right) \frac{\partial}{\partial \theta} + \frac{\partial}{\partial t}. \\ \frac{\partial}{\partial \hat{x}} &= \frac{\partial}{\partial \theta} \frac{\partial \theta}{\partial \hat{x}} = \frac{1}{4g} \frac{\partial}{\partial \theta}.\end{aligned}\tag{4.14}$$

Inserting the results of equation (4.14) into (4.6) we get

$$u_t - \left(\frac{\theta g'}{g} - \frac{f'}{4g} \right) u_\theta = \frac{1}{4\epsilon g} \frac{\partial}{\partial \theta} \left[\frac{1}{2}(u - u^2) + \frac{g}{4g} u_\theta + \frac{1}{2}\epsilon(4g\theta - f)u \right],\tag{4.15}$$

which can be re-expressed as

$$u_t + \frac{ug'}{g} - \left(\frac{\partial}{\partial \theta} \left(\frac{\theta ug'}{g} \right) - \frac{\partial}{\partial \theta} \left(\frac{f' u}{4g} \right) \right) = \frac{1}{4\epsilon g} \frac{\partial}{\partial \theta} \left[\frac{1}{2}(u - u^2) + \frac{g}{4g} u_\theta + \frac{1}{2}\epsilon(4g\theta - f)u \right].\tag{4.16}$$

And after further simplification (4.16) becomes

$$u_t + \frac{ug'}{g} = \frac{1}{4g} \frac{\partial}{\partial \theta} \left[\left((2g + 4g')\theta - \frac{f}{2} - f' \right) u + \frac{1}{4\epsilon} (2(u - u^2) + u_\theta) \right].\tag{4.17}$$

Now a series expansion of the form $u = \hat{u} + \epsilon \hat{v} + O(\epsilon^2)$ is sought. Doing this leads us the following form of (4.17),

$$\hat{u}_t + \frac{\hat{u}g'}{g} = \frac{1}{4g} \frac{\partial}{\partial \theta} \left[\left((2g + 4g')\theta - \frac{f}{2} - f' \right) \hat{u} + \frac{1}{4\epsilon} (2(\hat{u} - \hat{u}^2) + \hat{u}_\theta) + \frac{1}{4} (2\hat{v} - 4\hat{u}\hat{v} + \hat{v}_\theta) \right],\tag{4.18}$$

where terms of $O(\epsilon)$ or higher have been ignored. By comparing all the terms of order ϵ^{-1} in (4.18) we get

$$0 = \frac{\partial}{\partial \theta} \left[(2(\hat{u} - \hat{u}^2) + \hat{u}_\theta) \right].\tag{4.19}$$

Equation (4.19) has the solution previously found in (4.10), $\hat{u} = \frac{1}{2}(1 - \tanh(\theta))$. Now, comparing the terms of order 1 in (4.18) gives

$$\hat{u}_t + \frac{\hat{u}g'}{g} = \frac{1}{4g} \frac{\partial}{\partial \theta} \left[\left((2g + 4g')\theta - \frac{f}{2} - f' \right) \hat{u} + \frac{1}{4} (2\hat{v} - 4\hat{u}\hat{v} + \hat{v}_\theta) \right]. \quad (4.20)$$

Noting that $\hat{u}_t = 0$ and rearranging gives

$$\left((2g + 4g')\theta - \frac{f}{2} - f' \right) \hat{u} + \frac{1}{4} (2\hat{v} - 4\hat{u}\hat{v} + \hat{v}_\theta) = 4g' \left(\int \hat{u} d\theta \right). \quad (4.21)$$

Integrating \hat{u} gives $\int \hat{u} = \frac{1}{2} (\theta - \ln(\cosh \theta) + \hat{A})$. \hat{A} can be deduced by observing equation (4.21) in the limit of $\theta \rightarrow \infty$ and it can be deduced that $\hat{A} = -\ln 2$ giving

$$\left((2g + 4g')\theta - \frac{f}{2} - f' \right) \hat{u} + \frac{1}{4} (2\hat{v} - 4\hat{u}\hat{v} + \hat{v}_\theta) = 2g'(\theta - \ln(\cosh \theta) - \ln 2). \quad (4.22)$$

Letting $A = 8g + 16g'$, $B = -4f' - 2f$ and $C = 16g'$ and inserting $\hat{u} = \frac{1}{2}(1 - \tanh \theta)$ into (4.22) results in

$$\hat{v}_\theta + 2\hat{v} \tanh \theta = -\frac{A}{2}\theta(1 - \tanh \theta) - \frac{B}{2}(1 - \tanh \theta) - \frac{C}{2}(\ln(\cosh \theta) + \ln 2 - \theta). \quad (4.23)$$

Solving this, we arrive at

$$\begin{aligned} \hat{v} = & \frac{1}{\cosh^2 \theta} \left(K(t) + \frac{1}{16} \left[A (2\theta \cosh(2\theta) - 2\theta \sinh(2\theta) + \cosh(2\theta) - \sinh(2\theta) - 2\theta^2) \right. \right. \\ & + B (2 \cosh(2\theta) - 2 \sinh(2\theta) - 4\theta + 2) + C \left(2\theta \sinh(2\theta) - \text{dilin}(-e^{-2\theta}) \right. \\ & - \cosh(2\theta) + \sinh(2\theta) + 4\theta \ln \left(\frac{e^{-2\theta} + 1}{2} \right) - 4\theta \ln(\cosh(\theta)) \\ & \left. \left. \left. - 2 \sinh(2\theta) \ln(2 \cosh(\theta)) + 4\theta^2 - 2\theta \right) \right] \right), \end{aligned} \quad (4.24)$$

where dilin denotes the dilogarithm, $\text{dilin}(x) = -\int_1^x \frac{\ln t}{t-1} dt$. If we now take the limit of v as $\theta \rightarrow +\infty$, we arrive at

$$\lim_{\theta \rightarrow \infty} \hat{v} = 0,$$

and the boundary condition (4.13) is automatically satisfied. Similarly, letting $\theta \rightarrow -\infty$ gives

$$\lim_{\theta \rightarrow -\infty} \hat{v} = \left(\frac{1}{2}\theta + \frac{1}{4}\right) A + \frac{1}{2}B - \left(\frac{1}{2}\theta + \frac{1}{4}\right) C. \quad (4.25)$$

We can now insert the values of A , B , and C to transform (4.25) into

$$\lim_{\theta \rightarrow -\infty} \hat{v} = 4g\theta + 2g - 2f' - f, \quad (4.26)$$

Hence, we arrive at the following form for u as $\theta \rightarrow -\infty$

$$\lim_{\theta \rightarrow -\infty} u = 1 + \epsilon(4g\theta + 2g - 2f' - f). \quad (4.27)$$

Now we match (4.27) to the outer solution (4.5), $u = x = 1 + \epsilon\hat{x}$. From the definition of θ we have $\theta = \frac{\hat{x}+f}{4g}$. So (4.5) becomes

$$u = 1 + \epsilon(4g\theta - f), \quad (4.28)$$

and by comparing (4.27) and (4.28) we arrive at

$$2g - 2f' = 0 \quad (4.29)$$

Solving this for $g(t) = 1$, $\exp(t) + \exp(t_0) - 1/2$, $\exp(\exp(\frac{t}{t_0}))$, we get the following values of $f(t) = t$, $\frac{\exp(t)-1+(\exp(t_0)-1)t}{2}$, $\text{Ei}(\exp(\frac{t}{t_0}))$ corresponding to the plane, cylindrical and

spherical cases respectively. Inserting this result into equation (4.11) we get

$$u = \frac{1}{2} \left[1 - \tanh \left(\frac{x - (1 - \epsilon \int g(t))}{4\epsilon g(t)} \right) \right]. \quad (4.30)$$

These results correspond to the results obtained by Crighton and Scott in equation (3.8) in ‘Asymptotic Solutions of Model Equations in Nonlinear Acoustics’ [13]. Note, due to the anti-symmetric behaviour of Burgers’ equation we only need to consider the shock at $x = 1$ and impose the condition $u(0, t) = 0$ for all time.

The analysis presented in this chapter allows us to make improved observations of the shock structure as it is now fixed at leading order. In addition to this, this analysis puts us in a position where we have a greatly improved capability for numerical solutions which will form a key part of this thesis.

5 Numerical Schemes

There are a variety of possible schemes to use in order to generate a numerical solution to Burgers' equation. A commonly used numerical approach to the solution of nonlinear wave equations is the pseudospectral scheme [21]. Spatial derivatives are evaluated in spectral space, while the nonlinear term is evaluated in physical space and the solution is advanced forward in time in physical space. This approach has been successfully taken in previous work when the main focus was on determining the old-age solution [26, 47], which is the form Burgers' equation takes once the shock has suitably dispersed for the nonlinear term to only have a negligible effect on the waveform. An advantage of this technique is that near discontinuities in the spatial profile at early times are successfully handled, without the need for fine resolution of the shock structure.

Whilst the pseudospectral scheme is useful for the general solution of the shock, we are particularly interested in the exact form the shock takes. This requires fine resolution of the narrow shock region which, in spectral space, means that N , the number of spectral components which must be retained in a pseudospectral scheme, is unfeasibly large. Moreover, in the standard pseudospectral implementation, where the solution is advanced forwards in time via a Taylor series, the stability criterion takes the form $\Delta t < C/N^2$, where C is a constant and Δt is the time-step. Thus combining sufficient spatial resolution with wave evolution over long time scales is computationally expensive. For this reason, it was decided to use an implicit finite difference scheme rather than a pseudospectral scheme. However, there is still the issue of an unfeasibly large number of mesh points, so for the implicit finite difference scheme, we shall also be using a variable spatial mesh to concentrate mesh points around the shocks.

An advantage of the formulation introduced in §4 is that in terms of the new variables, weak shock theory predicts a shock centred at $x = 1$ with unit amplitude. Thus in a variable mesh finite difference scheme the location where a fine mesh is required is known and asymptotic theory predicts the width of this region. However, it was seen in §4 that asymptotic theory predicts that the shock centre moves slightly over long periods of time. For this reason we incorporated mesh refinement into the numerical scheme, where we can redefine the mesh at any point in time. Due to the fact that weak shock theory predicts a static shock does mean that the frequency of mesh refinement required is much reduced. The semi-infinite space, $x > 0$, will be approximated by the region $[0, a]$ where a is the smallest value such that $u(a, t) < 10^{-8}$ (we will require a to change with time according to the behaviour of the shock by either adding in more points according to a linear interpolation scheme or removing unnecessary points). We do not need to consider the region $x < 0$, due to the anti-symmetric behaviour, instead we just need to impose the condition that $u(0, t) = 0$ for all time.

A variable mesh scheme is used here based on the method described by Chong [7], which allows us to concentrate mesh points at the shock's location giving greater resolution of the shock whilst minimising the computational times.

5.1 Implicit Predictor-Corrector Scheme with a Variable Mesh

This following section will detail how the implicit predictor-corrector scheme works. If we take a Taylor series for $u_{i-1} = u(x_{i-1}, t)$ about $x = x_i$, we arrive at

$$u_{i-1} = u_i - h_i \frac{\partial u_i}{\partial x} + \frac{h_i^2}{2!} \frac{\partial^2 u_i}{\partial x^2} - \frac{h_i^3}{3!} \frac{\partial^3 u_i}{\partial x^3} + \frac{h_i^4}{4!} \frac{\partial^4 u_i}{\partial x^4}, \quad (5.1)$$

where $u_i = u(x_i, t)$, $h_i = x_i - x_{i-1}$ and u_i^- is evaluated at some point $x_{i-1} \leq x \leq x_i$.

By obtaining a similar expression for u_{i+1} we arrive at the following expressions for u_x at

$x = x_i$,

$$u_{i,x} = \Delta_x u_i - \frac{h_i h_{i+1}}{3!} u_{i,xxx} + \frac{h_i h_{i+1}}{4!(h_i + h_{i+1})} (h_i^2 u_{i,xxxx}^- - h_{i+1}^2 u_{i,xxxx}^+), \quad (5.2)$$

where $\Delta_x u_i$ is defined by

$$\Delta_x u_i = \frac{-h_{i+1}^2 u_{i-1} - (h_i^2 - h_{i+1}^2) u_i + h_i^2 u_{i+1}}{h_i h_{i+1} (h_i + h_{i+1})}. \quad (5.3)$$

By similar analysis we arrive at the following expression for the second derivative,

$$u_{i,xx} = \Delta_{xx} u_i - \frac{h_{i+1} - h_i}{3} u_{i,xxx} - \frac{h_{i+1}^3 u_{i,xxxx}^+ + h_i^3 u_{i,xxxx}^-}{12(h_i + h_{i+1})}, \quad (5.4)$$

where $\Delta_{xx} u_i$ is defined by

$$\Delta_{xx} u_i = \frac{h_{i+1} u_{i-1} - (h_i + h_{i+1}) u_i + h_i u_{i+1}}{h_i h_{i+1} (h_i + h_{i+1}) / 2}. \quad (5.5)$$

If the last two terms in (5.2) and (5.4) are relatively small we have that

$$u_{i,x} \approx \Delta_x u_i \quad \text{and} \quad u_{i,xx} \approx \Delta_{xx} u_i, \quad (5.6)$$

which can then be used as approximations in our numerical scheme. In order to keep the last two terms in (5.2) and (5.4) relatively small we require h_i to be small in the shock regions in order to keep the third and fourth derivatives small, whereas in the smooth regions we can afford a coarser mesh. Also, the $(h_{i+1} - h_i)$ term in (5.4) informs us that we need to change the mesh sizes gradually in order to keep this term small.

The governing wave equation (4.4) is then solved using an implicit predictor-corrector scheme. The implicit scheme used here is also described by Chong [7] and is designed for equations of the form

$$\delta u_{xx} = F(t_j, u, u_x, u_t), \quad (5.7)$$

at time $t = t_j$, where $u = u(x, t_j)$, $\delta \ll 1$ and F is some arbitrary function. The predictor step is given by

$$\delta(\Delta_{xx})\check{U} = F\left(t_j, u, (\Delta_x)u, \frac{\check{U} - u}{(\Delta t)/2}\right), \quad (5.8)$$

where Δ_t is the timestep, $\check{U} = u(x, t_{j+1/2})$ and $t_{j+1/2} = t_j + \Delta t/2$. From here we have the corrector step of

$$\frac{1}{2}\delta(\Delta_{xx})(\check{V} + u) = F\left(t_{j+1/2}, \check{U}, \frac{1}{2}(\Delta_x)(\check{V} + u), \frac{\check{V} - u}{\Delta t}\right), \quad (5.9)$$

where $\check{V} = u(x, t_{j+1})$ and $t_{j+1} = t_j + \Delta t$. We can solve (5.8) and (5.9) using matrix inversions as shall be demonstrated in the case of the modified general Burgers' equation (4.4). Here (5.7) becomes

$$\epsilon g(t)u_{xx} = u_t + \left(u - \frac{x}{2}\right)u_x - \frac{u}{2}. \quad (5.10)$$

Hence, we have a predictor step of

$$\begin{aligned} \epsilon g(t)(\Delta_{xx})\check{U} &= 2\frac{\check{U} - u}{\Delta t} + \left(u - \frac{x}{2}\right)(\Delta_x)u - \frac{u}{2}, \\ \left(\frac{1}{2}\epsilon g(t)(\Delta t)(\Delta_x)^2 - 1\right)\check{U} &= \frac{\Delta t}{2}\left[\left(u - \frac{x}{2}\right)(\Delta_x)u - \frac{u}{2}\right] - u. \end{aligned} \quad (5.11)$$

We can now solve (5.11) by using the expressions for $\Delta_x u_i$ and $\Delta_{xx} u_i$ found in (5.3) and

(5.5). Now (5.11) can be expressed as a tri-diagonal matrix

$$A\check{\mathbf{U}} = \mathbf{B},$$

where A is the tri-diagonal matrix whose elements are given by the coefficients of \check{U} in (5.11), the spatial derivatives are expressed as in (5.6), $\check{\mathbf{U}}$ is the vector of all the values of \check{U} and \mathbf{B} is the vector given by the right hand side of (5.11). Upon inverting this the matrix A , we can find an expression for $\check{\mathbf{U}}$, which is the values of u after we advance forwards half a time step. Similarly we arrive at a corrector step of

$$\begin{aligned} \frac{1}{2}\epsilon g \left(t + \frac{\Delta t}{2} \right) (\Delta_{xx})(\check{V} + u) &= \frac{\check{V} - u}{\Delta t} + \left(\check{U} - \frac{x}{2} \right) (\check{V} - u)(\Delta_x) - \frac{\check{U}}{2}, \\ \left(\frac{1}{2}\epsilon g \left(t + \frac{\Delta t}{2} \right) (\Delta t)(\Delta_{xx}) - \right. & \\ \left. \frac{\Delta t}{2}(\Delta_x) \left(\check{U} - \frac{x}{2} \right) - 1 \right) \check{V} &= -\frac{1}{2}\epsilon g \left(t + \frac{\Delta t}{2} \right) (\Delta t)(\Delta_{xx})u \\ &+ \frac{\Delta t}{2}(\Delta_x) \left(\check{U} - \frac{x}{2} \right) u - \frac{\Delta t}{2}\check{U} - u, \end{aligned} \quad (5.12)$$

where (5.12) is solved in a similar fashion to (5.11) in order to find \check{V} . The main advantage of using an implicit predictor-corrector scheme is the improved stability criterion, $\Delta t < C(h_i)_{\text{Min}}$, rather than $\Delta t < C(h_i)_{\text{Min}}^2$ of the explicit scheme [7], where h_i is the distance between to adjacent points. This results in significantly faster computational times.

As described in §4, the leading order solution of (4.4) from a unit N-wave involves a shock of unit amplitude centred at approximately $x = 1$ and hence we use a spatial mesh with a fine structure around $x = 1$ and a coarse mesh elsewhere. We define a variable mesh with the step size varying from h_0 (a constant value to be determined, typically $O(10^{-2})$) for the outer solution to $h_0/\max|u_x|$ for the centre of the shock with a gradually changing mesh in between the two regions. The algorithm used to perform this is shown in Figure

10.

One key thing worth noting is that, even though we keep the shock fixed at leading order, the shock may move or change form over time. This will cause our variable mesh to become unsuitable for the current waveform and, as such, at various times we need to re-define the variable mesh. This is accomplished by using cubic spline interpolation to get a uniform mesh and from here re-defining the variable mesh in the same fashion to how we initially set up the variable mesh as shown in Figure 10.

This numerical scheme now needs to be verified. For the planar case we can use the Cole-Hopf transformation (as described in §3.2) which converts the plane Burgers' equation into the linear diffusion equation which can be solved for arbitrary initial conditions. Upon solving the linear diffusion equation we can then transform back into the original variables to arrive at a solution for the plane Burgers' equation. Comparison between the exact solution and the numerical solution was performed on the whole waveform with $\epsilon = 0.001$ with a variable mesh with the mesh size varying from $h = 0.01$ for the outer solution and $h = 0.01/\max|u_x|$ for the centre of the shocks. The two solutions are presented in Figures 11 and 12 and are indistinguishable from each other for all times observed, thus verifying the numerical method described in the plane case.

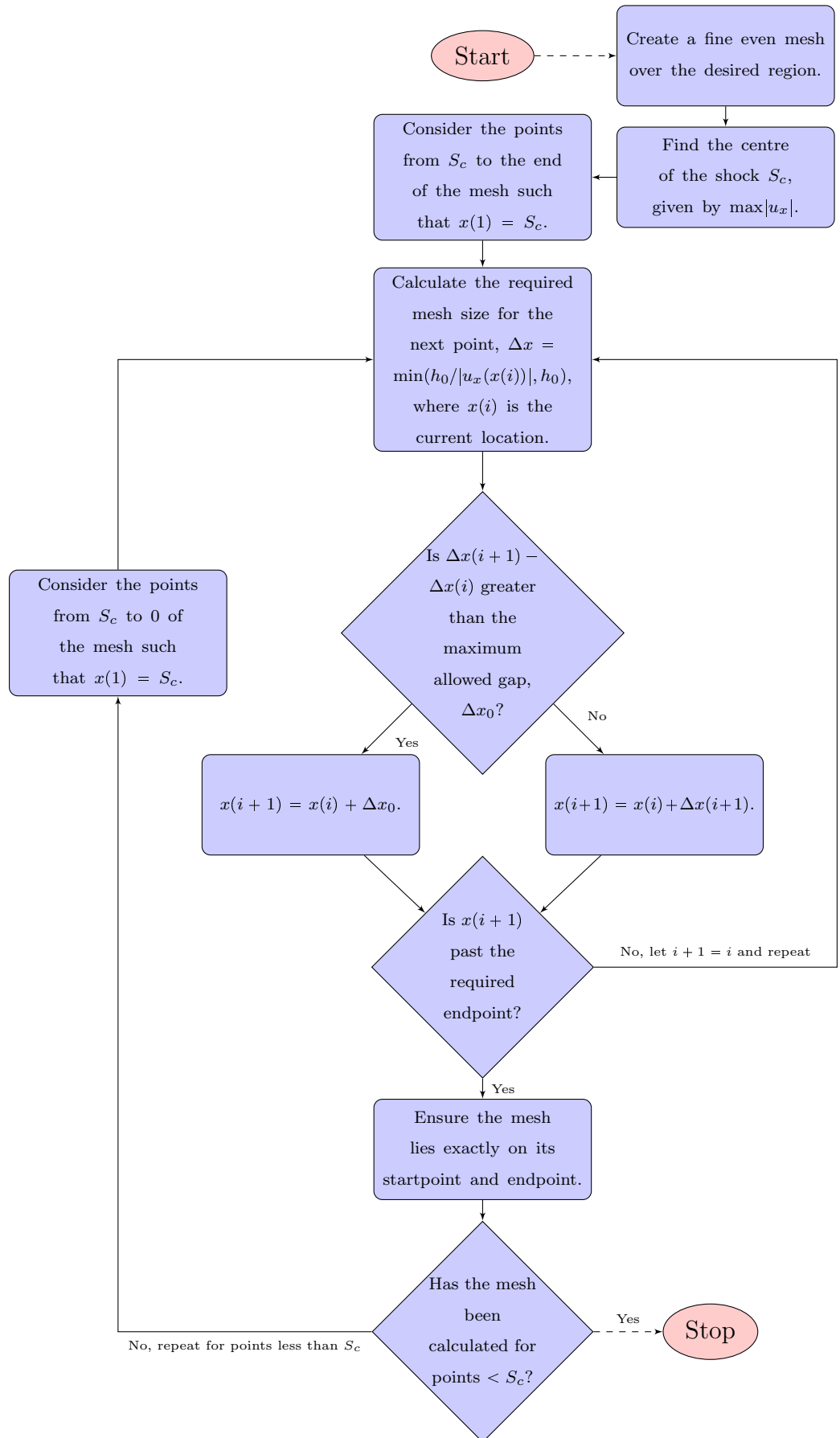


Figure 10: The Rezoning Algorithm.

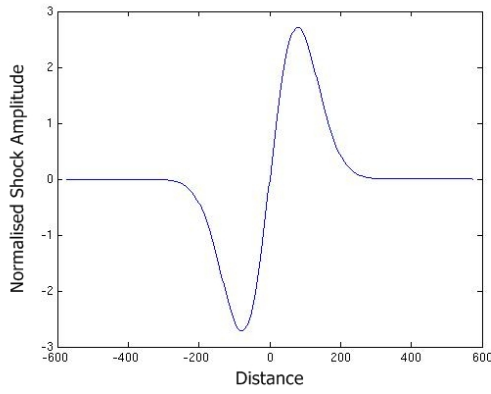


Figure 11: The numerical solution to Burgers' equations in the plane case with $t = 30,000$ and $\epsilon = 0.1$.

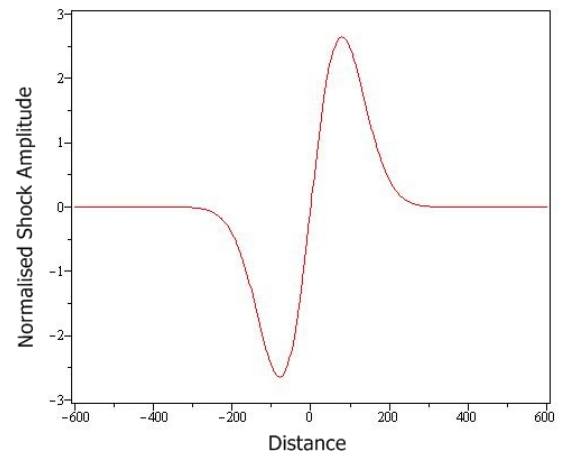


Figure 12: The exact solution to Burgers' equations in the plane case with $t = 30,000$ and $\epsilon = 0.1$.

6 Asymptotic Breakdowns

Asymptotic expressions similar to the one shown in (4.30) have been known for a long time. However, very little work has been done on verifying these expressions to see how accurate these predictions are and exactly when the solution breaks down compared to the asymptotic prediction. This section will take an in depth look at these predictions and how accurate they are. A condensed form of this work has been published in Schofield and Hammerton [49]. Recalling equation (4.30), the general form a shock will take is

$$U = \frac{1}{2} \left[1 - \tanh \left(\frac{X - (1 - \epsilon \int g(\tau) d\tau)}{4\epsilon g(\tau)} \right) \right] + \epsilon v + O(\epsilon^2),$$

where v is represented as

$$v = K(t)f_1(\theta) + \int g(t)dt f_2(\theta) + g(t)f_3(\theta) + g'(t)f_4(\theta). \quad (6.1)$$

Hence, weak shock theory can break down in three possible ways:

- The shock moves far away from its original location (i.e. $\epsilon \int g(t)dt = O(1)$)
- The shock width is no longer small compared to the size of the N-wave (i.e. $\epsilon g(t) = O(1)$)
- The leading order asymptotic solution is no longer significantly larger than the next order correction term (i.e any one of $\epsilon \int g(t)dt, \epsilon g(t), \epsilon g'(t) = O(1)$)

We can now verify these asymptotic results by comparing them to the numerical solutions of Burgers' equations. In particular, we will observe where the breakdowns first take place and find out which condition or conditions have been violated first.

6.1 Plane Waves

For plane waves we have $g(T) = 1$, giving that $\int g(T)dT = T$ and $g'(T) = 0$. Hence the first and third conditions are both violated when $T = O(\epsilon^{-1})$, whereas the second condition is always satisfied. From the leading order behaviour of the modified Burgers' equation we would expect the shock location to move along the path $1 - \epsilon t$ and the shock width to stay constant. We shall numerically define the shock location as the point at which the shock is at 50% of the maximum value of the shock and the shock width shall be defined as the distance between the points where the shock is at 10% and 90% of its maximum. The numerical results can be compared to the asymptotic predictions as is shown in Figures 13, 15 and 17. There is no asymptotic prediction for the shock width in Figures 14, 16 and 18 due to the fact that the asymptotic results only predict that the shock width will stay as a constant, but does not specify the exact value of the constant.

The results for the shock width show that as reduce the value of ϵ , we have better agreement with the asymptotic prediction for the width to stay constant. For the shock location we would expect that reducing the value of ϵ would improve the accuracy. When looking the Figures it can be seen that reducing the value of ϵ shows in improvement comparing Figures 13 and 15. However, this is not true when comparing Figures 15 and 17. This result is unexpected and as such, the asymptotic predictions will be analysed in more depth in §6.4.

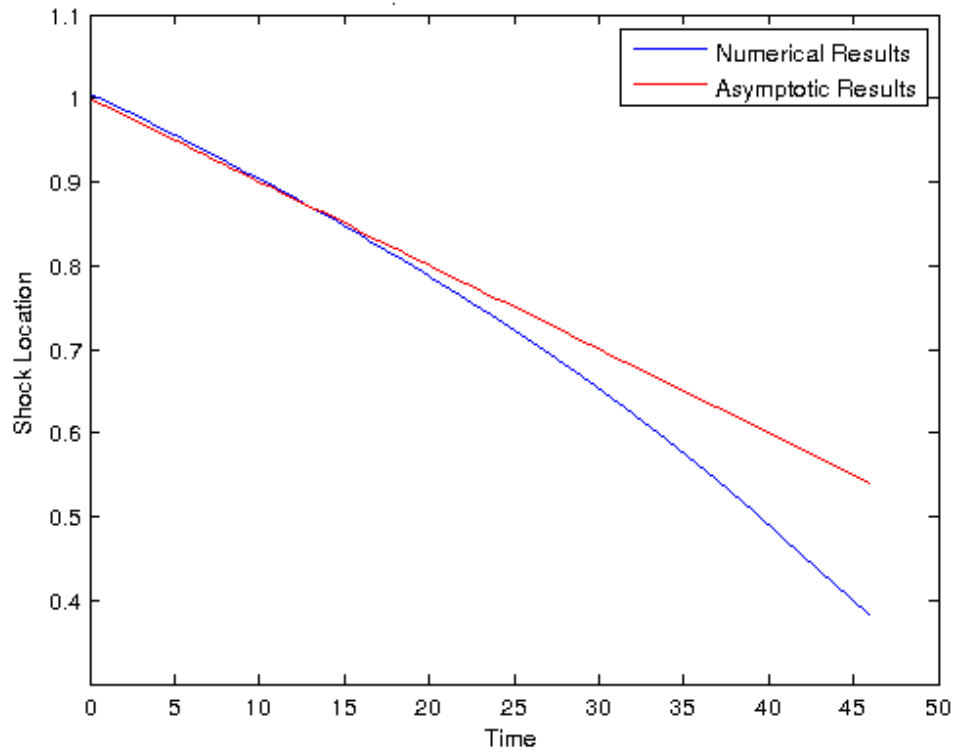


Figure 13: A comparison of the shock location from numerical results and asymptotic predictions for the plane case with $\epsilon = 0.01$

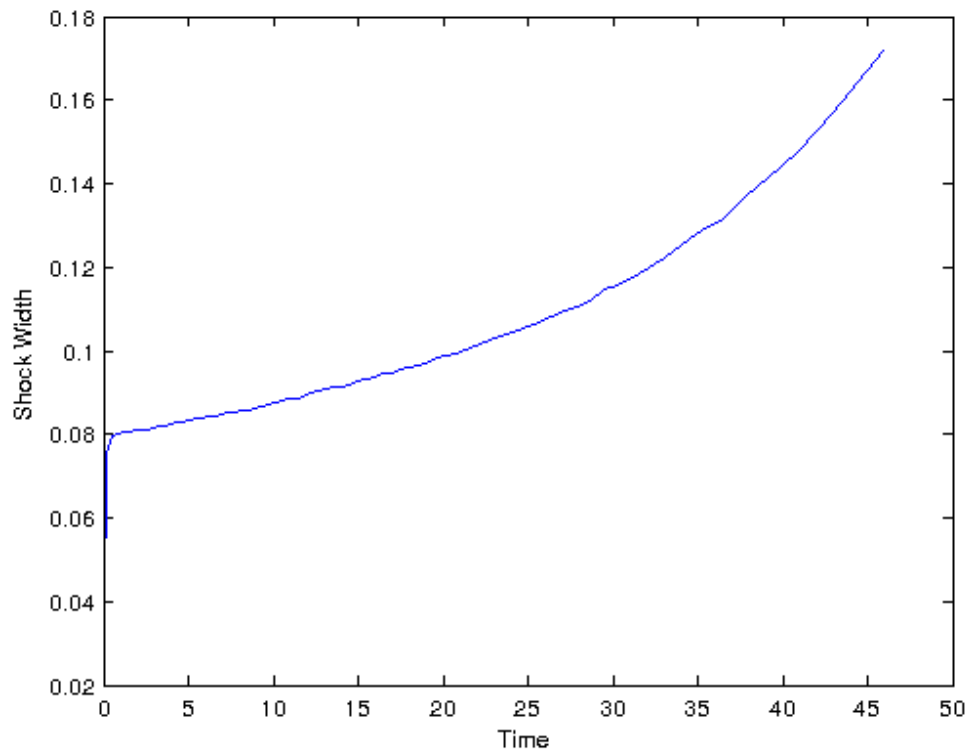


Figure 14: The shock width for the plane case with $\epsilon = 0.01$

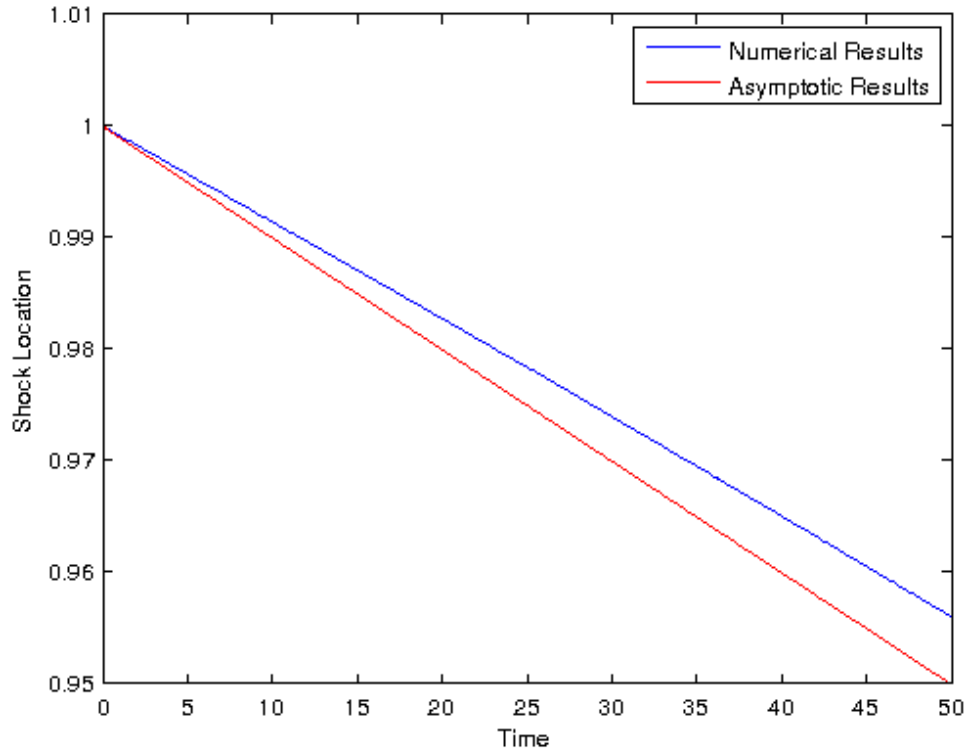


Figure 15: A comparison of the shock location from numerical results and asymptotic predictions for the plane case with $\epsilon = 0.001$

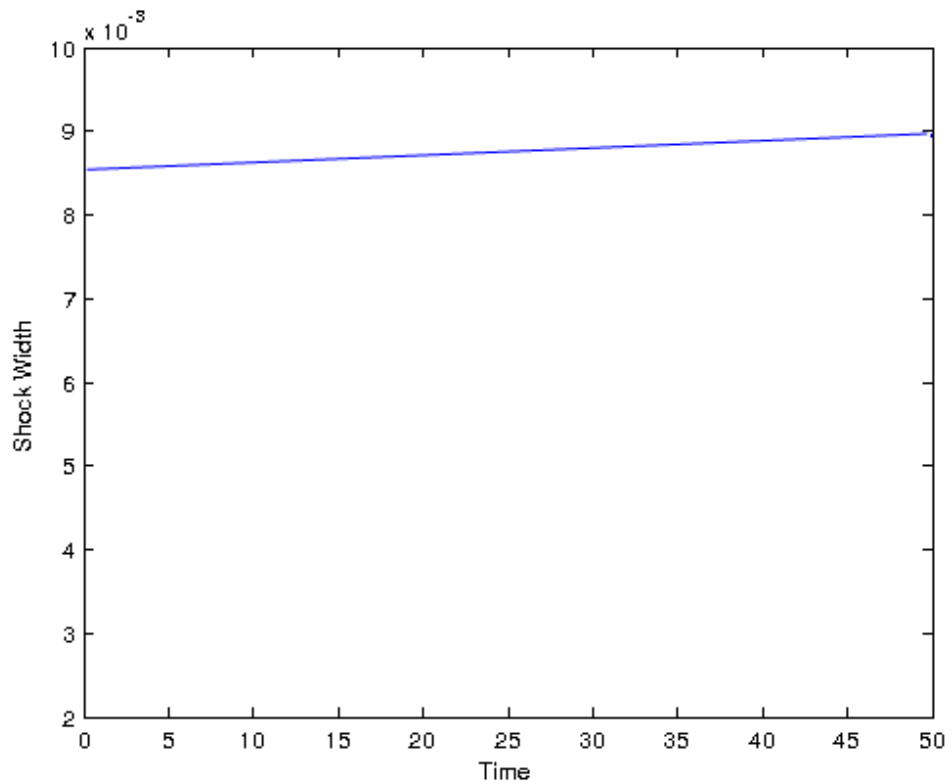


Figure 16: The shock width for the plane case with $\epsilon = 0.001$

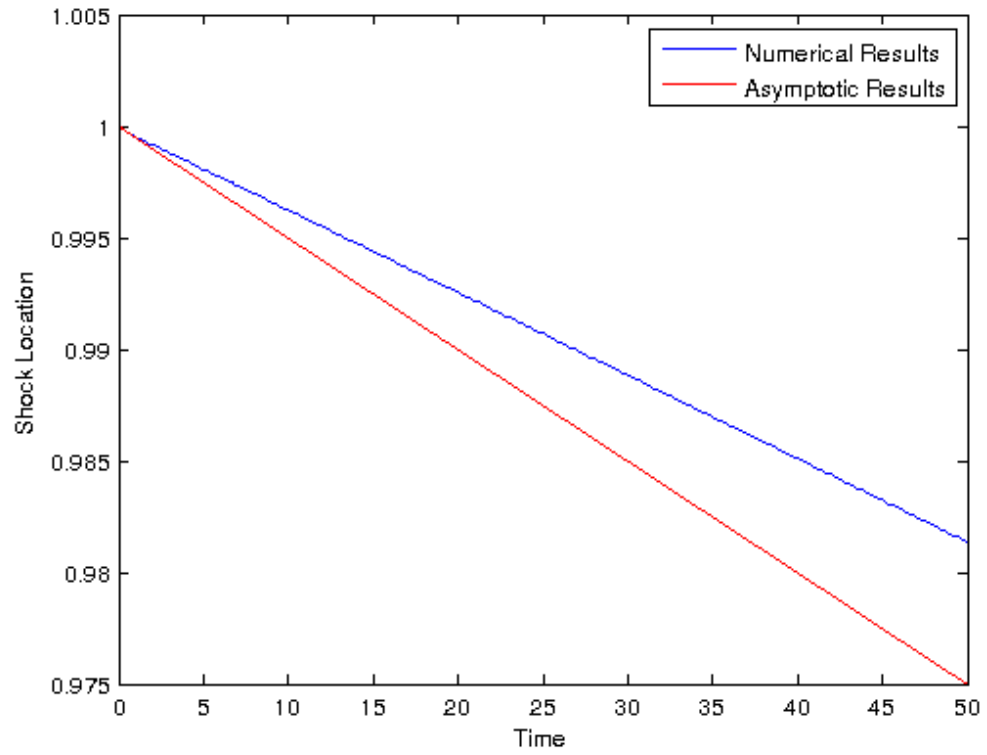


Figure 17: A comparison of the shock location from numerical results and asymptotic predictions for the plane case with $\epsilon = 0.0005$

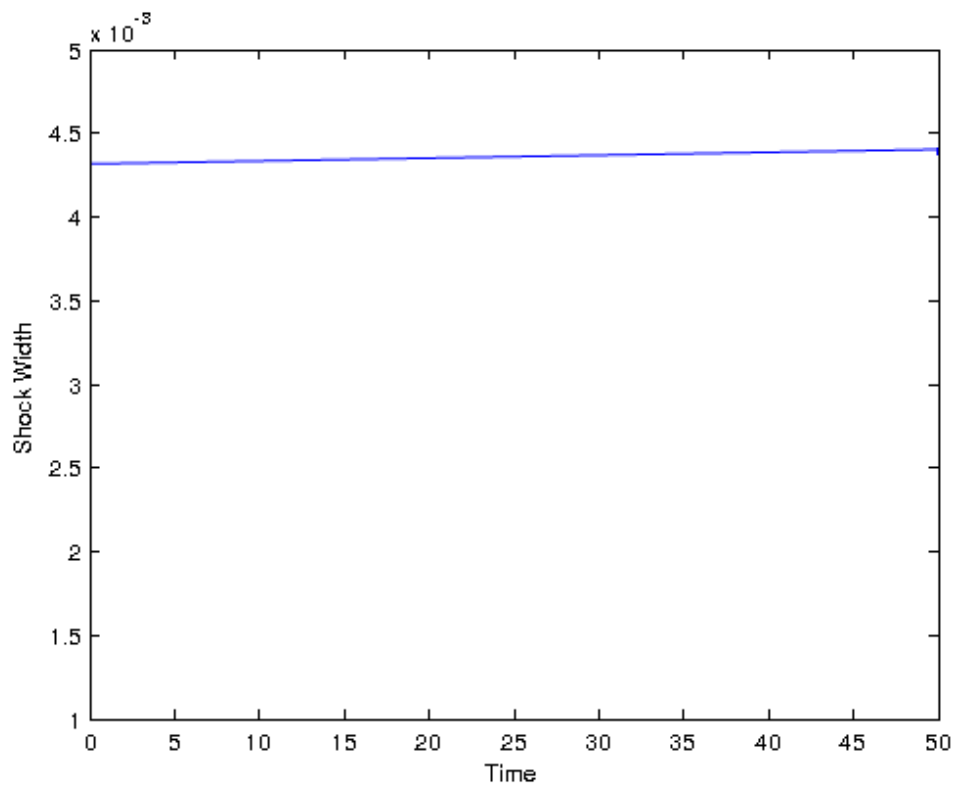


Figure 18: The shock width for the plane case with $\epsilon = 0.0005$

6.2 Cylindrical Waves

For cylindrical waves, we know that $\int g(T)dT = \exp(T)/2$, $g(T) = \exp(T)/2$ and $g'(T) = \exp(T)/2$. Hence the first, second and third condition are all violated when $\tau = O(\log(\epsilon^{-1}))$. Again, by looking at the modified Burgers' equation we would expect the shock location to move along the path $1 - \epsilon \exp(T)/2$ and the shock width to grow like $4\epsilon \exp(T)/2$. The shock location and width shall be defined as for the plane case and the results are shown in Figure 19 to 24. As can be seen agreement improves as ϵ decreases as is expected, however the results are not as accurate as was initially expected which shall be discussed further after we have looked at the spherical case.

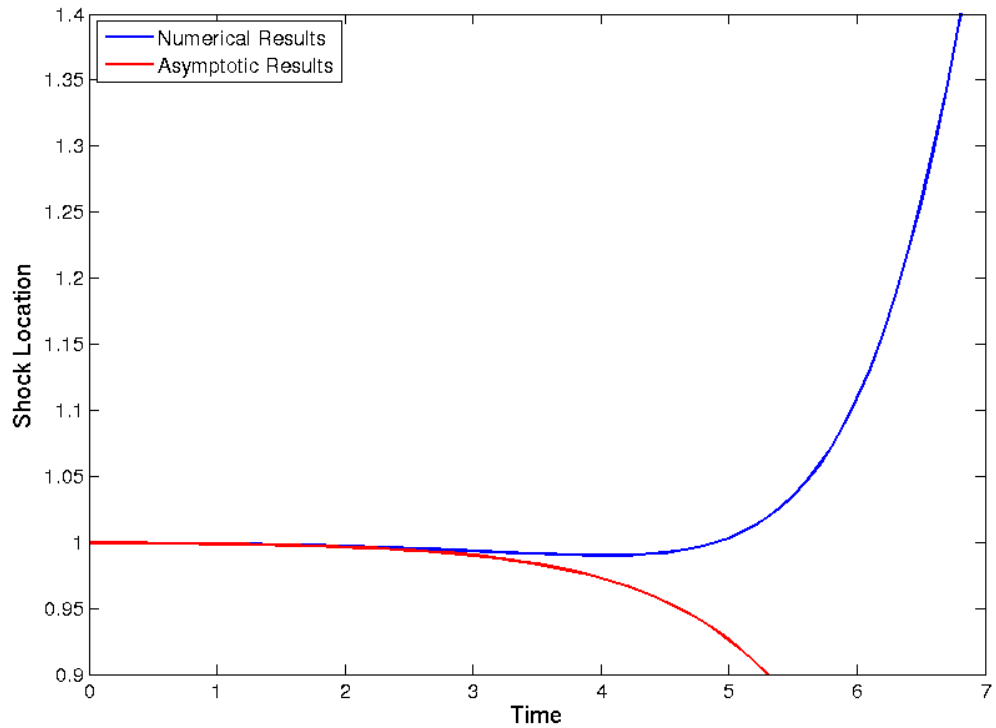


Figure 19: A comparison of the shock location from numerical results and asymptotic predictions for the cylindrical case with $\epsilon = 0.001$.

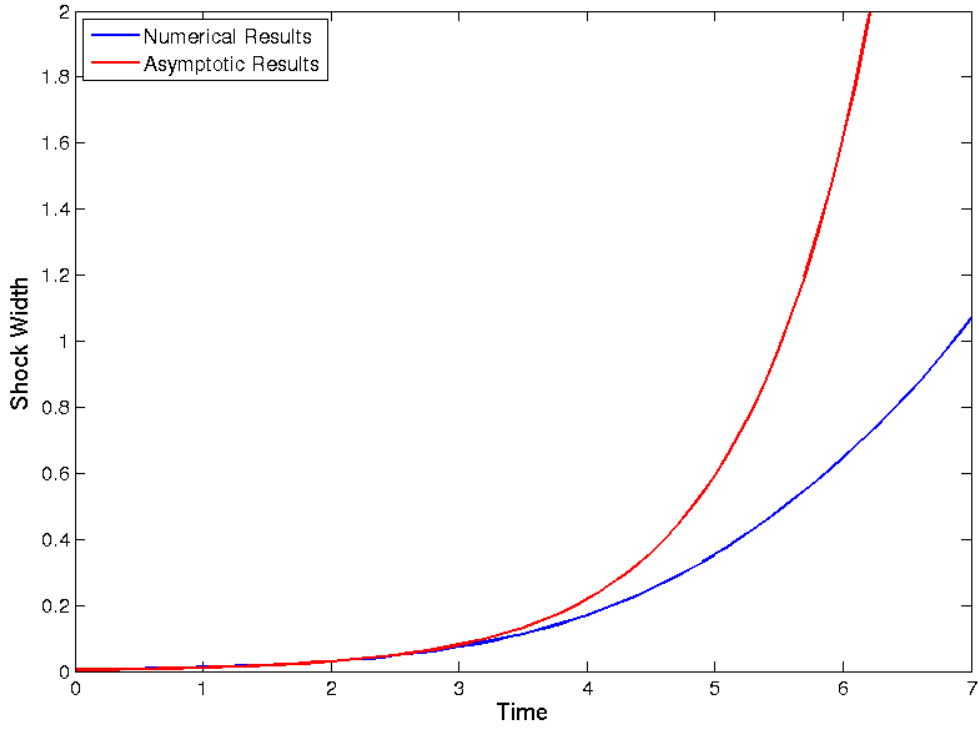


Figure 20: A comparison of the shock width from numerical results and asymptotic predictions for the cylindrical case with $\epsilon = 0.001$.

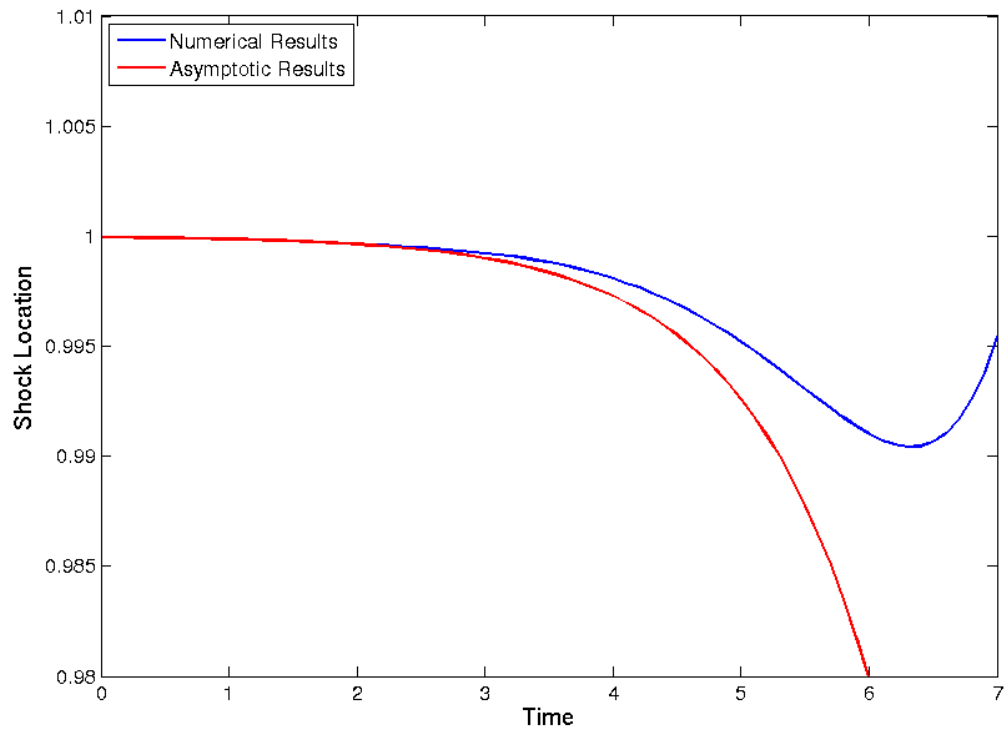


Figure 21: A comparison of the shock location from numerical results and asymptotic predictions for the cylindrical case with $\epsilon = 0.0001$.

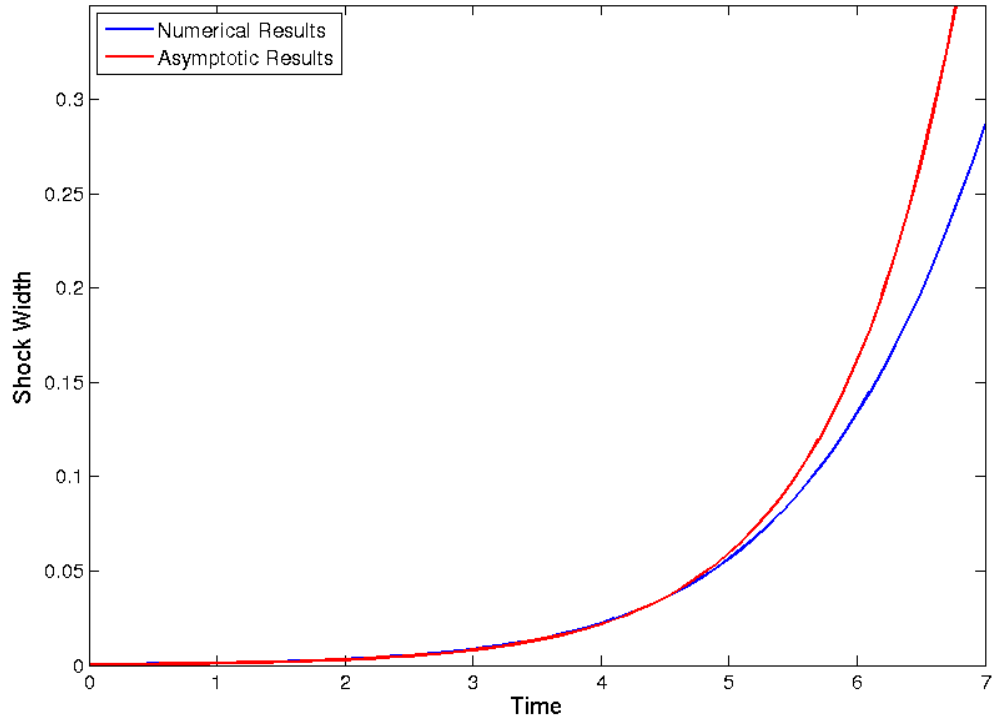


Figure 22: A comparison of the shock width from numerical results and asymptotic predictions for the cylindrical case with $\epsilon = 0.0001$.

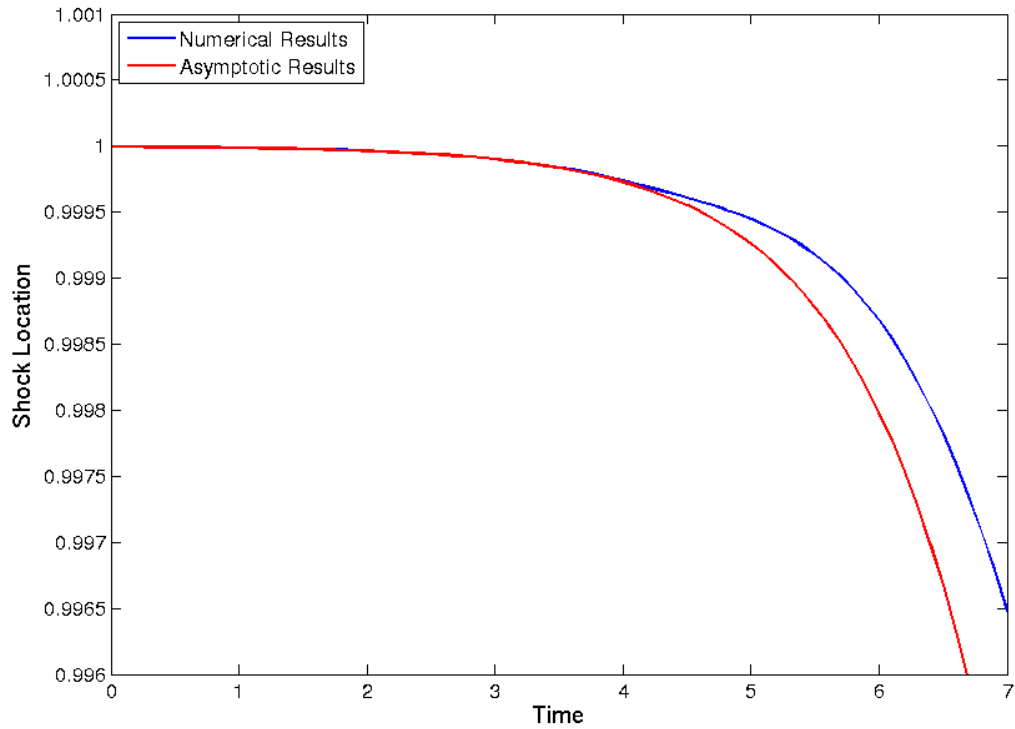


Figure 23: A comparison of the shock location from numerical results and asymptotic predictions for the cylindrical case with $\epsilon = 0.00001$.

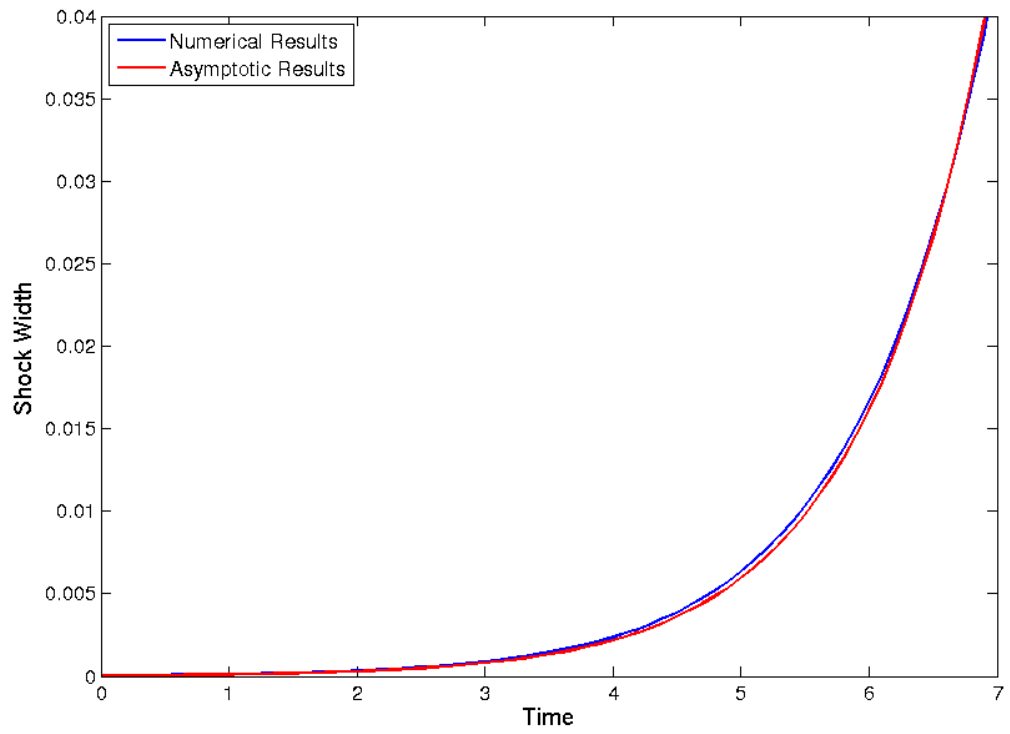


Figure 24: A comparison of the shock width from numerical results and asymptotic predictions for the cylindrical case with $\epsilon = 0.00001$.

6.3 Spherical Waves

For spherical waves, we know that $\int g(T)dT = \text{Ei}(\exp(T))$, $g(T) = \exp(\exp(T))$ and $g'(T) = \exp(T) \exp(\exp(T))$. From here it can be seen that the third condition will first be violated when $\exp(T) \exp(\exp(T)) = O(\epsilon^{-1})$. Looking at the modified Burgers' equation we would expect the shock location to move along the path $1 - \epsilon \text{Ei}(\exp(T))$ and the shock width to grow like $4\epsilon \exp(\exp(T))$. Again, these results show that as ϵ gets smaller the agreement with the asymptotic prediction improves. These results are shown in Figures 25 to 30.

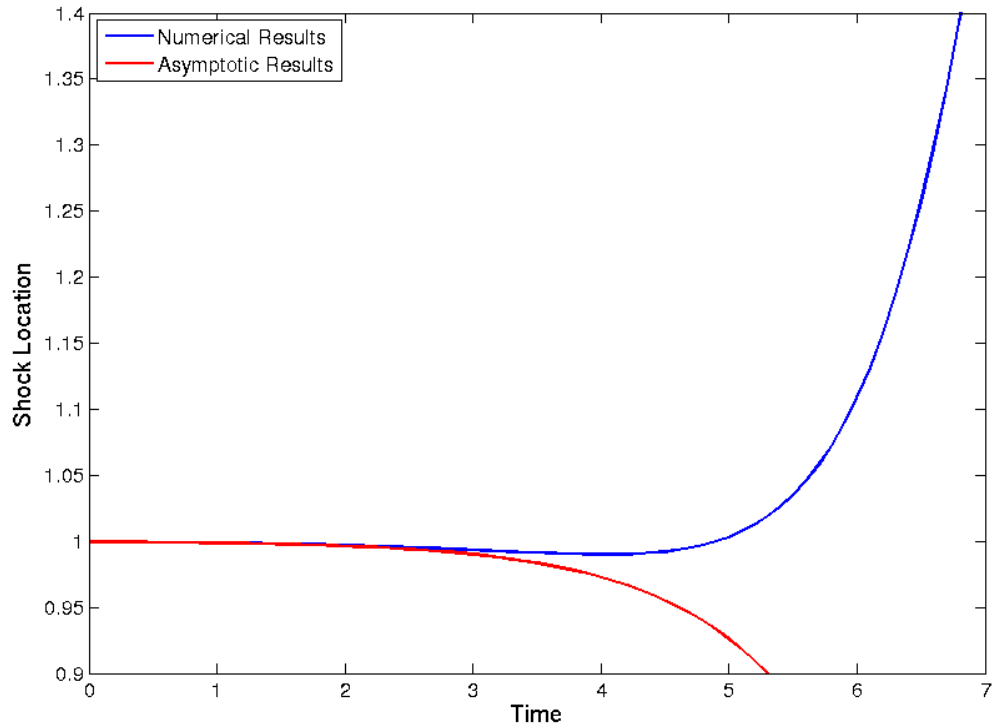


Figure 25: A comparison of the shock location from numerical results and asymptotic predictions for the spherical case with $\epsilon = 0.001$.

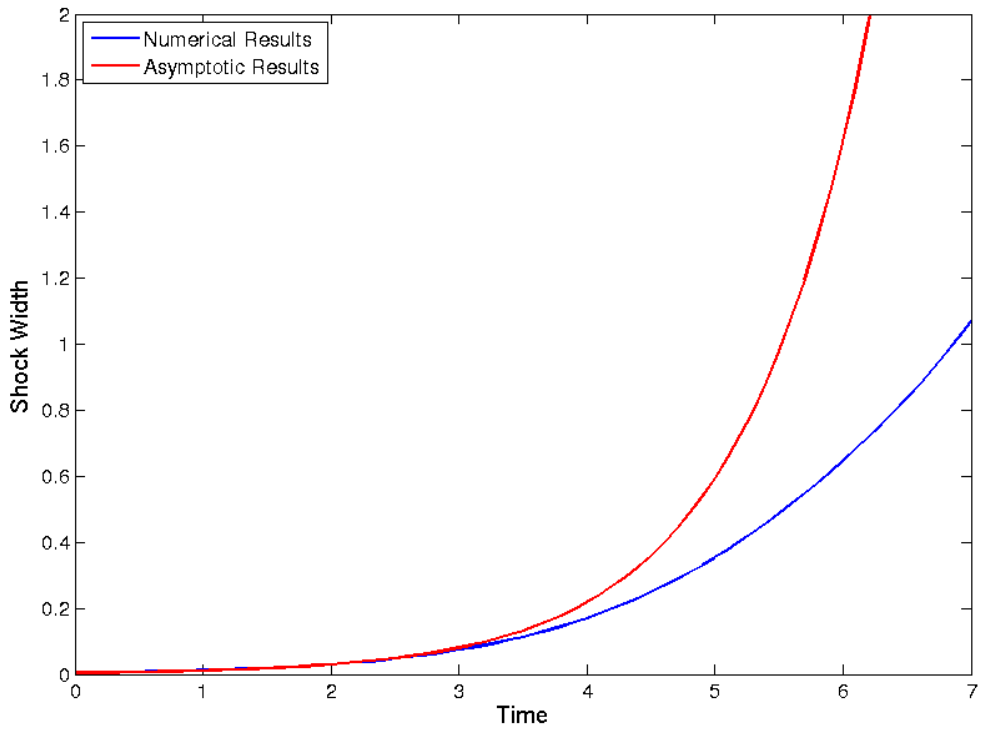


Figure 26: A comparison of the shock width from numerical results and asymptotic predictions for the spherical case with $\epsilon = 0.001$.

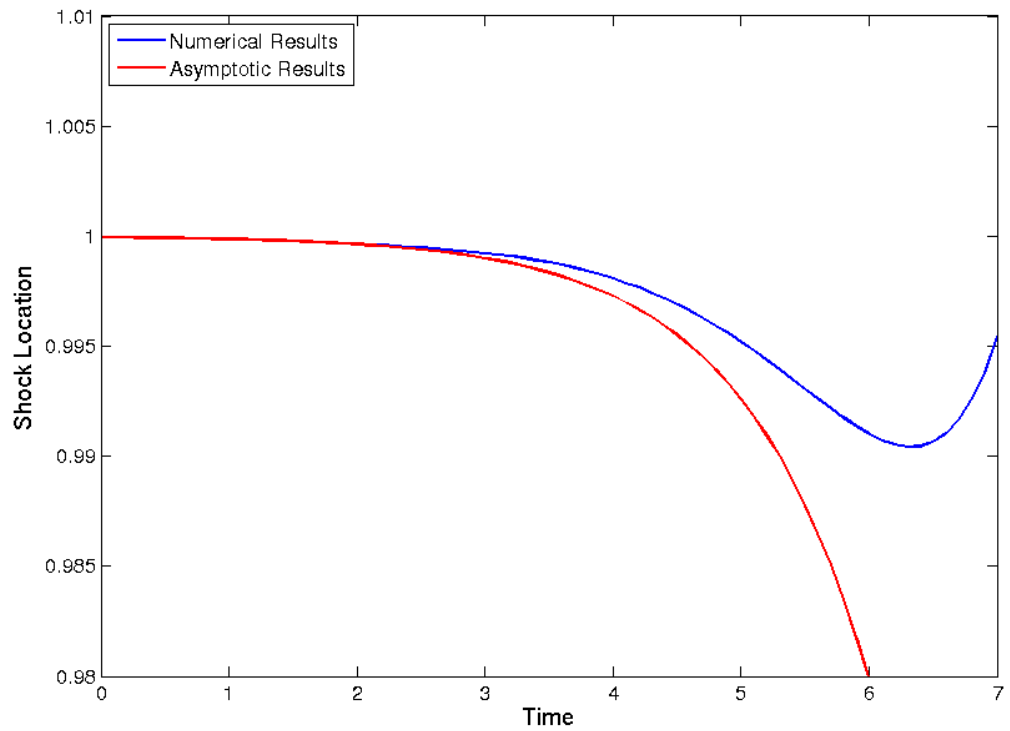


Figure 27: A comparison of the shock location from numerical results and asymptotic predictions for the spherical case with $\epsilon = 0.0001$.

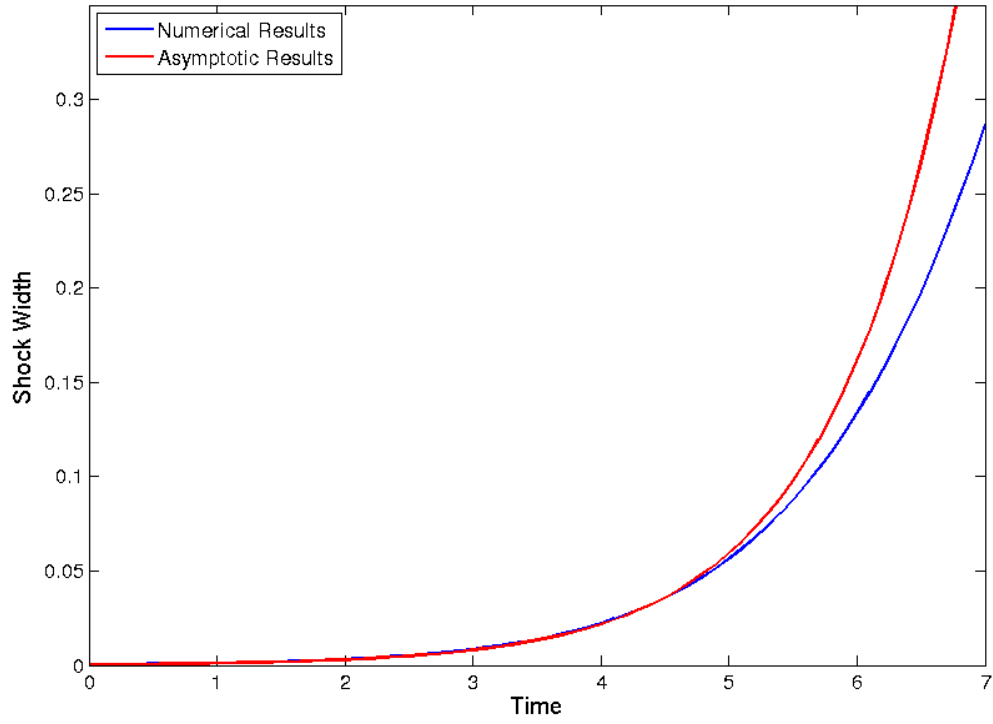


Figure 28: A comparison of the shock width from numerical results and asymptotic predictions for the spherical case with $\epsilon = 0.0001$.

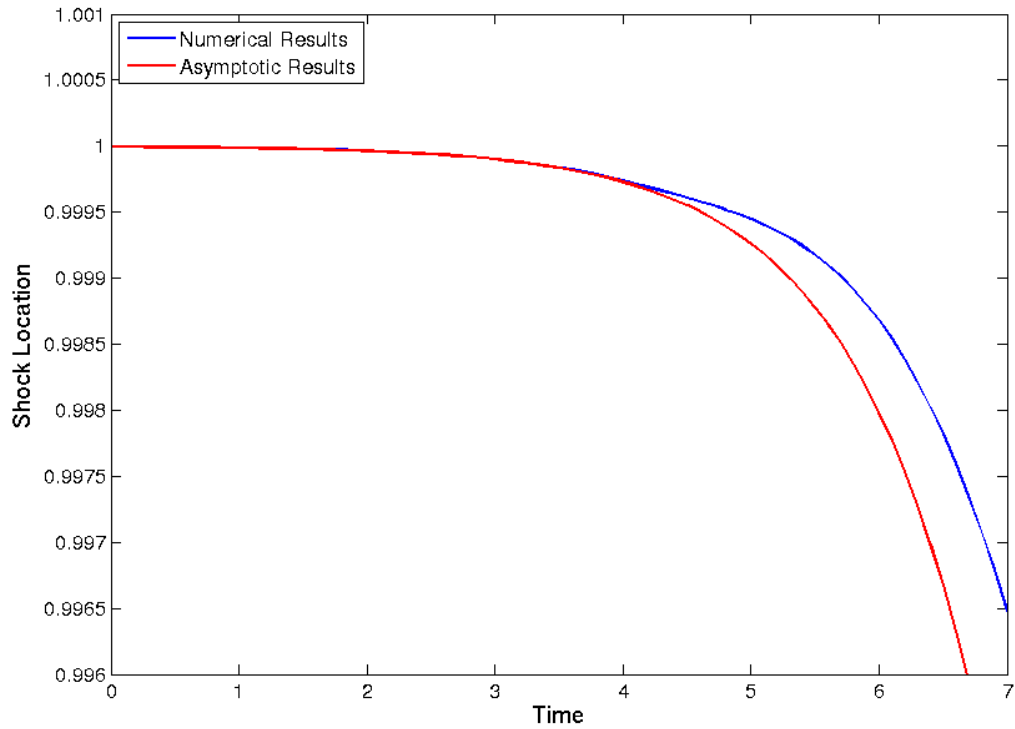


Figure 29: A comparison of the shock location from numerical results and asymptotic predictions for the spherical case with $\epsilon = 0.00001$.

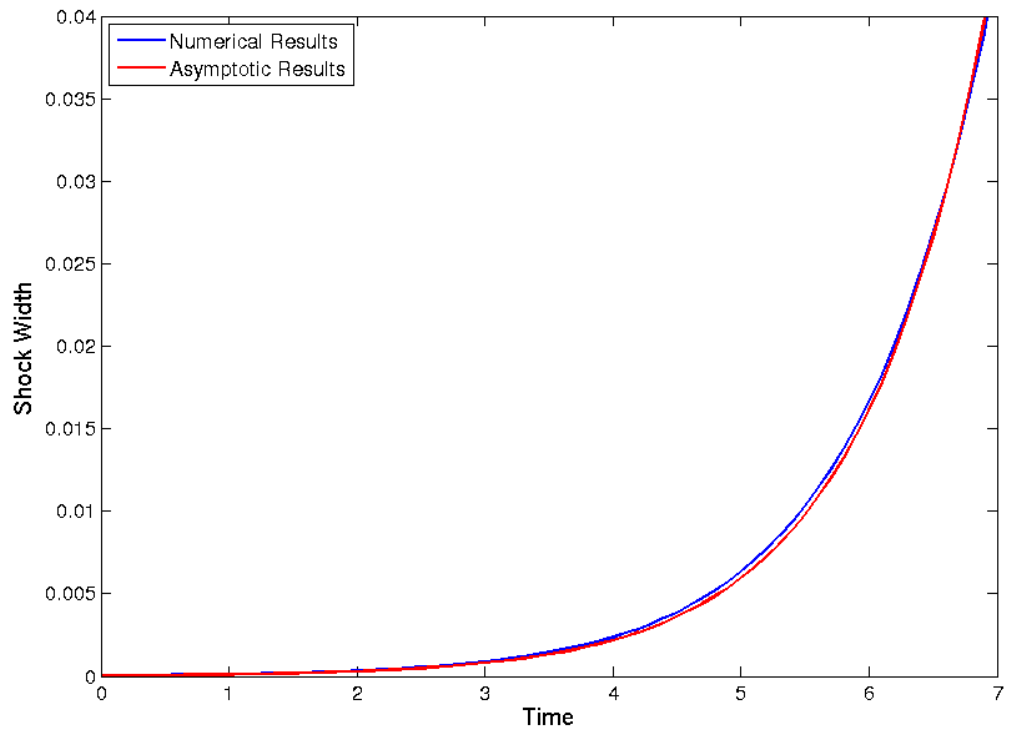


Figure 30: A comparison of the shock width from numerical results and asymptotic predictions for the spherical case with $\epsilon = 0.00001$.

6.4 Further Analysis

Looking at these results, it can be seen that on the whole the asymptotic prediction has the same characteristic shape as the numerical solution. However, in the Figures, it can be seen that the breakdowns occur much earlier than expected. For example in Figure 13 we breakdown seems to occur around $t \approx 20$ while asymptotic analysis predicts it to occur when $t = O(100)$. These unexpected errors give us reason to investigate the general asymptotic form further to see if we can improve these results. Here we will perform further analysis on exactly what form we expect from the asymptotic predictions.

Our basic asymptotic predictions are that the shock location will behave like $1 - \epsilon \int g(t)dt$ and the shock width will behave like $4\epsilon g(t)$ by simple analysis of (4.30). However, we can improve this estimate by performing further analysis of the basic shock structure. Recalling from 4.5 that the outer solution takes the form $u = x$ for $|x| < 1$ and $u = 0$ otherwise and recalling the Taylor shock located at $x = 1$ will have the following form

$$u = \frac{1}{2} \left[1 - \tanh \left(\frac{x - (1 - \epsilon \int g(t)dt)}{4\epsilon g(t)} \right) \right]$$

as given in 4.30. By combining these two solutions together we can consider the waveform to have a composite expression of the form

$$f(x, t) = \frac{x}{2} [1 - \tanh \theta], \tag{6.2}$$

where $\theta = x - (1 - \epsilon a)/\epsilon b$ with $a = \int g(t)dt$ and $b = 4g(t)$. We can now rewrite (6.2) as

$$f(\theta, t) = \frac{1}{2} [(1 - \epsilon a + \epsilon b\theta)(1 - \tanh \theta)]. \tag{6.3}$$

It is now possible to attempt to find the maximum value by solving $\partial f/\partial\theta = 0$ which gives us the following implicit equation for θ in terms of a , b and ϵ ,

$$\frac{1}{\epsilon b} + \left(\frac{a}{b} + \theta\right) = \frac{e^{-2\theta} + 1}{2}. \quad (6.4)$$

Now, we take the limit as $\epsilon \rightarrow 0$ and note that the only terms which are not $O(1)$ are

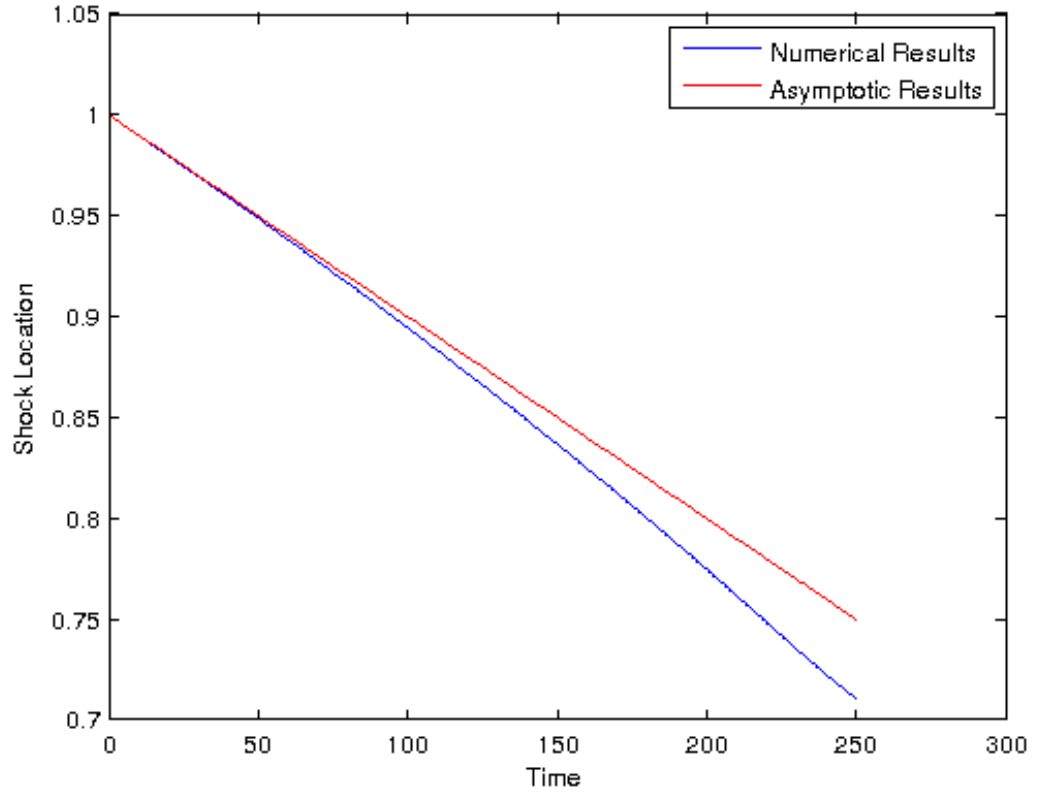


Figure 31: A comparison of the shock location from numerical results and asymptotic predictions for $\epsilon = 0.001$ for the plane case.

$1/\epsilon b$ and $e^{-2\theta}/2$. Therefore we must have

$$\frac{1}{\epsilon b} \approx \frac{e^{-2\theta}}{2}, \quad (6.5)$$

giving us that $\theta \approx -\frac{1}{2} \log\left(\frac{2}{\epsilon b}\right)$ and hence $x \approx 1 - \epsilon a - \frac{\epsilon b}{2} \log\left(\frac{2}{\epsilon b}\right)$. Now we need to find the maximum value of f , denoted by \hat{f} , corresponding to $\hat{\theta} = -\frac{1}{2} \log B = \log\left(B^{-\frac{1}{2}}\right)$ where

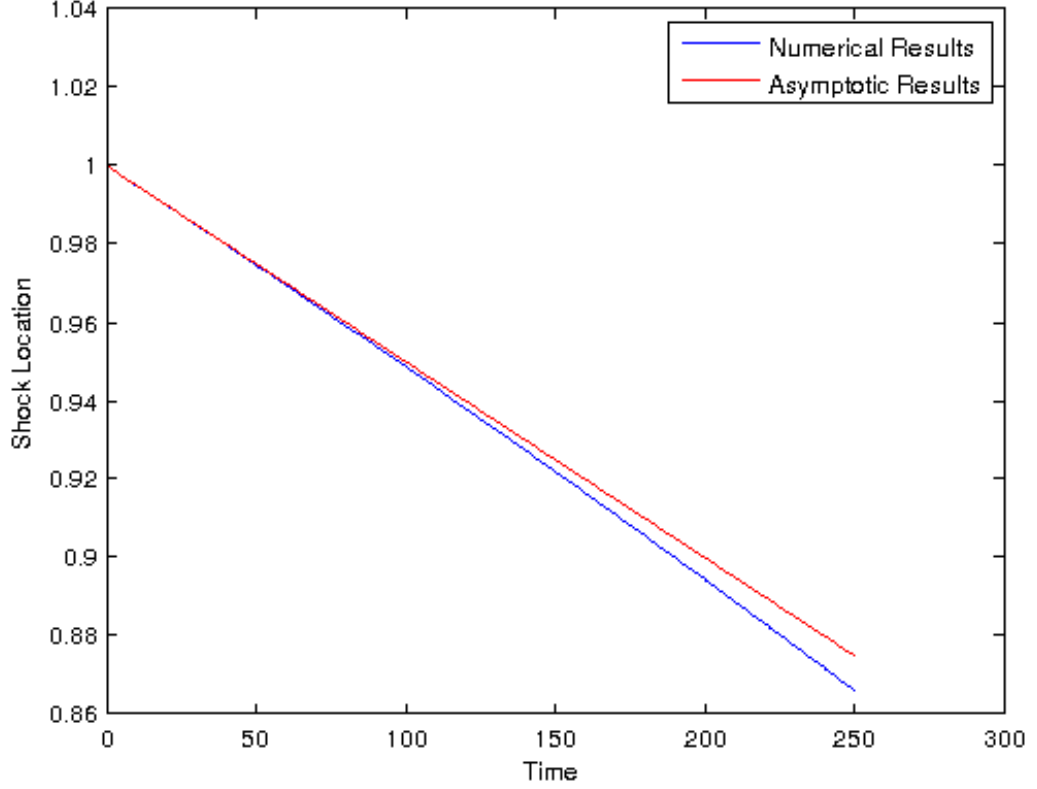


Figure 32: A comparison of the shock location from numerical results and asymptotic predictions for $\epsilon = 0.0005$ for the plane case.

$B = \left(\frac{2}{\epsilon b}\right)$. From (6.3) this maximum value of f at a given fixed t is given by

$$\hat{f}(\hat{\theta}, t) = \frac{1}{2} \left[\left(1 - \epsilon a - \frac{\epsilon b}{2} \log B \right) \left(1 - \tanh \left(\log B^{-\frac{1}{2}} \right) \right) \right]. \quad (6.6)$$

Now, seeking a simpler expression in the small ϵ limit, it can be noted that $\tanh(x) = \frac{e^x - e^{-x}}{e^x + e^{-x}} = \frac{e^{2x} - 1}{e^{2x} + 1}$, it can be seen that $\tanh(\log B^{-\frac{1}{2}}) = \frac{B^{-1} - 1}{B^{-1} + 1} = \frac{1 - B}{1 + B}$. Using this expression we can now see that $1 - \tanh \hat{\theta} = \frac{2B}{1 + B}$ and substituting $B = \left(\frac{2}{\epsilon b}\right)$ back in we arrive at $1 - \tanh \hat{\theta} = \frac{4}{\epsilon b + 2}$. This allows (6.6) to be written as

$$\hat{f}(\hat{\theta}, t) = \left[\left(1 - \epsilon a - \frac{\epsilon b}{2} \log B \right) \frac{1}{1 + \frac{\epsilon b}{2}} \right]. \quad (6.7)$$

This allows us to take a Taylor series expansion of $\frac{1}{1 + (\epsilon b/2)}$ about 1 giving us $\frac{1}{1 + (\epsilon b/2)} =$

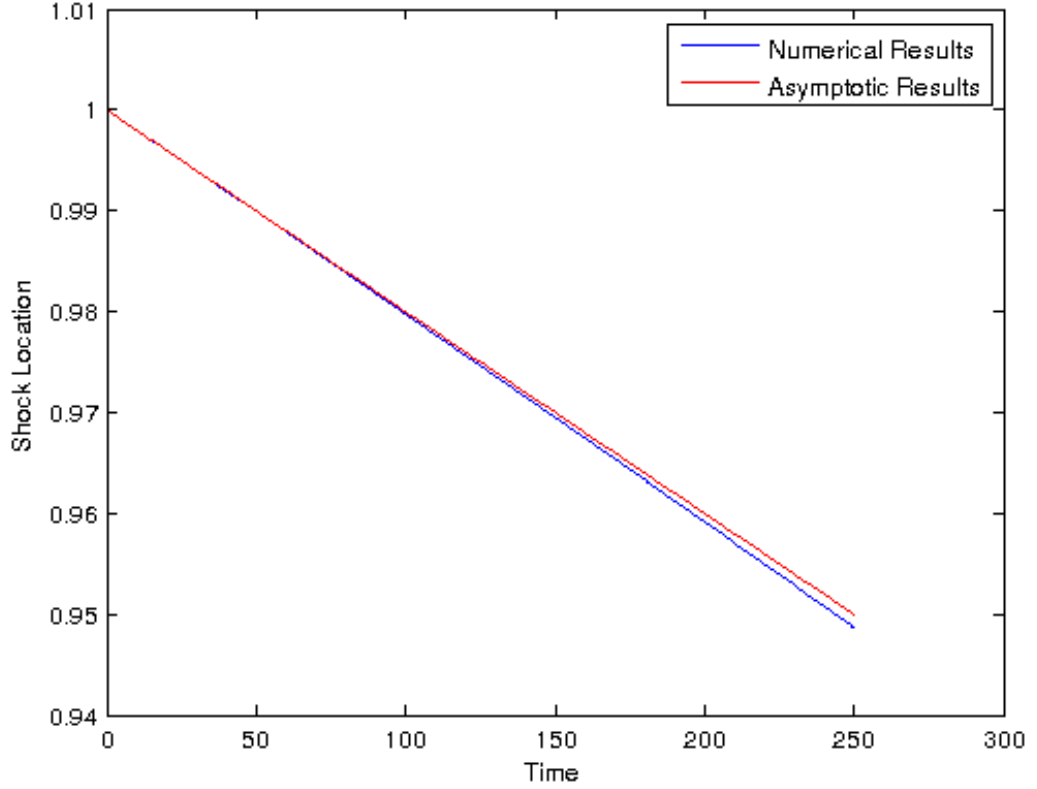


Figure 33: A comparison of the shock location from numerical results and asymptotic predictions for $\epsilon = 0.0002$ for the plane case.

$1 - \frac{\epsilon b}{2} + O(\epsilon^2)$ resulting in

$$\begin{aligned} \hat{f} &\approx 1 - \epsilon a - \frac{\epsilon b}{2} \log B - \frac{\epsilon b}{2}, \\ &\approx 1 - \frac{\epsilon b}{2} \left(\log \left(\frac{2}{\epsilon b} \right) \right) - \epsilon \left(a - \frac{b}{2} \right), \end{aligned} \quad (6.8)$$

where the size of the higher order terms in (6.8) are $O(\epsilon^2 \log(1/\epsilon))$. This result has been verified by comparing this value with the maximum of solving 4.30 using the numerical methods discussed in §5. Having now found the location of the maximum value of f , we can now find the shock centre and width by defining the shock centre as x_m where $f(x_m, t) = \frac{1}{2}\hat{f}$. We can similarly define the shock width as $x_{90\%} - x_{10\%}$ where $f(x_{90\%}, t) = 0.9\hat{f} = f_{90\%}$ and $f(x_{10\%}, t) = 0.1\hat{f} = f_{10\%}$. We now wish to find asymptotic expressions

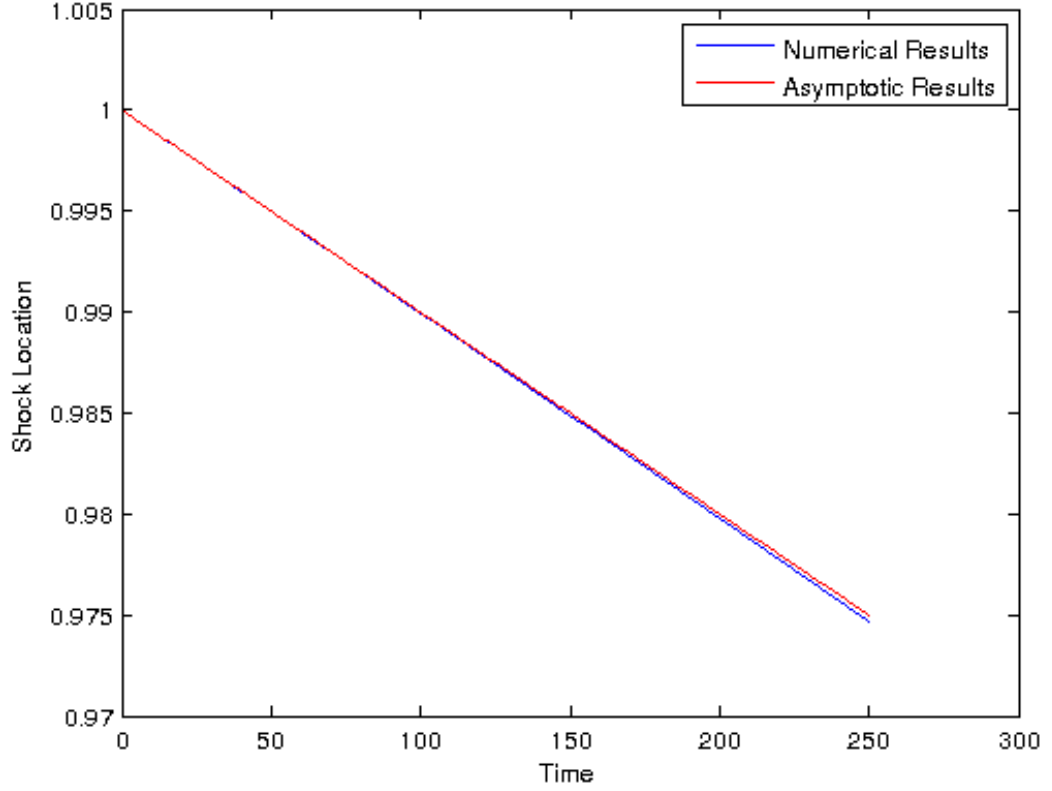


Figure 34: A comparison of the shock location from numerical results and asymptotic predictions for $\epsilon = 0.0001$ for the plane case.

for x_m , $x_{10\%}$ and $x_{90\%}$.

According to the weak shock theory we expect \hat{f} to remain constant at leading order, along with the shock centre and width. Hence, we can use a Taylor expansion on our initial shock, $f(\theta) = \frac{x}{2}(1 - \tanh \theta)$. From (6.8) it can be seen that $\hat{f} \sim 1 - \frac{cb}{2} \left(\log \left(\frac{2}{cb} \right) \right)$ and hence we solve $f(\theta) = \lambda \hat{f}$ by setting $\theta = \theta_0 + \Delta$, where $\Delta = O(\epsilon)$. This gives us the following equation to solve

$$f(\theta_0 + \Delta) = \lambda \hat{f}, \quad (6.9)$$

where θ_0 is the solution for the tanh shock and Δ represents a small permutation to the tanh shock solution. Taking the Taylor expansion about θ_0 , noting that $x = 1 + \epsilon(b\theta - a)$

and substituting for \hat{f} gives the following equation to be solved

$$\frac{1}{2}(1 - \tanh(\theta_0)) - \frac{1}{2}\Delta \operatorname{sech}^2 \theta_0 + O(\epsilon) = \lambda - \frac{1}{2}b\lambda\epsilon \log B + O(\epsilon), \quad (6.10)$$

where $\Delta \ll 1$. From here we can match terms to arrive at

$$\tanh(\theta_0) = 1 - 2\lambda, \quad \Delta = \frac{b\lambda\epsilon \log B}{\operatorname{sech}^2 \theta_0} = \frac{b\epsilon \log B}{4(1 - \lambda)}. \quad (6.11)$$

We can now substitute $\lambda = 0.1, 0.5$ and 0.9 into (6.11) to find $\theta_{10\%}, \theta_m$ and $\theta_{90\%}$ respectively, where $f(\theta_{10\%}) = 0.1\hat{f}$ and so on. For the case where $\lambda = 0.1$, we obtain

$$\theta_0 = \tanh^{-1}(1 - 2\lambda) = \alpha \approx 1.10. \quad (6.12)$$

From here we find that $\theta_{10\%}$ (corresponding to $x_{10\%}$) is given by

$$\theta_{10\%} = \alpha + A_{10\%}\epsilon b \log B, \quad \text{where} \quad A_{10\%} = \frac{1}{4 \times 0.9}. \quad (6.13)$$

Similarly, in the case where $\lambda = 0.9$, we obtain

$$\theta_{90\%} = -\alpha + A_{90\%}\epsilon b \log B, \quad \text{where} \quad A_{90\%} = \frac{1}{4 \times 0.1}. \quad (6.14)$$

From (6.13) and (6.14) we get the following expressions for $x_{10\%}$ and $x_{90\%}$

$$\begin{aligned} x_{10\%} &= 1 - \epsilon(a - \alpha b) + A_{10\%}\epsilon^2 b^2 \log B, \\ x_{90\%} &= 1 - \epsilon(a + \alpha b) + A_{90\%}\epsilon^2 b^2 \log B. \end{aligned} \quad (6.15)$$

Hence the shock width is given by

$$x_w = x_{90\%} - x_{10\%} = 2\alpha\epsilon b(1 - \beta\epsilon b \log B), \quad \text{where} \quad \beta = \frac{A_{90\%} - A_{10\%}}{2\alpha} \approx 1.01. \quad (6.16)$$

Note the $2\alpha\epsilon b$ term is analogous to what is predicted by weak shock theory and the $2\alpha\beta\epsilon^2 b^2 \log B$ represents the correction term. By inspecting the case when $\lambda = 0.5$ we can also find an expression for the centre of the shock. When $\lambda = 0.5$ we have $\theta_0 = 0$ and $\Delta = \frac{1}{2}b\epsilon \log B$. Hence the centre of the shock is located at

$$\begin{aligned} x_m &= 1 - \epsilon a + \frac{1}{2}(\epsilon b)^2 \log B, \\ &= 1 - \epsilon a + \frac{1}{2}(\epsilon b)^2 \log \frac{1}{2\epsilon}. \end{aligned} \quad (6.17)$$

These results should now improve the range over which we have good agreement between the numerical and asymptotic results and in the following section we shall look to see if this is true.

6.5 Results

In this section we will display the results for each of the three cases to observe how well the numerical and asymptotic results compare.

6.5.1 Plane Case

In the plane case we have that $a = t$ and $b = 4$ and so the perturbation expansions for the shock location, x_m , and width, x_w , takes the form

$$x_m = 1 - a_m \epsilon + b_m \epsilon^2, \quad a_m = t, \quad b_m = 8 \log \left(\frac{1}{2\epsilon} \right), \quad (6.18)$$

$$x_w = a_w \epsilon (1 - b_w \epsilon), \quad a_w = 8\alpha, \quad b_w = 4\beta \log \left(\frac{1}{2\epsilon} \right), \quad (6.19)$$

where α and β are as defined in (6.12) and (6.16). For the plane case this correction just represents a constant shift in the shock location and width, not a change to the actual shape. This is only true in the plane case, for the cylindrical and spherical cases the correction term makes a significant change to the shock location and width.

For this reasons, comparisons between the numerical and asymptotic solutions for the shock location are not plotted again and are shown in Figures 31 - 34. The results without the correction are not shown due to the fact that for these values of ϵ the two sets of results are too similar to notice any difference from the graphs in the results due to the correction term. The shock width is not displayed here, but agrees with the predicted behaviour from (6.16).

6.5.2 Cylindrical Case

In the cylindrical case we have that $a = \frac{1}{2}(\exp(t) - 1)$ and $b = 2 \exp(t)$, resulting in the following expressions for x_m and x_w

$$x_m = 1 - a_m \epsilon + b_m \epsilon^2, \quad a_m = \frac{1}{2}(e^t - 1), \quad b_m = 2e^{2t} \log\left(\frac{1}{\epsilon e^t}\right), \quad (6.20)$$

$$x_w = a_w \epsilon(1 - b_w \epsilon), \quad a_w = 4\alpha e^t, \quad b_w = 2\beta e^t \log\left(\frac{1}{\epsilon e^t}\right). \quad (6.21)$$

Comparisons between the numerical and asymptotic solutions for the shock location are shown in Figures 35 - 38 and comparisons for the shock width are shown in Figures 39 - 42.

From observing the Figures displaying the shock location it can be seen that the correction term significantly extends the region of agreement and, perhaps more importantly, captures the change in direction of the shock location from heading towards 0 to heading away from 0. For the shock width, there is no similar change in direction, however the correction term still offers a significantly improved region of agreement compared to not applying the correction.

6.5.3 Spherical Case

In the spherical case we have that $a = \text{Ei}(\exp(t))$, where $\text{Ei}(x)$ is the exponential integral and $b = 4 \exp(\exp t)$, giving

$$x_m = 1 - a_m \epsilon + b_m \epsilon^2, \quad a_m = \text{Ei}(e^t), \quad b_m = 2e^{2e^t} \log\left(\frac{1}{2\epsilon e^{e^t}}\right), \quad (6.22)$$

$$x_w = a_w \epsilon(1 - b_w \epsilon), \quad a_w = 8\alpha e^{e^t}, \quad b_w = 4\beta e^{e^t} \log\left(\frac{1}{2\epsilon e^{e^t}}\right). \quad (6.23)$$

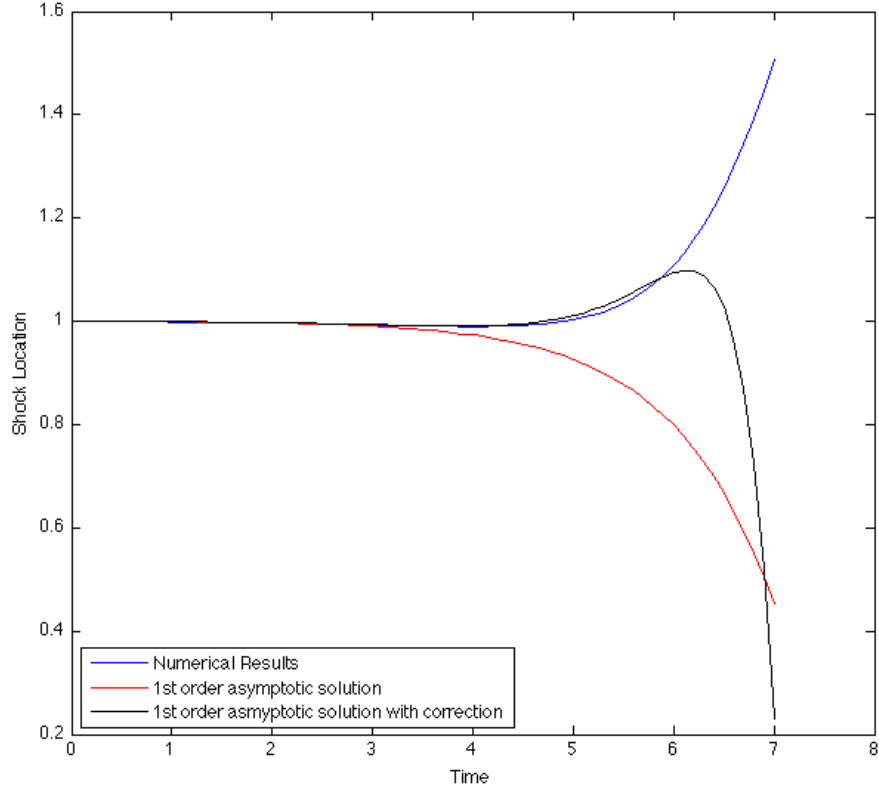


Figure 35: A comparison of the shock location from numerical results and asymptotic predictions for $\epsilon = 0.001$ for the cylindrical case.

The spherical case is unique due to the fact that the breakdown of weak shock theory occurs in a different fashion from the plane and cylindrical cases. Weak shock theory first breaks down when the first order approximation (the tanh shock) is no longer valid. This occurs when $\epsilon e^{e^t} e^t = O(1)$. In order to observe this behaviour we rescale the time such that $e^{t'} = e^t - e^{t_1}$, where $t_1(\epsilon)$ is given implicitly by $\epsilon e^{e^{t_1}} e^{t_1} = 1$. This reduces the modified general Burgers' equation (4.30) to

$$u_{t'} = \frac{u}{2} + \left(\frac{x}{2} - u\right) u_x + e^{e^{t'}} e^{-t_1} u_{xx}. \quad (6.24)$$

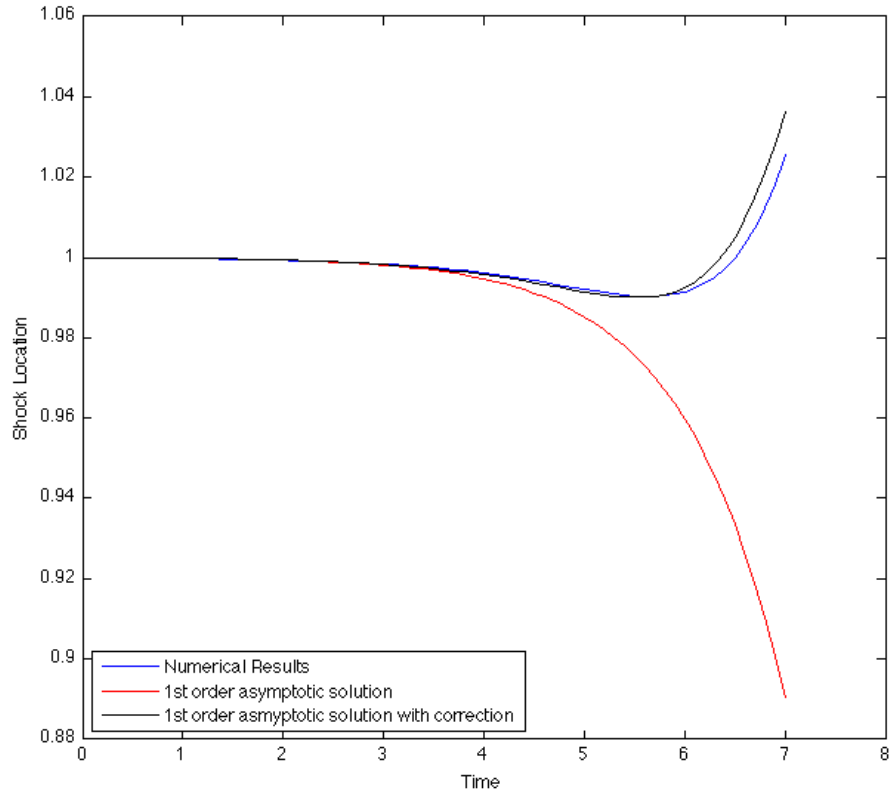


Figure 36: A comparison of the shock location from numerical results and asymptotic predictions for $\epsilon = 0.0002$ for the cylindrical case.

By examining the two term inner solution as done by Crighton [13] we arrive at the changes of variables, $u' = \sqrt{e^{t_1}}u - \frac{1}{2}$ and $x' = \sqrt{e^{t_1}}(x - 1)$. This reduces (6.24) to

$$u'_{t'} = \frac{u'}{2} + \left(\frac{x'}{2} - u' \right) u'_{x'} + e^{e^{t'}} u'_{x'x'} + \frac{1}{4}. \quad (6.25)$$

We now attempt to solve this equation in the limit as t' gets large. It can be seen that all terms will get large, except for the $1/4$ term. So by solving this equation we arrive at the following expression for u'

$$u' = \frac{1}{2}\sqrt{e^{t'}} \left(\operatorname{erfc} \left(\frac{1}{2}\sqrt{\frac{e^{t'}}{e^{e^{t'}}}}x' \right) - 1 \right). \quad (6.26)$$

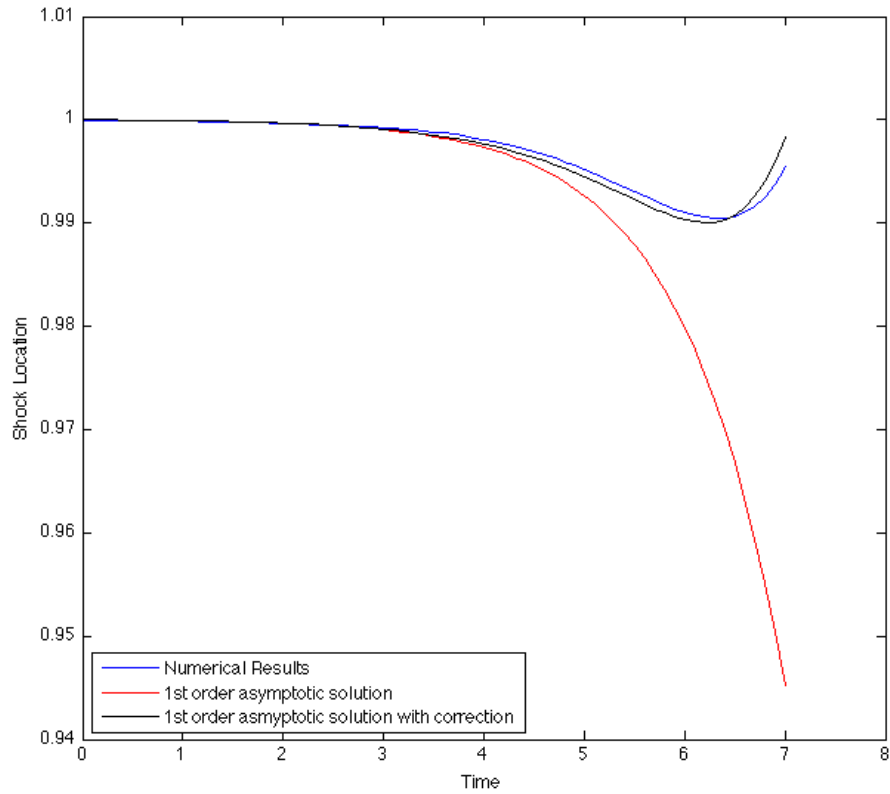


Figure 37: A comparison of the shock location from numerical results and asymptotic predictions for $\epsilon = 0.0001$ for the cylindrical case.

Note, this form corresponds to the result obtained by Crighton and Scott in (3.46) in ‘Asymptotic Solutions of Model Equations in Nonlinear Acoustics’ [13]. Upon substituting our original values back into (6.26), we obtain the following expression for u , once weak shock theory has broken down

$$u = \frac{1}{2} \left(\operatorname{erfc} \left(\frac{x-1}{\sqrt{4\epsilon e^{e^t}/e^t}} \right) \right). \quad (6.27)$$

From here it can easily be seen that the shock width is given by $A\sqrt{4\epsilon e^{e^t}/e^t}$, where A is to be determined. We can attempt the same analysis as used in §6.4 to find an asymptotic expression for the scaling of the shock width based on when the shock is at 90% and 10% of the maximum value of the N-wave. However, when this is attempted we obtain a solution

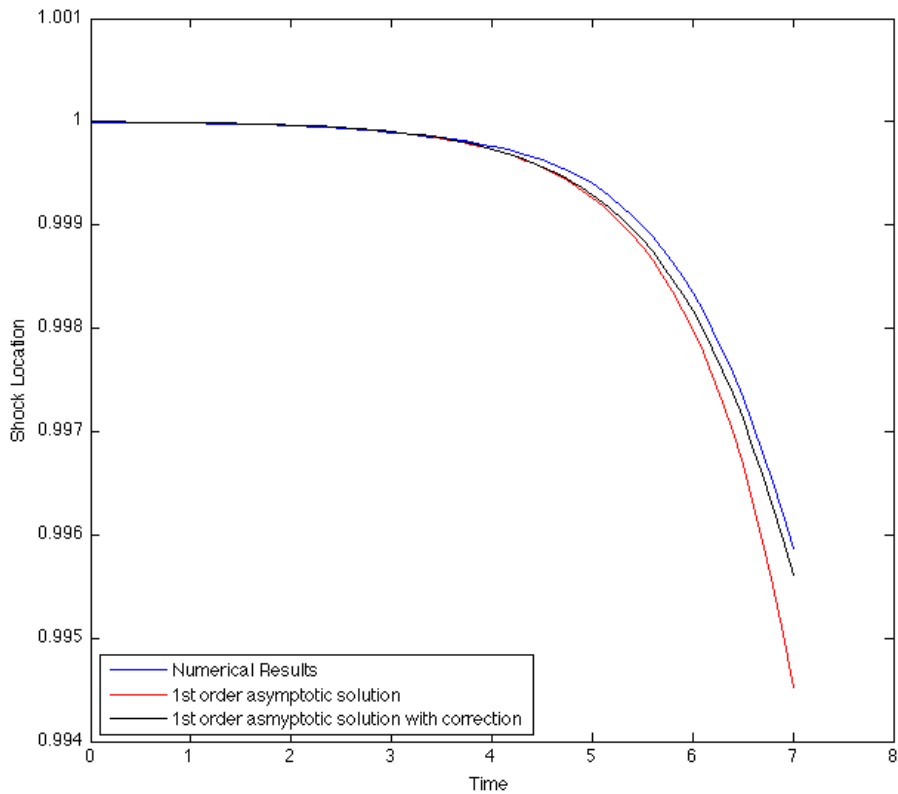


Figure 38: A comparison of the shock location from numerical results and asymptotic predictions for $\epsilon = 0.00001$ for the cylindrical case.

which is only suitable for trivially small values of ϵ .

In order to combat this, we adopted a numerical approach to find this scaling factor.

We considered the following function as an approximation to the erf N-wave in a similar fashion to as was done in (6.2)

$$u = \frac{1}{2}x \left(\operatorname{erfc} \left(\frac{x-1}{\sqrt{4\epsilon e^{e^t}/e^t}} \right) \right). \quad (6.28)$$

From here we compared the functions $w_{\text{num}}(t)$, given by the numerical width based on when the shock is at 90% and 10% of its maximum value and the asymptotic width, $w_{\text{asym}}(t) = A\sqrt{4\epsilon e^{e^t}/e^t}$. We noted that this form should be valid for values where $t \geq t_1$,

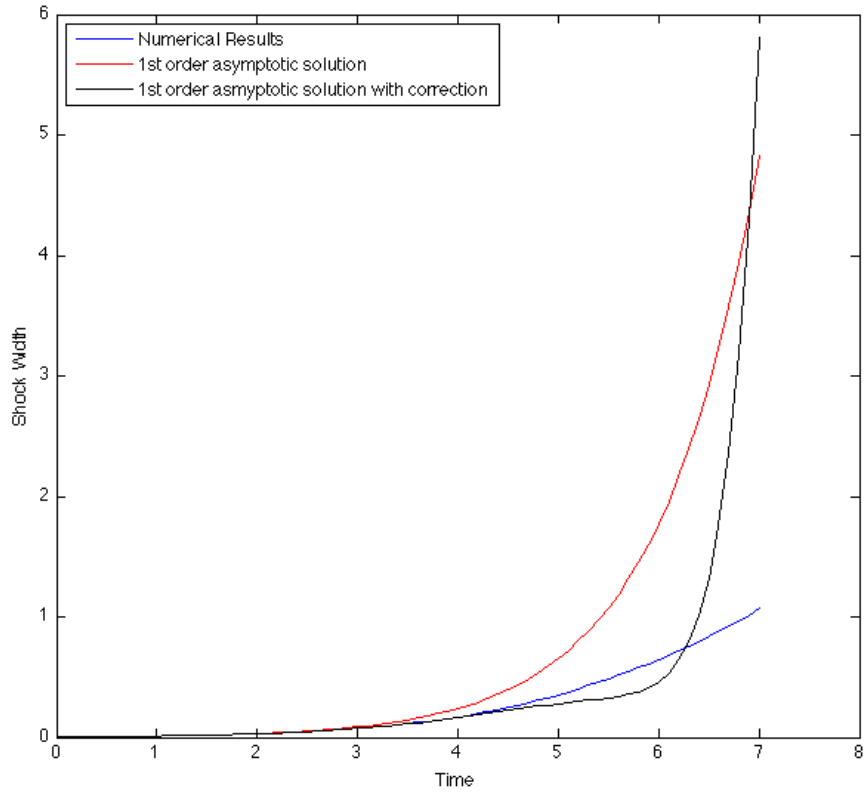


Figure 39: A comparison of the shock width from numerical results and asymptotic predictions for $\epsilon = 0.001$ for the cylindrical case.

hence it was decided to pick the scaling factor A such that

$$A = \frac{w_{\text{num}}(t_1)}{\sqrt{4\epsilon e^{t_1}/e^{t_1}}}. \quad (6.29)$$

We now expect $w_{\text{asym}}(t)$ to have good agreement with the numerical solution once the initial asymptotic prediction has broken down.

The comparisons between the numerical solution and the three asymptotic solutions for the shock width are shown in Figures 43 - 46. Looking in detail at Figure 43 we can see that we have good agreement with the initial asymptotic solution until $t \approx 0.7$. Inclusion of the correction term results in good agreement between the numerical and asymptotic results being maintained until $t \approx 1.3$. From here, it can be seen the shock is

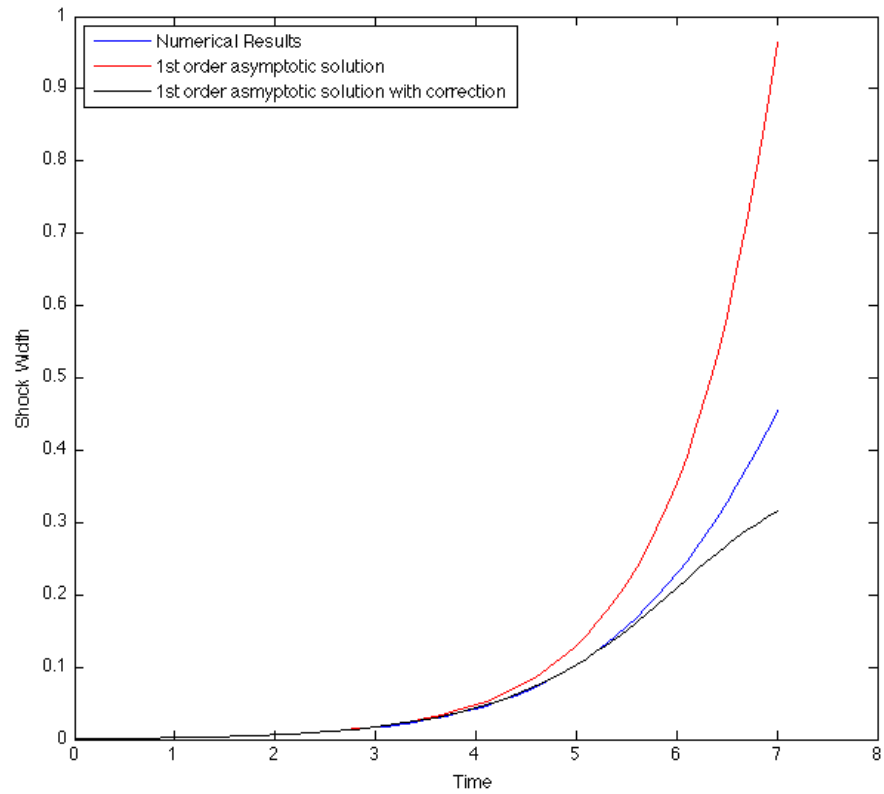


Figure 40: A comparison of the shock width from numerical results and asymptotic predictions for $\epsilon = 0.0002$ for the cylindrical case.

in a transitional phase until matching up with the Erfc solution at $t \approx 1.7$ which is to be expected as for $\epsilon = 0.0005$ we have a value of $t_1 \approx 1.764$. Similar results can be observed in the other three Figures.

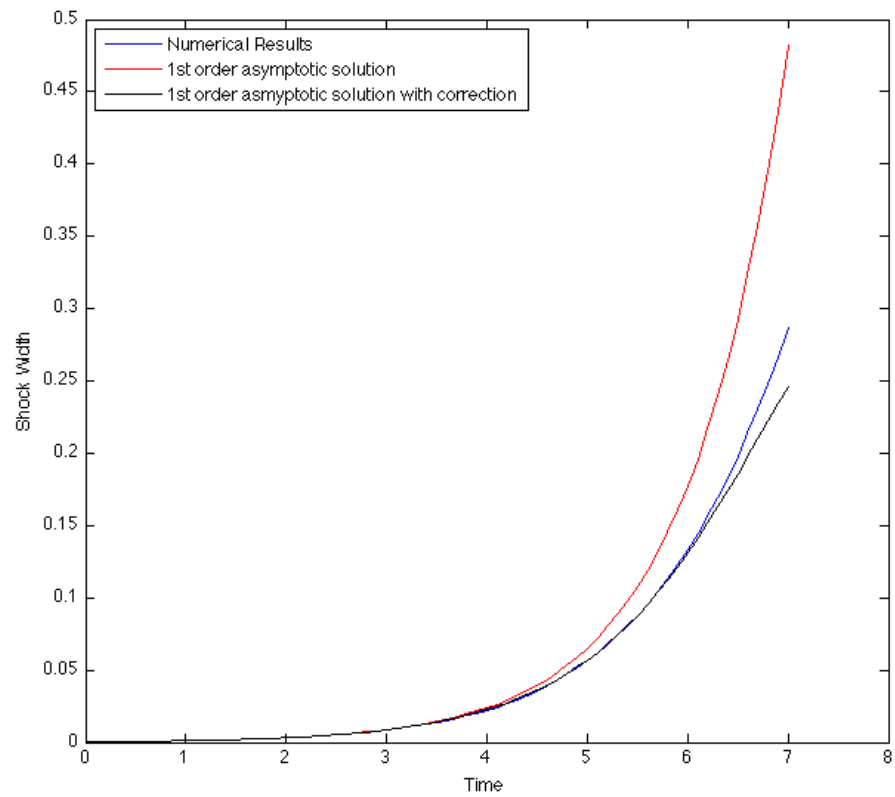


Figure 41: A comparison of the shock width from numerical results and asymptotic predictions for $\epsilon = 0.0001$ for the cylindrical case.

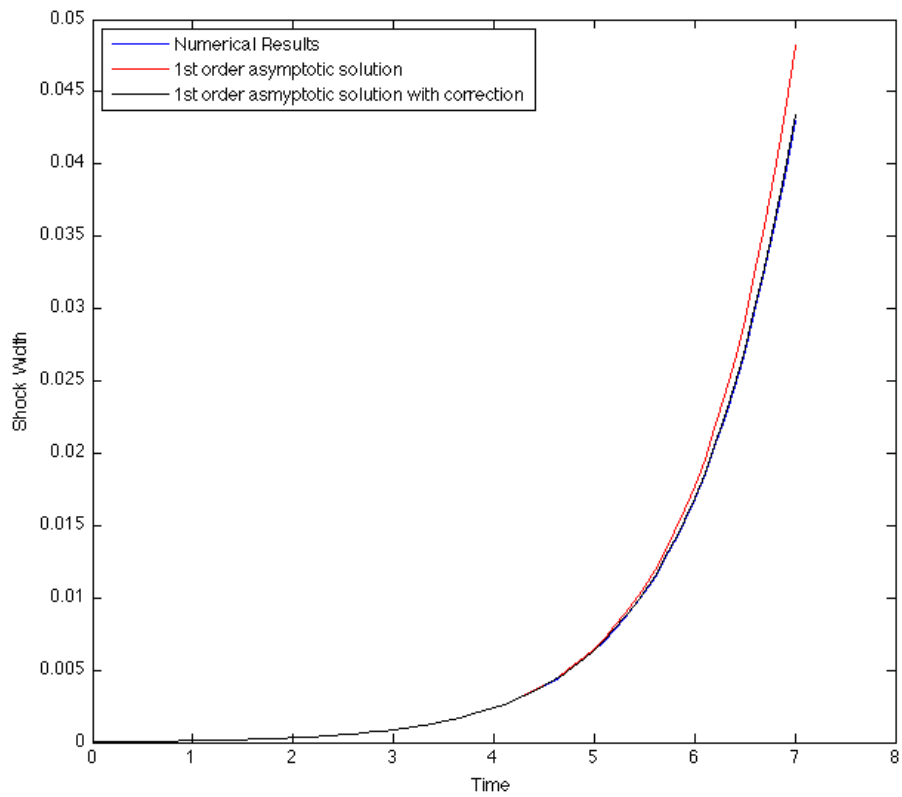


Figure 42: A comparison of the shock width from numerical results and asymptotic predictions for $\epsilon = 0.00001$ for the cylindrical case.

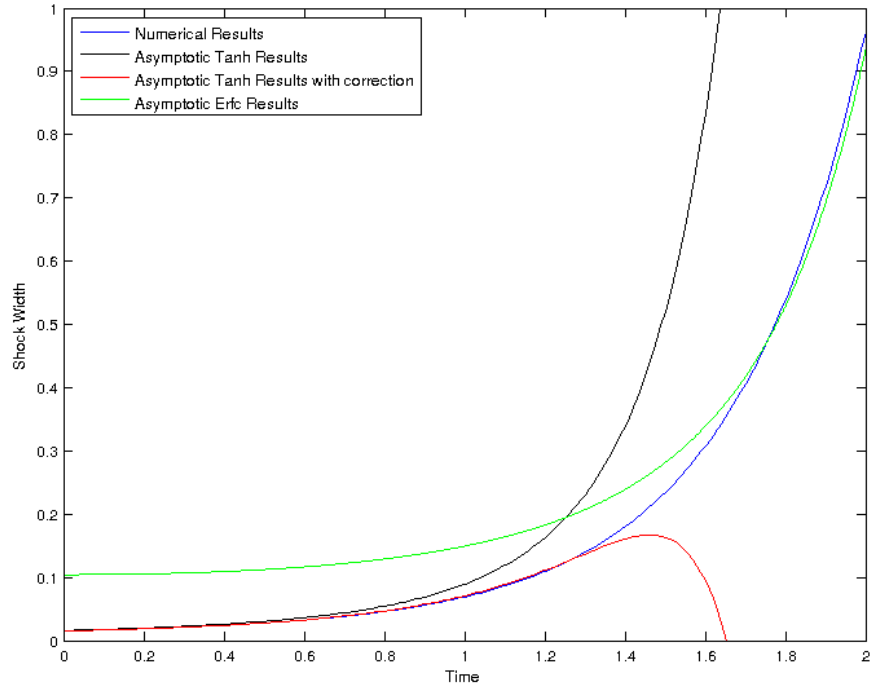


Figure 43: A comparison of the shock width from numerical results and asymptotic predictions for $\epsilon = 0.0005$ for the spherical case.

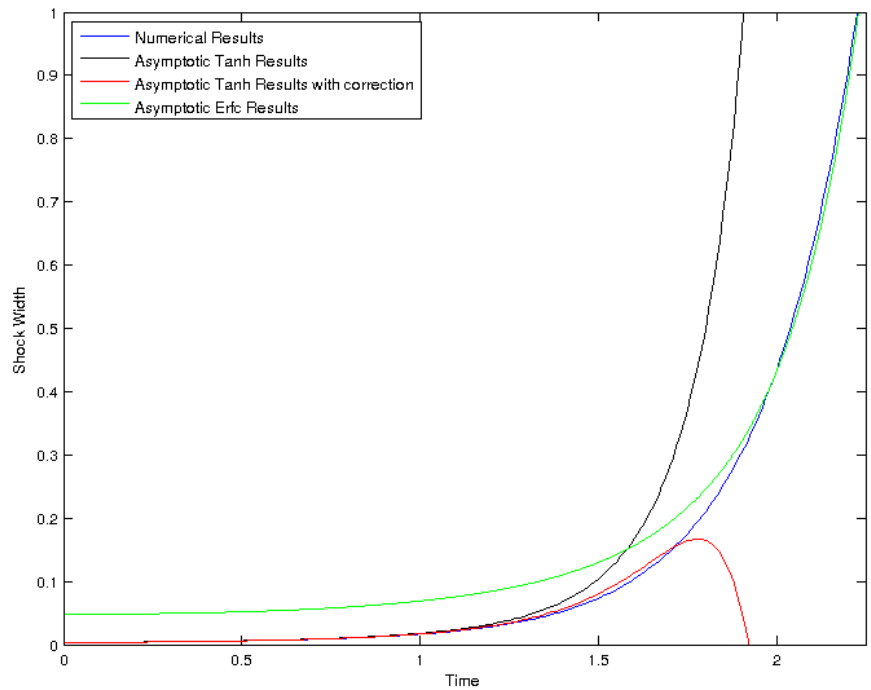


Figure 44: A comparison of the shock width from numerical results and asymptotic predictions for $\epsilon = 0.0001$ for the spherical case.

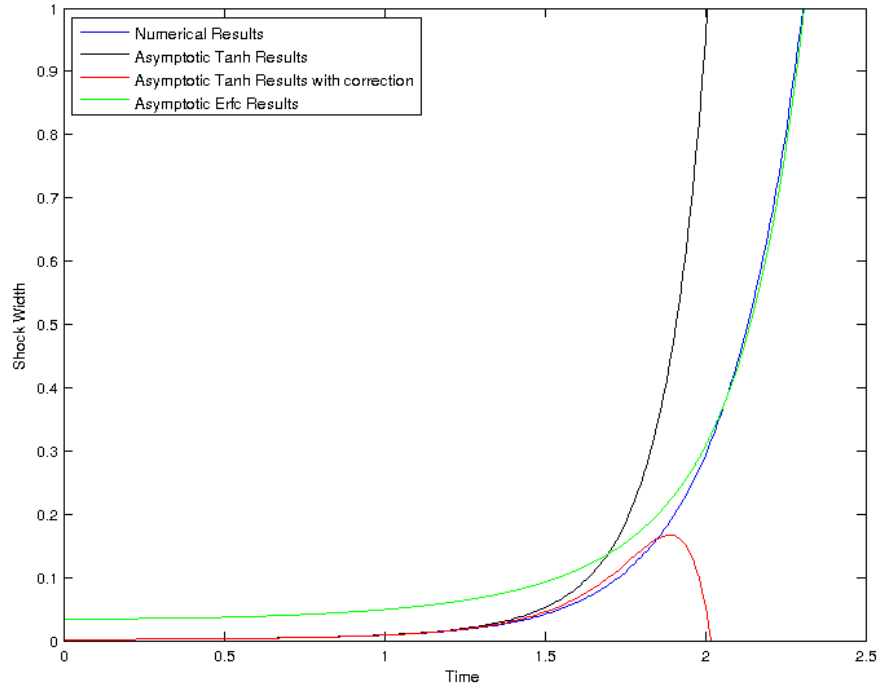


Figure 45: A comparison of the shock width from numerical results and asymptotic predictions for $\epsilon = 0.00005$ for the spherical case.

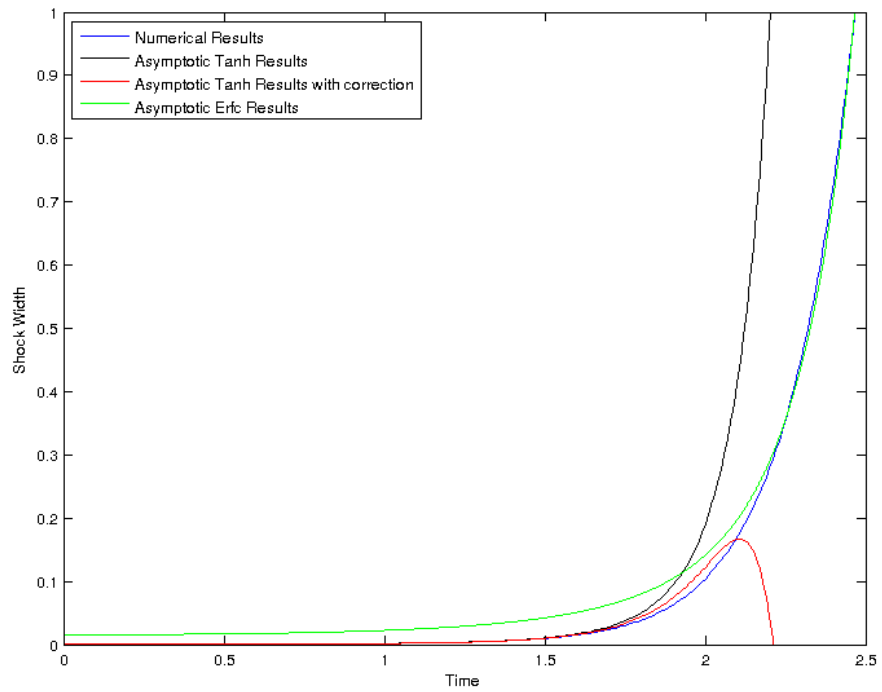


Figure 46: A comparison of the shock width from numerical results and asymptotic predictions for $\epsilon = 0.00001$ for the spherical case.

7 Solving for Long Time Asymptotics

Having discussed the behaviour of the shock for small times, it is also of interest to know what form the shock will take in the old age regime (once nonlinear effects are negligible). This is useful because once shock has fully diffused, it poses no adverse environmental effect to people or animals on the ground. Another advantage is that it allows further validation on the numerical method and to ensure that over long time frames we can maintain a high degree of accuracy. In the old age case we can assume that the waveform becomes small in amplitude. This allows Burgers' equation to be solved exactly in the old age case. Starting from Burgers' equation (3.13) we have

$$U_T = -UU_X + g(T)\epsilon U_{XX}, \quad (7.1)$$

where

$$g(t) = \begin{cases} 1 & \text{for the planar case} \\ \frac{1}{2}(T + T_0 - 1) & \text{for the cylindrical case} \\ \exp(\frac{T}{T_0}) & \text{for the spherical case} \end{cases} \quad (7.2)$$

For long time solutions we assume that $U \rightarrow 0$ as $T \rightarrow \infty$, hence we can ignore the nonlinear effects (being quadratically small) giving us the following PDE to solve

$$U_T = g(T)\epsilon U_{XX}. \quad (7.3)$$

From numerical investigations we know that this solution will form a similarity solution in terms of the function $X/(\epsilon \int g(T)dT)^{\frac{1}{2}}$, therefore we make the change of variables $y =$

$X/(\epsilon \int g(T)dT)^{\frac{1}{2}}$ (and $\tau = T$), we then obtain new expressions for the derivatives as follows

$$\begin{aligned}\frac{\partial}{\partial T} &= \frac{\partial}{\partial \tau} + \frac{\partial}{\partial y} \frac{\partial y}{\partial T} = \frac{\partial}{\partial \tau} + \left(-\frac{Xg(\tau)}{2\epsilon^{\frac{1}{2}}(\int g(\tau)d\tau)^{\frac{3}{2}}} \right) \frac{\partial}{\partial y}, \\ \frac{\partial}{\partial X} &= \frac{\partial}{\partial y} \frac{\partial y}{\partial X} = \frac{1}{(\epsilon \int g(\tau)d\tau)^{\frac{1}{2}}} \frac{\partial}{\partial y}, \\ \frac{\partial^2}{\partial X^2} &= \frac{1}{(\epsilon \int g(\tau)d\tau)} \frac{\partial}{\partial y}.\end{aligned}$$

Substituting this into (7.3), we obtain

$$U_{\tau} + U_y \left(-\frac{Xg(\tau)}{2\epsilon^{\frac{1}{2}}(\int g(\tau)d\tau)^{\frac{3}{2}}} \right) = \frac{g(\tau)}{\int g(\tau)d\tau} U_{yy}. \quad (7.4)$$

Rearranging this gives

$$\frac{\int g(\tau)d\tau}{g(\tau)} U_{\tau} = \frac{y}{2} U_y + U_{yy}. \quad (7.5)$$

Now we have the equation in a form which is separable, so we can express U as $U(y, \tau) = Y(y)\Gamma(\tau)$ in (7.5) to give the following equations to solve

$$\Gamma' = \frac{Ag(\tau)}{\int g(\tau)d\tau} \Gamma, \quad (7.6)$$

$$Y'' + \frac{y}{2} Y' - AY = 0. \quad (7.7)$$

where $Y \rightarrow 0$ as $y \rightarrow \pm\infty$ and A is a separation constant. The solution to (7.6) is given by

$$\Gamma(\tau) = Be^{A \ln(\int g(\tau)d\tau)} = B \left(\int g(\tau)d\tau \right)^A. \quad (7.8)$$

We wish to find A in order to get an expression for U . It turns out that A can be found by letting $Y(y) = \exp(-\eta^2)f(\eta)$ where $\eta = \frac{y}{2}$. Now (7.7) becomes

$$f'' - 2\eta f' - 2(2A + 1)f = 0, \quad (7.9)$$

which is the Hermite equation with eigenvalues $\lambda = -2(2A + 1)$. This standard equation has polynomial solutions (Hermite Polynomials) when $\lambda = 2n$ (n is a non-negative integer) and solutions that grow exponentially otherwise. Exponentially growing solutions are not appropriate physically, and hence we are restricted to $\lambda = 0, 2, 4, 6, \dots$ which corresponds to $A = -0.5, -1, -1.5, \dots$. The condition $Y(0) = 0$ restricts us to the integer values of A , of which $A = -1$ is the slowest decaying and the one that will dominate the behaviour at long times. Now substituting $A = -1$ and $Y(0) = 0$ into equation (7.7) and solving for Y we arrive at

$$Y(y) = Cy e^{-\frac{y^2}{4}} \quad (7.10)$$

We can now obtain an expression for $U(X, T) = Y\left(X/(\epsilon \int g(T)dT)^{\frac{1}{2}}\right) \Gamma(T)$

$$U(X, T) = \frac{D'_j \frac{X}{(\epsilon \int g(T)dT)^{\frac{1}{2}}} e^{-\frac{X^2}{4\epsilon \int g(T)dT}}}{\left(\int g(T)dT\right)} = D_j \left(\frac{X e^{-\frac{X^2}{4\epsilon \int g(T)dT}}}{\left(\int g(T)dT\right)^{\frac{3}{2}}} \right), \quad (7.11)$$

where D_j is a constant to be determined. The solution of (7.3) has now been found for arbitrary D_j . D_j depends on the waveform's particular evolution through the nonlinear regime. Recalling that each one of the three cases breaks down in a different way. This means that $D_j = D_j(\epsilon)$ has to be determined uniquely for the plane, cylindrical and spherical cases.

Having now found the old age form, the next challenge is how to obtain accurate

numerical solutions for the cases of large T and how to judge when exactly the old age form has been reached. The method used to obtain the numerical solutions in the long age regime is to use the variable mesh numerical scheme described in §5 for early times. Once the shock has become sufficiently smooth, we will use a change of variables to cause the PDE to tend to a constant solution in time, for each of the three cases. After the change of variables, we will then solve the new PDE using an evenly spaced mesh.

7.1 Planar Case

For the planar case, we make the change of variables $\bar{X} = \frac{X}{T^{\frac{1}{2}}}$, $\bar{T} = \ln T$ and $\bar{U} = UT$, then Burgers' equation becomes

$$\bar{U}_{\bar{T}} = \bar{U} + \left(\frac{\bar{X}}{2} - \frac{\bar{U}}{(e^{\frac{\bar{T}}{2}})} \right) \bar{U}_{\bar{X}} + \epsilon \bar{U}_{\bar{X}\bar{X}}, \quad (7.12)$$

with the following long age behaviour

$$\bar{U} = D \left(\bar{X} e^{-\frac{\bar{X}^2}{4\epsilon}} \right). \quad (7.13)$$

Here, the constant D has been determined by Crighton and Scott [13] to be $D = \exp(\frac{1}{4\epsilon})$ from the Cole-Hopf transformation. This result can be tested using numerical solutions of the modified Burgers' equation and shows excellent agreement, however obtaining numerical results for the smaller values of ϵ proves challenging due to the long time scale before the old age solution is reached.

7.2 Cylindrical Case

As in the planar case we are guided by the old-age form (7.11) and set $\bar{X} = X/T$, $\bar{T} = \ln T$ and $\bar{U} = UT^2$, so that the old age solution takes the form

$$\bar{U} = D_1 f_1(\bar{X}), \quad f_1(\bar{X}) = \bar{X} \exp\left(-\frac{\bar{X}^2}{\epsilon}\right), \quad (7.14)$$

where the constant D_1 depends on the nonlinear evolution from the specified initial condition. In terms of the new variables the generalised Burgers' equation becomes

$$\bar{U}_{\bar{T}} = 2\bar{U} + \left(\bar{X} - \frac{\bar{U}}{e^{2\bar{T}}}\right) \bar{U}_{\bar{X}} + \frac{\epsilon}{2} \bar{U}_{\bar{X}\bar{X}}. \quad (7.15)$$

For large \bar{T} the solution approaches the universal form (7.14) and, once this has occurred, D_1 can then be obtained by considering the maximum value of \bar{U}/f_1 , excluding the region where $\bar{U} \ll 1$. The dependence of D_1 on ϵ is readily determined, at least at leading order, through the log-log plot of Figure 47 and we see that D_1 varies as ϵ^{-2} . Obtaining a quantitative prediction of D_1 has proved a challenge and 'its determination remains an important unsolved canonical problem of nonlinear acoustics' [13]. By considering the tail of the shock (which satisfies a linear equation) and matching to the main part of the shock, Enflo [20] was able to determine an approximation to the constant D_1 ,

$$D_E = \frac{1}{\epsilon^2} \frac{27}{16} \frac{1}{\sqrt{6e}} \left[(1 + 2\epsilon) - \frac{1}{2} \left(1 + \frac{8}{3}\epsilon \right) \left(\frac{\pi^2}{6} - \ln 2 - \frac{11}{36} \right) \right]. \quad (7.16)$$

It should be noted that this is not a perturbation expansion in small ϵ , rather the first two terms in a summation that is assumed to converge reasonably quickly. Due to algebraic complexity, obtaining subsequent terms in the summation is unrealistic. In order to assess

the accuracy of (7.16) in Figure 48 we plot D_1/D_E as a function of ϵ . Thus, it appears that the terms ignored in [20] contribute approximately 26% to the estimate of D_1 .

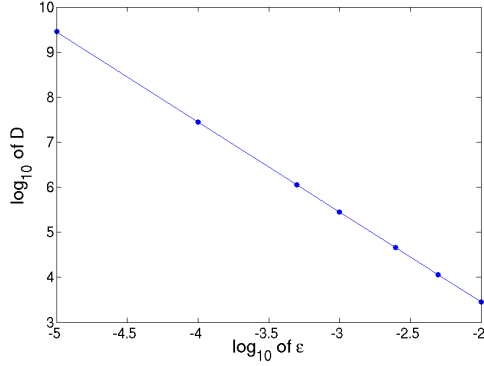


Figure 47: The values of D for various values of ϵ for the cylindrical case.

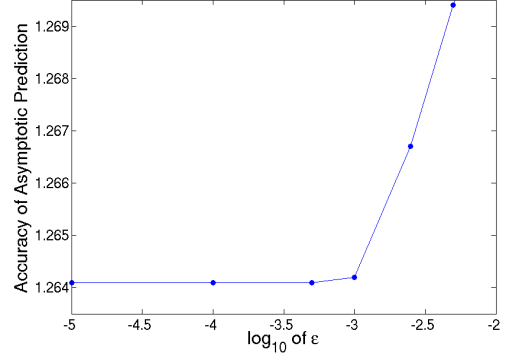


Figure 48: A comparison of the values of ϵ and the accuracy of the asymptotic predictions for the cylindrical case.

7.3 Spherical Case

For the spherical case we take a similar approach to that outlined above. We make the change of variables $\bar{X} = X/e^{-T/2}$, $\bar{T} = T$ and $\bar{U} = Ue^T$, so that the old-age form becomes

$$\bar{U} = D_2 f_2(\bar{X}), \quad f_2(\bar{X}) = \bar{X} \exp\left(-\frac{\bar{X}^2}{4\epsilon}\right). \quad (7.17)$$

with the generalised Burgers' equation in terms of the new variables becoming

$$\bar{U}_{\bar{T}} = \bar{U} + \left(\frac{\bar{X}}{2} - \frac{\bar{U}}{\epsilon^{3\bar{T}/2}}\right) \bar{U}_{\bar{X}} + \epsilon \bar{U}_{\bar{X}\bar{X}}. \quad (7.18)$$

A numerical value of D_2 is obtained by considering \bar{U}/f_2 as described for the cylindrical case. However, in contrast to the cylindrical case, an expression for D_2 can be obtained as a formal asymptotic limit [13], $D_2 = C^{1/2}/6\pi^{1/2}\epsilon^{3/2}$, where C is such that $\epsilon \exp(C)/C = 1$.

Again we can plot the ratio of the asymptotic constant and the numerical constant as a

function of ϵ . From Figure 50 it is reasonable to conclude that as $\epsilon \rightarrow 0$, the numerical value of D_2 approaches the asymptotic approximation of Crighton & Scott [13], though close agreement is only obtained for very small values of ϵ .

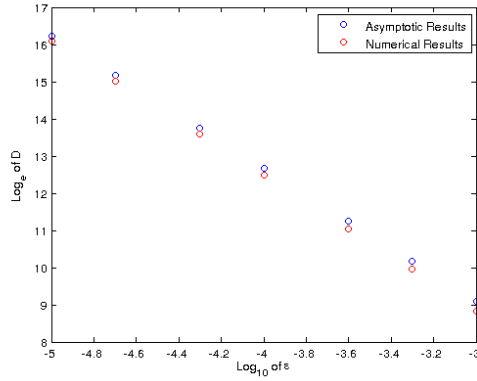


Figure 49: The values of D for various values of ϵ for the spherical case.

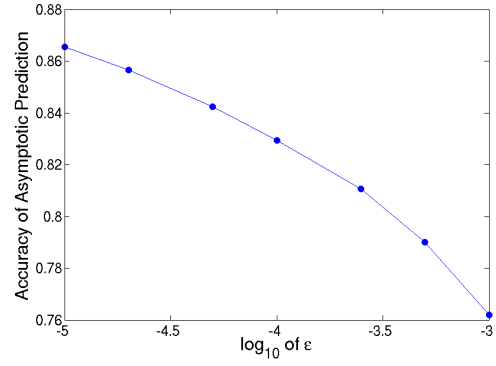


Figure 50: A comparison of the values of ϵ and the accuracy of the asymptotic predictions for the spherical case.

8 Including the effects of relaxation

8.1 Introduction

So far in this thesis we have only considered one absorption or dispersion mechanism. This has been thermoviscous diffusion and accounts for the translational and rotational kinetic energies of the molecules in the thermally and calorically perfect gas as is found in Burgers' equation which was derived in §3.1. However, for polyatomic molecules, such as Nitrogen and Oxygen, we must also consider the internal vibrational energies of the molecules in the gas aswell. These vibrational energies are caused by the molecules absorbing energy from sound waves propagating through the atmosphere. With each molecule there is a characteristic relaxation time, τ_i , which represents the time over which the molecules releases its energy and the non-dimensional change in linear sound speed between low and high frequency signals, Δ_i .

As discussed by Pierce [45], for air, the dominant relaxation modes are determined by the Nitrogen and Oxygen molecules, with contributions from Carbon Dioxide becoming more important at higher altitudes. Water vapour must also be considered as the amount of water vapour present in the air affects the relaxation times associated with Nitrogen and Oxygen as they are more likely to release their energy upon collision with a water molecule.

The effects of relaxation require the inclusion of an additional term to Burgers' equation for each molecule we consider. Therefore the plane Burgers' equation (3.13) with the

inclusion of n relaxation modes becomes

$$U_T + UU_X + \sum_{i=1}^n \Delta_i U_{iX} = \epsilon U_{XX}, \quad (8.1)$$

where the U_i terms can be interpreted as partial pressures and are given by the following equation

$$\left(1 + \tau_i \frac{\partial}{\partial T}\right) U_i = \tau_i \frac{\partial U}{\partial T}. \quad (8.2)$$

Moreover, we can assume forward travelling waves at leading order as we did in (3.6), so we can re-express (8.2) as

$$\left(1 - \tau_i \frac{\partial}{\partial X}\right) U_i = -\tau_i \frac{\partial U}{\partial X}. \quad (8.3)$$

Introducing the effects of relaxation makes a key change to the general behaviour of Burgers' equation as we now have a break from the anti-symmetric behaviour which has been a key feature of the earlier analysis as we must now consider both shocks in the positive and negative regions.

8.2 Numerical Method

The PDE described in (8.1) can be solved using the implicit method as described by Chong [7] described in §5, where we express the PDE as a tri-diagonal matrix to be inverted. However, we also need to find an expression for U_i separately which can also be found by expressing (8.3) as a tri-diagonal matrix also to be inverted.

In §5, we adopted a variable mesh scheme to solve Burgers' equation for the region $[0, a]$ where a was the smallest value such that $u(a, t) < 10^{-8}$. This was possible due

to the fact that we knew zero was a fixed point due to the wave being antisymmetric about zero. However, upon the inclusion of relaxation effects, the wave will no longer be antisymmetric. Hence we must consider both of the shocks centred approximately at $X = \pm 1$ when $t = 0$. This requires us to alter the numerical method in terms of setting up and re-zoning the variable mesh (shown in the algorithm in Figure 10).

For the simple cases of two well behaved shocks (i.e. no sub-shocks or multiple shocks [33]), we can split the x -domain into two regions and rezone each region separately as demonstrated in the algorithm in Figure 10. In this case we need to make sure the connecting points between the two regions match up perfectly, which involves calculating the overlap in the middle and then compressing each side of the mesh about their shock until the two regions meet up perfectly.

It is possible to have an initial disturbance that is not an N-wave and may contain multiple shocks or multiple shocks may arise from a single N-wave. In this case, a more complicated algorithm will be required to rezone the variable mesh. This will involve locating all the shocks and then defining a mesh which will offer enough resolution for them all. This method can be fairly computationally intensive and as such we use the more basic algorithm for the cases where we do not expect to have more than two shocks or any sub-shocks appearing.

9 Understanding the effects of relaxation

9.1 Finding an analytic form for U_1

In order to understand the effects of relaxation we will only consider one relaxation term in this section, characterised by U_1 . As in Chapter 4, it is useful to introduce a change of variables which will highlight the effects of the relaxation terms. We consider the plane Burgers' equation, which only accounts for nonlinear steepening and thermoviscous diffusion, acting upon a unit N-wave. It has previously been seen in §4.1 that, at leading order, the shock location moves with speed $T^{\frac{1}{2}}$ while the amplitude changes like $T^{-\frac{1}{2}}$. In order to combat this, we introduce a similar change of variables as in §4.1,

$$x = T^{-\frac{1}{2}}X, \quad u = T^{\frac{1}{2}}U, \quad u_1 = T^{\frac{1}{2}}U_1, \quad t = \ln T.$$

Recalling from §4.1, this change of variables is designed to keep the shocks fixed at leading order. However, this change of variables does not take into account any effects of relaxation. In terms of the new variables the governing equation is now given by

$$u_t = \frac{u}{2} + \left(\frac{x}{2} - u\right)u_x - e^{\frac{t}{2}}\Delta_1 u_{1x} + \epsilon u_{xx}, \quad (9.1)$$

where the relaxation term is now given by

$$\left(\frac{e^{\frac{t}{2}}}{\tau_1} - \frac{\partial}{\partial x}\right)u_1 = -\frac{\partial u}{\partial x}. \quad (9.2)$$

Considering a relaxation mode with the limits of $\tau_1 \gg 1$ or $\tau_1 \ll 1$ we can gain some understanding of how the relaxation term affects the waveform. In the case where $\tau_1 \ll 1$,

(9.2) can be approximated as $e^{\frac{t}{2}}u_1/\tau_1 = -u_x$. Inserting this into (9.1) gives

$$u_t = \frac{u}{2} + \left(\frac{x}{2} - u\right)u_x + \left(\epsilon + \frac{\Delta_1\tau_1}{e^{\frac{t}{2}}}\right)u_{xx}. \quad (9.3)$$

As can be seen, this results in the relaxation mode acting as an additional diffusive term.

However, if we consider the case where $\tau_1 \gg 1$, (9.2) can now be approximated as $\frac{\partial u_i}{\partial x} \approx \frac{\partial u}{\partial x}$ which results in the following form of (9.1)

$$u_t = \frac{u}{2} + \left(\frac{x}{2} - u - e^{\frac{t}{2}}\Delta_1\right)u_x + \epsilon u_{xx}. \quad (9.4)$$

This means, in this case, the relaxation term is acting as additional advection term.

We can verify these results by comparing the asymptotic forms with numerical solutions. The cases of $\tau_1 \ll 1$ and $\tau_1 \gg 1$ are plotted in Figures 52 and 53 respectively (all with $\epsilon = 0.001$), where Figure 51 is the control case with no relaxation modes. In a physically realistic atmosphere we have that $\Delta_1 \ll 1$, however in order to better see the effects of relaxation, Δ_1 was set to be 1 for the results presented in Figures 52 and 53. In Figure 52 it can be seen that the effect of the relaxation is to cause more dispersion around the shocks, whereas in Figure 53 the effect of the relaxation is to cause a further advection effect.

These two results corroborate our earlier assertions and we can offer physical interpretations to these results. In the case where $\tau_1 \ll 1$, the diatomic molecules have plenty of time to absorb and release the energy before they get excited again. Hence, they act like an additional diffusive term. Whereas, when $\tau_1 \gg 1$ the molecules don't have time to lose energy, this results in the molecules staying permanently in an excited state. This causes

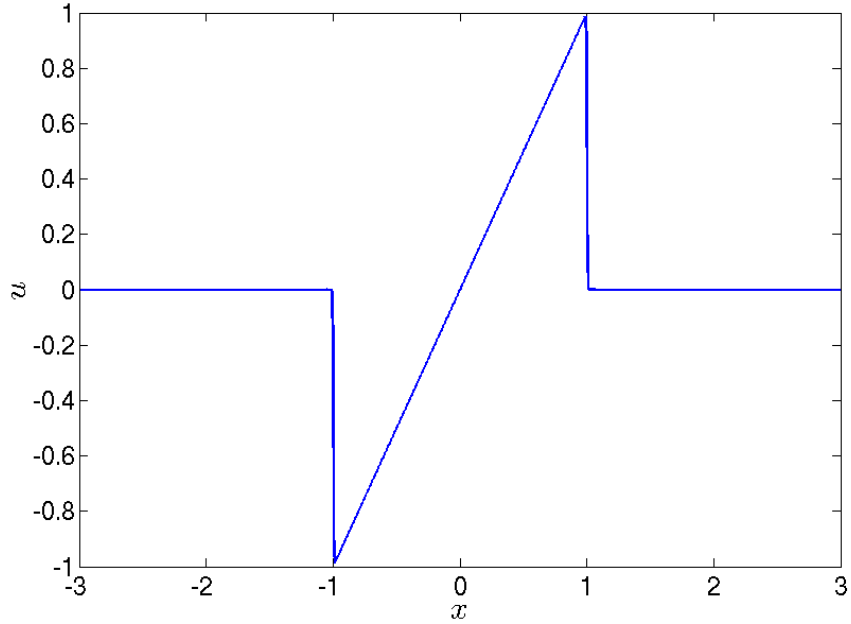


Figure 51: Burgers' equation with no relaxation modes, plotted at $t = 0, 2, 4, 6, 8$ and 10 .

an increase in the sound speed (referred to as the frozen sound speed) of Δ_1 , hence the term acts like an additional advection term.

Having considered the cases where $\tau_1 \ll 1$ and when $\tau_1 \gg 1$, it is also of interest to consider the more interesting and physically relevant case where $\tau_1 = O(1)$. Here one would expect there to be both effects of advection and diffusion, although there may be other effects to the waveform that cannot be easily anticipated. In Figure 54, we present numerical solutions of the case when $\tau_1 = 1$, also with $\Delta_1 = 1$ and $\epsilon = 0.001$.

Upon observing Figure 54, the first thing to notice is the break from the antisymmetric waves present in the previous cases where $\tau_1 \ll 1$ and $\tau_1 \gg 1$. There are also a number of unexpected features of the wave. One thing to note is the fact that the shock decays much more compared to Figure 52, where $\tau_1 \ll 1$ and the relaxation mode acted like an additional diffusive term. In addition the loss of energy is not confined to the shocks as it is in Figure 52. Also we seem to have the same amount of advection as in the case where

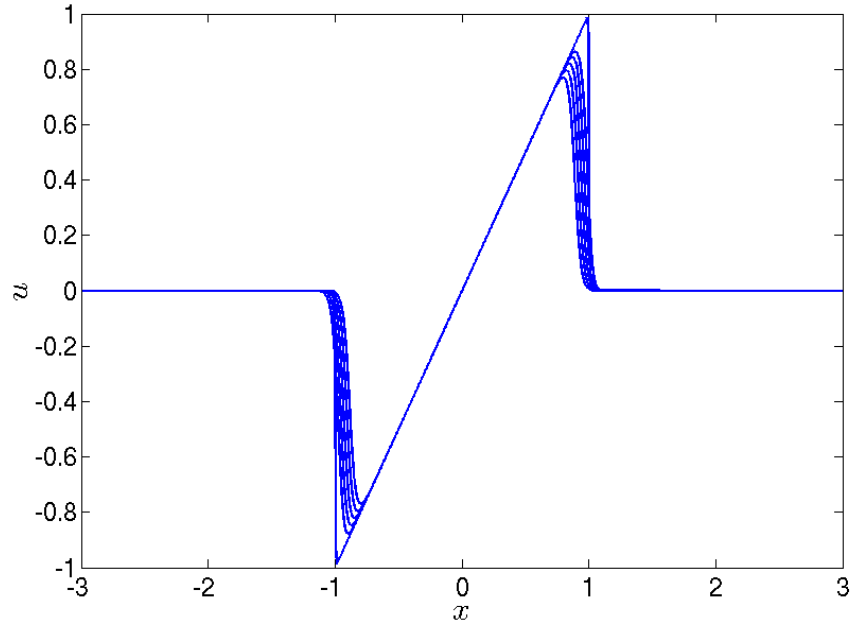


Figure 52: Burgers' equation with one relaxation mode where $\tau_1 \ll 1$ ($\tau_1 = 0.01$), plotted at $t = 0, 2, 4, 6, 8$ and 10 , where an increase in time is seen by a decrease in amplitude.

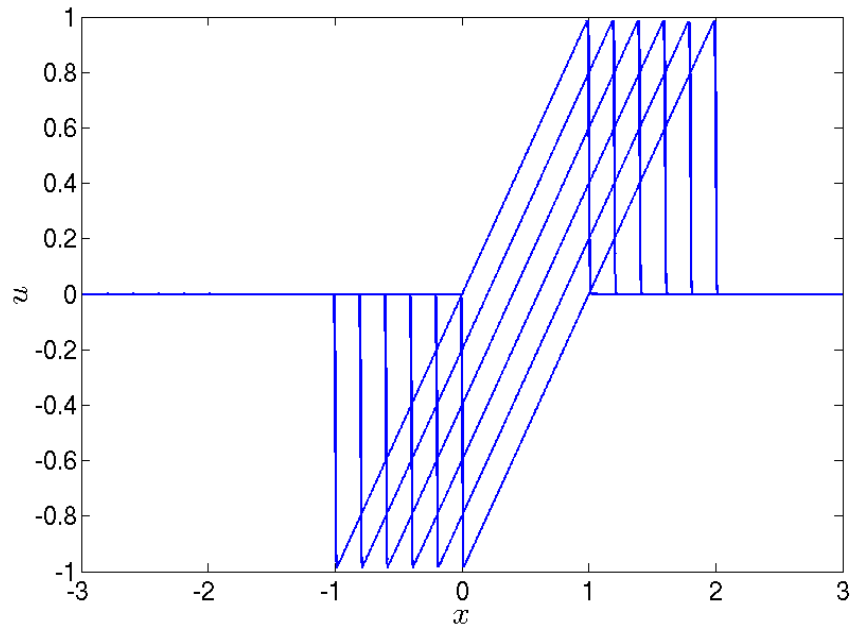


Figure 53: Burgers' equation with one relaxation mode where $\tau_1 \gg 1$ ($\tau_1 = 100$), plotted from $t = 0$ to $t = 1$ with intervals of 0.2 , where an increase in time is seen by a decrease in amplitude.

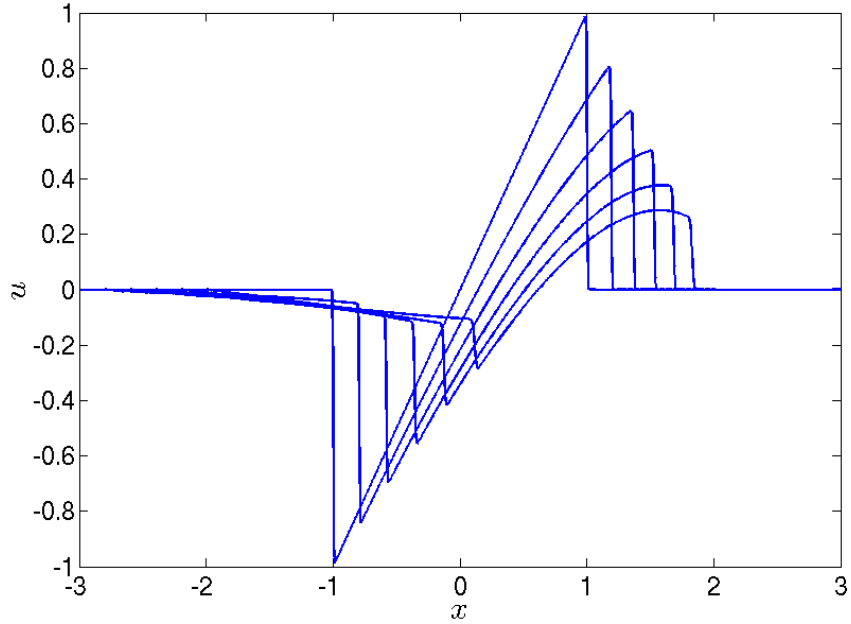


Figure 54: Burgers' equation with one relaxation mode, $\tau_1 = 1$, plotted from $t = 0$ to $t = 1$ with intervals of 0.2, where an increase in time is seen by a decrease in amplitude.

$\tau_1 \gg 1$ in Figure 53. Another unexpected feature of the waveform is the slowly decaying tail in Figure 54 for the region $x < -1$. This result is unexpected as a slowly decaying tail does not feature in either of the cases when $\tau_1 \ll 1$ or $\tau_1 \gg 1$. However, the slow decaying tail is a feature that has been observed in numerous experiments (e.g. Figure 5(a) in [57], Slide 9 in [25] and Figure 26 in [44]) so cannot be attributed to numerical error. Experimental results will be covered in more detail in §10.6.

In order to explain this behaviour we need to consider (9.2) when $\tau_1 = O(1)$. Whilst we cannot find an exact closed form solution for u_1 for arbitrary functions of u . If we consider a unit N-wave with an $O(\Delta_1)$ correction, where $\Delta_1 \ll 1$, then a perturbation solution is obtainable. A solution can be found by separating the N-wave into five regions; $x < -1$, $-1 < x < 1$, $x > 1$ and the two shocks at $x = \pm 1$. This separation results in the following

equations

$$\begin{aligned}\frac{e^{\frac{t}{2}}}{\tau_1}u_1 - u_{1x} &= O(\Delta_1), & x < -1, \\ \frac{e^{\frac{t}{2}}}{\tau_1}u_1 - u_{1x} &= -1 + O(\Delta_1), & -1 < x < 1, \\ \frac{e^{\frac{t}{2}}}{\tau_1}u_1 - u_{1x} &= O(\Delta_1), & x > 1.\end{aligned}$$

We can also arrive at jump conditions by integrating (9.2) giving

$$\frac{e^{t/2}}{\tau_1} \int_{x-\delta}^{x+\delta} u_1 dx' = [u_1]_{x-\delta}^{x+\delta} - [u]_{x-\delta}^{x+\delta}.$$

Letting $\delta \rightarrow 0$ gives us that $[u_1]_{x-\delta}^{x+\delta} = [u]_{x-\delta}^{x+\delta}$. Applying this at the shocks centred around $x = \pm 1$ gives us that

$$u_1^- - u_1^+ = 1 + O(\Delta_1), \quad x = \pm 1.$$

Solving these equations gives us the following results

$$u_{1a} = A \exp\left(\frac{e^{\frac{t}{2}}x}{\tau_1}\right) + O(\Delta_1), \quad x < -1, \quad (9.5)$$

$$u_{1b} = B \exp\left(\frac{e^{\frac{t}{2}}x}{\tau_1}\right) - \frac{\tau_1}{e^{\frac{t}{2}}} + O(\Delta_1), \quad -1 < x < 1 \quad (9.6)$$

$$u_{1c} = C \exp\left(\frac{e^{\frac{t}{2}}x}{\tau_1}\right) + O(\Delta_1), \quad x > 1, \quad (9.7)$$

$$u_{1a} - u_{1b} = 1 + O(\Delta_1), \quad x = -1, \quad (9.8)$$

$$u_{1b} - u_{1c} = 1 + O(\Delta_1), \quad x = 1. \quad (9.9)$$

The constants A , B , and C can be found by using the matching shock conditions (9.8) and (9.9) along with the farfield condition that $u_1 \rightarrow 0$ as $x \rightarrow \pm\infty$ (in accordance with

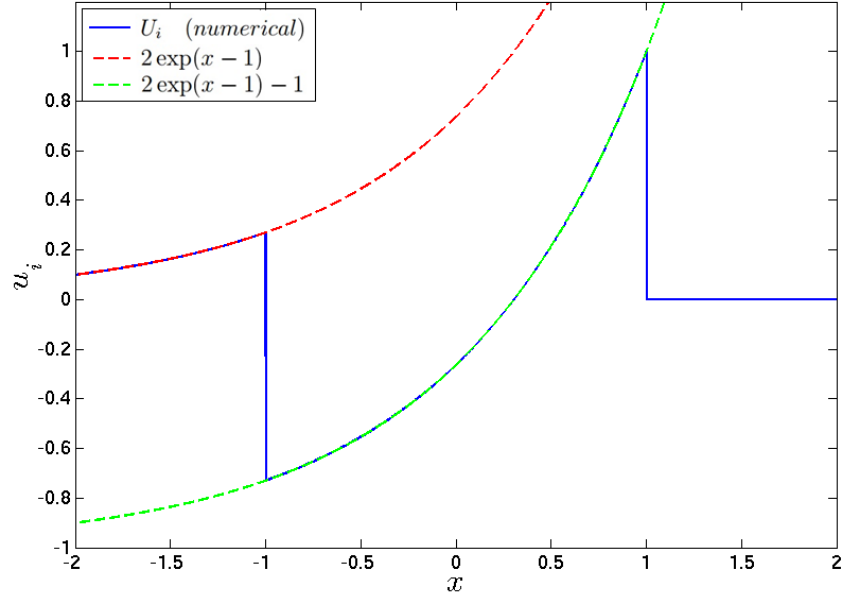


Figure 55: A comparison between the numerical and analytical solution of the relaxation mode with $\tau_1 = 1$ and a perfect unit N-wave, where $2 \exp(x - 1)$ corresponds to (9.10) and $2 \exp(x - 1) - 1$ corresponds to (9.11).

the behaviour of u). Combining all this together results in the following equations for u_1

$$u_{1a} = 2 \left(\cosh \left(\frac{e^{\frac{t}{2}}}{\tau_1} \right) - \frac{\tau_1}{e^{\frac{t}{2}}} \sinh \left(\frac{e^{\frac{t}{2}}}{\tau_1} \right) \right) \exp \left(\frac{x e^{\frac{t}{2}}}{\tau_1} \right) + O(\Delta_1), \quad x < -1, \quad (9.10)$$

$$u_{1b} = \left(1 + \frac{\tau_1}{e^{\frac{t}{2}}} \right) \exp \left(\frac{(x - 1) e^{\frac{t}{2}}}{\tau_1} \right) - \frac{\tau_1}{e^{\frac{t}{2}}} + O(\Delta_1), \quad -1 < x < 1, \quad (9.11)$$

$$u_{1c} = O(\Delta_1), \quad x > 1. \quad (9.12)$$

This result can be verified by a simple comparison with the numerical solution of the relaxation mode when we are considering a unit N-wave with $\tau_1 = 1$. This is shown in Figure 55 and shows excellent agreement which holds true for all values of τ_1 .

9.2 The effect of the relaxation term upon the waveform when

$$\tau_1 = \mathbf{O}(1)$$

Having found an analytical expression for the relaxation term when $\tau_1 = \mathbf{O}(1)$, we now wish to see what effect this relaxation term has on the waveform. From observing Figure 54 it can be seen that one of the effects of relaxation is to cause the shock to move at a rate that is approximately the same when $\tau_1 \gg 1$. In order to make the numerics simpler, it helps to keep the shocks fixed at leading order. Looking back to (9.1), that equation was designed to keep the shocks fixed at $x = \pm 1$ (at leading order), however it did not take into account any relaxation effects. We now attempt to eliminate the advective effect of relaxation by shifting to a moving frame. By combining (9.1) and (9.2) we arrive at the following equation

$$u_t = \frac{u}{2} + \left(\frac{x}{2} - u\right) u_x - e^{\frac{t}{2}} \Delta_1 u_x - \Delta_1 \frac{e^t}{\tau_1} u_1 + \epsilon u_{xx}, \quad (9.13)$$

where u_1 is still as defined in (9.2). We now wish to eliminate the $e^{\frac{t}{2}} \Delta_1 u_x$ term by introducing a change of variables $\bar{x} = x - q(t)$, where $q(t)$ is to be determined. With this change of variables (9.13) becomes

$$u_t = \frac{u}{2} + \frac{\bar{x}}{2} u_{\bar{x}} - u u_{\bar{x}} + \left(q'(t) + \frac{1}{2} q(t) - e^{\frac{t}{2}} \Delta_1\right) u_x - \Delta_1 \frac{e^t}{\tau_1} u_1 + \epsilon u_{\bar{x}\bar{x}}. \quad (9.14)$$

Solving $q'(t) + \frac{1}{2} q(t) = e^{\frac{t}{2}} \Delta_1$ along with the condition that $q(0) = 0$ results in $q(t) = \Delta_1 (e^{\frac{t}{2}} - e^{-\frac{t}{2}})$ and (9.14) becomes

$$u_t = \frac{u}{2} + \frac{\bar{x}}{2} u_{\bar{x}} - u u_{\bar{x}} - \Delta_1 \frac{e^t}{\tau_1} u_1 + \epsilon u_{\bar{x}\bar{x}}, \quad (9.15)$$

where the shocks are now fixed at $x = \pm 1$ at leading order as long as the relaxation term, $\Delta_1 e^t / \tau_1$, is small, hence we are restricted to values of $\tau_1 \gg \Delta_1$.

It is now desirable to perform a perturbation analysis for the relaxation term. However, in order to do that we must first show that u_1 is bounded so here we will show that $|u_1| \leq 1$ for all values of x .

Assuming we start with a N-wave shock, then we will have a relaxation term as is shown in (9.10) to (9.12), where u_{1a} , u_{1b} and u_{1c} describe the relaxation term u_1 in the intervals $-\infty < x < -1$, $-1 < x < 1$ and $1 < x < \infty$ respectively. Moreover, we must have $u_{1b}(1) = u_{1c}(1) + 1$, where $u_{1c} = 0$ and $u_{1a}(-1) = u_{1b}(-1) + 1$. Since both u_{1a} and u_{1b} are increasing functions and $u_{1a} > 0$ for all values of x , we only need to show that $-1 \leq u_{1b}(-1) \leq 0$ in order to show that $|u_1| \leq 1$ for all values of x .

In order to show that $-1 \leq u_{1b}(-1) \leq 0$, we express $u_{1b}(-1)$ as $\exp(-2\lambda) + 1/\lambda(\exp(-2\lambda - 1))$, where $\lambda = e^{t/2}/\tau_1$. Now the domain $-\infty < t < \infty$ corresponds to the domain $0 < \lambda < \infty$ and it can be seen that as $\lambda \rightarrow \infty$, $u_{1b}(-1) \rightarrow 0$ and as $\lambda \rightarrow 0$, $u_{1b}(-1) \rightarrow -1$ with no turning points in between. Hence, we can say that $|u_1| < 1$ for all values of x .

Now, we know that $|u_1| < 1$ for all values of x , this implies that $\Delta_1 u_1 \frac{e^{t/2}}{\tau_1} < \Delta_1 \frac{e^{t/2}}{\tau_1}$ and assuming that $\Delta_1 \frac{e^{t/2}}{\tau_1} \ll 1$, we can perform a perturbation analysis for $\epsilon \ll \Delta_1 \ll 1$ in order to see what effect the relaxation term has on the waveform. If we write $u = U + \Delta_1 V + \epsilon W$ and use a similar expansion for u_1 , we can obtain equations for U , V and W of the form

$$\begin{aligned}
U_t &= \frac{U}{2} + \frac{\bar{x}}{2} U_{\bar{x}} - U U_{\bar{x}}, \\
V_t &= \frac{V}{2} + \frac{\bar{x}}{2} V_{\bar{x}} - U V_{\bar{x}} - V U_{\bar{x}} - \frac{e^t}{\tau_1} U_1, \\
W_t &= \frac{W}{2} + \frac{\bar{x}}{2} W_{\bar{x}} - U W_{\bar{x}} - W U_{\bar{x}} + U_{\bar{x}\bar{x}},
\end{aligned} \tag{9.16}$$

where U_1 is given from the form found in (9.12)

$$\begin{aligned}
U_{1a} &= 2 \left(\cosh \left(\frac{e^{\frac{t}{2}}}{\tau_1} \right) - \frac{\tau_1}{e^{\frac{t}{2}}} \sinh \left(\frac{e^{\frac{t}{2}}}{\tau_1} \right) \right) \exp \left(\frac{\bar{x} e^{\frac{t}{2}}}{\tau_1} \right), & \bar{x} < -1, \\
U_{1b} &= \left(1 + \frac{\tau_1}{e^{\frac{t}{2}}} \right) \exp \left(\frac{(\bar{x} - 1) e^{\frac{t}{2}}}{\tau_1} \right) - \frac{\tau_1}{e^{\frac{t}{2}}}, & -1 < \bar{x} < 1, \\
U_{1c} &= 0, & \bar{x} > 1.
\end{aligned} \tag{9.17}$$

Away from the shock regions at $\bar{x} = \pm 1$, the solution for U is given as the unit N-wave

$$U = \begin{cases} 0, & \bar{x} < -1, \\ \bar{x}, & |\bar{x}| \leq 1, \\ 0, & \bar{x} > 1. \end{cases}$$

This results in the following PDEs governing the correction term due to relaxation effects

$$V_t = \frac{V}{2} + \frac{\bar{x}}{2} V_{\bar{x}} - \frac{e^t}{\tau_1} U_{1a}, \quad \bar{x} < -1, \tag{9.18}$$

$$V_t = -\frac{V}{2} - \frac{\bar{x}}{2} V_{\bar{x}} - \frac{e^t}{\tau_1} U_{1b}, \quad -1 < \bar{x} < 1, \tag{9.19}$$

$$V_t = \frac{V}{2} + \frac{\bar{x}}{2} V_{\bar{x}}, \quad \bar{x} > 1. \tag{9.20}$$

When $\bar{x} > 1$, it can be seen that in order to satisfy the far field conditions that $V \rightarrow 0$ as $\bar{x} \rightarrow \infty$, we require that $V = 0$ for (9.20). In the region $\bar{x} < -1$, progress can be made by writing $V = v(\lambda) e^{\lambda \bar{x}}$, where $\lambda = e^{\frac{t}{2}}/\tau_1$. By using the chain rule and the fact that $\lambda_t = \frac{1}{2} \lambda$

we arrive at the following form for (9.18)

$$\begin{aligned}
\frac{1}{2}\lambda \left(\frac{dv}{d\lambda} + \bar{x}v \right) &= \frac{1}{2}(\lambda\bar{x}v + v) - 2\tau_1\lambda^2 \left(\cosh(\lambda) - \frac{\sinh(\lambda)}{\lambda} \right), \\
\frac{dv}{d\lambda} - \frac{v}{\lambda} &= -4\tau_1\lambda \left(\cosh(\lambda) - \frac{\sinh(\lambda)}{\lambda} \right), \\
\frac{d}{d\lambda} \left(\frac{v}{\lambda} \right) &= -4\tau_1 \left(\cosh(\lambda) - \frac{\sinh(\lambda)}{\lambda} \right), \\
v(\lambda) &= -4\lambda\tau_1 \left(\sinh(\lambda) - \int_{\lambda_0}^{\lambda} \frac{\sinh(\lambda)}{\lambda} d\lambda + C \right), \tag{9.21}
\end{aligned}$$

where C is defined such that $V(\bar{x}, 0) = 0$ resulting in $C = 0$. This gives us the following form for V

$$V(\bar{x}, t) = -4\lambda\tau_1 e^{\lambda\bar{x}} \left(\sinh(\lambda) - \int_{\lambda_0}^{\lambda} \frac{\sinh(\lambda)}{\lambda} d\lambda \right), \quad \lambda = \frac{t}{\tau_1}. \tag{9.22}$$

For the region where $|\bar{x}| < 1$, no similar simplification can be found. However, progress can be made using the method of characteristics, first introduced in §2.1. By rewriting the governing equation as

$$V_t + \frac{\bar{x}}{2}V_{\bar{x}} = -\frac{V}{2} - \lambda^2\tau_1 \left(1 + \frac{1}{\lambda} \right) \exp((\bar{x} - 1)\lambda) + \lambda\tau_1. \tag{9.23}$$

We define the characteristics as

$$\frac{d\bar{x}}{dt} = \frac{1}{2}\bar{x}, \tag{9.24}$$

which results in the following characteristics for \bar{x}

$$\bar{x} = \bar{x}_0 e^{\frac{t}{2}} = \bar{x}_0 \tau_1 \lambda, \tag{9.25}$$

and allows us to express $\frac{dV}{dt} = V_t + \frac{\bar{x}}{2}V_{\bar{x}}$. So, we can now re-express (9.23) and solve for V

along the characteristics as is shown

$$\begin{aligned}
\frac{dV}{dt} + \frac{V}{2} &= -\lambda^2 \tau_1 \left(1 + \frac{1}{\lambda}\right) \exp((\bar{x}_0 \tau_1 \lambda - 1)\lambda) + \lambda \tau_1, \\
\frac{d}{dt} \left(e^{\frac{t}{2}} V\right) &= e^{\frac{t}{2}} \left(-\lambda^2 \tau_1 \left(1 + \frac{1}{\lambda}\right) \exp((\bar{x}_0 \tau_1 \lambda - 1)\lambda) + \lambda \tau_1\right), \\
\frac{d\lambda}{dt} \frac{d}{d\lambda} (\tau_1 \lambda V) &= -\lambda^3 \tau_1^2 \left(1 + \frac{1}{\lambda}\right) \exp((\bar{x}_0 \tau_1 \lambda - 1)\lambda) + \lambda^2 \tau_1^2, \\
\frac{d}{d\lambda} (\lambda V) &= -2\lambda^2 \tau_1 \left(1 + \frac{1}{\lambda}\right) \exp((\bar{x}_0 \tau_1 \lambda - 1)\lambda) + 2\lambda \tau_1, \\
\lambda V &= -2\tau_1 \int_{\lambda_0}^{\lambda} \gamma^2 \left(1 + \frac{1}{\gamma}\right) \exp(\bar{x}_0 \tau_1 \gamma^2 - \gamma) d\gamma + \lambda^2 \tau_1, \\
V &= -2\frac{\tau_1}{\lambda} \int_{\lambda_0}^{\lambda} \gamma^2 \left(1 + \frac{1}{\gamma}\right) \exp(\bar{x}_0 \tau_1 \gamma^2 - \gamma) d\gamma + \lambda \tau_1. \tag{9.26}
\end{aligned}$$

We can now use this form to compare with numerical solutions. However, there is a slight problem in obtaining a numerical solution for V and that is the form of the wave is $u = U + \Delta_1 V + \epsilon W$, where W is not known. To compensate for this we take $\epsilon \ll \Delta_1$ and plot $(u - x)/\Delta_1$ as an approximation to V , where we take $U \approx x$ in accordance with the outer solution. Results of this are shown in Figures 56 to 61, where $\tau_1 = 1$ for all results. In Figures 56 and 57 we plot the comparison well away from the shocks, In Figures 58 and 59 we plot the comparison close to the shock at $x = 1$ and in Figures 60 and 61 we plot the comparison close to the shock at $x = -1$.

As can be seen good agreement is found, except when we get close to the shocks. This is due to the fact that the shocks at $x = \pm 1$ are of width proportional to ϵ , so we do not have a perfect N-wave which was our assumption in deriving the expression for V in (9.26). This means that in Figures 58 and 60, we have a constant error for a short time until t increases and the shocks start to move at speeds $1 - \epsilon t$ and $-1 + \epsilon t$ for the shocks at $x = \pm 1$ respectively. This causes the shocks to move towards the points 0.99 and -0.99

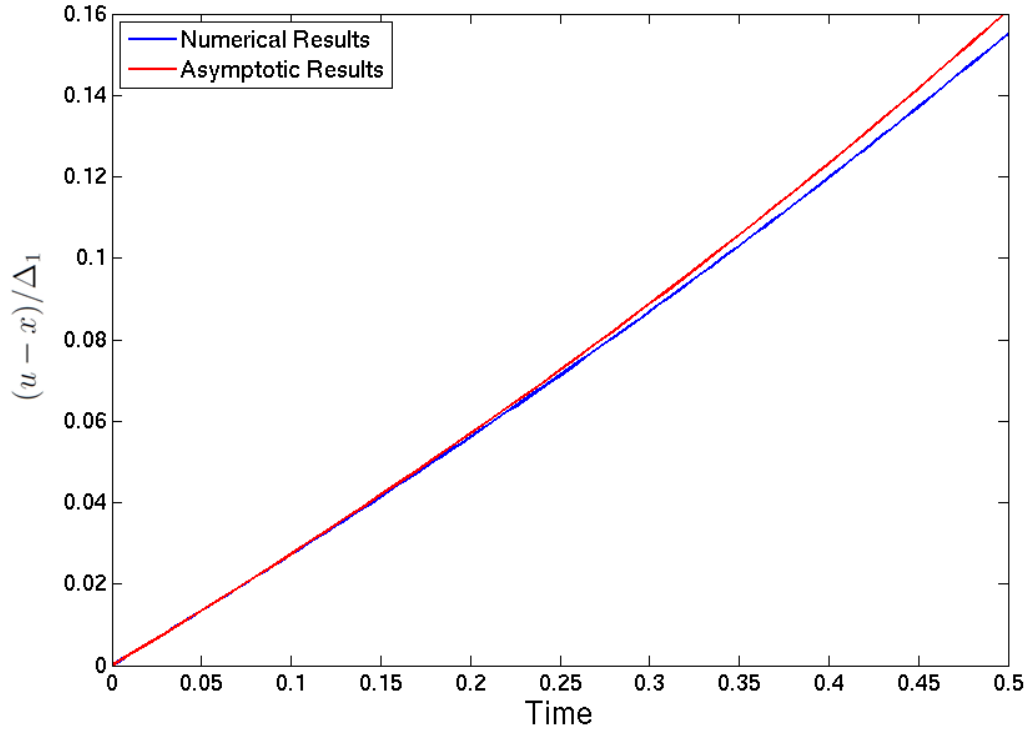


Figure 56: A comparison between the numerical and analytical results for V at the point $x = 0$ with $\Delta_1 = 0.1$ and $\epsilon = 0.001$.

causing the comparisons to diverge further. It is worth noting that for Figures 59 and 61, if we replace the point $x = \pm 0.99$ with $x = \pm 0.999$, a similar effect will be seen to that seen in Figures 58 and 60.

It is perhaps more valuable to observe the general agreement by comparing the values of $V(x, t)$ for a fixed value of t for the numerical and asymptotic results. This is shown in Figures 63 to 65, where the comparisons are plotted for values of Δ_1 of 0.01, 0.1, 0.25, 0.5 respectively with $t = 0.5$.

It is worth noting that the numerical results have not been plotted around the shocks due to poor agreement caused by the tanh shock which invalidates our assumption of a perfect N-wave. Also of worth noting is that the compact domain used extends far past $x = -3$ in order to get reliable results due to the nature of the slow decaying tail. With

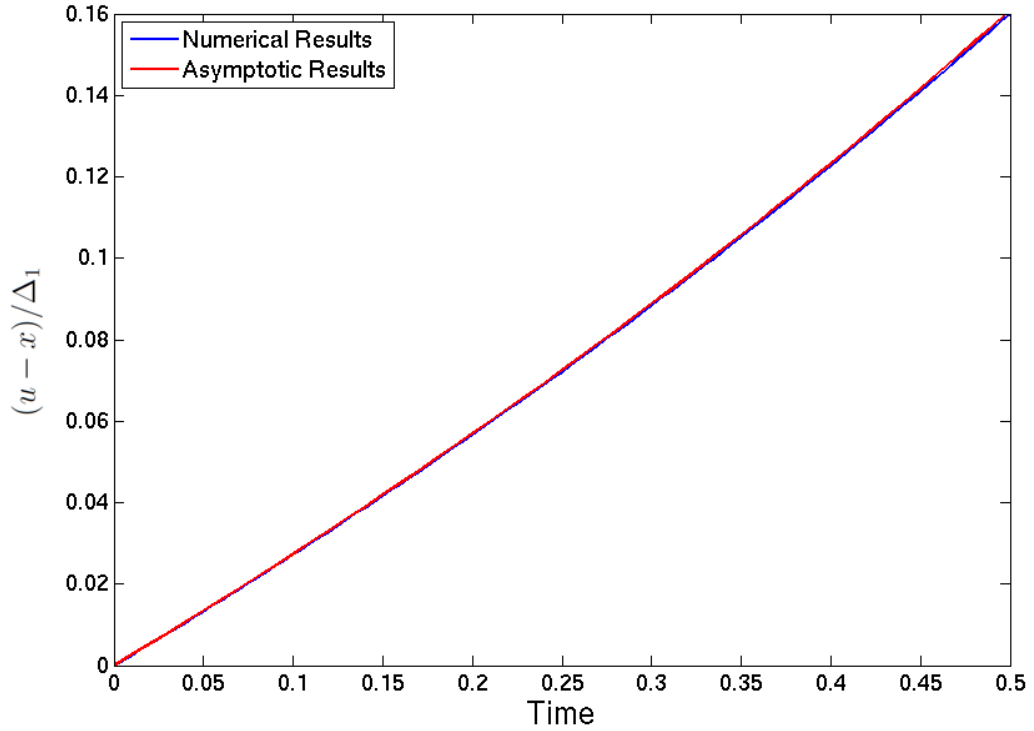


Figure 57: A comparison between the numerical and analytical results for V at the point $x = 0$ with $\Delta_1 = 0.01$ and $\epsilon = 0.0005$.

$t = 0.5$ it was found a lower limit of $x_{\min} = -10$ was sufficient to capture the behaviour of the shock. Extending the lower limit to $x_{\min} = -30$ made no noticeable difference to the final result. As can be seen from Figures 63 and 62, we have excellent agreement for $\Delta_1 = 0.1$ and $\Delta_1 = 0.01$ with near perfect agreement in the region $|x| < 1$. The errors in the region $x < -1$ are suspected to come from the ignore $O(\epsilon)$ term from our initial expression that $u = U + \Delta_1 V + \epsilon W$. Only when Δ_1 is increased to larger values as is shown in Figure 64 and 65 do we start to see noticeable differences between the asymptotic and numerical solutions in the region $-1 < x < 1$. On the whole these results validate the previous asymptotic work and offer a good foundation for explaining the effects of relaxation, in particular the slowly decaying tail for $x < -1$.

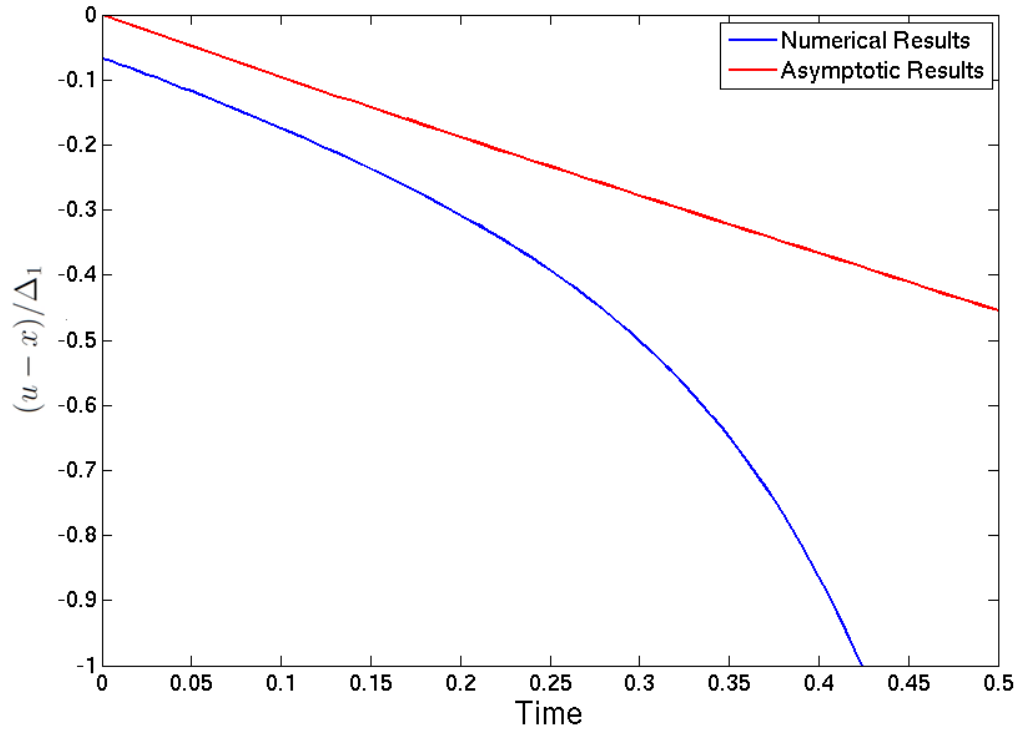


Figure 58: A comparison between the numerical and analytical results for V at the point $x = 0.99$ with $\Delta_1 = 0.1$ and $\epsilon = 0.001$.

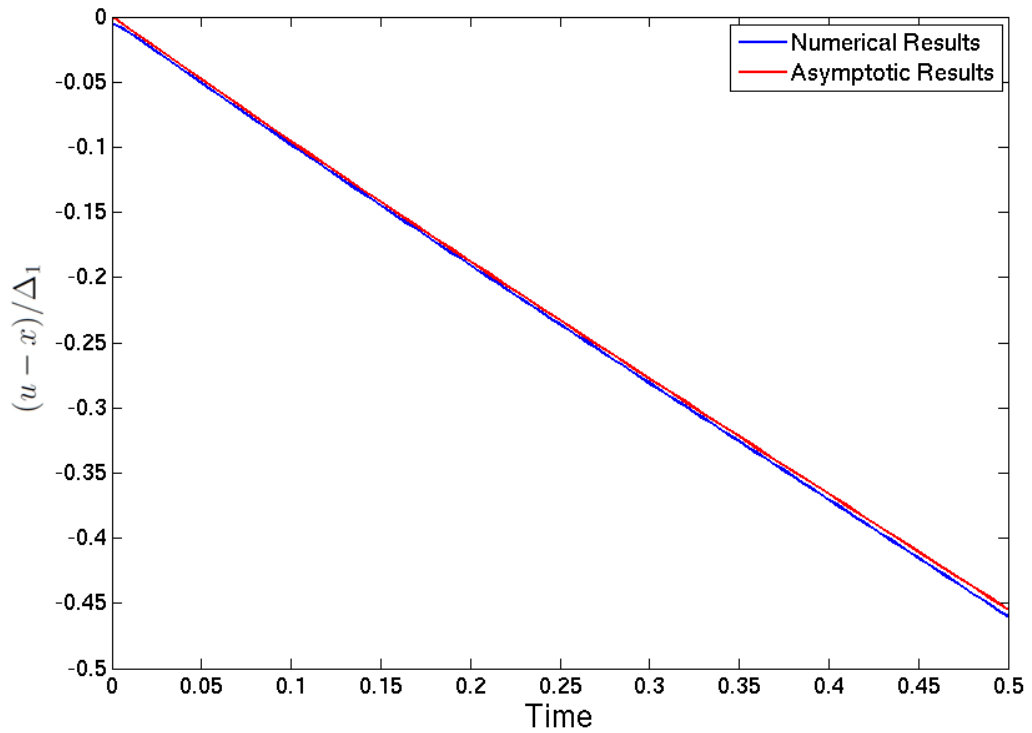


Figure 59: A comparison between the numerical and analytical results for V at the point $x = 0.99$ with $\Delta_1 = 0.01$ and $\epsilon = 0.0005$.

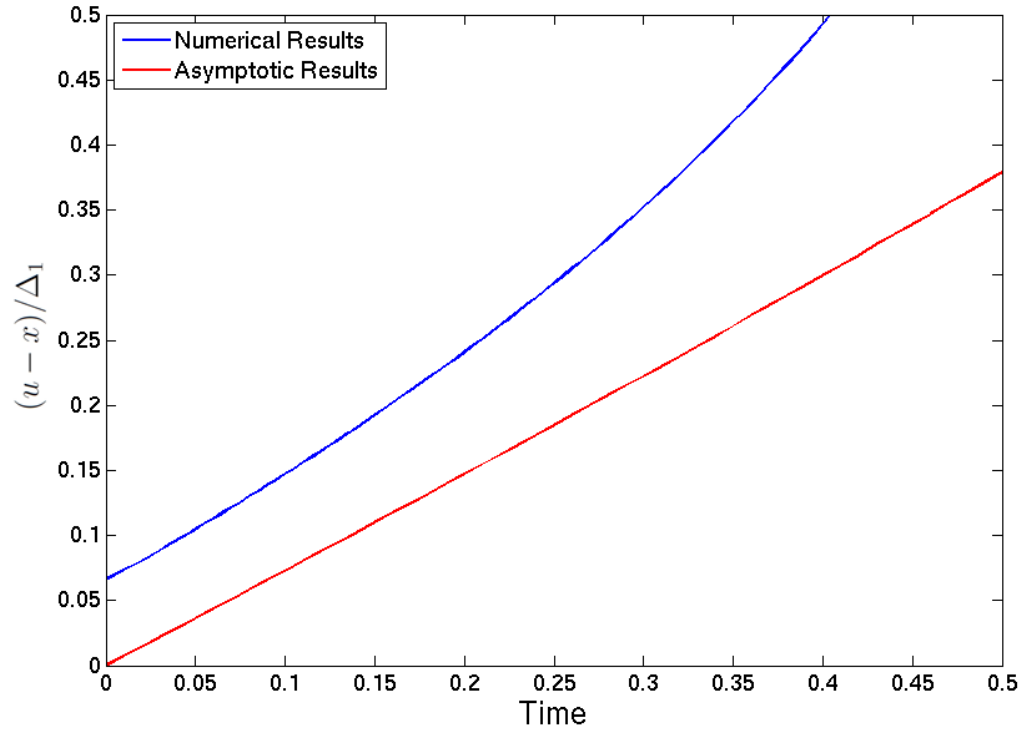


Figure 60: A comparison between the numerical and analytical results for V at the point $x = -0.99$ with $\Delta_1 = 0.1$ and $\epsilon = 0.001$.

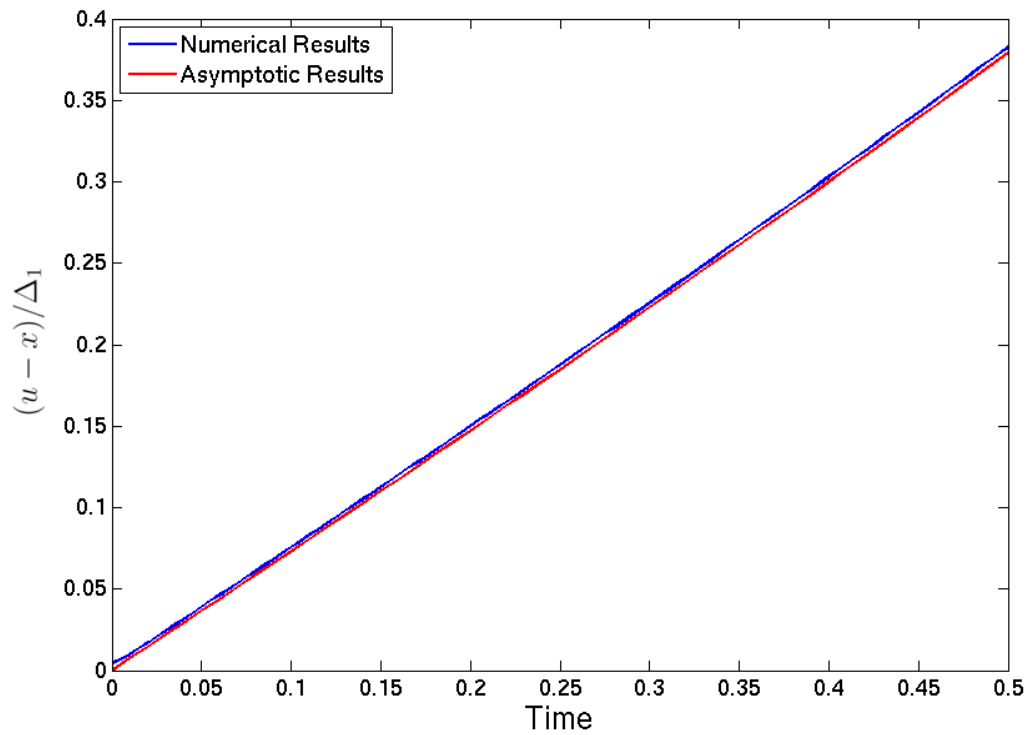


Figure 61: A comparison between the numerical and analytical results for V at the point $x = -0.99$ with $\Delta_1 = 0.01$ and $\epsilon = 0.0005$.

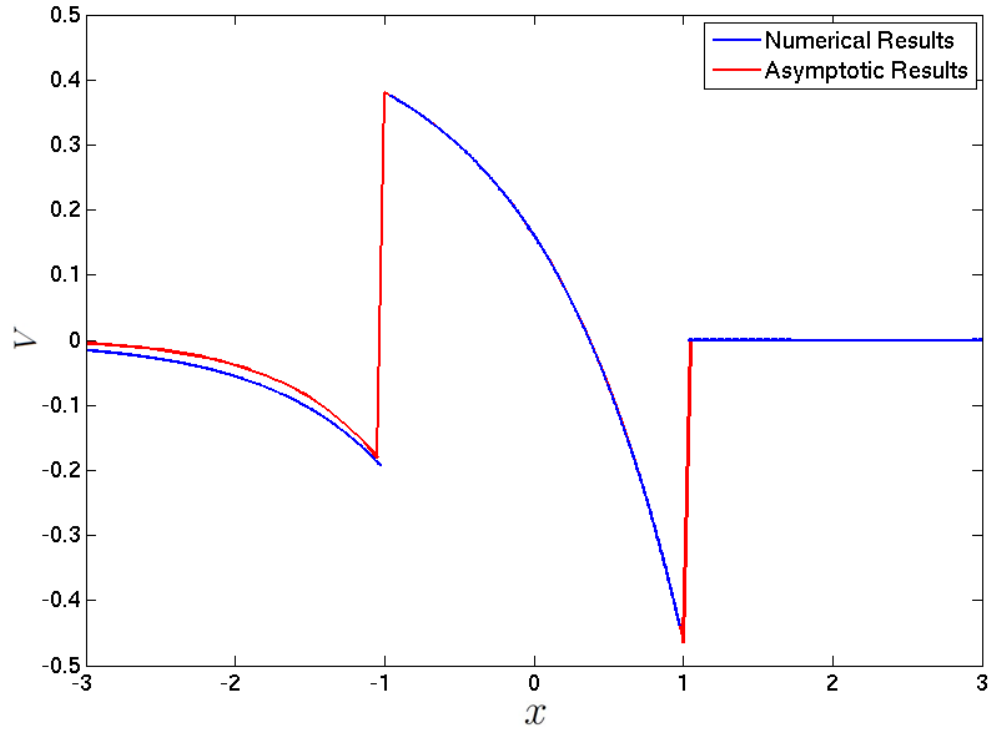


Figure 62: A comparison between the numerical and analytical results for whole waveform where $t = 0.5$ with $\Delta_1 = 0.01$ and $\epsilon = 0.0005$.

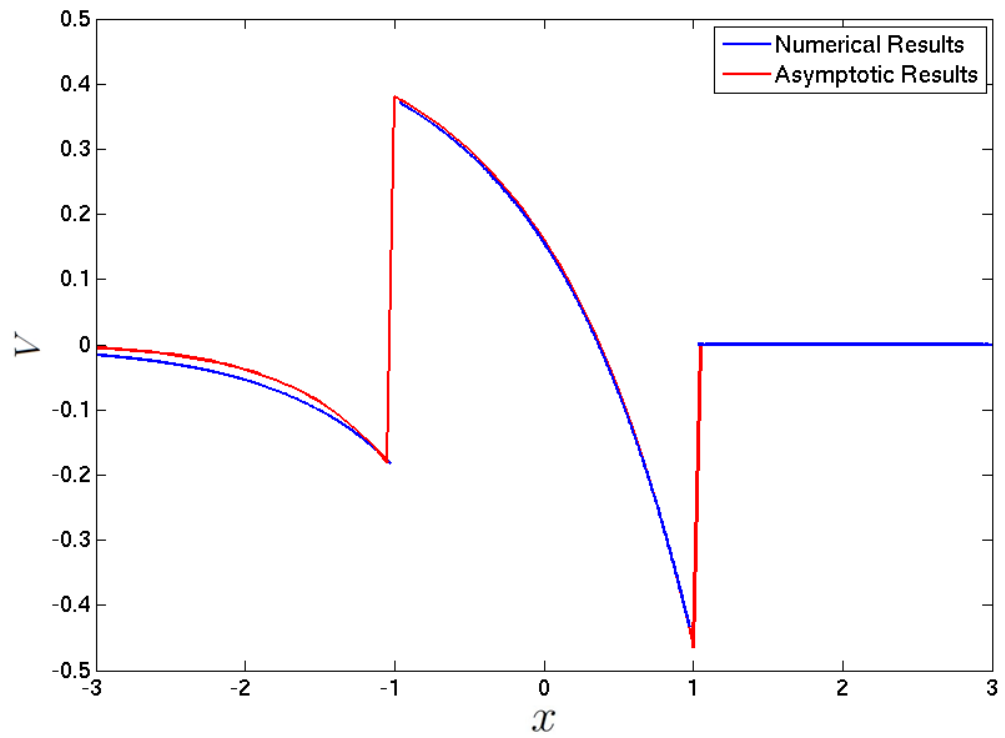


Figure 63: A comparison between the numerical and analytical results for whole waveform where $t = 0.5$ with $\Delta_1 = 0.1$ and $\epsilon = 0.001$.

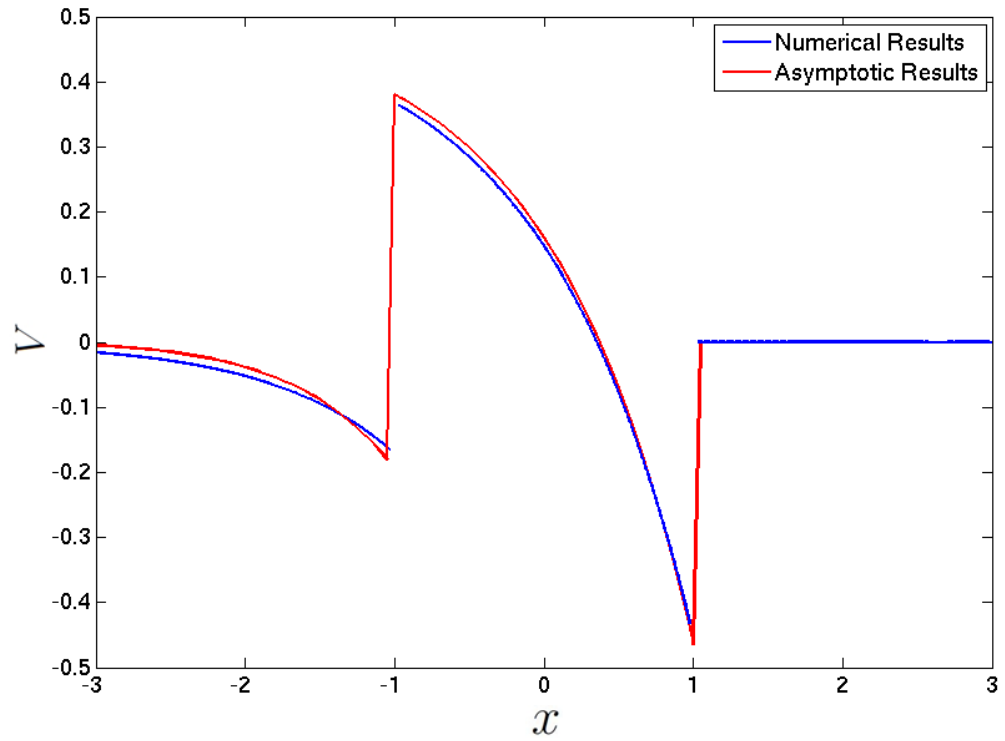


Figure 64: A comparison between the numerical and analytical results for whole waveform where $t = 0.5$ with $\Delta_1 = 0.25$ and $\epsilon = 0.001$.

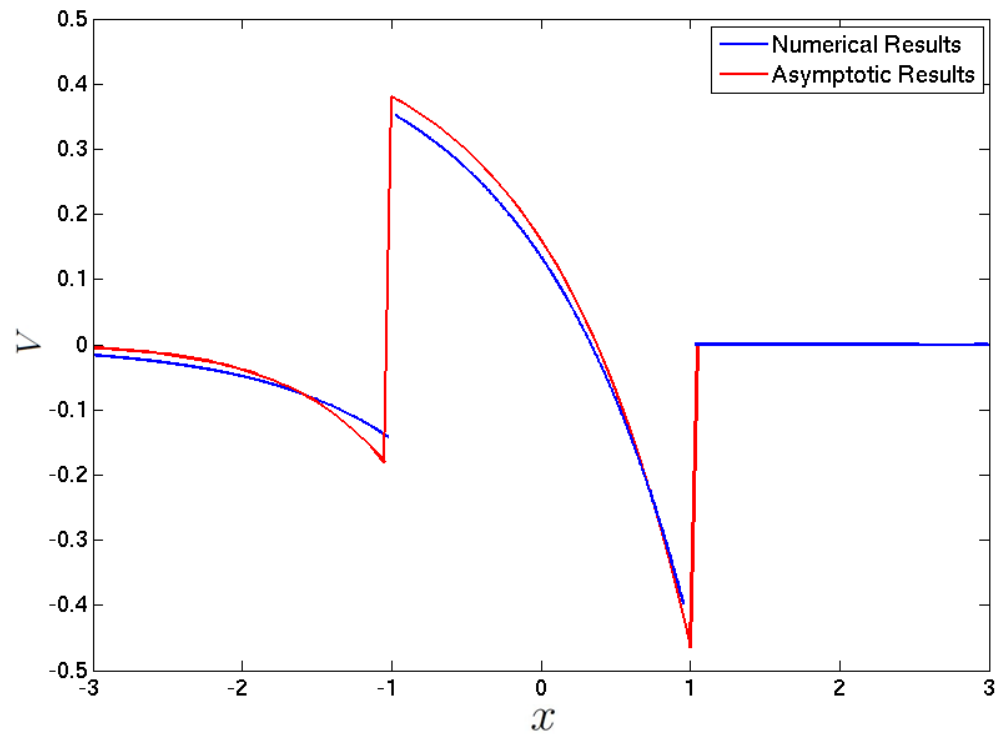


Figure 65: A comparison between the numerical and analytical results for whole waveform where $t = 0.5$ with $\Delta_1 = 0.5$ and $\epsilon = 0.001$.

10 Full Atmospheric Model

10.1 Introduction

In this chapter we will use our knowledge of Burgers' equation developed over the previous chapters to generate a complete atmospheric model of how sonic booms propagate through a realistic atmosphere.

The task of adapting previous work for a full atmospheric model will involve numerous steps. A brief description of the steps will be given here. In §10.1, an introduction will be given outlining the problem and highlighting the differences from earlier methods. The full atmospheric model will involve considering numerous new parameters and how they change with altitude. These parameters will be discussed in §10.2. In §10.3, we are faced with the challenging problem of calculating along what paths the rays will travel. We can no longer assume spherical symmetry due to changes in sound speed with altitude causing the sound waves to have curved paths. A form for the ray tube area is obtained by assuming a linear sound speed in the atmosphere which allows us to predict the sonic boom carpet, that is the area on the ground where a sonic boom will be heard from a supersonic object in the atmosphere. Having defined all the parameters needed, §10.4 will incorporate these into a numerical model where the key differences are the need to redefine certain parameters as the wave propagates. Finally, in §10.5 and §10.6, numerical results will be presented a brief comparison made to experimental results.

The key differences from the method approached here to the method used in previous work is the focus on the detailed shock structure. For example Cleveland, [9], solved the nonlinear PDE in the frequency domain which causes a loss of resolution of the in-depth

shock structure. Johnson, [32], considered a travelling wave as an approximation to a shock, so an in-depth shock analysis was not possible.

One further thing to be mentioned is that this section is unique in the fact that we perform no asymptotic analysis on the equation. This is because the varying atmospheric parameters make it much more complicated in obtaining an accurate asymptotic prediction.

In previous chapters, we have considered propagation through a homogeneous medium which means that many of the governing parameters can be treated as constants. However, in a realistic atmosphere, many of these parameters vary with altitude, temperature and water vapour content, which means that the ray paths no longer travel along straight lines. This means we need to develop a new system to replace the idea of considering either plane, cylindrical or spherical spreading. In order to understand this problem, it is useful to consider exactly how these ray paths are being generated as is shown in Figure 66. Sonic booms will travel along the ray paths which are perpendicular to the Mach cone, where the angle is given by $\psi = \sin^{-1}(c/v) = \sin^{-1}(1/M)$, where c is the speed of sound and v is the velocity of supersonic object. This means that in a homogeneous (e.g. isothermal) atmosphere, for a supersonic object at an altitude of 10,000m travelling at Mach 1.5, the waves from directly beneath the object will travel 13,416m in total before reaching the ground 8,944m away from directly beneath the point at which the boom was generated as shown in Figure 67. However in a stratified atmosphere the sound speed is not constant, but varies with altitude. In Earth's atmosphere the sound speed varies approximately linearly from 295ms^{-1} at 10,000m to 343.2ms^{-1} at sea level [6]. This results in the ray paths being curved and, in some cases, it is possible for the waves to start travelling upwards, back into the atmosphere, before they hit the ground. This case is of

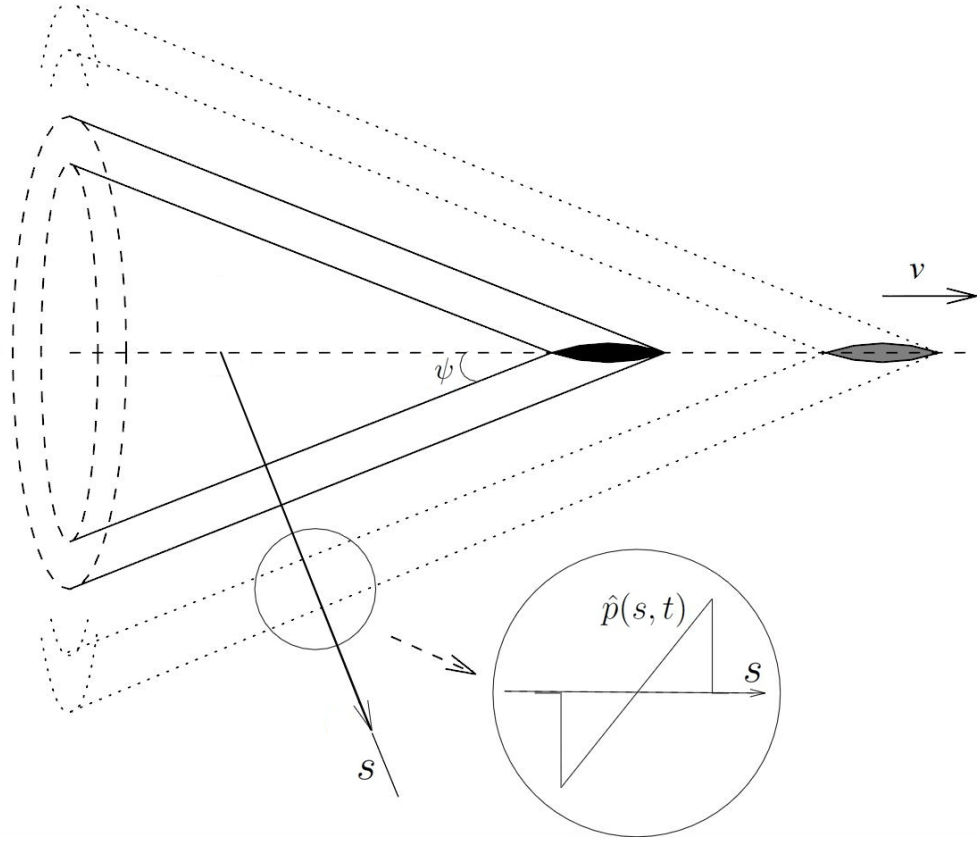


Figure 66: The ray paths generated by a supersonic object.

particular interest as there would be minimal environmental impact to people or animals on the ground.

A ray tube is defined by the area enclosed by paths of four rays that have trajectories varying by some small amount. Propagation of sound down a ray tube is similar to the previous cases we have considered of plane, cylindrical or spherical symmetry where we assume that there is no particle velocity perpendicular to the propagation direction. In ray theory this translates to there being no interaction from adjacent ray tubes, hence it is important to note that in the case of turbulence this assumption becomes invalid, decreasing the accuracy of the results. Equation (2.69) by Cleveland [9] gives the generalised Burgers' equation for propagation in a ray tube as

$$\frac{\partial \hat{p}}{\partial s} + \frac{1}{2A(s)} \frac{\partial A}{\partial s} \hat{p} = \frac{\beta}{\rho c^3} \frac{\partial \hat{p}}{\partial \xi} \hat{p} + \frac{1}{c^2} \sum_i (\Delta c)_i \frac{\partial \hat{p}_i}{\partial \xi} + \frac{\hat{\delta}}{2\rho c^3} \frac{\partial^2 \hat{p}}{\partial \xi^2}, \quad (10.1)$$

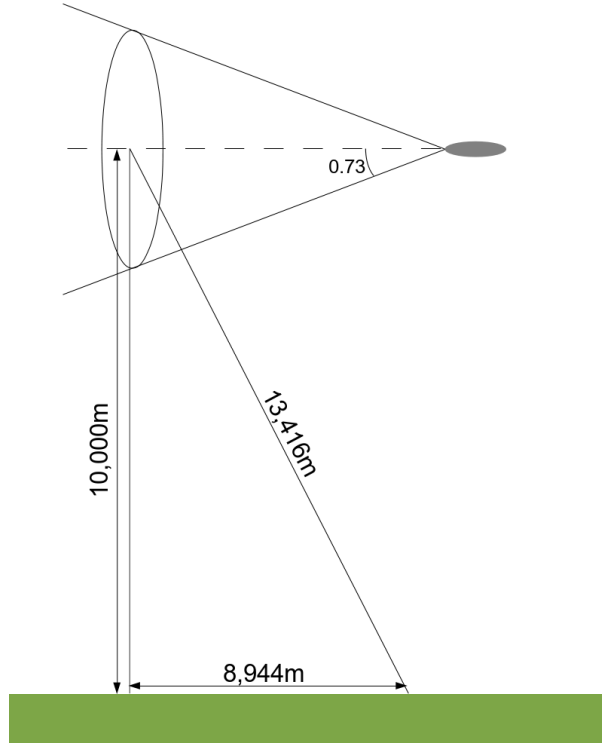


Figure 67: The distance a sonic boom travels from a supersonic object at 10,000m traveling at Mach 1.5.

where

$$\left(1 + c\hat{\tau}_i \frac{\partial}{\partial \xi}\right) \hat{p}_i = \hat{\tau}_i \frac{\partial \hat{p}}{\partial \xi}. \quad (10.2)$$

Here \hat{p} is the acoustic pressure (the local pressure deviation from the ambient atmospheric pressure), s is the distance the sonic boom has propagated and $\xi = t - s/c$ is the retarded time where t is the time. A represents the ray tube area, ρ is the ambient density, β the coefficient of nonlinearity and δ is a combination of the coefficients of viscosity and thermal conductivity.

In the case of plane, cylindrical or spherically spreading waves, A is proportional to r^j where $j = 0, 1, 2$ corresponds to plane, cylindrical and spherical symmetry respectively. It can be seen that the $\frac{\partial A}{\partial s}/2A(s)$ term reduces to $j/2r$, which leads us to the expression found in (3.12) in §3.1.

Including variation of density and sound speed with altitude leads us to the following equation to describe the propagation of a sonic boom through a realistic atmosphere

$$\frac{\partial \hat{p}}{\partial s} + \frac{1}{2A(s)} \frac{\partial A}{\partial s} \hat{p} - \frac{1}{2\rho(s)} \frac{\partial \rho}{\partial s} \hat{p} - \frac{1}{2c(s)} \frac{\partial c}{\partial s} \hat{p} = \frac{\beta}{\rho c^3} \frac{\partial \hat{p}}{\partial \xi} \hat{p} + \frac{1}{c^2} \sum_i (\Delta c)_i \frac{\partial \hat{p}_i}{\partial \xi} + \frac{\hat{\delta}}{2\rho c^3} \frac{\partial^2 \hat{p}}{\partial \xi^2}, \quad (10.3)$$

where

$$\left(1 + c(s) \hat{\tau}_i(s) \frac{\partial}{\partial \xi}\right) \hat{p}_i = \hat{\tau}_i(s) \frac{\partial \hat{p}}{\partial \xi}, \quad (10.4)$$

as described in equation (2.84) by Cleveland [9]. In §4, it was discussed how a shock is formed from a balance between the nonlinear steepening and the diffusive forces. This balance causes the formation of the tanh shock as has been previously discussed. Typically a supersonic object creates a waveform which contains many sub-shocks determined by the geometry of the supersonic object as shown in Figure 68. While we are primarily concerned with the propagation of well formed sonic booms (the N-waves), it is worth considering how long it will take for all the sub-shocks to merge into one well defined shock, so we can then find an approximate numerical solution for any initial disturbance.

For a specific source, the disturbance close to a supersonic profile can be described in terms of Whitham functions as summarised by Pierce [45]. This theory has been extended by Johnson [32] and remains valid provided the object is slower than Mach 3. From this, the approximate length-scale of N-wave formation for supersonic objects, s_0 , can be obtained as

$$s_0 = O\left(\frac{L^5(M^2 - 1)}{8\beta^2 M^7 S_{\max}^4 \Phi_{\max}^2}\right), \quad (10.5)$$

where L is the craft length, S_{\max} is the maximum cross-sectional area of the craft, $\beta \approx 1.402$ is the ratio of specific heats and $\Phi_{\max} \approx 6$ is a function describing the pressure disturbance caused by the projectile. From observing the expression for s_0 , it can be seen that s_0 is

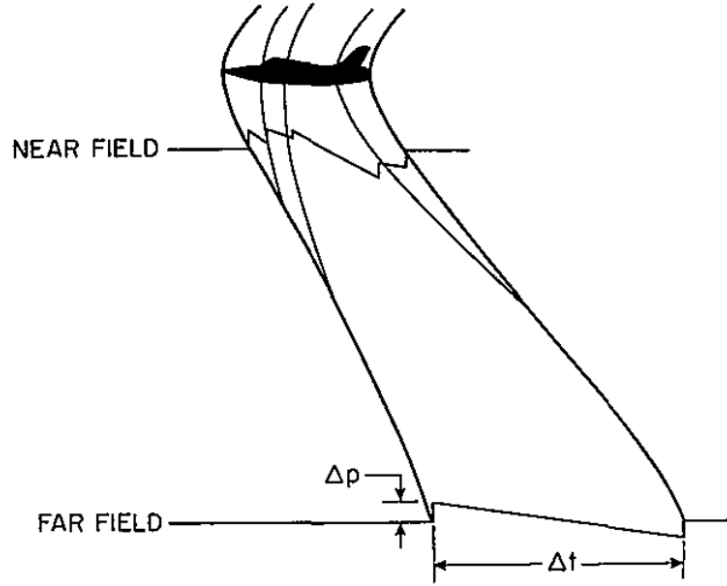


Figure 68: An example showing the waveform close to, and far from, the supersonic object. Taken from Figure 17, 6th Weather Wing [15].

smaller, corresponding to a shorter length scale, for geometries similar to fighter jets and s_0 is a lot larger for larger aircrafts, for example a body with similar dimensions to Concorde.

An initial amplitude for a shock can be calculated from knowledge of the dimensions of the supersonic object, the Mach number, the propagation distance, s_0 , at which an N-wave will have formed by, the sound speed and the density at the altitude of the location of the supersonic object. This results in the following form for the initial, positive overpressure, p_0 , defined by Pierce [45] as

$$p_0 = \frac{c^2 \rho (M^2 - 1)^{-\frac{1}{4}} M^{\frac{3}{4}} S_{\max}^{\frac{1}{2}} K}{2^{\frac{1}{4}} \beta^{\frac{1}{2}} s_0^{\frac{3}{4}} L^{\frac{1}{4}}}, \quad (10.6)$$

where K is a dimensionless constant between 0.57 and 0.85 depending on the shape of the object. The equations, (10.5) and (10.6) provide initial conditions with which we can use to solve the general equation (10.3) with (10.4). However, before we can generate a full solution we need to calculate the ray tube area, A , for a given set of atmospheric parameters and to find the dependence of c and ρ on the propagation distance, s .

Of all the quantities mentioned above, the one which will provide the most challenge in finding will be the ray tube area, A . In previous sections we have included cylindrical and spherical symmetry when considering how this sonic booms propagate. However, when considering the atmosphere, the assumption that the rays travel in straight lines is insufficient to model the complexities of the atmosphere. This is primarily due to the fact that the speed of sound varies with altitude, causing the ray paths to curve according to how the sound speed varies. So before we can develop a full atmospheric model, we must consider how the sound waves will travel through the atmosphere which will be discussed in §10.3. However, we will first discuss how the parameters in the atmosphere vary with altitude.

10.2 Constants varying with Altitude

In order to generate a description of the behaviour of sonic booms through a realistic atmosphere we need to have accurate measurements of how parameters vary with altitude. In this section we wish to establish a series of parameters which can be used as a test case for numerical investigation. The choice of parameters will be guided by empirical formulae derived from experimental data. During numerical investigations, the parameters will change according to the local conditions. In particular we expect temperature and humidity to change noticeably for different locations.

10.2.1 Temperature

Temperature is one of the hardest parameters to get an accurate measurement of how it behaves in relation to altitude due to the varying weather conditions. We will assume a

fairly cold ground temperature of 10°C which will decrease linearly to a temperature of -53°C at 11,000m which stays approximately constant to 20,000m, which is an appropriate approximation [24]. However, the numerical model will allow for the temperature to be changed according to the specific local conditions.

10.2.2 Gravity

The gravitational attraction between two bodies is proportional to the inverse square of the distance between the two bodies. Typically we treat the acceleration due to gravitational attraction, g , as a constant. However, when considering bodies at altitude of around $z = 11,000\text{m}$, this assumption becomes less acceptable. Here we will define the acceleration due to gravitational attraction as

$$g = g_0 \left(\frac{r_e}{r_e + z} \right)^2, \quad (10.7)$$

where z is the altitude, $g_0 = 9.8067\text{ms}^{-2}$ is the standard gravitational attraction and $r_e = 6,371,000\text{m}$ is the Earth's mean radius. This results in the gravitational attraction changing from g_0 at ground level to $g = 9.7729\text{ms}^{-2}$ at 11,000m which makes a small impact on the behaviour of the sonic boom but has been included for completeness.

10.2.3 Speed of Sound

The speed of sound is primarily dependent on temperature and can be found to be

$$c = (1 + 0.0016h)\sqrt{\gamma R_{\text{air}}t}, \quad (10.8)$$

where h is the percent mole fraction of water vapour in the air, $R_{\text{air}} = 287.06$ is the ideal gas constant for dry air, $\gamma = 1.402$ is the ratio of specific heats and t is the temperature in Kelvin [6]. Since the percent mole fraction of water vapour in the air is typically around one percent we ignore this term leaving us with

$$c = \sqrt{\gamma R_{\text{air}} t}. \quad (10.9)$$

10.2.4 Ambient Pressure

In order to find ambient pressure, we must assume that the sound speed and acceleration due to gravity vary slowly with altitude which is a reasonable assumption. This results in the following form for the ambient pressure, P_{amb}

$$P_{\text{amb}} = P_r \exp\left(-\frac{\gamma g z}{c^2}\right), \quad (10.10)$$

where $P_r = 1.013 \times 10^5$ is the reference pressure, [1].

10.2.5 Humidity

Humidity is similar to temperature in that it can vary with the weather conditions. Here, we will assume a relative humidity of 60% at ground level and a linear increase up to 75% at 6,000m followed by a linear decrease to 27% at 11,000m. Relative humidity, h_r , is defined as the ratio of vapour pressure P_w to the saturation pressure, P_{sat} , giving $h_r = 100P_w/P_{\text{sat}}$. However, we need humidity in terms of the ratio of vapour pressure to the ambient atmospheric pressure, P_0 , giving $h = 100P_w/P_0$. In order to convert from relative humidity to actual humidity we need the following empirical law [35], giving the

dependence of saturation pressure on the temperature as

$$\log_{10} \left(\frac{P_{\text{sat}}}{P_r} \right) = -6.8346 \left(\frac{273.16K}{t} \right)^{1.261} + 4.6151.$$

From here we can find a relation between relative humidity and actual humidity which allows us to find h from our initial assumption of the relative humidity.

10.2.6 Density

The density, ρ , is defined by $\rho = \gamma P_{\text{amb}}/c^2$. Therefore this can easily be found from (10.10) to be

$$\rho = \left(\frac{P_r \gamma}{c^2} \right) \exp \left(-\frac{\gamma g z}{c^2} \right). \quad (10.11)$$

10.2.7 Diffusivity of Sound

The diffusivity of sound was first discussed in §3.1 and is made up of a combination of the coefficients of viscosity, bulk viscosity and thermal conduction, defined as

$$\delta = \frac{1}{\rho} \left(\frac{4}{3} \mu + \mu_B + \frac{(\gamma - 1) \kappa}{c_p} \right), \quad (10.12)$$

where μ is the viscosity, μ_B is the bulk viscosity defined as $\mu_B = 0.6\mu$, κ is the coefficient of thermal conductivity and $c_p = \gamma R/(\gamma - 1)$ is the coefficient of specific heat at a constant pressure [38]. Pierce [45] gives the dependence of μ and κ on temperature t in ($^{\circ}\text{K}$) as

$$\begin{aligned} \frac{\mu}{\mu_{20}} &= \left(\frac{t}{t_{20}} \right)^{\frac{3}{2}} \frac{t_{20} + t_s}{t + t_s}, \\ \frac{\kappa}{\kappa_{20}} &= \left(\frac{t}{293.16} \right)^{\frac{3}{2}} \frac{t_{20} + t_a \exp(-t_b/t_{20})}{t + t_a \exp(-t_b/t)}. \end{aligned} \quad (10.13)$$

where $\mu_{20} = 1.8134 \times 10^{-5} \text{ kg}/(\text{ms})$, $\kappa_{20} = 2.571 \times 10^{-2} \text{ W}/(\text{mK})$, $t_{20} = 293.16\text{K}$, $t_s = 110.4\text{K}$, $t_a = 245.4\text{K}$ and $t_b = 27.6\text{K}$. Here μ_{20} and κ_{20} are reference values taken at 20°C .

10.2.8 Relaxation Terms

As has been mentioned in §8.1, the relaxation times for Nitrogen and Oxygen are highly variant on the humidity. This is due to the fact that the molecules are a lot more likely to lose their energy upon collision with a water molecule than another Nitrogen or Oxygen molecule. The ISO standard (ISO 9613-1 1993) gives the relaxation frequencies for Oxygen and Nitrogen as

$$\begin{aligned} f_{r,\text{O}} &= \frac{P_0}{P_r} \left(24 + 40400 \frac{0.02 + h}{0.391 + h} \right) \text{Hz}, \\ f_{r,\text{N}} &= \frac{P_0}{P_r} \sqrt{\frac{t_{20}}{t}} \left(9 + 280h \exp \left(-4.170 \left(\frac{t_{20}}{t} \right)^{\frac{1}{3}} - 1 \right) \right) \text{Hz}, \end{aligned} \quad (10.14)$$

where h is the humidity and the relaxation time can be found as $\tau_r = 1/2\pi f_r$ and t_{20} is still defined at $t_{20} = 293.16\text{K}$. Similarly, the change in sound speed due to each relaxation process is defined as

$$(\Delta c)_r \approx \frac{A_r c^2}{2\pi},$$

where A_r are defined for Nitrogen and Oxygen by the ISO standard (ISO 9613-1 1993) as

$$\begin{aligned} A_{r,\text{O}} &= 0.01275 \left(\frac{t_{20}}{t} \right)^{\frac{5}{2}} \exp \left(\frac{-2239.1}{t} \right) \text{Npm}^{-1}\text{Hz}^{-2}, \\ A_{r,\text{N}} &= 0.1068 \left(\frac{t_{20}}{t} \right)^{\frac{5}{2}} \exp \left(\frac{-3352}{t} \right) \text{Npm}^{-1}\text{Hz}^{-2}. \end{aligned} \quad (10.15)$$

10.3 Ray Tubes

10.3.1 Introduction and Ray Paths

To propagate sonic booms in a realistic atmosphere, we need to find accurate values for all of the parameters mentioned in (10.3). Most of these can easily be found, but we need to find an expression for the ray tube area $A(s)$. This section will present an overview of ray tube theory based upon the work done by Johnson [32] and Cleveland [9]. This will allow us to integrate ray tube theory into our full atmospheric model.

A ray tube is defined as the area enclosed by the paths of four rays that have trajectories varying by some small amount as shown in Figure 69. As these rays diverge, the acoustic energy is spread over a larger area and hence the amplitude of the shock decreases. In order to find expressions for these ray paths we need to generate some sort of notation to describe the ray angles. This is presented in Figures 70 and 71 where ψ is the Mach angle, ϕ is the azimuthal angle (the angle between the ray path and the vertical plane), ν is the ray heading (the angle made between the ray path and the flight line) and θ is the grazing angle (the angle made between the ray path and the horizontal plane). We also say the wave is travelling in direction \vec{s} and $s = |\vec{s}|$ is the distance along the ray path as previously defined. We define \vec{r} as the projection of \vec{s} onto the $x - y$ plane, which is introduced to make deriving certain expressions simpler.

As the rays propagate through the atmosphere, the fact that the sound speed varies with altitude means that the ray paths are curved, hence the quantities θ and ϕ also vary. We begin by introducing the quantities θ_0 and ϕ_0 to represent the initial values of these angles. Since there is no horizontal variation in the parameters, a ray path will lie in a

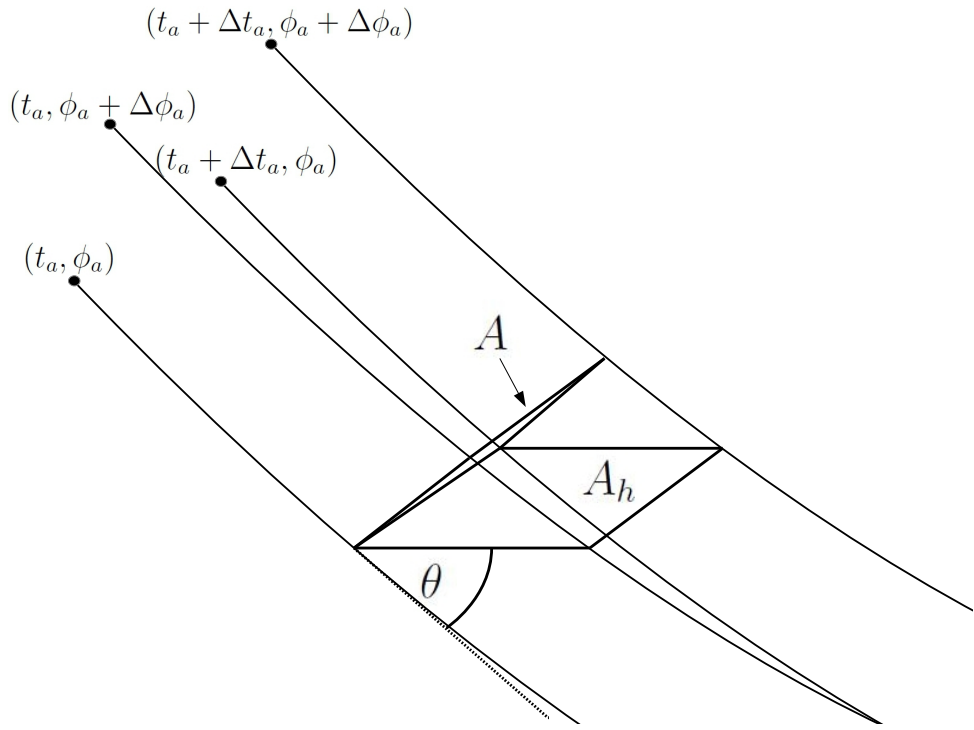


Figure 69: The ray tube area enclosed by four rays.

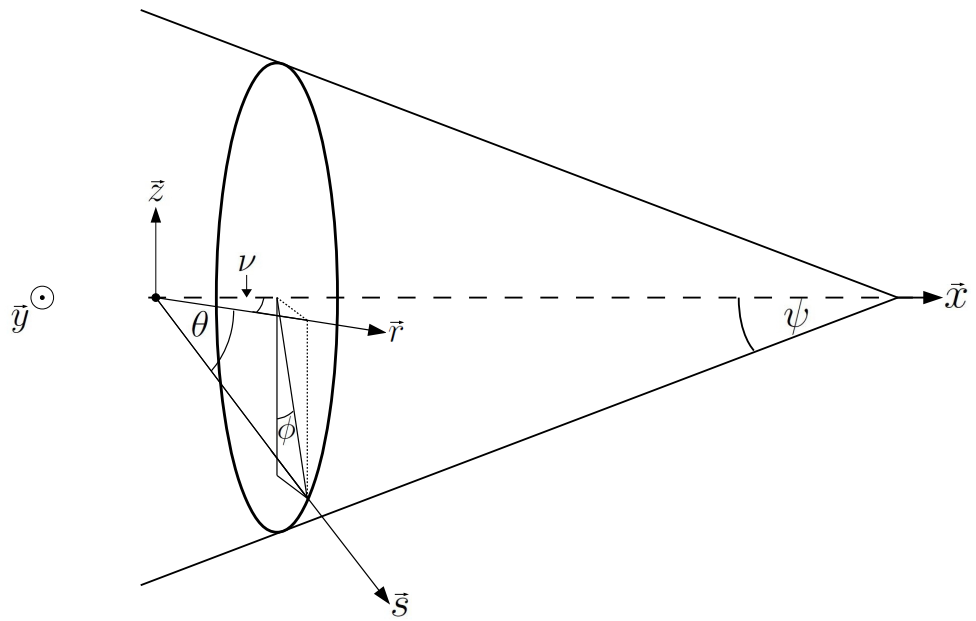


Figure 70: The notation used to describe the ray paths (side view).

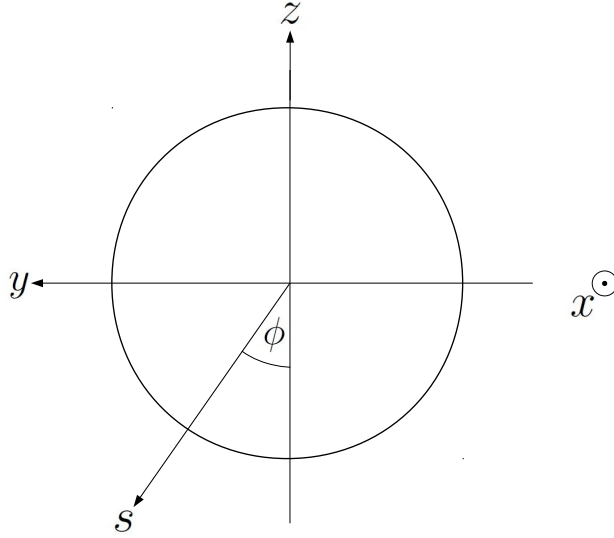


Figure 71: The notation used to describe the ray paths (front view).

single vertical plane and hence the ray heading, ν , is constant for a particular ray. These changes also impact on the direction of the wave \vec{s} , hence \vec{s}_0 will be used to represent the initial direction of the wave.

10.3.2 General Ray Tube Theory

Before we start to derive expressions for the area of ray tubes it is useful to derive a couple of relations between ϕ_0, θ_0, ν and ψ . By looking at Figure 72 and considering expressions for Δy , a small movement in the y -direction (with Δx , Δz and Δs similarly defined), it can be seen that $\Delta y = -\Delta z \tan \phi$. Similarly, it can also be seen that $\Delta y = -\Delta r \sin \nu = \Delta z \sin \nu / \tan \theta$. This results in the following relation

$$\sin \nu = \tan \theta \tan \phi, \quad (10.16)$$

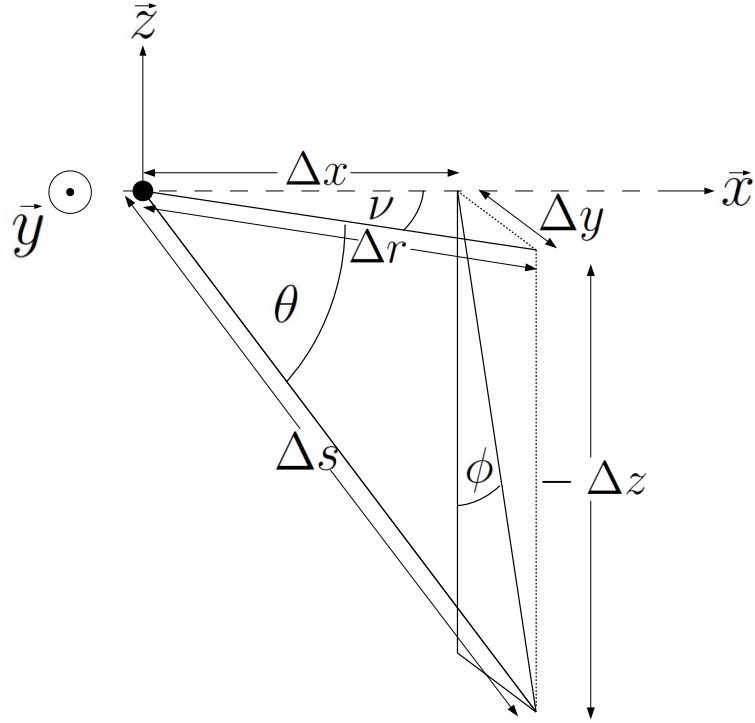


Figure 72: The relation between the various angles for the ray path problem from Figure 70.

which is valid at all points along the ray path. Since this is true for all points along the ray path, we must also have that

$$\sin \nu = \tan \theta_0 \tan \phi_0. \quad (10.17)$$

Initially the direction of the ray path is normal to the Mach cone (with semi-angle ψ). This provides a relationship between the initial propagation angles, θ_0 and ϕ_0 . From Figures 70 and 72, Δz can be expressed as $\Delta z = -\Delta s \cos \phi_0 \cos \psi$ and $\Delta z = -\Delta s \sin \theta_0$, giving us the following relation

$$\sin \theta_0 = \cos \psi \cos \phi_0. \quad (10.18)$$

Now we have found these two relationships, we are in a position to find an expression for $A(s)$ which will allow us to solve (10.3). Recall that a ray tube is defined as the area enclosed by paths of four rays that have trajectories varying by some small amount. Here we will take an arbitrary ray tube as the area enclosed by the rays launched at (t_a, ϕ_a) , $(t_a + \Delta t_a, \phi_a)$, $(t_a, \phi_a + \Delta \phi_a)$ and $(t_a + \Delta t_a, \phi_a + \Delta \phi_a)$ for some time t_a and some azimuthal angle ϕ_a , introduced by Hayes, [27]. This is illustrated in Figure 69. The rays launched at t_a and $t_a + \Delta t_a$ follow parallel trajectories, while the rays launched at angles ϕ_a and $\phi_a + \Delta \phi_a$ will follow slightly different trajectories. The cross sectional ray tube area is denoted by A and is shown in Figure 69, which will be a function of $t_a, \phi_a, \Delta t_a, \Delta \phi_a$ and s , the propagation distance along with ray tube.

By observing Figure 69 we can obtain an expression for the horizontal ray tube area,

A_h

$$A_h(\phi_0, s) = \frac{\partial x}{\partial t_a} \Delta t_a \frac{\partial y}{\partial \phi_0} \Delta \phi_0, \quad (10.19)$$

where $\frac{\partial x}{\partial t_a}$ is the velocity of the supersonic object, v , which we take to be a constant. Hence $\frac{\partial y}{\partial \phi}$ represents the effects of atmospheric stratification. However, in (10.3), we need to find an expression for A instead. The ray tube area normal to the ray, A , can be found in terms of A_h to be

$$A(\phi, s) = A_h(\phi_0, s) \sin \theta = v \Delta t_a \frac{\partial y}{\partial \phi_0} \Delta \phi_0 \sin \theta, \quad (10.20)$$

where the only value which cannot be easily found is $\frac{\partial y}{\partial \phi}$. Hence, in order to find an explicit expression for A , we must first find an expression for $\frac{\partial y}{\partial \phi}$. To do this we need to find expressions for $\frac{dy}{dz}$, $\frac{dx}{dz}$ and $\frac{dy}{dx}$, which are obtained using expressions for $\Delta x, \Delta y$ and Δz . These can then be found by considering Figure 72, which results in the following

expressions,

$$\begin{aligned}
\Delta x &= \Delta r \cos(\nu) = \Delta s \cos(\nu) \cos(\theta), \\
\Delta y &= \Delta r \sin(\nu) = \Delta s \sin(\nu) \cos(\theta), \\
\Delta z &= -\Delta s \sin \theta.
\end{aligned} \tag{10.21}$$

From here we can obtain that

$$\begin{aligned}
\frac{dx}{dz} &= -\frac{\cos \nu}{\tan \theta}, \\
\frac{dy}{dz} &= -\frac{\sin \nu}{\tan \theta}.
\end{aligned} \tag{10.22}$$

We can now integrate (10.22), noting that ν is independent of z , giving us

$$\begin{aligned}
x(\phi_0, z) &= \cos \nu \int_{z_0}^z \frac{\cos \theta}{\sin \theta} dz, \\
y(\phi_0, z) &= \sin \nu \int_{z_0}^z \frac{\cos \theta}{\sin \theta} dz.
\end{aligned} \tag{10.23}$$

The variation of θ with z for a given sound speed $c(z)$ is determined using Snell's law [50]. Based on the principle that the signal travels along the path that minimises travel time, for a continuous variation of c , Snell's law informs us that $\cos \theta/c = \text{constant}$, hence $\cos \theta/c = \cos \theta_0/\bar{c}$, where \bar{c} is the starting sound speed. Now (10.23) can be used to determine the path once we have a relation between z and θ . Returning to the determination of the ray tube, derivatives of the angles with respect to ϕ_0 can now be found. Differentiating

(10.18) with respect to ϕ_0 leads to

$$\begin{aligned}
\cos \theta_0 \frac{\partial \theta_0}{\partial \phi_0} &= -\cos \psi \sin \phi_0, \\
\frac{\partial \theta_0}{\partial \phi_0} &= -\frac{\sin \theta_0 \sin \phi_0}{\cos \phi_0 \cos \theta_0}, \\
&= -\tan \theta_0 \tan \phi_0, \\
&= -\sin \nu.
\end{aligned} \tag{10.24}$$

Similarly differentiating (10.16) with respect to ϕ_0 leads to

$$\begin{aligned}
\cos \nu \frac{\partial \nu}{\partial \phi_0} &= \sec^2 \theta_0 \tan \phi_0 \frac{\partial \theta_0}{\partial \phi_0} + \tan \theta_0 \sec^2 \phi_0, \\
\frac{\partial \nu}{\partial \phi_0} &= \frac{\tan \theta_0}{\cos^2 \phi_0 \cos \nu} - \frac{\tan \phi_0 \tan \nu}{\cos^2 \theta_0}.
\end{aligned} \tag{10.25}$$

An expression for $\frac{\partial \theta}{\partial \phi_0}$ can be obtained by considering Snell's law differentiated with respect to ϕ_0

$$\begin{aligned}
-\cos \theta \frac{\partial \theta}{\partial \phi_0} &= -\frac{c}{c_0} \sin \theta_0 \frac{\partial \theta_0}{\partial \phi_0}, \\
\frac{\partial \theta}{\partial \phi_0} &= \frac{\sin \theta_0 \cos \theta}{\sin \theta \cos \theta_0} \frac{\partial \theta_0}{\partial \phi_0}, \\
&= -\frac{\tan \theta_0}{\tan \theta} \sin \nu.
\end{aligned} \tag{10.26}$$

We can now combine (10.23), (10.25) and (10.26) to find $\frac{\partial y}{\partial \phi_0}$ which provides an explicit expression for the ray tube area A defined in (10.20).

$$\begin{aligned}
\frac{\partial y}{\partial \phi_0} &= -\left[\cos \nu \frac{\partial \nu}{\partial \phi_0} \int \frac{\cos \theta}{\sin \theta} dz + \sin \nu \int -\frac{1}{\sin^2 \theta} \frac{\partial \theta}{\partial \phi_0} dz \right], \\
&= \left(\frac{\tan \theta_0}{\cos^2 \phi_0} - \frac{\tan \phi_0 \sin \nu}{\cos^2 \theta_0} \right) I_1 + \sin^2 \nu \tan \theta_0 I_2,
\end{aligned} \tag{10.27}$$

where

$$I_1 = - \int_{z_0}^z \frac{\cos \theta}{\sin \theta} dz, \quad I_2 = - \int_{z_0}^z \frac{\cos \theta}{\sin^3 \theta} dz. \quad (10.28)$$

Hence, the ray tube area, A , can be defined as

$$A(\phi_0, s) = \sin(\theta) v \Delta t_a \Delta \phi_0 (a I_1 + b I_2), \quad (10.29)$$

where

$$a = \frac{\tan \theta_0}{\cos^2 \phi_0} \left(1 - \frac{\sin^2 \phi_0}{\cos^2 \theta_0} \right), \quad b = \tan^3 \theta_0 \tan^2 \phi_0, \quad (10.30)$$

using the relation found in (10.17). Now a and b only depend on the initial quantities and, as such, are constant for a particular ray. Observing the governing equation, (10.3), we can see that A only appears in the form $\frac{\partial A}{\partial s}/A$ which can be found to be

$$\begin{aligned} \frac{1}{A} \frac{\partial A}{\partial s} &= \frac{1}{A} \frac{\partial A}{\partial z} \frac{\partial z}{\partial s}, \\ &= \frac{1}{A} \sin \theta \frac{\partial A}{\partial z}, \\ &= \sin \theta \frac{1}{a I_1 + b I_2} \left(a \frac{\cos \theta}{\sin \theta} + b \frac{\cos \theta}{\sin^3 \theta} \right), \\ &= \frac{\cos \theta}{a I_1 + b I_2} \left(a + \frac{b}{\sin^2 \theta} \right). \end{aligned} \quad (10.31)$$

From here it can be seen that the choice of the constants $v \Delta t_a \Delta \phi_0$ is irrelevant. This form now allows us to solve (10.3), provided we can find an expression for I_1 and I_2 .

10.3.3 Ray Tubes in an atmosphere with a linear sound speed profile

In order to use the expression found in (10.31) to solve (10.3), we need to find explicit forms of I_1 and I_2 . As was discussed in §10.2.3, we have the speed of sound given by

the following equation, $c = \sqrt{\gamma R_{\text{air}} t}$, where γ is the ratio of specific heats, R_{air} is the ideal gas constant for dry air and t is the temperature in Kelvin. In §10.2.1 we saw how temperature decreased approximately linearly from sea level, where $t \approx 283\text{K}$ to 11,000m, where $t \approx 220\text{K}$. Since this represents a fairly small percentage change, we can make the approximation that the sound speed also decreases linearly with altitude. Therefore we have an alternative form for the sound speed $c = c(0)(1 + \hat{e}z)$, where $c(0) = 337.58\text{ms}^{-1}$ is the ground sound speed at 10°C and, by considering the sound speed at 11,000m, we can arrive at $\hat{e} = -1.0749 \times 10^{-5}\text{m}^{-1}$. We also define $\hat{g} = c(0)\hat{e} = -0.0036\text{s}^{-1}$ as the sound speed gradient.

We can use this form, along with Snell's law $\bar{c}/\cos\theta_0 = c/\cos\theta$, where \bar{c} is the sound speed at the launch altitude to give us an expression for θ , the grazing angle

$$\cos\theta = \frac{\cos\theta_0}{\bar{c}}c(0)(1 + \hat{e}z). \quad (10.32)$$

It can now be shown that ray paths with a linear sound speed are arcs of circles. From (10.22) it can be seen that

$$\begin{aligned} \frac{dr}{dz} &= -\tan\theta, \\ &= -\sqrt{\frac{1}{\cos^2\theta} - 1}, \\ &= -\frac{\sqrt{1 - \cos^2\theta}}{\cos\theta}, \\ &= -\frac{\sqrt{1 - \cos^2\theta_0 c^2/\bar{c}^2}}{\cos\theta_0 c/\bar{c}}, \end{aligned}$$

using Snell's law. We now need to express c in terms of z . Previously we have stated that

$c = c(0)(1 + \hat{e}z)$. This is equivalent to $c = \bar{c} + \hat{g}(z - z_0)$ which gives

$$\frac{dz}{dr} = -\frac{\sqrt{1 - (\cos \theta_0/\bar{c})^2(\bar{c} + \hat{g}(z - z_0))^2}}{(\cos \theta_0/\bar{c})(\bar{c} + \hat{g}(z - z_0))}. \quad (10.33)$$

From here we can obtain a relation between r and z by manipulating (10.33) and integrating giving

$$\begin{aligned} \frac{dr}{dz} &= -\frac{(\cos \theta_0/\bar{c})(\bar{c} + \hat{g}(z - z_0))}{\sqrt{1 - (\cos \theta_0/\bar{c})^2(\bar{c} + \hat{g}(z - z_0))^2}}, \\ r &= -\frac{\bar{c}}{\cos \theta_0 \hat{g}} \sqrt{1 - \left(\frac{\cos \theta_0}{\bar{c}}\right)^2 (\bar{c} + \hat{g}(z - z_0))^2} + C, \\ (r - C)^2 \left(\frac{\cos \theta_0 \hat{g}}{\bar{c}}\right)^2 &= 1 - \left(\frac{\cos \theta_0}{\bar{c}}\right)^2 (\bar{c} + \hat{g}(z - z_0))^2, \\ (r - C)^2 &= \left(\frac{\bar{c}}{\cos \theta_0 \hat{g}}\right)^2 - \left(\frac{\bar{c}}{\hat{g}} + (z - z_0)\right)^2, \\ (r - C)^2 + \left(\frac{\bar{c}}{\hat{g}} + (z - z_0)\right)^2 &= \left(\frac{\bar{c}}{\cos \theta_0 \hat{g}}\right)^2, \end{aligned} \quad (10.34)$$

where C is a constant. Now it can be seen that these ray paths are arcs of circles with a radius R_c given by

$$R_c = -\frac{\bar{c}}{\hat{g} \cos \theta_0}. \quad (10.35)$$

We know that our initial conditions are that at $r = 0$, we have $z = z_0$ which leads us to the final form of (10.34)

$$(r - R_c \sin \theta_0)^2 + (z - z_0 - R_c \cos \theta_0)^2 = R_c^2. \quad (10.36)$$

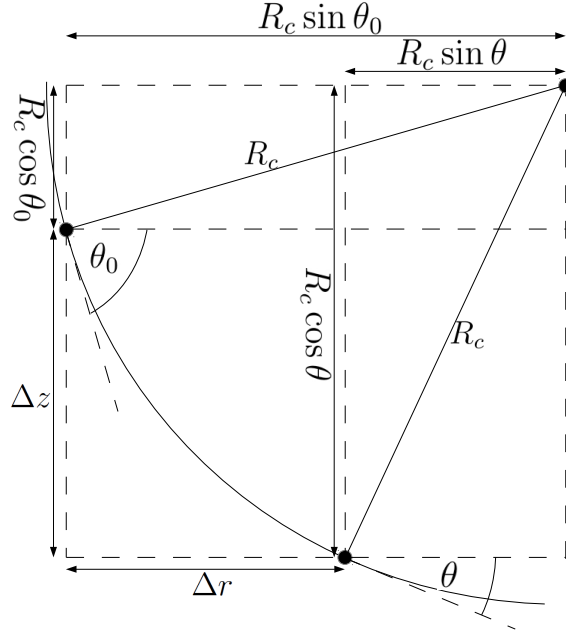


Figure 73: Circular ray paths for a linear sound speed profile.

From here we can obtain expressions for the trajectories of rays, which are given by

$$x = R_c \cos \nu (\sin \theta_0 - \sin \theta), \quad (10.37)$$

$$y = R_c \sin \nu (\sin \theta_0 - \sin \theta), \quad (10.38)$$

$$z = z_0 - R_c (\cos \theta - \cos \theta_0), \quad (10.39)$$

as can be seen from Figure 73. Similarly we can obtain an expression for θ based on θ_0 and the distance travelled, namely, $\theta = \theta_0 - s/R_c$. Also, a linear sound speed allows us to find solutions for the integrals in (10.28) as we now have a relationship between z and θ from (10.39), which leads to

$$\frac{dz}{d\theta} = R_c \sin \theta. \quad (10.40)$$

From here we can solve I_1 ,

$$\begin{aligned}
I_1 &= - \int_{z_0}^z \frac{\cos \theta}{\sin \theta} dz, \\
&= -R_c \int_{\theta_0}^{\theta} \cos \theta d\theta, \\
&= R_c(\sin \theta_0 - \sin \theta),
\end{aligned} \tag{10.41}$$

and similarly we can solve for I_2 ,

$$\begin{aligned}
I_2 &= - \int_{z_0}^z \frac{\cos \theta}{\sin^3 \theta} dz, \\
&= -R_c \int_{\theta_0}^{\theta} \frac{\cos \theta}{\sin^2 \theta} d\theta, \\
&= R_c \left(\frac{1}{\sin \theta} - \frac{1}{\sin \theta_0} \right), \\
&= R_c \frac{1}{\sin \theta \sin \theta_0} (\sin \theta_0 - \sin \theta),
\end{aligned} \tag{10.42}$$

giving us a closed form for the ray tube area normal to the ray of

$$A(\phi_0, s) = v \Delta t_a \Delta \phi_0 R_c \left(a \sin \theta + \frac{b}{\sin \theta_0} \right) (\sin \theta - \sin \theta_0), \tag{10.43}$$

where a and b are defined as in (10.30). This allows us to now find an expression for $\frac{\partial A}{\partial s}/A$,

namely

$$\frac{1}{A} \frac{\partial A}{\partial s} = \frac{\cos \theta \sin \theta_0}{R_c(\sin \theta_0 - \sin \theta)(a \sin \theta \sin \theta_0 + b)} \left(a \sin \theta + \frac{b}{\sin \theta} \right). \tag{10.44}$$

Having now found this expression for $\frac{\partial A}{\partial s}/A$, we are finally in a position where we can solve (10.3). However, before solving any equations, it is of worth to calculate which ray paths will hit the ground, as the others are of minimal significance. Therefore, the next section will deal with this topic.

10.3.4 Sonic Boom Carpet

Having now found the behaviour of the rays, it is of interest to calculate the sonic boom carpet, that is, the area on the ground where we would hear a sonic boom from a supersonic object in the atmosphere.

We can uniquely define a ray path from the velocity of the supersonic object, its altitude and the initial azimuthal angle, ϕ_0 . For example, if we consider the case where we have a supersonic object, in steady flight, at a height of 11,000m moving at speed Mach 2, which corresponds to a value of $\psi = \pi/6$ (recalling that $\psi = \sin^{-1}(1/M)$). We can now uniquely define a particular ray-path provided we have a value of ϕ_0 , the initial azimuthal angle. From (10.18) we know that $\sin \theta_0 = \cos \psi \cos \phi_0$. This allows us to determine the value of $\theta_0 = \sin^{-1}(\cos \psi \cos \phi_0)$. From here we can find the radius of the circle the rays are travelling on, $R_c = -\frac{\bar{c}}{\hat{g} \cos \theta_0}$. Having now found R_c , we can now solve (10.39), with $z = 0$ to find the value of θ , which then can be used to find values for x and y in (10.37) and (10.38) to give us a complete description of the ray paths. We define our sonic boom carpet as is illustrated in Figure 74, which involves taking all possible values of ϕ_0 and seeing whether or not that particular ray path hits the ground or if it starts travelling upwards into the atmosphere. It is important to note in Figure 74 that we only receive rays on the solid black line. However, as the supersonic object moves in the x -direction, it will generate further sonic booms displaced on the ground by the same amount that the supersonic object has moved by. Hence, the most relevant quantity regarding a sonic boom carpet is the width.

The sonic boom carpet corresponding to a supersonic object moving at Mach 2 with an altitude of 11,000m is shown in Figure 76, where it can be seen we have quite an

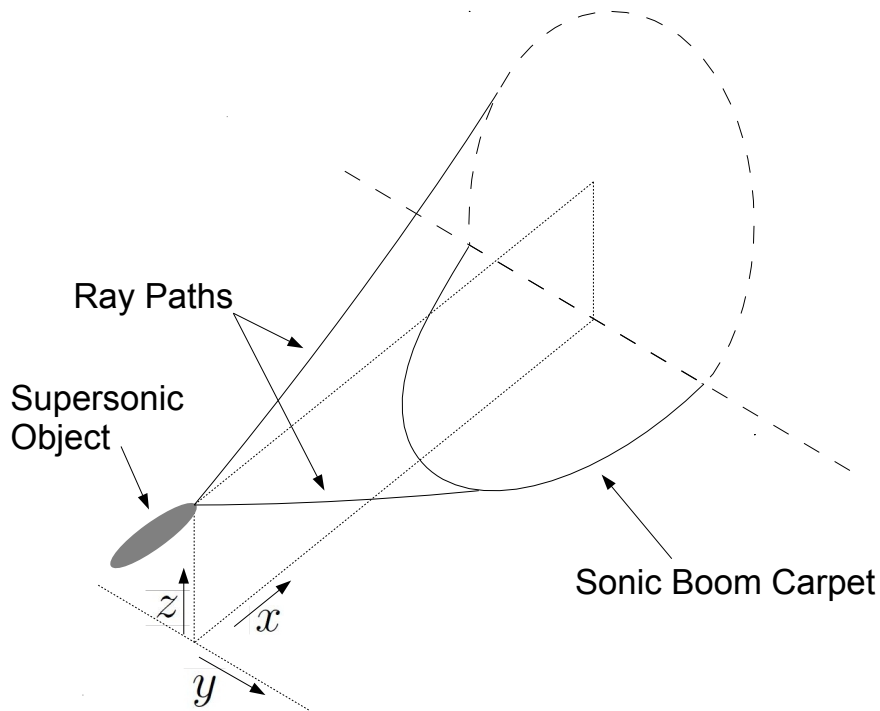


Figure 74: An illustration to how the sonic boom carpet is defined.

extensive sonic boom carpet. It can be seen that as this supersonic object travels in the x -direction, it will generate a carpet with a width of around 60km. It is also worth noting why the sonic boom carpet is limited to a width of 60km and why it does not extend any further. As was previously mentioned, each individual ray path forms a circular arc and this results them in bending away from the ground. So what happens for the rays which would correspond to a width of more than 30km away from the flight path is that they start heading back upwards into the atmosphere and do not actually hit the ground.

We can also plot similar results for different speeds and starting altitudes, for example in Figure 77 we plot the sonic boom carpet for a supersonic object travelling at Mach 4 (also at 11,000m) and as can be seen we have a small increase in the width of the carpet. However, the sonic booms hit the ground much earlier (indicated by the reduction in distance on the x -axis) which would result in louder sonic booms as the waves have had less time to diffuse their energy before they hit the ground. Also, we can assume that, since

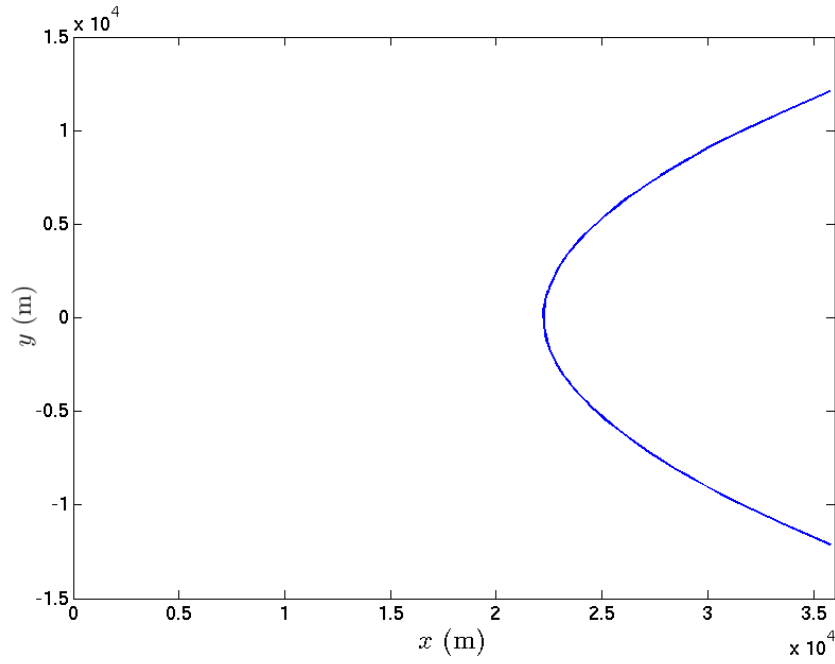


Figure 75: The sonic boom carpet, created by a supersonic object at $(0, 0, 11000)$ travelling at Mach 1.2.

the geometry is similar to that of the spherically symmetric case, the shocks will widen as they propagate. Hence, we would expect a shorter propagation distance to correspond to a narrower shock which is one of the key factors when determining environmental impact.

The case where we have a supersonic aircraft travelling at Mach 1.2 at 11,000m is plotted in Figure 75 and, as can be seen, the width of the carpet is much narrower and the waves must travel a lot further before they hit the ground, giving more time for the energy to diffuse. The reason for this drastic reduction in width is that most of the waves travel back upwards before they can hit the ground. In fact, for the case of a supersonic aircraft at a height of 11,000m travelling at Mach 1.1, no sonic booms reach the ground for the reason of them refracting back upwards into the atmosphere.

From these results, one may question the need to perform numerical analysis on the actual shock since we can determine its path using simple trigonometry. However, especially when ϕ_0 is quite large (representing the points furthest away from the flight path), the

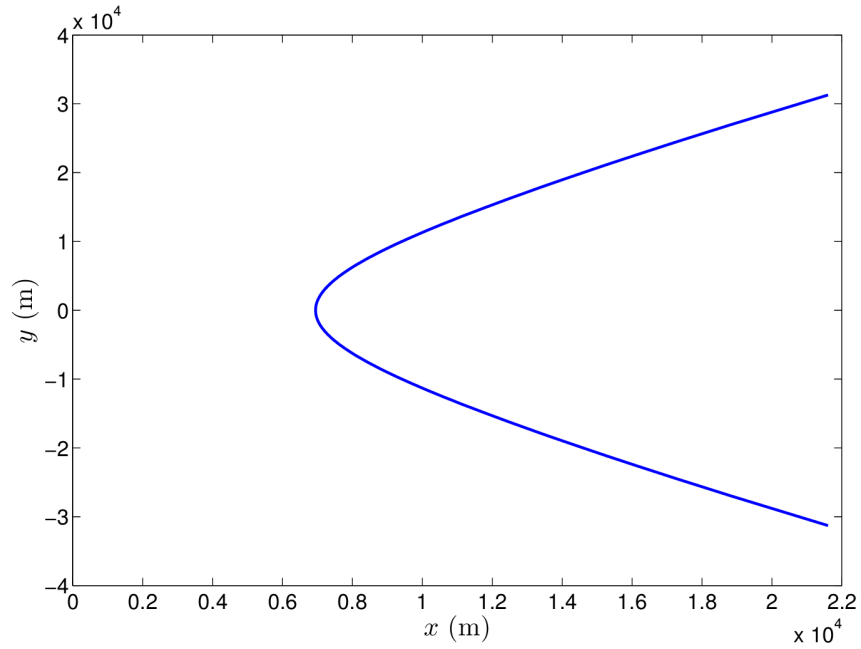


Figure 76: The sonic boom carpet, created by a supersonic object at $(0, 0, 11000)$ travelling at Mach 2.

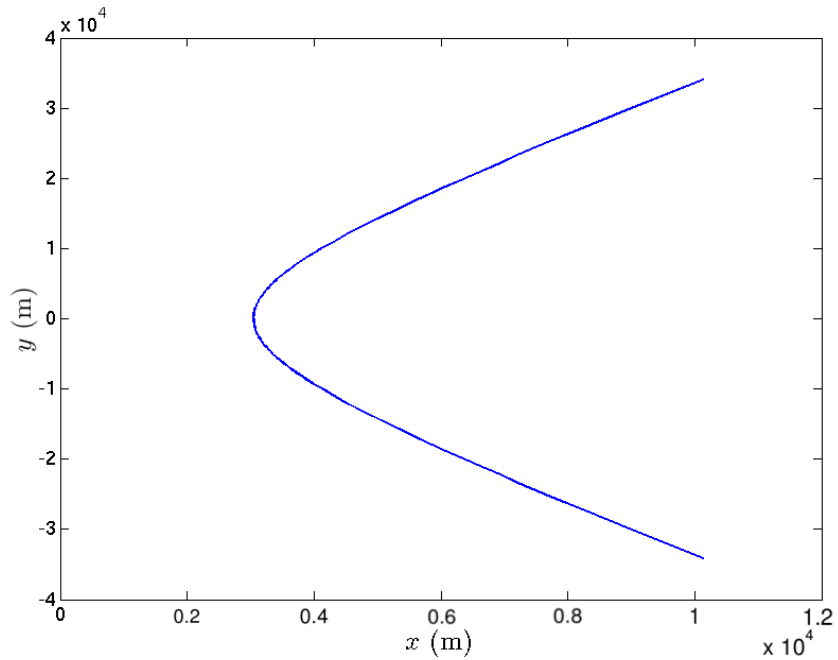


Figure 77: The sonic boom carpet, created by a supersonic object at $(0, 0, 11000)$ travelling at Mach 4.

shock may completely disperse before reaching the ground reducing the size of the actual sonic boom carpet. Also, of great interest is the environmental impact of sonic booms on people and animals. This is generally determined by the change in pressure (the shock amplitude) and how quickly the pressure changes to this value from its ambient value (the shock thickness or rise time). As a result of these reasons, the next segment will be devoted to developing a numerical model to propagate shock waves through the atmosphere to the ground, while taking account of the curved ray tubes and the fact that numerous parameters change with altitude and humidity.

10.4 Numerical Model

In previous chapters we have used various forms of Burgers' equation to investigate how shocks propagate through a medium with various effects (such as spherical symmetry and molecular relaxation). In the case where we have a realistic atmosphere, given in (10.3), it can be seen that the equation bears little resemblance to the equations previously studied. Hence, we need to normalise (10.3) before we can efficiently use a numerical model to get results as to how these waves propagate. First of all, we can rewrite (10.3) in an equivalent form,

$$\frac{\partial \hat{p}}{\partial s} - \frac{\partial}{\partial s} \left(\ln \sqrt{\frac{\rho c}{A}} \right) \hat{p} = \frac{\beta}{\rho c^3} \frac{\partial \hat{p}}{\partial \xi} \hat{p} + \frac{1}{c^2} \sum_i (\Delta c)_i \frac{\partial \hat{p}_i}{\partial \xi} + \frac{\hat{\delta}}{2\rho c^3} \frac{\partial^2 \hat{p}}{\partial \xi^2}, \quad (10.45)$$

where \hat{p}_i is as defined in (10.2). Following this we introduce the following change of variables introduced by Johnson [32]

$$\begin{aligned}
\tau_i(s) &= \frac{\hat{\tau}_i(s)}{t_0}, \\
\Delta_i &= \frac{j(s)}{j(s_0)} \frac{c(s)\rho(s)}{\beta p_0} (\Delta c)_i, \\
\epsilon &= \frac{j(s)}{j(s_0)} \frac{\rho(s)}{2\beta p_0 t_0} \hat{\delta}, \\
U &= \frac{j(s)}{j(s_0)} \frac{\hat{p}}{p_0}, \\
U_i &= \frac{j(s)}{j(s_0)} \frac{\hat{p}_i}{p_0}, \\
X &= -\frac{\xi}{t_0}, \\
T &= 1 + \frac{\beta p_0 j(s_0)}{t_0} \int_{s_0}^s \frac{ds}{\rho(s)c^3(s)j(s)}, \tag{10.46}
\end{aligned}$$

where

$$j(s) = \sqrt{\frac{A(s)}{c(s)\rho(s)}}.$$

Here, t_0 is the waveform half period, c_0 and ρ_0 are, respectively, the sound speed and density at $s = s_0$, the initial location, and p_0 is the initial acoustic overpressure as defined in (10.6). Note, that since Δ_i and ϵ are dependent on parameters varying with altitude these will need to be redefined at every time step in accordance with the current altitude.

This change of variables reduces (10.45) to

$$\frac{\partial U}{\partial T} = -U \frac{\partial U}{\partial X} + \epsilon \frac{\partial^2 U}{\partial X^2} - \sum_i \Delta_i \frac{\partial U_i}{\partial X}, \tag{10.47}$$

where

$$\left(1 - \tau_i \frac{\partial}{\partial X}\right) U_i = -\tau_i \frac{\partial U}{\partial X}, \tag{10.48}$$

which are the same equations as considered in (8.1) and (8.3) with the key difference being that $\epsilon, \Delta_i, \tau_i$ are now functions of time T . We can now introduce the same change of variables as was introduced in §4.1 to keep the shocks fixed at leading order, thus making it a lot easier to solve numerically. This leads us to the following change of variables

$$x = T^{-\frac{1}{2}}X, \quad u = T^{\frac{1}{2}}U, \quad u_i = T^{\frac{1}{2}}U_i, \quad t = \ln T, \quad (10.49)$$

which results in the following governing equation

$$u_t = \frac{u}{2} + \left(\frac{x}{2} - u\right)u_x - e^{\frac{t}{2}}\Delta_i u_{ix} + \epsilon u_{xx}, \quad (10.50)$$

where the relaxation terms are now given by

$$\left(\frac{e^{\frac{t}{2}}}{\tau_i} - \frac{\partial}{\partial x}\right)u_i = -\frac{\partial u}{\partial x}. \quad (10.51)$$

The method to solve (10.50) with (10.51) was described in §8.2. Here the main difficulty lies in extracting a physically meaningful result from (10.50). Previously we have just advanced the solution forward in time until a fixed endpoint, where all the parameters are constant throughout the run. Now, we wish to advance the solution forward in time until the rays hit the ground or have sufficiently diffused (the cases where the waves start travelling upwards before they hit the ground will not be considered as they are deemed to be of minimal relevance to the impact of sonic booms). Also, in between time-steps we need to re-calculate some of our parameters based upon the current altitude. The steps required to perform this are illustrated in Figure 78.

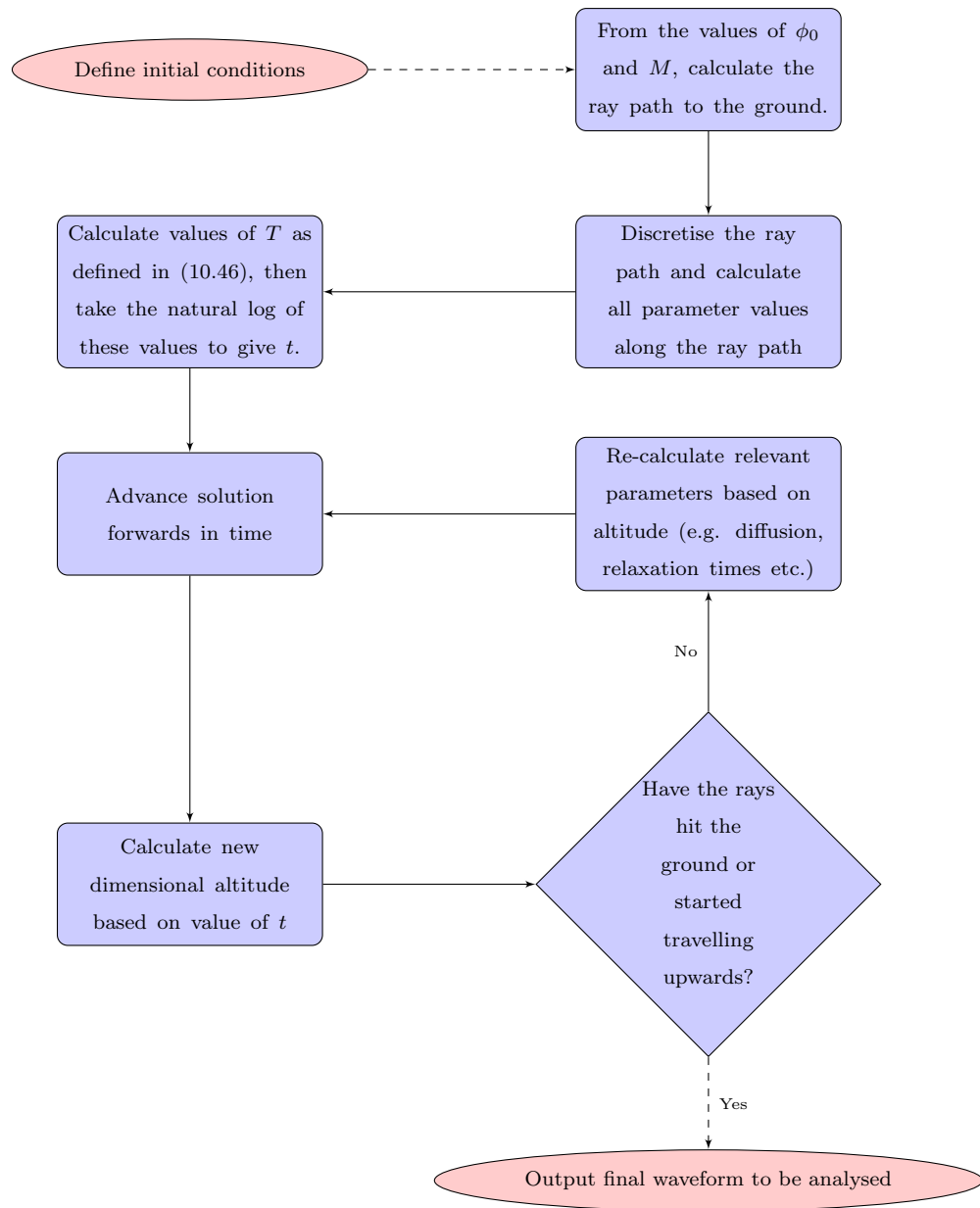


Figure 78: The algorithm needed to trace the rays trajectory to the ground.

10.5 Numerical Results

Now we have developed a numerical model capable of predicting the behaviour of sonic boom propagation in a physically realistic atmosphere it is time to run a test case. However, it is worth noting that in all previous numerical models we were able to compare the results to some asymptotic prediction in order to validate our results. In this case because the governing parameters are dependent on the propagation distance in the atmosphere, with certain parameters varying drastically with altitude, no accurate asymptotic prediction is available so the only comparison available to us is to use experimental results.

10.5.1 Test Case

We shall now consider a test case and interpret the results to find out what the impact is on the ground. The main purpose of this test case is to serve as proof of concept of the work undertaken so far to predict the propagation of a sonic boom from the atmosphere to the ground. For this test case the following governing criteria are selected:

Craft Length	17m	Maximum Radius	1m
Cruise Altitude	8,000m	Mach Speed	2
Azimuthal Angle, ϕ_0	0	Ground Temperature	10°C

From the previous asymptotic work, we expect the shock to initially behave according to weak shock theory before relaxation effects start to become more important as the shock propagates. For this numerical run, we assume an initial N-wave propagation distance of around 100m, meaning that we expect any sub-shocks to have merged into an N-wave by 100m as is shown in Figure 68. The main result we are concerned with is what form will the shock take once it reaches the ground.

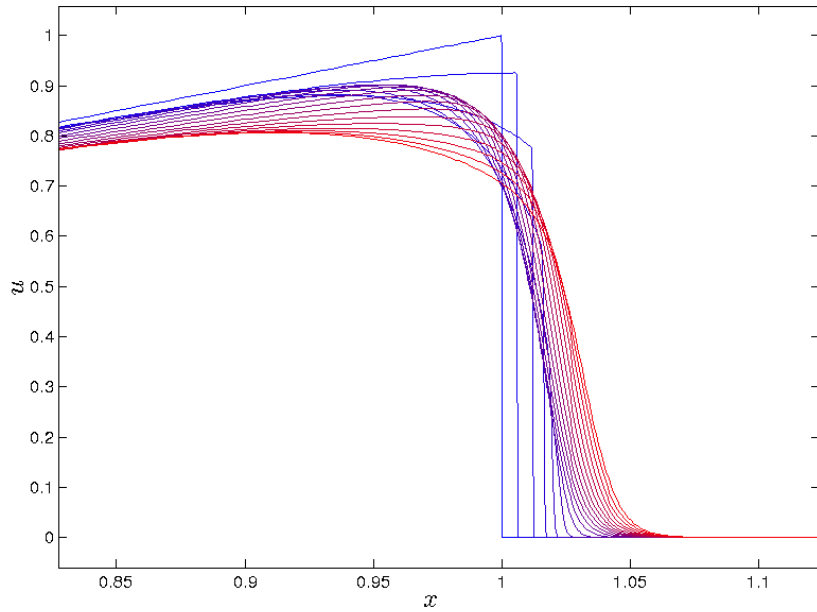


Figure 79: The leading shock of a sonic boom generated at 8,000m from a supersonic object at Mach 2 plotted at every 500m the wave propagates. The lines transition from blue to red in accordance to how far the wave has propagated.

The waveform results was calculated as described earlier in this section until the sonic boom reaches the ground and the results are shown for the waveform around the front and tail shock in Figures 79 and 80 respectively. From looking at the tail shock we can see that relaxation plays a key part in the development of the shock, however the key result is that of the final waveform once the shock reaches the ground as this waveform will determine the environmental impact of the sonic boom and that is shown in Figure 81. Having now obtained an expression for the waveform at the ground, the next thing to do is to extract the key information from it, in terms of how loud this shock is. The key parameters to be considered are the shock height and width (or rise time).

In order to extract the key parameters from these Figures we need to convert the dimensionless variables back into their dimensional counterparts by considering (10.46) and (10.49). Doing this for the final waveform in Figure 81 we can see that the front shock shows a change of 19.3 Pascals over 11ms over its steepest region while the tail

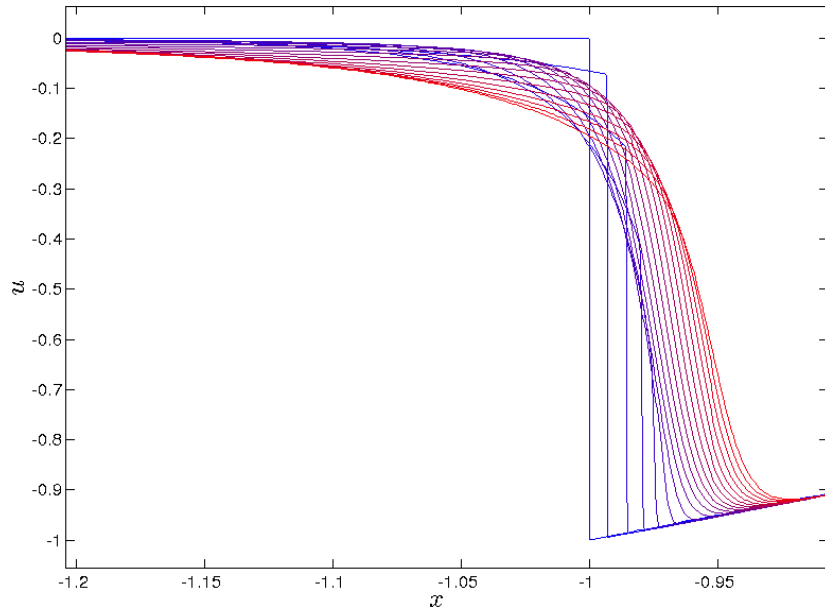


Figure 80: The tail shock of a sonic boom generated at 8,000m from a supersonic object at Mach 2 plotted at every 500m the wave propagates. The lines transition from blue to red in accordance to how far the wave has propagated.

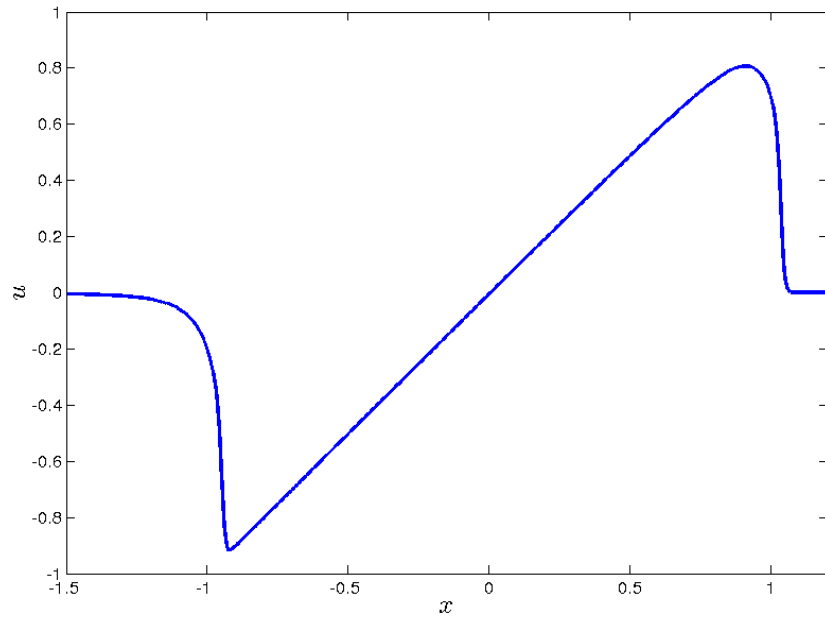


Figure 81: The final waveform of a sonic boom generated at 8,000m from a supersonic object at Mach 2 once it reaches the ground.

shock shows a change of 23.5 Pascals over 25ms over its steepest region which is of the same order of magnitude as many experimental results [41, 5]. The reason for a shallower shock in the tail shock can be explained due to the slowly decaying tail which has the effect of slowly diffusing energy out of the tail shock over time (this phenomenon is also seen in experimental results).

10.6 Comparison with Experimental Results

There have been limited experimental results on the structure of sonic booms which are of relevance to this research. The main reasons for this is that the analysis here is only suitable for sonic boom propagation in the air and from supersonic objects in steady flight. Another factor worth mentioning is the effect of wind and turbulence on sonic boom propagation which can cause significant variations in the peak overpressure and rise times [46]. This results in sonic booms signatures from a few hundred metres apart being vastly different.

In order to perform any comparisons with experimental results we would require the weather conditions on the day of the test and numerous final waveforms. Then, we could compare the numerical solution for that specific test case with the average received waveform from the experimental results.

11 Conclusion

11.1 Concluding Remarks

In this work, the main attention has been focused on the shock structure and validating the asymptotic predictions. In order to validate the asymptotic predictions, an in depth variable mesh scheme has been developed which can propagate the waveform forward in time whilst maintaining a high resolution around the shocks to allow for in-depth analysis of the shock structure. This approach of maintaining high resolution of the shocks, along with further analysis of the shock structure, allowed new validation of the asymptotic results. In §8 we considered the effects of molecular relaxation and what effects the inclusion of Nitrogen and Oxygen molecules would have on the waveform. Here, asymptotic techniques were developed to find a short time asymptotic solution for the behaviour of the waveform with the inclusion of a relaxation term. Again, these were validated with the numerical model offering excellent agreement for small ϵ .

Following this in §10 we developed a numerical scheme which modelled the Earth's atmosphere, taking into account the sound waves bending according to the change in sound speed, parameters such as temperature and humidity varying with altitude. Due to the complexity of the numerical scheme, no appropriate asymptotic solution was found so the only comparison available is that of experimental results. The numerical model has been designed to allow specific tailoring to the conditions where the sonic boom is generated and the supersonic aircraft design.

11.2 Future Work

There is considerable scope for future work from the work already undertaken in this thesis. This section will now list a few key areas for future research.

11.2.1 Experimental Comparisons

In the future, research could be taken to try and match this numerical model to experimental results. Particularly the results presented by Hilton et al. [41] and Blumrich et al. [5] provide detailed information of the temperature, wind speeds and sound speeds at various altitudes which could be matched by this model to see how accurately the model performs against experimental data.

11.2.2 The sonic boom strength from the centre of the sonic boom carpet

In §10.3.4 we plotted the sonic boom carpet for sonic booms from supersonic objects travelling at various speeds. It would be of interest to see how the strength of the sonic boom (in terms of peak overpressure and rise time) varies as we travel away from the centre of the sonic boom carpet. It is possible that the sonic booms received at the edge of the sonic boom carpet will be sufficiently diffused to be safely ignored.

11.2.3 The effect of varying weather conditions

A number of atmospheric parameters in this model which vary significantly with location. In particular temperature, humidity and wind can all vary significantly. By running similar numerical solutions where we slowly vary one of these parameters we can begin to

understand the subtle effect weather has on sonic boom propagation.

11.2.4 Sub-shocks

Sub-shocks were briefly mentioned in §8 and §10. A sub-shock is where we have, in essence, a smaller shock inside of a larger shock. In this case, we need to reconsider our parameters for the effect this shock has in terms of peak overpressure and rise time. This is because a sub-shock would have a small region with a significant change in the percentage of peak overpressure but only a small change of the rise time. It would be of interest to look at what conditions would cause a sub-shock to appear and how long the sub-shock would remain a key feature of waveform.

Part B

Inverse Scattering

12 Introduction

In this part of the thesis, the focus is on signal processing. The aim being to try and improve the target detection rate of a landmine detector. The target detection rate is defined as the average number of false positives for every genuine target. The landmine detector used here was a MINEHOUND detector, developed by Cobham Technical Services, which makes use of ground penetrating radar (GPR) to detect any impedance discontinuities in the ground which may be caused by a landmine or any improvised explosive device (IED). Ideally, any method developed here could be implemented directly into a landmine detector and, as such, will need to be performed in real time.

The work in this section has been summarised and published in IEEE, transactions on Geoscience and Remote Sensing [48]. After the introduction, there will be a literature review, which will be presented offering a brief overview of the main methods that were considered to improve the target detection rate. There has been lots of research on these topics for seismic data and there are strong parallels between seismology and GPR with the main difference being that GPR signals have much stronger diffraction effects due to the smaller wavelengths used in the propagating signal. This may cause certain problems if we try and convert a method developed for seismic data into a method for GPR data. We will also develop algorithms for the most promising methods to get a more complete idea

of how that particular method works and any possible flaws it might have (e.g. sensitivity to noise, excessive computational time etc.). Then, based on the performance of these algorithms, the one producing the most promising results will then be developed further which will involve seeing what improvements and new features can be added. Once the complete algorithm has been developed, it shall be tested on multiple samples of real data and used with an autonomous target detection process to quantify what improvement it offers.

Due to the fact that landmines are such a widespread issue throughout the world, a considerable amount of research has conducted in this field. Some of the key research material worth mentioning include ‘The history of landmines’ by Croll, [14], which provides a general overview of the development of landmines over the years and the techniques used to find buried landmines. Another key piece of literature is ‘Ground penetrating radar for high-resolution mapping of soil and rock stratigraphy’ by Davis and Annan, [11], which discusses the basic principles of using ground penetrating radar to identify sub-surface features. Lastly it also worthwhile to mention ‘Seismic migration: Theory and practice’ by Stolt and Benson, [51], where they provides a broad overview on how to combat the effect of migration (where a received sub-surface signal differs from the actual sub-surface image due to the waves been sent out and received over a wide angle) which is an issue that greatly reduces the ability to distinguish between objects in landmine detection.

12.1 Historical Background

Out of the many issues for countries recovering from conflict, one of the key problems is that of landmines. Landmines have been used in many conflicts over the years and this

has resulted in between 45-100 million unexploded landmines in the ground today spread across over 75 countries [14].

The danger of landmines is that they kill indiscriminately and, quite often, years after the conflict that led to their implementation has been resolved. Landmines still kill or injure around 15 to 20 thousand people each year, often children wandering into old war zones as landmines can remain active for over 50 years [14]. As a result of this, considerable research has gone into trying to find a cost effective, efficient way of detecting landmines.

The most primitive technique is to prod the ground with a metal prodder in the hope of hitting a mine; however this is time consuming and has the problem of only being able to find mines up to a limited depth. So this led to the development of the metal detector, which would pick up the metal from the landmine in order to highlight its location.

Metal detectors only have limited success due to the fact they cannot distinguish between the small pieces of metal in landmines and other small pieces of metal buried in the ground, which are common in areas of past conflict. In practice, metal detectors have a poor target detection rate of around 100-150 indications of scrap metal to every mine. The main reason behind this poor target detection rate are minimum metal landmines which were introduced during World War 2. These seriously compromised the efficiency of the metal detector, so in order to combat this problem Ground Penetrating Radar was introduced to improve the detection rate.

12.2 Technical Background

Ground Penetrating Radar is an electromagnetic technique for finding the location of objects and any other impedance discontinuities beneath the Earth's surface [18, 16]. GPR works by sending electromagnetic waves into the ground as shown in Figure 82 and detecting the reflected signal caused by any impedance discontinuities in the ground, which can then be investigated if required. Typical GPR detectors have a target detection rate of around 30-50 indications of clutter for every genuine target.

The GPR image is highly dependent on the propagation characteristics of the ground as well as the antenna characteristics. Consider the idealised case where we are detecting a point source target. Here we have the point spread function of the target being convolved with the antenna beam function (the form that the wave is sent out from the detector) and this spreads the received signal in time and space causing the well known diffraction hyperbola as can be seen in Figure 83 [22]. The problem with this idealised case is that the wavelengths used by GPR devices can be half the diameter of an anti-tank (AT) mine and, as such, the AT mines do not always act like point spread functions. However, the geometry of AT mines means they still form hyperbolic scattering because of the multiple scattering centres. Therefore, throughout this report we will be making the assumption that we are dealing with perfect hyperbolas which is a reasonable assumption considering the scattering patterns caused by the AT mines used in the investigation.

A typical scan will pick up many impedance discontinuities in any single scan. These responses are typically caused by antenna coupling between the two antennas, a surface reflection from when the signal hits the ground and additionally from any impedance discontinuities under the surface which could be a potential target (see Figure 82). Impedance

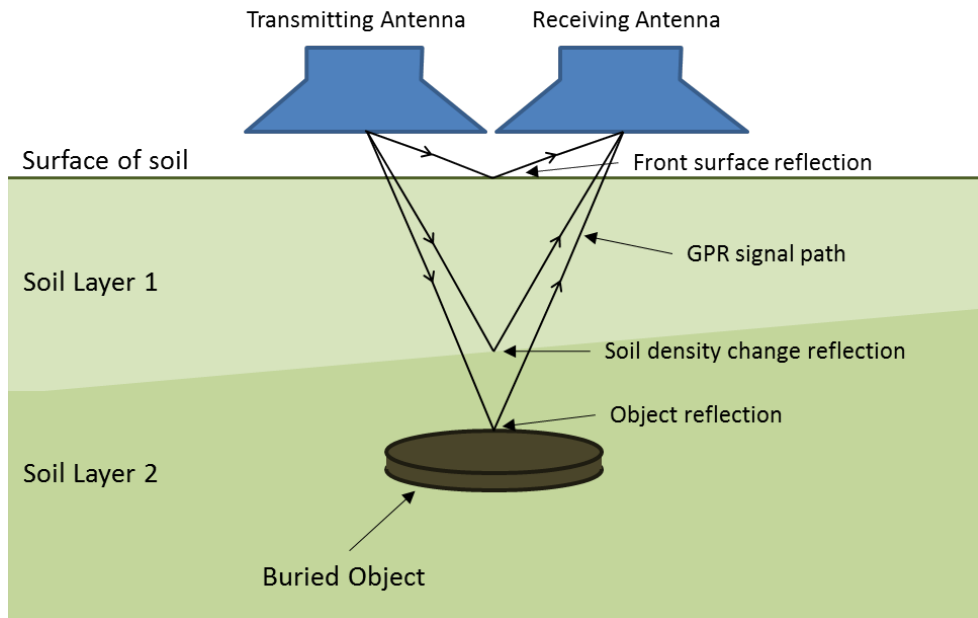


Figure 82: A standard GPR arrangement demonstrating how to detect buried objects.

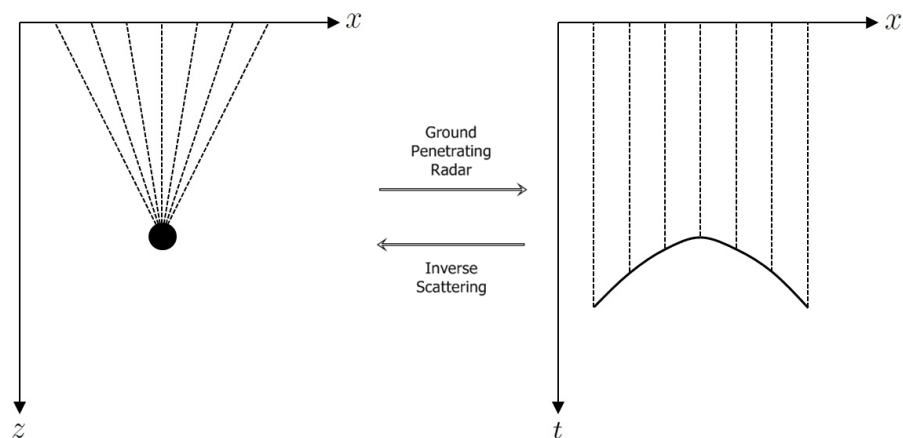


Figure 83: A comparison of the subsurface layer to the image seen from a GPR device.

discontinuities can be caused by changes in the ground density, the water content in the ground or, more interestingly, buried objects in the ground which could be a mine. A typical signal response is presented in Figure 84. Note how the response from the air/ground barrier and antenna coupling return is significantly stronger than the target return which is one of the main problems in mine detection.

The most basic scan in GPR terminology is the A-Scan [17] which is just a one dimensional discrete measurement measuring the strength of the response against time as shown

in Figure 84. From looking at an A-Scan, it is possible to extract some information on whether or not a target is present. However, in order to make a definitive decision, another nearby A-Scan is needed without a target in order to compare the two responses together. As we can see in Figure 84 the red line has a strong response at around 75 nanoseconds implying the possibility of target there. However, the response at 75 nanoseconds could just be a feature of the ground, so ideally we need a second A-Scan from a nearby location to inform us that the response is not a universal feature of the ground, which is presented by the blue line in Figure 84. The most prominent features of an A-Scan are the crossover pulse from the transmitting to receiving antenna and the reflection from hitting the surface of the ground. These can be seen in Figure 84 for the first 40 nanoseconds.

In order to compare A-Scans it is helpful to plot them successively in a line where each A-Scan is from a nearby spatial location. This gives us a two dimensional representation of the ground and is called a B-Scan [17]. Extending this idea, we can plot successive B-Scans together to give a three dimensional representation of the ground (a C-Scan [17]). Examples of these scans are shown in Figure 85, however in this thesis only consider B-Scans will be considered.

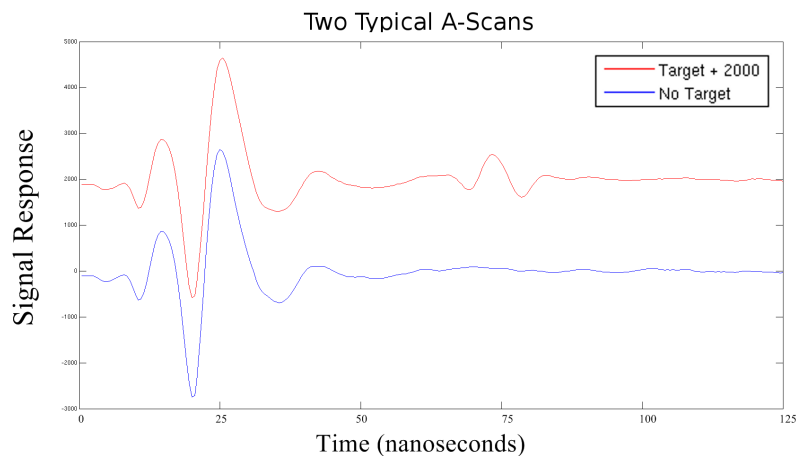


Figure 84: An A-Scan with a target response (red) and an A-Scan without a target response (blue).

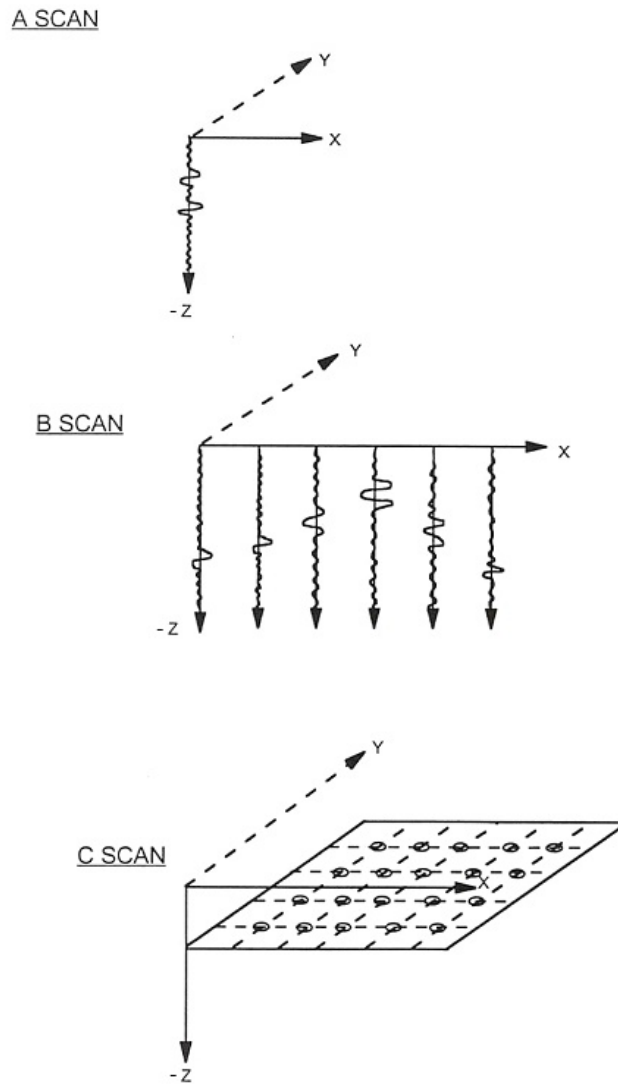


Figure 85: Examples of A-Scans, B-Scans and C-Scans [17].

Having obtained a B-Scan, we can perform various processing algorithms on the data to eliminate the crossover pulse and any other features which are present in all A-Scans in order to show the locations of any potential targets more clearly. Another important processing step is the time-varying gain, as the signal propagates through the ground it gradually loses energy due to the lossy nature of the soil. To combat this we increase the signal strength proportional to the depth, where the constant of multiplication can be changed according to different ground conditions.

In Figure 86 two B-Scans are presented, one without any processing and one with all

the processing steps mentioned above performed to try and eliminate the effects of the surface and counteract the effects of lossy soil. It is important to note that all the methods discussed here are assuming we start with a processed B-Scan.

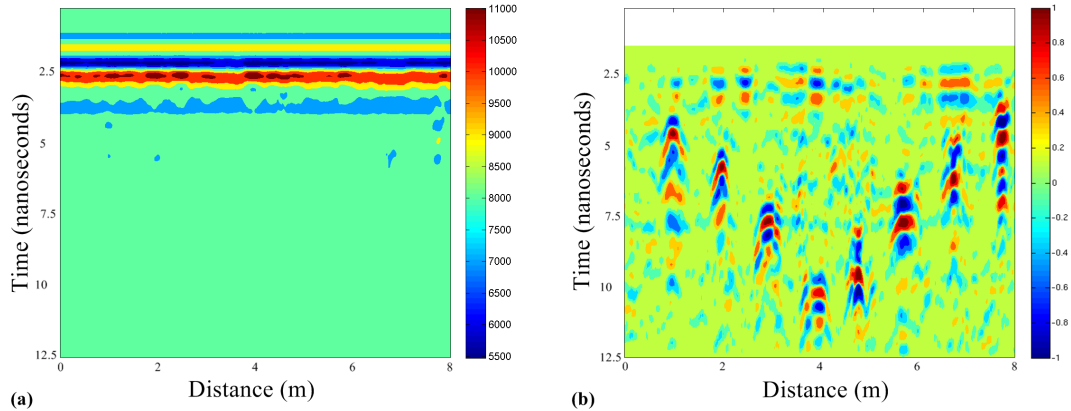


Figure 86: An unprocessed B-Scan next to a processed B-Scan.

Even after these pre-processing steps, the measurements in a processed B-Scan still suffer from a few problems such as noise and poor object definition. This is partly due to the signal being attenuated as it propagates through the ground. However, this can be combated fairly successfully using the time-varying gain. The main problem with the data is that the GPR devices suffer from low directivity (i.e. the rays are sent out and received at a wide angle meaning we receive signal responses from regions which are not directly beneath the antennas). This is because high directivity from the antenna requires a significantly large aperture in relation to the operating wavelength, but at the frequencies of operation of GPR this would result in a large and impractical antenna. For operator convenience most GPR antennas are small and exhibit low directivity with a wide beam width. This causes the GPR image to bear little resemblance to the actual target scattering centres and one that is highly dependent on the propagation characteristics of the ground.

A consequence of this is that it is hard to find the exact location of a target once it

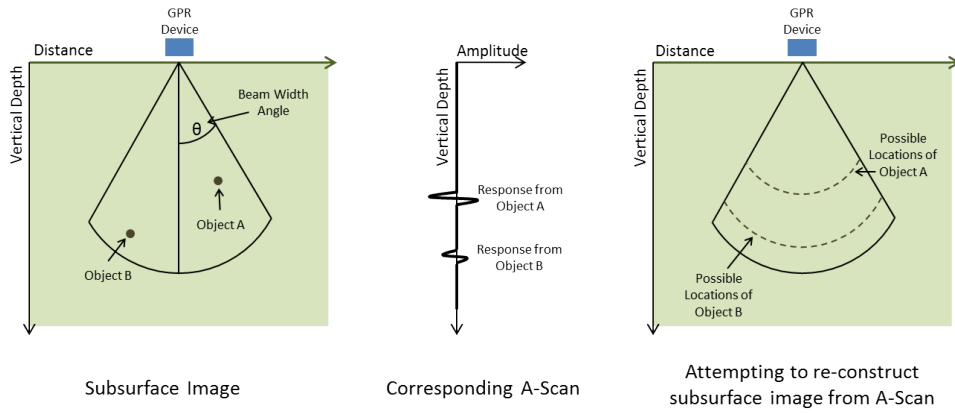


Figure 87: An example of trying to reconstruct the subsurface image from an A-Scan.

has been detected. An illustration of this is shown in Figure 87. Instead, we receive a signal response from a particular target in numerous adjacent A-Scans which is shown in Figure 83. These factors result in there being poor contrast between targets. The aim of this work is to develop new techniques in order to eliminate these effects to improve the target detection rate as a high false alarm rate is a serious problem and can result in complacency from the operator of the mine detector. The main way this problem will be tackled is to use various inverse scattering methods with the aim of converging the diffraction hyperbola (caused by the wide beam width of the propagating signal) back into its actual subsurface image as demonstrated in Figure 83.

13 Literature Review

We will now review various techniques previously proposed as methods to improve the clarity of received signals, whether the research is based in using GPR data, seismic data or any other kind of data. Algorithms shall also be developed for the most promising techniques to work on B-Scans to see what improvements are offered when faced with real data.

13.1 Deconvolution

13.1.1 Introduction and Basic Idea of Deconvolution

This basic premise of this idea is to simplify the received signal in order to better interpret the data. The idea presented here follows the work discussed in ‘Ground Penetrating Radar’ by David J. Daniels[17]. The idea of deconvolution is to remove the main effects which distort the data. When a signal is sent out from the transmitting antenna, rather than being sent out as a distinct pulse, it has a particular function (the transfer function) which is then convolved with any impedance discontinuities encountered. The same is true of the receiving antenna, where the received signals are also convolved with a transfer function.

It can be deduced that the received voltage $V_R(t)$ (from which the GPR output is taken from) is of the form

$$V_R(t) = \sqrt{\frac{z_c}{z_0}} \mathbf{h}_{\text{rec}}(\theta, \phi, t) * \mathbf{E}_{\text{rec}}(t), \quad (13.1)$$

where $*$ represents a convolution in time, z_0 and z_c represent the impedances of free space

and the ground respectively, \mathbf{h}_{rec} is the transfer function of the receiving antenna, \mathbf{E}_{rec} is the field at the receiving antenna and θ, ϕ, t are two space variables (in spherical coordinates) and time. The field at the receiving antenna is purely dependent on the field transmitted from the transmitting antenna and any impedance discontinuities encountered giving

$$\mathbf{E}_{\text{rec}}(t) = \mathbf{R}(r, \theta, \phi, t) * \mathbf{E}_{\text{trans}}(t), \quad (13.2)$$

where $\mathbf{R}(r, \theta, \phi, t)$ are the impedance discontinuities encountered, r is the radial distance and $\mathbf{E}_{\text{trans}}$ is the transmitted signal sent out from the transmitting antenna. Inserting (13.2) into (13.1) and letting $\mathbf{h}_{\text{total}}(\theta, \phi, t) = \sqrt{\frac{z_c}{z_0}} \mathbf{h}_{\text{rec}}(\theta, \phi, t) * \mathbf{E}_{\text{trans}}(t)$ we arrive at

$$V_R(t) = \mathbf{h}_{\text{total}}(\theta, \phi, t) * \mathbf{R}(r, \theta, \phi, t). \quad (13.3)$$

We can express the impedance discontinuities $\mathbf{R}(r, \theta, \phi, t)$ as either target responses, clutter (e.g. surface reflection, animal burrow, etc.) or general noise giving us

$$V_R(t) = \mathbf{h}_{\text{total}}(\theta, \phi, t) * (\mathbf{T} + \mathbf{Cl}) + n, \quad (13.4)$$

where \mathbf{T} is target responses, \mathbf{Cl} is clutter responses and n represents the inclusion of noise.

Now we can deconvolve $V_R(t)$ to remove the effects of $\mathbf{h}_{\text{total}}$ leaving us with

$$V_{R_1}(t) = \mathbf{T} + \mathbf{Cl} + \tilde{n}, \quad (13.5)$$

where \tilde{n} also represents the inclusion of noise. Without the effects of $\mathbf{h}_{\text{total}}$ distorting the received image, it will be a lot simpler to differentiate between what is a target and what is clutter.

The key idea here is to deconvolve the effects of $\mathbf{h}_{\text{total}}$. However, finding an accurate expression for $\mathbf{h}_{\text{total}}$ is a lot more complicated as will be documented later on in this section. Numerous methods to perform deconvolution exist and an example of partial Claerbout deconvolution [43] can be seen in Figure 88 where we deconvolve the transfer function of the transmitting antenna. As can be seen it goes some way to improve the clarity of the signal. However, there is still a lot of noise in the signal which needs to be addressed. The two strong peaks at around 40 nanoseconds are caused by the presence of an AT mine. The reason there are two peaks is that there are large impedance discontinuities first when the waves enter the mine from the soil and secondly when the waves exit the mine back into the soil. However, it is worth noting that this is only a partial deconvolution and does not take into account the transfer function of the receiving antenna.

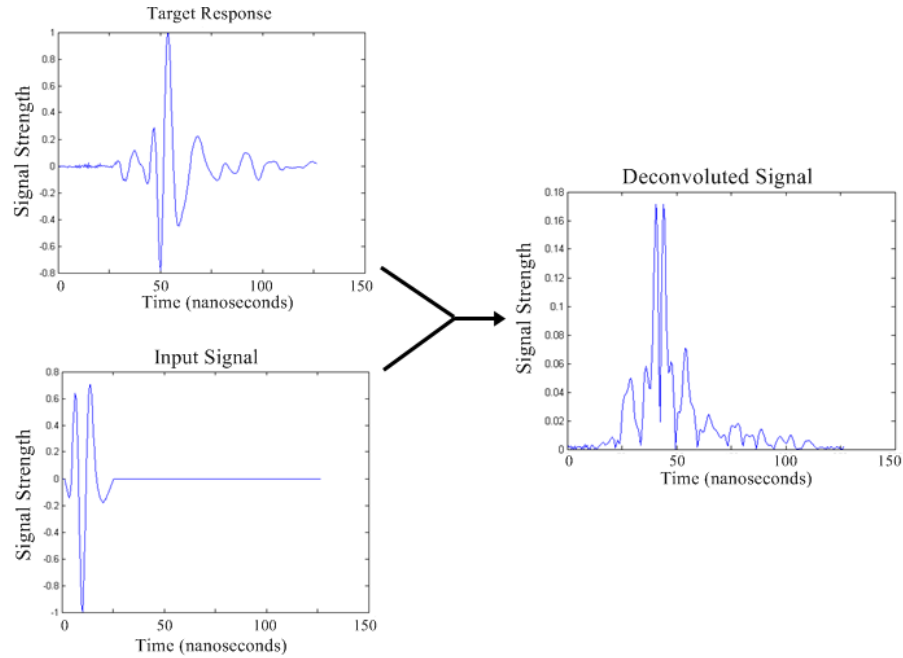


Figure 88: An example of deconvolving an A-Scan using Claerbout deconvolution.

13.1.2 1-D Deconvolution using Stochastic Mutation

One of the most basic deconvolution ideas is that of 1-D deconvolution using stochastic mutation. Here, the idea is to solve the deconvolution problem by using a genetic algorithm which will be tailored in order to find a simplistic solution. This solution will hopefully accurately describe what is underneath the surface by working on the principle that the target response (A-Scan) will most likely be caused by small number of large responses (rather than a large number of small responses). The idea of the algorithm is to generate one spike at a time (similar to the two spikes at around 40 nanoseconds in Figure 88) and shift them along the time axis and convolve them with the transfer function. Where the spike best fits in best will be judged by minimising the L_2 norm of the error,

$$\text{Error} = \|S(t) - C(t)\|_2 = \sqrt{(S(1) - C(1))^2 + (S(2) - C(2))^2 + \dots + (S(n) - C(n))^2}, \quad (13.6)$$

where $S(t)$ is the signal response and $C(t)$ is our convolved function and $t = 1 \dots n$ represents the discrete time responses of the A-Scan. Then the L_2 norm would have to be minimized for each spike with relation to its location and size. In order to try and obtain a fairly simplistic model, they will have to be a strict limit on the number of spikes.

The advantage of this algorithm is that it is fairly simple and hopefully this will correlate to a fairly small computational time. Also the fact that this method is searching for a distinct number of spikes will hopefully ‘ignore’ most of the noise since each spike will have a minimum magnitude. The disadvantage of this is that faint signals from subtle impedance discontinuities may fall into noise, so careful calibration will be required. Also, it is possible this algorithm may struggle with more complicated objects which are not defined by a small number of impulse response. However, it is hoped that these objects

will be rare in the ground and of little direct significance.

13.1.3 A Short Comparison of other Deconvolution Techniques

The following examples are taken from the need to find the input function $f(t)$ after it has been convolved in the following way

$$c(t) = \int_{-\infty}^{\infty} f(\tau)g(t - \tau)d\tau, \quad (13.7)$$

which is analogous to the problem described in §13.1.1 where $c(t)$ is our received signal and we have $g(t) = \mathbf{h}_{\text{total}}$ and $f(t) = \mathbf{R}(r, \theta, \phi, t)$. The techniques considered here are taken from ‘A Comparison of Six Deconvolution Techniques’ by Francis N. Madden et al. [40] and include Fourier transform based deconvolution; system identification; a constrained deconvolution technique; a method using spline basis functions; maximum entropy and finally a genetic algorithm to recreate the input function. The aim of the paper was to evaluate the performance of the different algorithms by testing them on simulated data generated from several input functions. When the data sets did not suffer from noise, all six algorithms performed fairly well in re-creating the input functions. However, with the inclusion of noise it was clear that certain methods performed better than others. The performance was judged by the square of the norm of the input function, $f(t)$, subtracted from the recreated input function, $\hat{f}(t)$,

$$\mu_1 = \|f - \hat{f}\|_2^2, \quad (13.8)$$

where the smaller the value of μ_1 , the more successful the method was deemed to be. From observing the results presented in [40] it can be seen that the best two methods of

deconvolution are the methods using spline basis functions and maximum entropy, where spline basis functions have less bias, but maximum entropy has less variance.

It is important to note that the results from [40] are taken from pharmacokinetics, and in order to relate this to the deconvolution problem in GPR, certain changes will be required which may alter the effectiveness of the algorithms. It is also of note to mention that these deconvolution methods require us to know the transfer function, $\mathbf{h}_{\text{total}}$. When we are dealing with GPR data $\mathbf{h}_{\text{total}}$ is an unknown and must be found using various techniques. These may include sending a known pulse through the system in order to obtain the transfer function, or possibly obtaining $\mathbf{h}_{\text{total}}$ by considering the antenna coupling return which is not dependent on the ground conditions.

13.1.4 Blind Deconvolution

Numerous blind deconvolution algorithms exist and here one will be studied briefly in order to give a flavour of the ideas employed. In regular deconvolution we are presented with a problem of the form

$$c(t) = \int_{-\infty}^{\infty} f(\tau)g(t - \tau)d\tau,$$

as shown in (13.7), where we need to find $f(t)$ given that we know $c(t)$ and $g(t)$. In blind deconvolution we aim to find both $f(t)$ and $g(t)$ with only the knowledge of $c(t)$. The method here is discussed in ‘Iterative blind deconvolution method and its applications’ by G. R. Ayers et al. [3]. Some a-priori information concerning the functions $f(t)$ and $g(t)$ is generally required (for example, the functions may be known to be non-negative everywhere) and from there the algorithm attempts to deconvolve the two functions. The

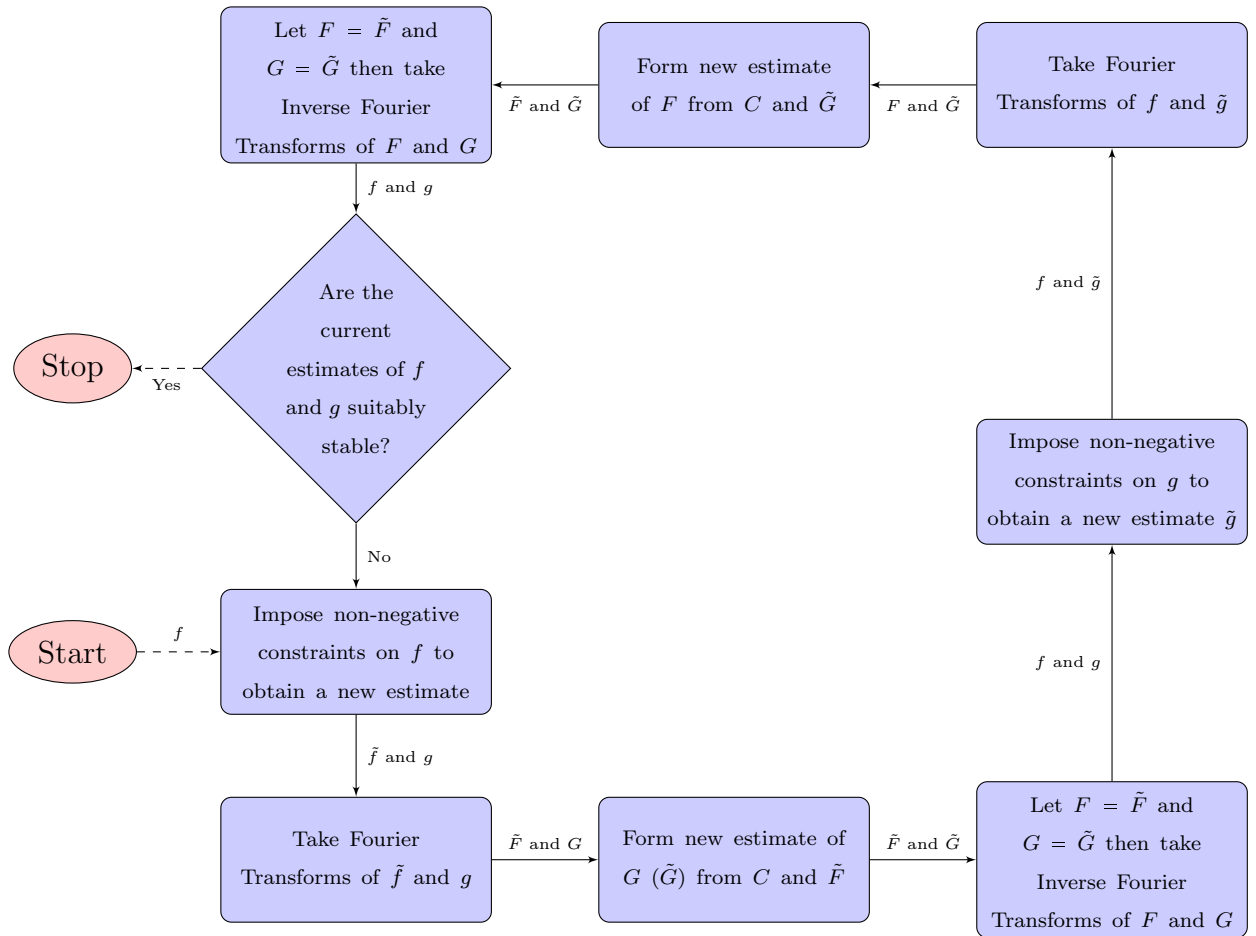


Figure 89: A blind deconvolution algorithm, where the initial estimate for f is a vector of ones.

deconvolution algorithm presented here works by taking Fourier transforms of $f(t)$, $g(t)$ and $c(t)$ so (13.7) becomes

$$C(u) = F(u)G(u).$$

From here, estimates of $f(t)$ and $g(t)$ are found by imposing the non-negative constraints. Repeatedly doing this allows us to iteratively converge on the true values of $f(t)$ and $g(t)$ as shown in Figure 89. While this algorithm relies on an iterative scheme, there are many other types of blind deconvolution based on different ideas (e.g. the total variational minimisation method [55], which works in a similar fashion to Tikhonov regularisation discussed later).

The main problem with all blind deconvolution algorithms is making sure they will

deconvolve the image to the desired target response. Also there is no guarantee that deconvolving the received signal will have a unique solution. Hence, it is possible for blind deconvolution to distort the image further.

13.1.5 Deconvolution versus Blind Deconvolution

Seeing how both the deconvolution methods are strongly related, it makes sense to compare the two methods directly to see which is better suited for use with GPR data. The main advantage of deconvolution is that it is much easier to solve than blind deconvolution. However the main problems encountered are the difficulties of finding the transfer function which blind deconvolution sidesteps. It is possible to find the transfer function by sending known signals to the receiving antenna, which we can then deconvolve to find the transfer function (as deconvolving to find the input signal or transfer function given the other are equivalent problems). This is relatively feasible providing the transfer function will not change significantly while in operation, as every time the transfer function changes we will have to re-calculate it. The advantage of blind deconvolution is the fact it can easily adapt for changes in the transfer function as most blind deconvolution methods involve solving an iterative optimisation algorithm, so a slight change in the transfer function will result in only a few steps to re-optimize for the new transfer function.

Another important factor is that deconvolution has had limited success in GPR applications because the ground conditions fluctuate quickly and dispersion effects are considerably stronger than in seismic data where there has been some success in using deconvolution to improve image clarity. However, it is possible that this problem may be accounted for (or at least minimised) by using appropriate pre-processing steps.

13.2 Feature Extraction Methods

13.2.1 Introduction and Basic Idea

One of the fundamental problems with GPR is resolving the measurements obtained into a distinct answer of threat or no threat. This leads us to the idea of feature extraction which involves simplifying the amount of resources required to describe a large set of data accurately. In ‘Feature Extraction and Classification of Echo Signal of Ground Penetrating Radar’ by Hui-Lin et al. [30], the dyadic wavelet transform is used to provide a transformation of a signal from the time domain to the scale frequency domain. A wavelet transform is the representation of a function by wavelets which allows us to look at certain frequencies of the signal in a way that is not possible by looking at the raw data [2]. The idea behind using a dyadic wavelet transform is to extract the key features from the subsurface layer to better identify whether or not a target is present in the ground. A standard dyadic wavelet transform is of the following form

$$W(j, k) = \sum_{n=0}^{N-1} x(n)\psi_{j,k}(n), \quad \text{where} \quad \psi_{j,k}(n) = 2^{-\frac{1}{2}}\psi(2^{-j}n - k). \quad (13.9)$$

Here $W(j, k)$ is the dyadic wavelet transform decomposition of $x(n)$, our A-Scan and $\psi_{j,k}(n)$ is obtained from the wavelet ψ which can be any standard wavelet (e.g. the coiflet wavelets [23]).

The dyadic wavelet transform of a finite energy sequence (in our case an A-Scan) can be computed fairly simply in order to give us the wavelet energy for each A-Scan. However, before we can use the wavelet energy to distinguish between a target and from clear ground or clutter, we will need to perform further feature extraction techniques in order to pick

out the most telling characteristics in terms of target detection.

Alternative feature extraction methods include using short time Fourier transforms which have been shown to identify targets from certain types of clutter. Short time Fourier transforms are used to determine the sinusoidal frequency and phase content of local sections of a signal as it changes over time (i.e. it is designed to work in conditions where the ground varies over time). Another approach is to use pole/zero analysis, which is a useful method for studying the behaviour of linear, time invariant networks [36] and has shown some promise in locating targets in GPR data.

These are fairly novel ideas at improving target detection as the actual image from the ground is transformed into something that is unrecognisable from the original B-Scan and from here various extraction algorithms need to be performed in order to highlight the locations of possible targets. The potential problem with this idea is that, even after all the feature extraction, there still might not be a clear way to decide what is and what is not a target. One possible idea is to use one of these methods in conjunction with another, more robust, method.

13.3 Diffraction Tomography for Ground Penetrating Radar Imaging

13.3.1 Introduction and Basic Idea

Ground penetrating radar inversion works by first generating a forward model of the process of mine detection using Maxwell's equations. Then the forward model is inverted in order to give us an inverse scattering algorithm. The methods discussed here have

been developed in ‘Diffraction tomography for multi-monostatic ground penetrating radar imaging’ by Ross Deming et al. [19] and ‘Linear GPR Inversion for Lossy Soil and a Planar Air-Soil Interface’ by Peter Meincke [42]. In order to combat the ill-posed nature of the problem, the forward model will be inverted using the Tikhonov-regularized pseudo-inverse operator [54]. This involves two steps; filtering of the received data and back-propagation. The filtering is carried out by numerically solving Fredholm integral equations of the first kind and the back-propagation is performed using fast Fourier transforms (FFTs). This method will be discussed omitting most of the details which are present in [19] and [42].

13.3.2 Method

13.3.3 Forward Model

The first step is to create a forward model of the scattering problem. In developing the forward model we use the configuration presented in Figure 90 as a guide. The forward model is defined to give an expression for s_o (the output signal) which is solely due to the field scattered by the buried object (note: in order to achieve this, a first order Born approximation is needed which will neglect all multiple scattering effects).

To obtain the forward scattering model we start with Maxwell’s equations

$$\epsilon \frac{\partial \bar{\mathbf{E}}}{\partial t} = \nabla \times \bar{\mathbf{H}} - \bar{\mathbf{J}}, \quad (13.10)$$

where $\mathbf{J} = \mathbf{J}(\omega, \mathbf{r}', \mathbf{r}_t)$ is the forcing term, and

$$\frac{\partial \bar{\mathbf{H}}}{\partial t} = -\frac{1}{\mu_0} \nabla \times \bar{\mathbf{E}}. \quad (13.11)$$

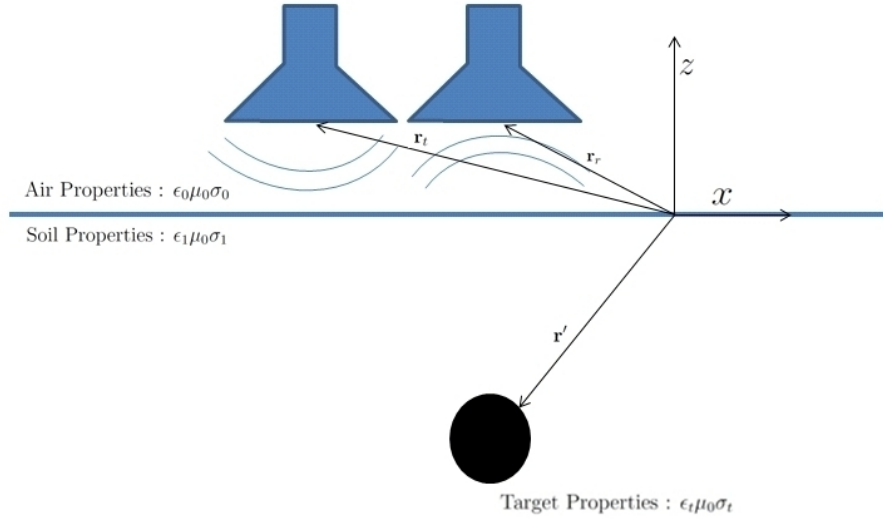


Figure 90: Fixed-offset GPR configuration where the air has the permittivity ϵ_0 , conductivity σ_0 and permeability μ_0 , whereas the lossy soil has the permittivity ϵ_1 , conductivity σ_1 and permeability μ_1 . The target is located in the lossy soil and has permittivity ϵ_t , conductivity σ_0 and permeability μ_t . The receiving antenna is located at $\mathbf{r}_r = x_r\mathbf{i} + z_r\mathbf{z}$ and the transmitting antenna is located at $\mathbf{r}_t = x_t\mathbf{i} + z_r\mathbf{z}$.

where $\bar{\mathbf{E}}$ is the electric field, $\bar{\mathbf{H}}$ is the magnetic field, ϵ is the dielectric field strength and μ_0 is the magnetic permeability of free space given as $\mu_0 \approx 1.256 \times 10^{-6}$. Taking Fourier transforms of (13.10) and (13.11) we arrive at

$$i\omega\epsilon\mathbf{E} = \nabla \times \mathbf{H} - \mathbf{J}, \quad (13.12)$$

and

$$i\omega\mathbf{H} = -\frac{1}{\mu_0}\nabla \times \mathbf{E}. \quad (13.13)$$

Now we have an equation for \mathbf{E} , we can obtain a solution using Green's functions and by separating \mathbf{E} into the incident and scattered field, $\mathbf{E} = \mathbf{E}_{\text{inc}} + \mathbf{E}_{\text{sca}}$, and using a first order Born approximation we can find an expression for \mathbf{E}_{sca}

$$\mathbf{E}_{\text{sca}}(\mathbf{r}) = -\omega^2\mu_0 \iiint_{z \leq 0} \bar{\mathbf{G}}(\mathbf{r}, \mathbf{r}') O(\mathbf{r}) \mathbf{E}_{\text{inc}}(\mathbf{r}') d\mathbf{r}'. \quad (13.14)$$

where $O(\mathbf{r}) = \epsilon(\mathbf{r}) - \epsilon_2(\mathbf{r})$ (the differences in dielectric constants in the soil due to the target) and $\bar{\mathbf{G}}(\mathbf{r}, \mathbf{r}')$ is the dyadic Green's function

We can now use the expression for the scattered field, (13.14), along with the dyadic Green functions and the plane-wave characteristic $\mathbf{R}(\mathbf{K}, \omega)$ to find the output $s_o(\mathbf{r}_r, \omega)$ of the antenna. By taking a Fourier Transform of $s_o(\mathbf{r}_r, \omega)$ with respect to the horizontal components \mathbf{r}_r of the observation point and taking an asymptotic limit for when the objects are located deep in the soil (more than two wavelengths deep) and assuming the GPR antennas are close to the ground gives us an expression for $\tilde{s}_o(\mathbf{K}, z_r, \omega)$, where \mathbf{K} is the two dimensional Fourier space and the expression is given in equation (12) in [42]. This expression for $\tilde{s}_o(\mathbf{K}, z_r, \omega)$ consists of our forward model to be inverted and it gives realistic results for depths greater than two wavelengths and for $|\mathbf{K}| < 2\text{Re}(k_1(\omega))$ which prohibits any evanescent waves in this model.

13.3.4 Inversion

In order to carry out the inversion we are going to assume that $\omega\Delta\epsilon \gg \Delta\sigma$, (the permittivity varies faster than the conductivity) when $\omega_{\min} < \omega < \omega_{\max}$ so $\tilde{s}_o(\mathbf{K}, z_r, \omega)$ can be expressed as

$$\tilde{s}_o(\mathbf{K}, z_r, \omega) = \mathcal{L}\Delta\epsilon_1. \quad (13.15)$$

As was mentioned earlier we need to apply Tikhonov regularisation in order to obtain stable and useful solutions. Hence, a minimisation problem of the following form is considered

$$\min_{\Delta\epsilon_1} \left(\|\mathcal{L}\Delta\epsilon_1 - \tilde{s}_o\|_2^2 + \lambda^2 \|\Delta\epsilon_1\|_2^2 \right), \quad (13.16)$$

where λ has to be carefully picked in order to get stable and useful results. This minimisation problem is solved by applying the Tikhonov-regularised pseudo-inverse operator

$$\Delta\epsilon_1 \approx \mathcal{L}^\dagger (\mathcal{L}\mathcal{L}^\dagger + \lambda^2\mathbf{I})^{-1} \tilde{s}_o, \quad (13.17)$$

where the adjoint operator \mathcal{L}^\dagger is defined by $\langle \tilde{s}_o, \mathcal{L}\Delta\epsilon_1 \rangle = \langle \mathcal{L}^\dagger \tilde{s}_o, \Delta\epsilon_1 \rangle$. The next step is to introduce the filtered data \tilde{s}_o^f

$$(\mathcal{L}\mathcal{L}^\dagger + \lambda^2\mathbf{I}) \tilde{s}_o^f = \tilde{s}_o, \quad (13.18)$$

which allows us to obtain the final expression

$$\Delta\epsilon_1 \approx \mathcal{L}^\dagger \tilde{s}_o^f. \quad (13.19)$$

Note that \mathcal{L}^\dagger can be found easily using FFTs while the filtering in equation (13.18) is typically more complicated.

13.3.5 Algorithm

Having now developed the model used for this method, we now develop an algorithm which we can efficiently implement using Matlab. First we take a spatial Fourier transform of the B-Scan, then we need to perform filtering to improve the stability due to the ill-posed nature of the problem (finding \tilde{s}_o^f) and finally we invert the data to give us the object profile of any discontinuities in the ground. The algorithm to be used is shown in Figure 91.

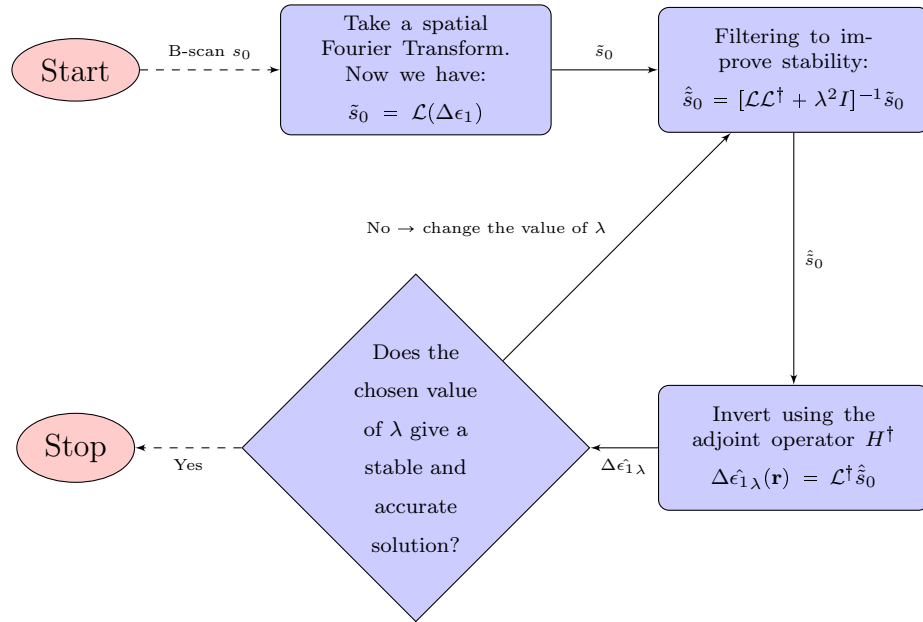


Figure 91: An Algorithm for Diffraction Tomography where $\Delta\epsilon_1$ represents the changes in the impedance of the ground and \mathcal{L} is the operator described in (13.15).

13.3.6 Summary of Results

The results in this case suffered from extreme sensitivity to noise, even after changing the value of λ to try to increase the stability. The problem here seems to be the fact that since the algorithm is a purely mathematical based inversion, it struggles to cope with heavily distorted data. While the algorithm worked well at inverting simulated data (see Figure 92), it struggled with the task of inverting real data.

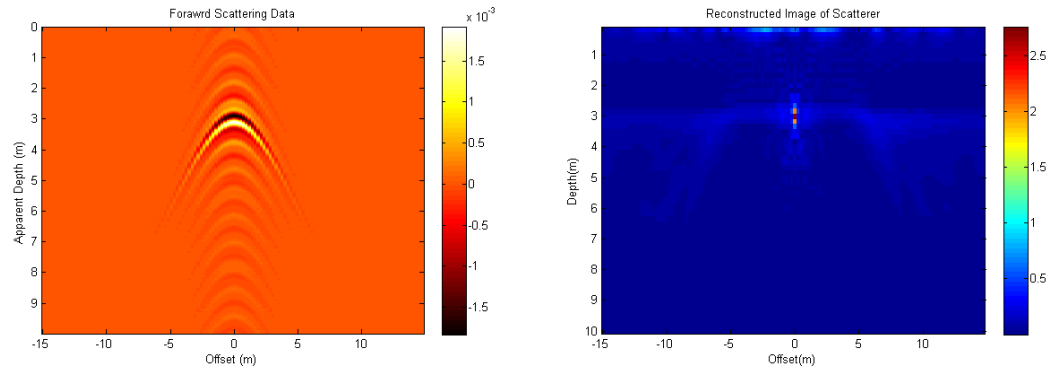


Figure 92: The ‘measured’ data (simulated) of a point scatterer and the result of Diffraction Tomography.

13.3.7 Strengths and Weaknesses

This method employs quite an elegant method in order to generate an inverse scattering algorithm. However, this elegance carries the potential weakness of being unstable (even with the stabilising factor λ) so there is a concern that this algorithm will perform poorly on noisy data, such as a B-Scan.

13.4 A Matched Filter

13.4.1 Introduction and Basic Idea

In a matched filter the idea is to determine the true subsurface location of the target scattering centres by matching the received data with forward scattering models of varying object profiles. The hope is that if we pick an object profile for our forward scattering model that is similar to the object profile for the measured data then we should get very similar scattering patterns. The idea demonstrated here was partially developed from ‘A Matched Filter Based Reverse Time Migration Algorithm for Ground Penetrating Radar Data’ by C.J Leuschen et al. [37].

13.4.2 Method

The algorithm for this method involves generating numerous forward scattering models and matching these to the measured data. These forward scattering models can be based upon expecting hyperbolas of certain curvatures and creating forward scattering data based upon these hyperbolas. Alternatively we can generate forward scattering models

from Maxwell's equation by a finite difference time domain (FDTD) scheme.

$$\epsilon \frac{\partial \mathbf{E}}{\partial t} = \nabla \times \mathbf{H} - \mathbf{J}, \quad (13.20)$$

where $J = J(\omega, \mathbf{r}', \mathbf{r}_t)$ is the forcing term, and

$$\frac{\partial \mathbf{H}}{\partial t} = -\frac{1}{\mu_0} \nabla \times \mathbf{E}, \quad (13.21)$$

where \mathbf{E} is the electric field, \mathbf{H} is the magnetic field, ϵ is the dielectric field strength and μ_0 is the magnetic permittivity of free space. A full explanation is given in Appendix A. Once we have this set of forward scattering models, these can then be used to generate an algorithm for finding targets. If we want to check whether there is a target present at (I, J) (where I represents the I th A-Scan of the B-Scan and J represents the J th reading of that A-Scan) we must find the set of points $S_{I,J} = \{(p, q)\}$ such that we expect a target response at points $\{(p, q)\}$ from a target at (I, J) . This can be found from Maxwell's equation or by expecting hyperbolas of a specific curvature as mentioned in the previous paragraph.

Having found $S_{I,J}$, we now need to find the matrix $Q_{I,J}(i, j)$ such that

$$Q_{I,J}(i, j) = \begin{cases} 1, & \text{if } (i, j) \in S_{I,J}, \\ 0, & \text{otherwise.} \end{cases} \quad (13.22)$$

Now, by considering the element-wise multiplication $T_{I,J} = \sum_{i,j} Q_{I,J}(i, j) \cdot |R(i, j)|$ where $R(i, j)$ is the B-Scan to be tested and $T_{I,J}$ is a measure of how likely it is a target is present at that location. Now we can determine if there is a target at (I, J) by assuming the higher the value of $T_{I,J}$ the more likely it is that there is a target present at that location.

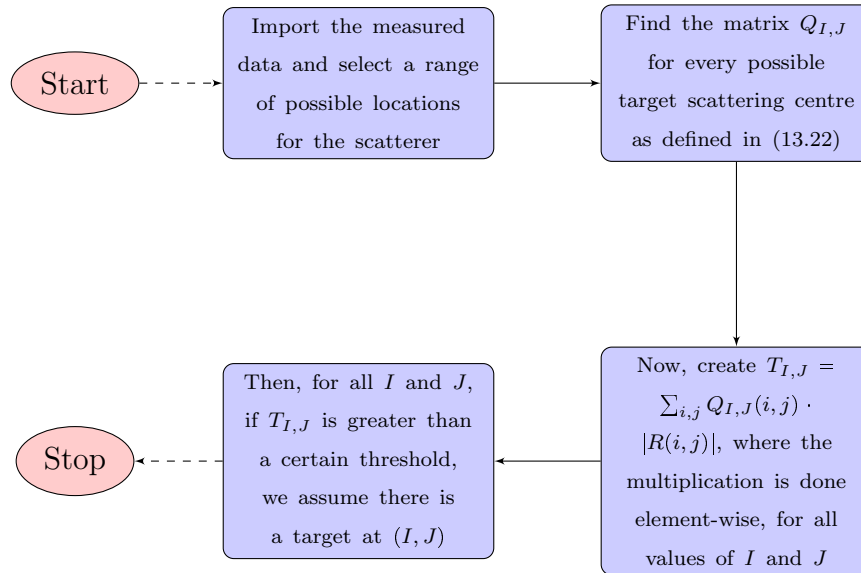


Figure 93: A Matched Filter Algorithm.

13.4.3 Algorithm

The first step is to select a range of possible scatterer locations by looking at the measured data. From here, numerous forward scattering models need to be created as described in the previous section. We then observe the values of $T_{I,J}$, recalling that a high value of $T_{I,J}$ indicates a high likelihood that a target is present at that location. This gives us the algorithm shown in Figure 93.

13.4.4 Strengths and Weaknesses

As can be seen in Figure 94 the measured data used here is very ideal and, while the matched filter did a good job at inverting the data, there is still the bigger question of how well it will perform on real data. One possible concern is that if we have a heavily deformed hyperbola, the algorithm may pick out a result that is vastly different from the true location of the scatterer which would be a major concern. This method is fairly simple, so it should boast strong stability with regard to the effects of noise. However,

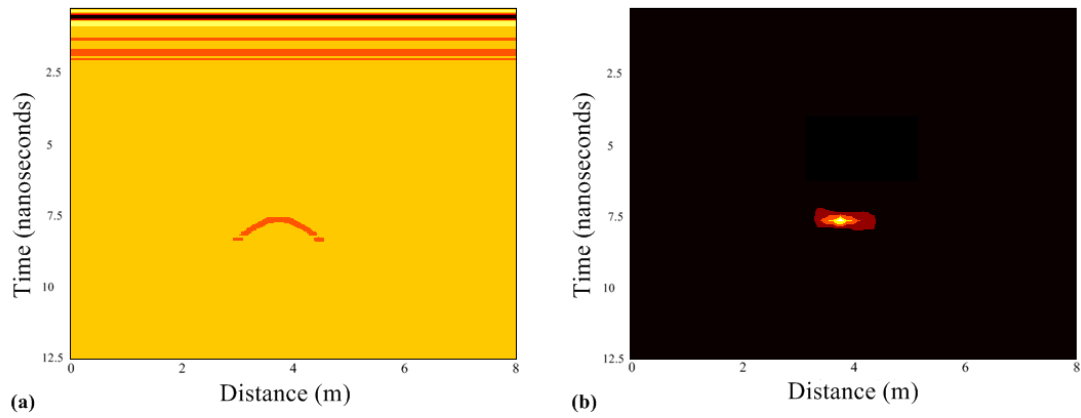


Figure 94: The ‘measured’ data (simulated) of a point scatterer (a) and the result of inverse scattering via a matched filter (b).

it may be computationally intensive as it has to calculate numerous forward scattering models or, alternatively, store a large number of data sets.

13.5 Reverse Time Migration

13.5.1 Introduction and Basic Idea

For reverse time migration, the idea is to take the signal received at the surface and back-propagate the waves to the location from which they originated. The strength of this method is that, in comparison to using a matched filter (§13.4), no assumptions are made in regard to what shape we expect to find. In reverse time migration we simply try and find the location of the buried object which caused the scattering. This method is described in more detail in ‘A Matched-Filter-Based Reverse-Time Migration Algorithm for Ground-Penetrating Radar Data’ by C.J. Leuschen et al. [37]. Here we provide a brief overview of the main techniques used.

13.5.2 Method

The method employed here is based upon the fact that since the GPR signal is sent out with a wide beam width as discussed in §12.2 (producing the well known hyperbola shape), the back-propagated waves also need to be sent back into the ground with a wide beam width in order to converge the diffraction hyperbolas back to something more like the actual target scattering centre as can be seen in Figure 95. The end result of this will be all the rays converging on the location of the scatterer.

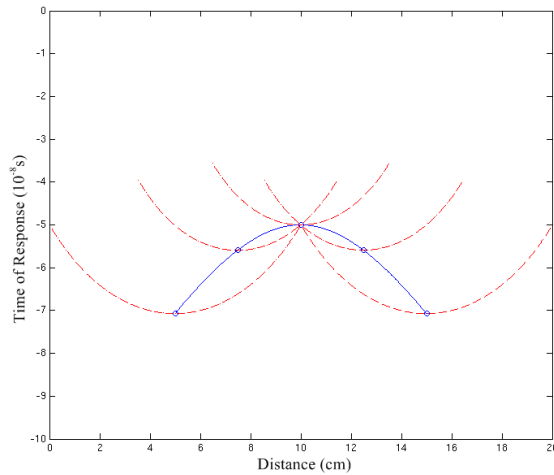


Figure 95: An example of how reverse time migration works. The red dashed lines represent possible origins for a signal response at that location. Note how all red dashed lines meet at the peak of the hyperbola which is the location of a point scatterer $(10, -5)$.

13.5.3 Algorithm

Having observed the basic example in Figure 95 the next step is to build an algorithm to perform reverse time migration for an entire B-Scan. To accomplish this, the first thing we do is separate the data into horizontal strips of constant time (i.e. the data from the same timestep from all the A-Scans in the B-Scan to be investigated). Then we insert the data received last (corresponding to the deepest) into a reverse time migration map where

we propagate them backwards in time. This involves imitating the effect of the wide beam width (spreading the signal out in an arc) for the duration of time between the strips of data, which has to be found experimentally.

After one strip of data has been inserted into the RTM map and propagated back in time, we then go to the next deepest strip and repeat (insert each strip into the map and propagate the map backwards in time for the duration of time between the strips of data). We continue doing this until we insert and propagate the final (shallowest) strip of data. Once we have done this, then the reverse time migration map will hopefully approximate the data at time $t = 0$ and, as such, the RTM map should now contain the true location of the target scattering centres ready to be analysed. The algorithm used to accomplish this is described in Figure 96

13.5.4 Summary of Results

The results for reverse time migration is shown in Figure 97 and uses the same simulated forward scattering data as was used for ‘A Matched Filter’ (§13.4). As can be seen, the reverse time migration algorithm identifies the location of the scatterer effectively. It is also hoped that this will be a fairly robust algorithm and should not suffer from many problems when faced with real data. Also worth mentioning is that, since this algorithm does not require us to generate any forward scattering models, it is considerably faster than using a matched filter.

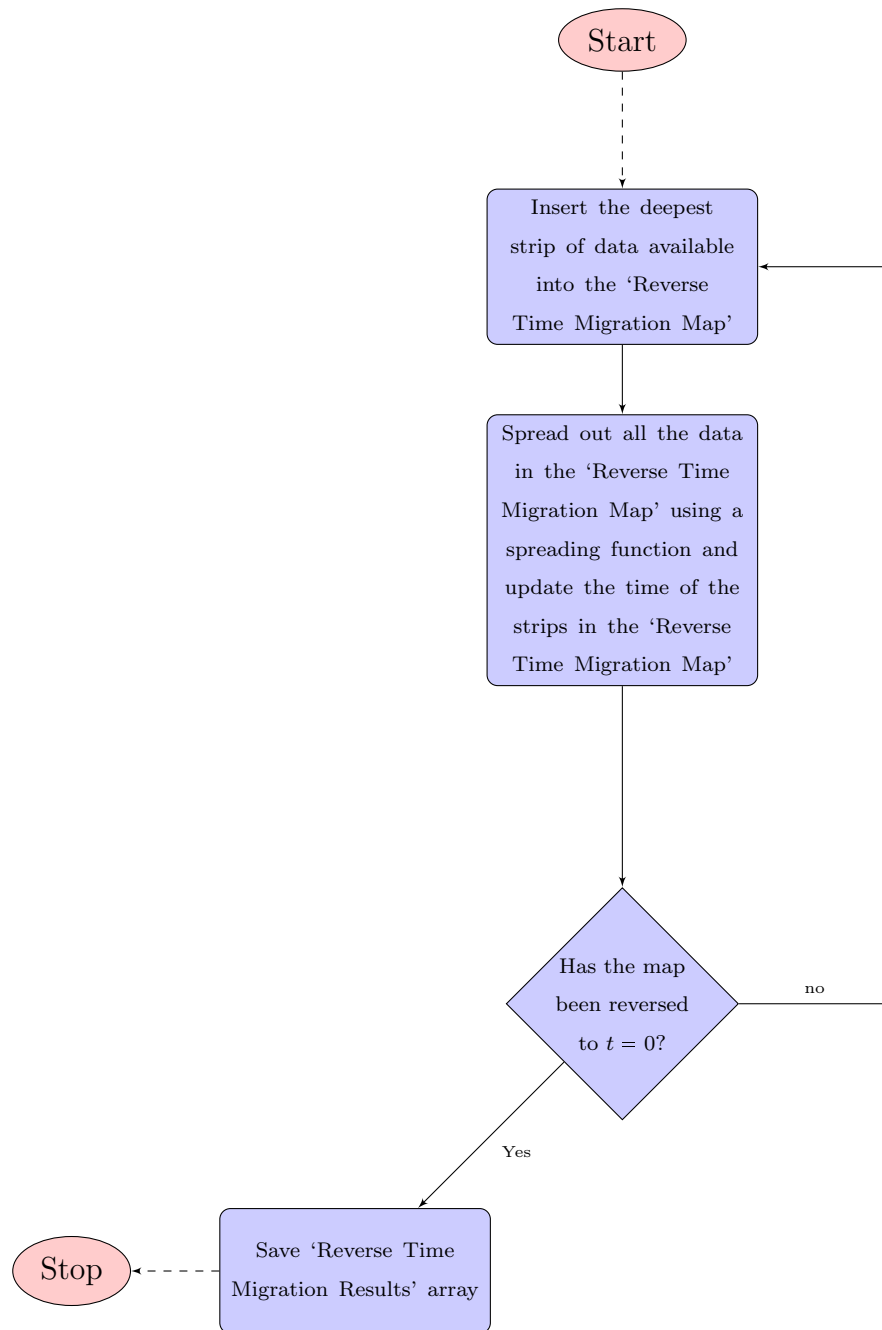


Figure 96: The Reverse Time Migration Algorithm.

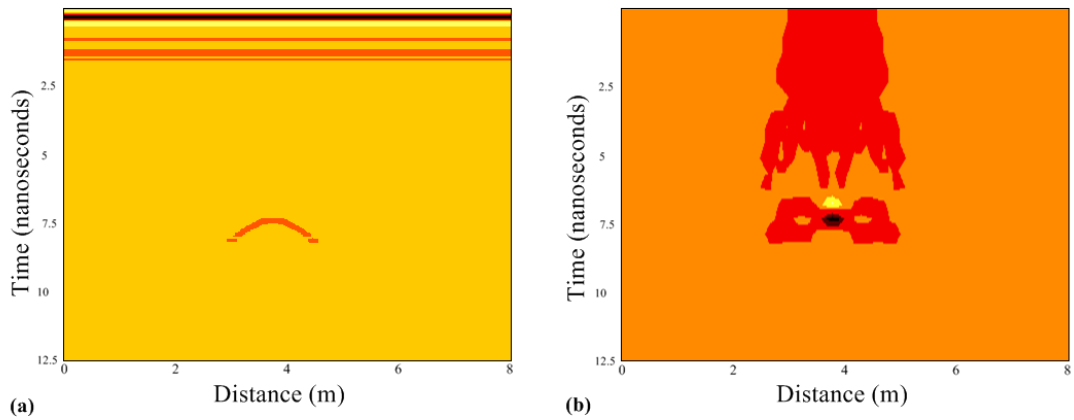


Figure 97: The ‘measured’ data (simulated) of a point scatterer (a) and the result of reverse time migration (b). Note, the result of reverse time migration has a lot of low level background noise. However, this is an order of magnitude smaller than the two ‘dots’ at around 7.5 nanoseconds.

13.5.5 Strengths and Weaknesses

Again this method boasts simplicity which will give it strong stability with regard to noise. Also, it is hoped that this method will not be too computationally intensive. This method also has the advantage over ‘A Matched Filter’ of making no assumptions about the shape of objects we expect to find.

13.6 Summary of Methods

All of these methods will go some way to improving the target detection rates of the B-Scans. Due to the nature of GPR data, the key thing to be considered is ensuring that the method can cope with noisy, fluctuating data. Also, the nature of landmine detection means that a false negative is much more problematic than a false positive, hence any method should have robustness at the heart of it to try and avoid any false negatives. Considering all of this, the first method to be discarded was feature extraction due to the suspected issues regarding its robustness. For similar reasons linear GPR inversion was

also discarded. Blind deconvolution seems infeasible for GPR data as we do not have a suitable constraint to place on the transfer function and regular deconvolution has the problem of accurately finding the transfer function before we can deconvolve any signals. This, along with the fact that the transfer function might change subtly throughout a B-Scan, led to deconvolution being discarded.

The remaining two methods, the matched filter and reverse time migration, both seem to offer good stability and may offer good improvements to the target detection rates. Looking at the these two methods' limitations, no clear weakness could be seen with reverse time migration, whereas for a matched filter we have to make assumptions about what shape we are trying to find. This, along with the fact that generating numerous forward scattering models is a computationally intensive process, meant that reverse time migration was the algorithm chosen to be investigated further.

14 Reverse Time Migration - A Multiple Migration and Stacking Algorithm

14.1 Aims

Having decided to look further into reverse time migration it made sense to come up with a specific list of objectives with which to test the effectiveness of any algorithm developed. The purpose of this is so we can see how much an improvement performing reverse time migration offers and, hence the following objectives were set:

- Collect numerous data sets to get reliable results on how well reverse time migration performs on real data,
- Observe how well the algorithm performs to see if there are any improvements which need to be made,
- Develop an independent algorithm to perform target detection, which when given a B-Scan attempts to highlight all the possible target locations, to impartially test what improvement the reverse time migration algorithm offers on improving the target detection rate.

14.2 Full Reverse Time Migration

As was described in §13.5, we need to propagate strips of data of the same depth back into the ground and spreading them back to their original spatial location (corresponding to $t = 0$). The relation between time and depth has been found experimentally to be

depth(m) = $\frac{1}{2} \cdot \text{time(s)} \cdot 10^8$ (e.g. 10 nanoseconds correspond to 50cm deep). Then, we collect all the time-reversed data together and use that image as our final reverse time migrated image.

The main problem with this algorithm was the fact it was very computationally intensive due to having to split up the data into strips corresponding to the same timestep and propagating them into the ground individually. To combat this problem, larger strips of around ten timesteps were sent into the ground at once. This produces notably faster results and showed good results for the shallower targets as is shown in Figure 98 (b). However, for deeper targets small discontinuities were observed between the strips of data (most notable at around 7.5m from 8 nanoseconds onwards in Figure 98 (b)) which unfortunately reduced the clarity of the image.

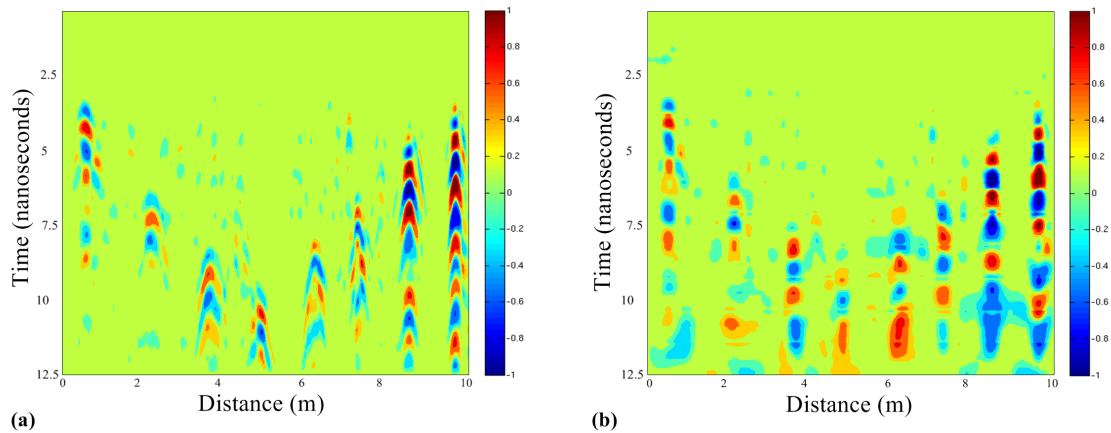


Figure 98: An image to show the B-Scan (a) and the results of the full reverse time migration (b).

14.3 Plain Migration

Looking at the algorithm in Figure 96, the most computationally demanding part is where we need to perform repeated spreading on the data. From here, the most basic case was considered where we group the whole B-Scan together as one strip of data. In this method

there is no ‘reverse time’ idea, so it is simply referred to as ‘Plain Migration’.

This approach considerably simplifies the algorithm, allowing it to be performed much quicker. Also, the issue of small discontinuities between strips of data is no longer a problem, neither is there an issue of the deeper strips being weaker than shallower strips. The results of this algorithm are presented in Figure 99 and, as can be seen, there is a clear improvement to the clarity of the scan upon performing the migration.

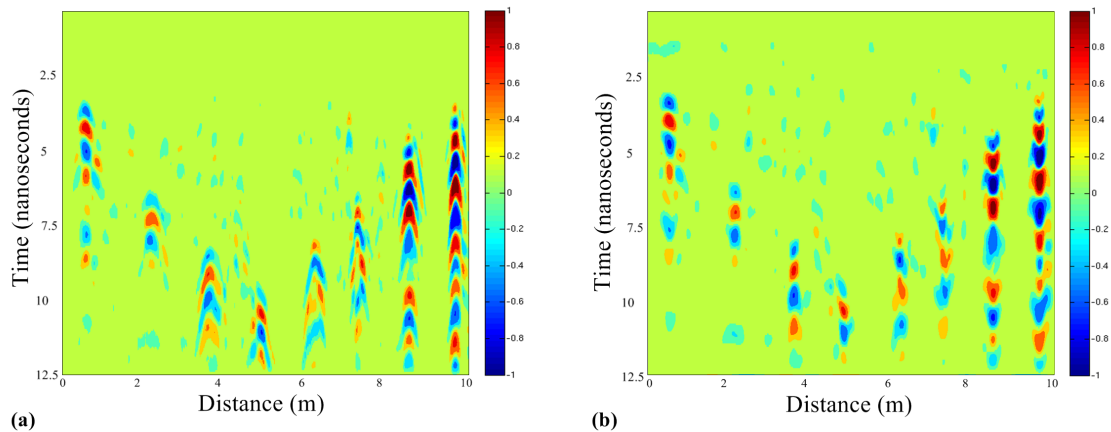


Figure 99: An image to show the B-Scan (a) and the results of the plain migration (b).

14.4 Full Reverse Time Migration versus Plain Migration

Having developed algorithms for both full reverse time migration and plain migration, the next step is to decide which algorithm performs the best and is to be investigated further. For shallower and mid-range targets, full reverse time migration seems to produce marginally better results. However, for the deeper targets plain migration produces significantly better results. This can be seen in Figure 100 where the migrated images from Figures 98 and 99 are presented side-by-side. This, combined with the fact that the plain migration method is by far the faster of the two methods, means that plain migration will be used to test how well the algorithm performs on numerous data sets with different

ground conditions.

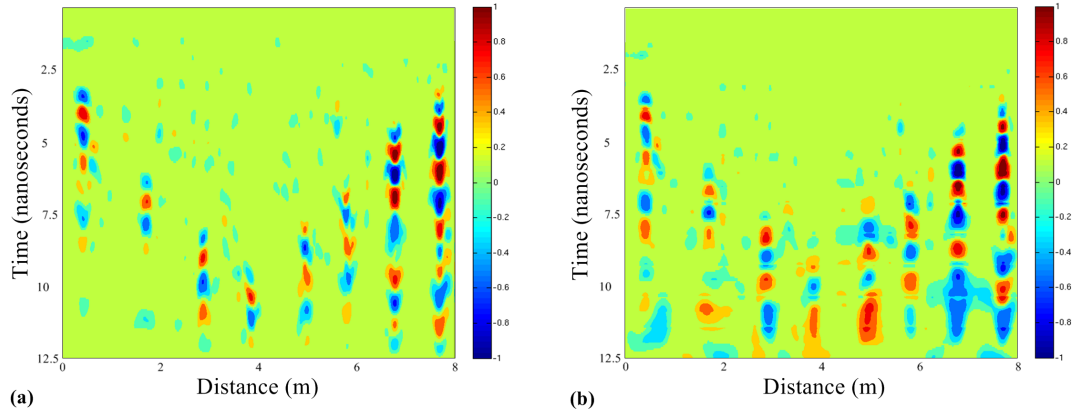


Figure 100: A comparison between plain migration (a) and full reverse time migration (b).

14.5 Mathematical Modelling

Having decided to pursue the idea of using plain migration, we will now formally develop the algorithm used. Following this, we will test the algorithm on numerous data sets in different ground conditions and develop a target detection algorithm to quantify the improvement offered by the migration algorithm.

For each B-Scan we expect to find hyperbolas with an unknown curvature in a region which also contains a significant amount of noise and clutter. This technique aims to detect hyperbolas of any curvature within a reasonable range and highlight them for the user.

Recall that due to the wide beam width, signals are received from a variety of locations other than directly above a target. We assume a beam width of θ , as illustrated in Figure 87 (the GPR device which produced the scans used in this paper had a value of $\theta \approx 45^\circ$). It can be seen that by looking at a single A-Scan, there are a wide range of possible

locations for a signal response to originate from, also illustrated in Figure 87. A result of this is that multiple signal responses exist will from the same target in a B-Scan. We aim to correlate these signal responses in order to find the target's actual location.

Consider a sequence of A-Scans corresponding to the horizontal positions x_I , where $I = 1, \dots, N$, equivalent to a B-Scan. For each of these A-Scans, a response of amplitude $R_{I,J}$ is recorded corresponding to a propagation distance z_J , where $J = 1, \dots, M$. We consider a buried object at (x_a, z_b) and we expect to receive a signal response from the object at (x_i, z_j) , where z_j is the distance from the detector $(x_i, 0)$ to the buried object (x_a, z_b) , provided the beam width is wide enough. From here we wish to converge the set of points in a B-Scan, which belong to a single object, back into a point-like object which will allow us to see the target's location. In order to do this, we need to find the set of points, $S_{I,J} = \{(x_i, z_j)\}$, satisfying

$$(x_i - x_I)^2 + z_j^2 = z_J^2 \pm \delta \quad \text{and} \quad \left| \frac{(x_i - x_I)}{z_J} \right| \leq \beta, \quad (14.1)$$

where $S_{I,J}$ represents the set of points we would expect to receive a target response at from a target at (I, J) and $\beta = \tan \theta$ and δ is the smallest correction term to ensure that $i \in \{1, \dots, N\}$ and $j \in \{1, \dots, M\}$. We need to find $S_{I,J}$ for all I and J (i.e. the whole B-Scan). Now, given a new point (x_p, z_q) , we create the set $T_{p,q}$, which is defined as

$$T_{p,q} = \{(I, J) \text{ such that } (x_p, z_q) \in S_{I,J}\}, \quad (14.2)$$

which represents all the points a target responds at (p, q) could have originated from. Finally

we define the migrated point $\hat{R}_{p,q}$ as

$$\hat{R}_{p,q} = \sum_{I,J \in T_{p,q}} R_{I,J}, \quad (14.3)$$

which is sum of all the points where a signal response could be generated from an object at (x_p, z_q) . Now the migration map, $\hat{R}_{I,J}$ for $I = 1, \dots, N$ and $J = 1, \dots, M$, can be generated for the entire B-Scan which will allow better object definition for the purpose of finding targets. This method is similar to that presented in Figure 95 where the red dashed lines represent $\hat{R}_{p,q}$ for various values of p and q .

14.6 Real Data Modelling

The formulation of the previous section is based upon horizontal and vertical distances, whereas the data presented in a B-Scan consists of a sequence of A-Scans. This means that for the previous section, where we worked in the (x, z) domain, the angle with which the rays spread out from the GPR detector (the beam width), was fixed. However, a B-Scan is a sequence of A-Scans, where the data is gathered at a set frequency, not related to the speed of the detector. As such, changes in the velocity cause apparent changes in the angle with which the rays have been sent out from the detector (even though the beam width is constant) when viewing the data in the (x, t) domain. For example, if the GPR device moves at twice the speed, then the angle with which the rays are sent out will appear to halve. In this section, we assume that the GPR detector moves at a constant velocity, which is an appropriate approximation as we would expect a roughly constant velocity in each individual B-Scan.

Another key difference from the previous section is that the A-Scans measure responses

that arrive at the GPR detector in fixed time-steps rather than fixed distances. In order to combat this, we make the assumption that the propagation velocity through the ground is constant, hence we can assume there is a linear relation between time, t_J , of the signal response and the depth of the target response, z_J . This is not strictly true due to changes in soil type as a function of depth and lateral distance, as well as the varying water content of the ground, again as a function of depth and lateral distance, and objects in the ground. These all affect the propagation velocity, however we consider this to be an acceptable assumption for the local region associated with an individual hyperbola. The relation between t_J and z_J is given by $z_J = \hat{c}t_J/2$ where \hat{c} is the propagation velocity of the radar waves through the ground.

In order to use the formulation of migration from the previous section we need to find expressions for the horizontal and vertical distances. We have that $z_j = j\hat{c}\Delta t/2$ and $x_i = i\Delta x$, where Δx and Δt are the step sizes in x and t respectively, i is the i th A-Scan and j is the j th signal response from an A-Scan. Note, Δx is taken as a constant, corresponding to a uniform velocity of the detector, but the algorithm allows for fluctuations as will be described later. Because of this change, we need to express (14.1) in terms of the new notation and now we need to find the set of points $S_{I,J}^\alpha = \{(x_i, z_j)\}$ satisfying

$$\frac{1}{\alpha^2}(i - I)^2 + j^2 = J^2 \pm \delta \quad \text{and} \quad \left| \frac{(i - I)}{J} \right| \leq \alpha\beta, \quad (14.4)$$

where $\alpha = \hat{c}\Delta t/2\Delta x$ and will now be referred to as the spreading factor. Now, (14.2) remains the same giving the set $T_{p,q}^\alpha$, defined as

$$T_{p,q}^\alpha = \{(I, J) \text{ such that } (x_p, z_q) \in S_{I,J}^\alpha\}. \quad (14.5)$$

Again we define the migrated point $\hat{R}_{p,q}^\alpha$ as

$$\hat{R}_{p,q}^\alpha = \sum_{I,J \in T_{p,q}^\alpha} R_{I,J}, \quad (14.6)$$

This leads to the migration map $\hat{R}_{I,J}^\alpha$ for the whole B-Scan with spreading factor α .

In order for this method to work we need to find the value for $\alpha = \hat{c}\Delta t/2\Delta x$. In this report the B-Scans have been generated using a MINEHOUND landmine detector developed by Cobham Technical Services with a bandwidth of approximately 500MHz to 2,500MHz. With this GPR device, Δt (the sampling time) was 50ps and the propagation velocity \hat{c} is given by $\hat{c} = c/\sqrt{\epsilon}$, where c is the speed of light in a vacuum and ϵ is the ground's relative dielectric constant. An appropriate value of ϵ for most ground types can be found to be $\epsilon \approx 6.25$, which results in $\hat{c} \approx 1.2 \times 10^8 \text{ms}^{-1}$. The step sizes in x , Δx , can be calculated by considering the data acquisition frequency (DAF). The MINEHOUND detector has a DAF of 62.5Hz. Δx can be calculated as $\Delta x = \text{Velocity}/\text{DAF}$. If we assume the average velocity of the detector to be 0.5ms^{-1} this gives $\Delta x = 0.008 \text{m}$. Combining all this together gives $\alpha = 0.375$.

Adopting a fixed value of α can lead to problems due to the fact that both the propagation velocity, \hat{c} , and the speed with which the GPR device is moved are subject to variations which make any fixed estimate of α unreliable. The propagation velocity varies with changes in the ground type and the moisture content of the ground. The speed with which the GPR device is moved depends on the operator, and while you would expect an approximately constant velocity from the same operator, there will be some fluctuations. However, any change to the curvature of the hyperbolas we are trying to resolve can be accounted for by a change to α . Typically, in a single B-Scan, multiple spreading factors will

be needed to resolve every target back into something resembling a point source. This can be seen in Figure 101 where we attempt to migrate eight AT mines, presented in the layout described in Figure 104, back into point-like sources using various spreading factors and, as can be seen, no single spreading factor migrates all targets back into point-like sources. In Figure 101, the four mines on the left are metal TMM-1 (Tenkovska Mina Metalna-1) AT landmines, whereas the four on the right are minimum metal TMA-2 (Tenkovska Mina Antimagnetna-2) AT landmines. The multiple reflections in the minimum metal mines can be explained due to the GPR waves entering the mine and reflecting internally inside the mine before returning to surface, hence causing the resonance effect. This is not possible with the metal mines as they act as a Faraday cage and, as such, allow no energy inside the mine.

To try and deal with this problem of ensuring we have the correct spreading factor to successfully migrate the hyperbolas back into point sources, various techniques were investigated. One idea was to create a metric in order to determine the correct spreading factor. The normalised metrics look for various features which are hoped to represent a correctly focused image and are presented in Figure 102 of a single target from the migrated B-Scans presented in Figure 101.

All the metrics work on similar principles, where by we hope to find a small number of strong responses as opposed to a large number of weak responses. For example ‘top10%’ measures the sum of the highest 10% values in the data set in the hope that a correctly migrated data set will have a few very strong responses corresponding to the targets, whereas an incorrectly focused image will have a larger number of fairly strong responses and will hopefully get a lower score on this metric. Also, we can apply a basic thresholding algorithm to reduce the B-Scan into a number of distinct blobs which will hopefully

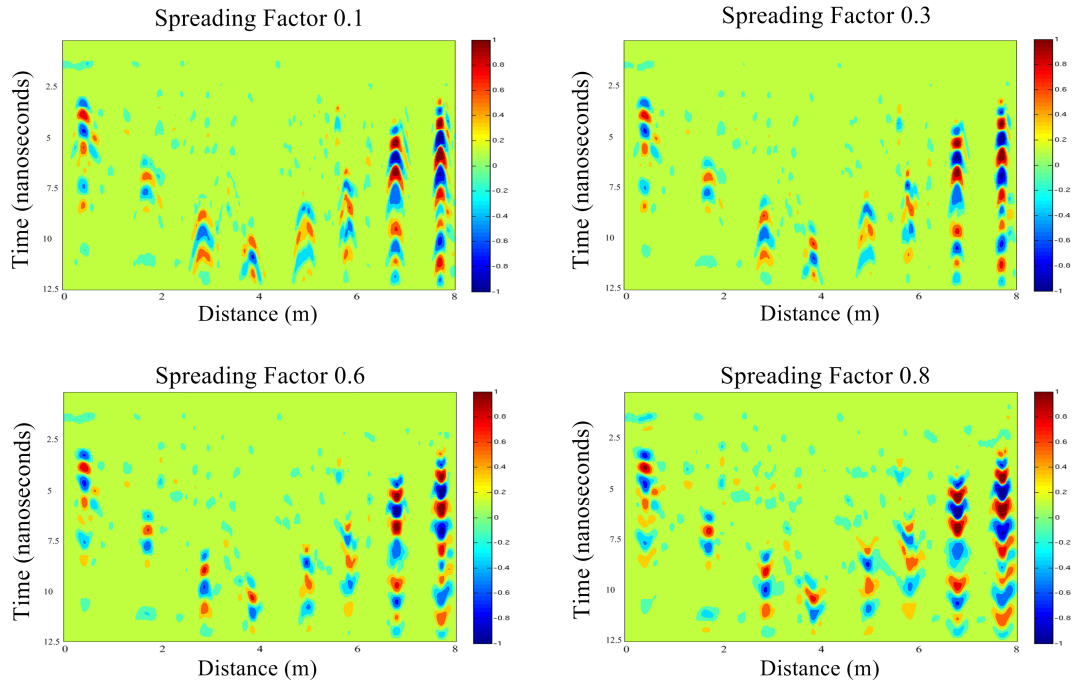


Figure 101: Four images of the same migrated B-Scan showing the importance of using the correct spreading factor.

represent the targets. We can use the size of these blobs as a metric, assuming that smaller blobs represent more focused targets. We can also consider the number of blobs as a metric as well. Another possible metric is to consider the shapes of these blobs, where we hope that a focused B-Scan will have circular targets. In Figure 102 this is represented in ‘circleness’.

As can be seen, the metrics do not seem to agree on which spreading factor is the most appropriate. So a lot of further work will be needed in order to develop a conclusive and accurate metric. A flaw in this method is the fact that in order to determine the correct spreading factor you need to know where the target is. One possible way to circumvent this problem would be to run a target detection algorithm first and then run the function to determine the correct spreading factor. However, the problem of this is that it will a lot easier to detect where a target is after the spreading factor has been performed and it is impossible to apply the correct spreading factor until the target has been detected.

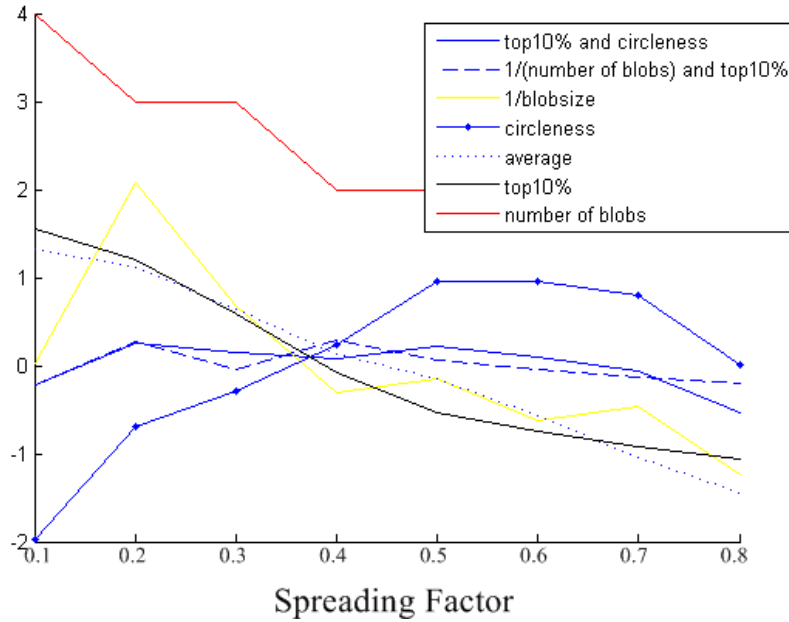


Figure 102: Various metrics for a target. Note, all results have been standardised.

Rather than be faced with the difficult problem of finding the optimal spreading factor, an alternative idea is to superimpose all the images together from Figure 101. This results in an image where we have a strong response from the targets' locations due to the fact there is a signal response at this location in all of the images. Conversely, any signal responses caused by the hyperbolic scattering or an incorrect spreading factor will only appear in one or two images and as such will not show up strongly in the overlaid image. Mathematically we can represent this as

$$\tilde{R}_{I,J} = \sum_{\gamma=1}^r \hat{R}_{I,J}^{\alpha} \Big|_{\alpha=\frac{\gamma}{10}} \quad (14.7)$$

where $r = 8$ has been used corresponding to spreading factors of $\alpha = 0.1, 0.2, \dots, 0.8$. However, this may need to be changed according to the type of equipment, the velocity of the detector and the ground conditions. The result of this overlay is presented in Figure 103. It is important to note that a 33% change in the spreading factor (from changes of velocity or ground conditions) makes a minimal difference to the final image. It may be

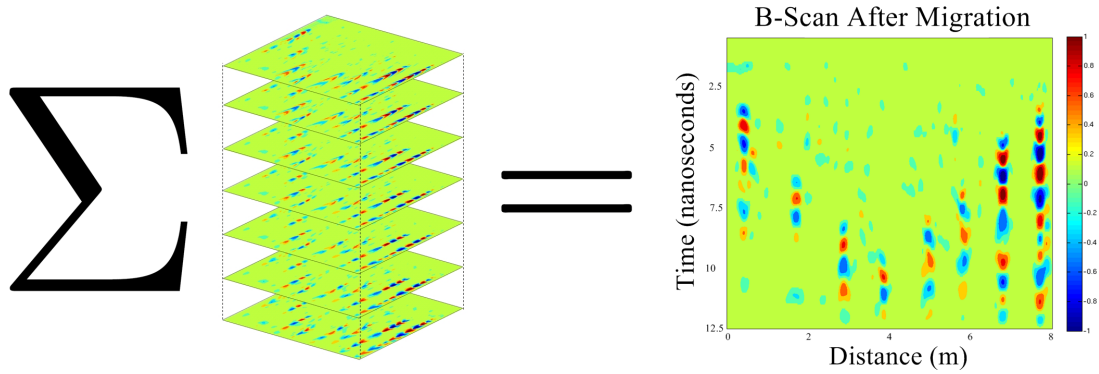


Figure 103: An example of how overlaying the images from Figure 101 with various spreading factors works. Note how the diffraction effects visible in Figure 101 can no longer be seen.

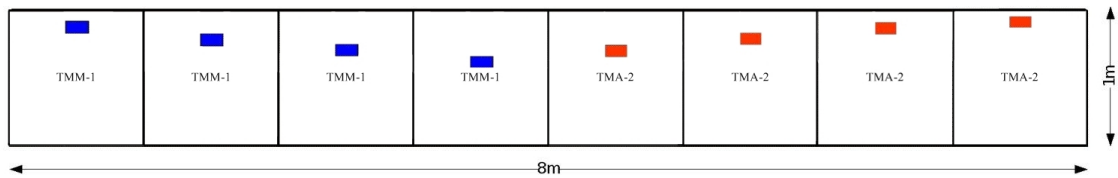


Figure 104: The layout of the mines from left to right as shown in Figures 101, 103 and 106

possible to implement an adaptive algorithm that alters r based on the data however this is beyond the current scope of the research.

14.7 The Algorithm

In practical terms, the algorithm used is based on a simplistic version of the algorithm described in Figure 96. It was found that the fastest way to perform the migration with a single spreading factor was to simply apply a spreading factor to the whole B-Scan as shown in Figure 105. Here we take each A-Scan (the column on the left hand side of Figure 105) and spread the points into neighbouring A-Scans according to the spreading factor (represented in the right hand side of Figure 105). When you consider this method for an entire B-Scan, it is equivalent to the method described above in §14.6, but can be implemented a lot faster. This can then be performed multiple times for different

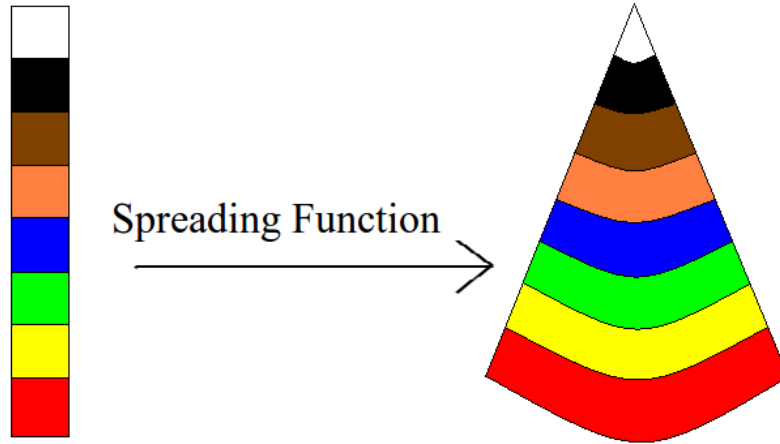


Figure 105: An illustration of how the algorithm for this method works.

spreading factors before we overlay all the images together to give us our final image as shown in Figure 103.

The end result of the migration is similar to what could be achieved using a Hough transform designed to detect hyperbolas of a specific curvature. The Hough transform (HT) [29] and generalized Hough transform (GHT) [4], are basic feature extraction techniques used to find imperfect instances of a certain class of shapes. Typically the GHT is used for detecting basic shapes such as lines or circles [31], although more complicated shapes can also be considered [56], such as hyperbolas.

15 Statistical Testing

15.1 Introduction

In order to impartially test how well the multiple migration and stacking algorithm performs, this section will show the results of testing this method on numerous data sets. The test site where these measurements were taken was prepared by burying replica mines in various ground types. These are genuine TMM-1 and TMA-2 mines with the explosives removed and replaced with an inert material with similar dielectric properties as the explosive. Three test sites were prepared with either mines laid in ballast, a mixture of sand and shingle or Ministry of Transport grade crushed concrete (MOT). Therefore, each ground type offering slightly different conditions such as subsurface anomalies and propagation characteristics. It is worth noting that rocks and boulders do not pose much of a problem causing false alarms as they have much smaller radar scattering cross sections and vastly different internal structures. The results have been gathered with the TMM-1 and TMA-2 mines laid in the configuration described in Figure 104 in each of the three ground types to test how well the algorithm copes with varying conditions.

Each of the three test sites contained eight AT mines laid in the configuration described in Figure 104. The data set consisted of 66 B-Scans following a pre-determined path directly above the mines with 22 B-Scans from each ground type, resulting in a total of 528 AT mines. All the results were obtained by the same operator and half of the data was collected a day after a substantial rainfall, while the other half was collected after a prolonged dry spell. The target detection algorithm was then used in order to measure the effect of the multiple migration and stacking algorithm against not using the algorithm

for the same data sets.

15.2 Norm of each A-Scan

A simple method of target detection is to consider the norm squared for each A-Scan which is denoted by $\|\mathbf{R}_i\|^2$, where $\mathbf{R}_i = \{R_{i,1} \dots R_{i,M}\}$ represent the i th A-Scan and is given by

$$\|\mathbf{R}_i\|^2 = \sum_{j=1}^M (R_{i,j})^2. \quad (15.1)$$

This can be quickly calculated for the entire B-Scan and from there we assume that the higher the norm squared, the more likely it is that a target is present at that location.

Upon inspecting the norm squared it became clear low level background noise was providing mild interference. In order to reduce this background noise, thresholding was introduced to the B-Scan based upon a test section of ground with no mines present, which was performed on both the original and migrated data sets. However, it is worth mentioning that this step is optional and has been mainly introduced in order to improve the clarity of the results. The results from applying the thresholding first and then calculating the energy in each A-Scan are shown in Figure 106. As can be seen from Figure 106 the effect of migration is to increase the energy from a target and reduce the distance over which the energy is spread over, both consistent with what was expected from the algorithm. A further effect is that the migration algorithm will only pick out and highlight objects that are hyperbola shaped. Any artefacts without this key shape are reduced into the level of the background noise which leads to a reduction in the false alarm rate.

With the energy of each A-Scan extracted we can now quantify how much of an im-

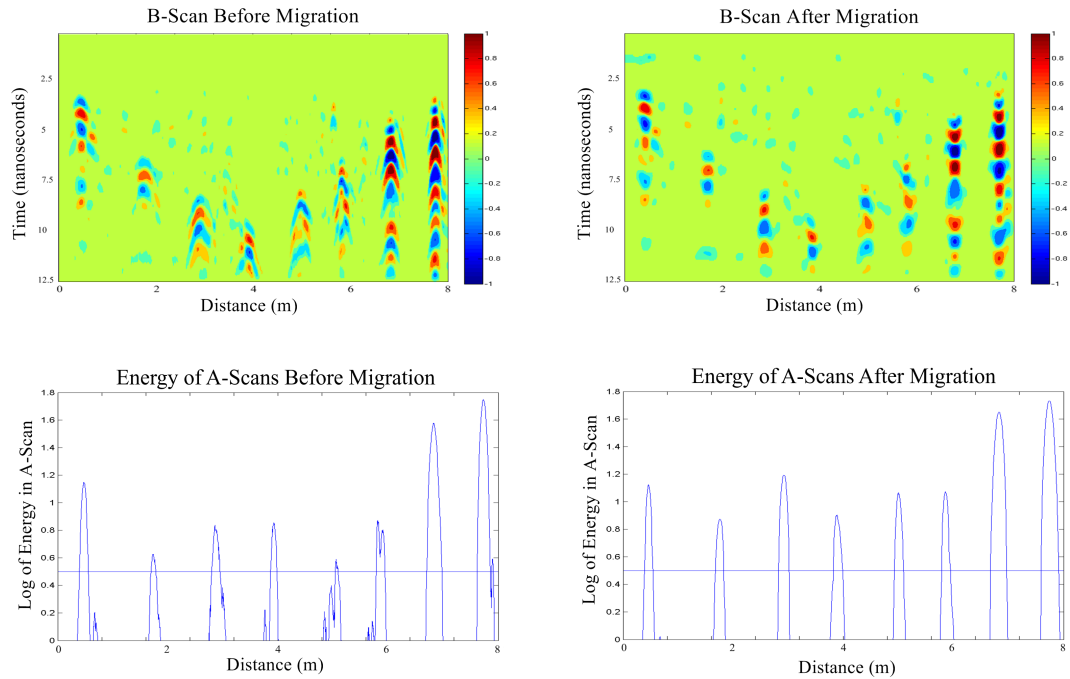


Figure 106: The energy of each A-Scan in a B-Scan showing the effect of performing migration with an energy cut-off.

provement performing migration offers in terms of locating potential targets. This is accomplished by setting a cut-off value where any peaks over this value are classified as a target, as seen in Figure 106 where a cut-off value has been included of $\frac{1}{2}$. By varying this cut-off value we can compare the results from performing and not performing migration. Arbitrary cut-off values have been used as all the data sets have been normalised. If a peak of energy is within a window predefined to be the location of a target from knowledge of the mine locations, then it is regarded as a successful detection. However, if the peak is outside this predefined window then it is regarded as a false alarm.

15.3 Target Recognition

Target recognition is where we attempt to find regions of the B-Scan which have the characteristics resembling a target. This is done by considering a region of a certain size and if the region contains both a positive and negative value above the set threshold then

we designate that region as a target. Having used the target recognition algorithm to find these regions, we then correlate their location with the library containing the target locations and mark the regions accordingly. The results of this method are shown in Figure 107. Again we run numerous data sets through this target detection algorithm and we can vary the threshold required before a region is clarified as a target in order to compare the effect of performing and not performing migration.

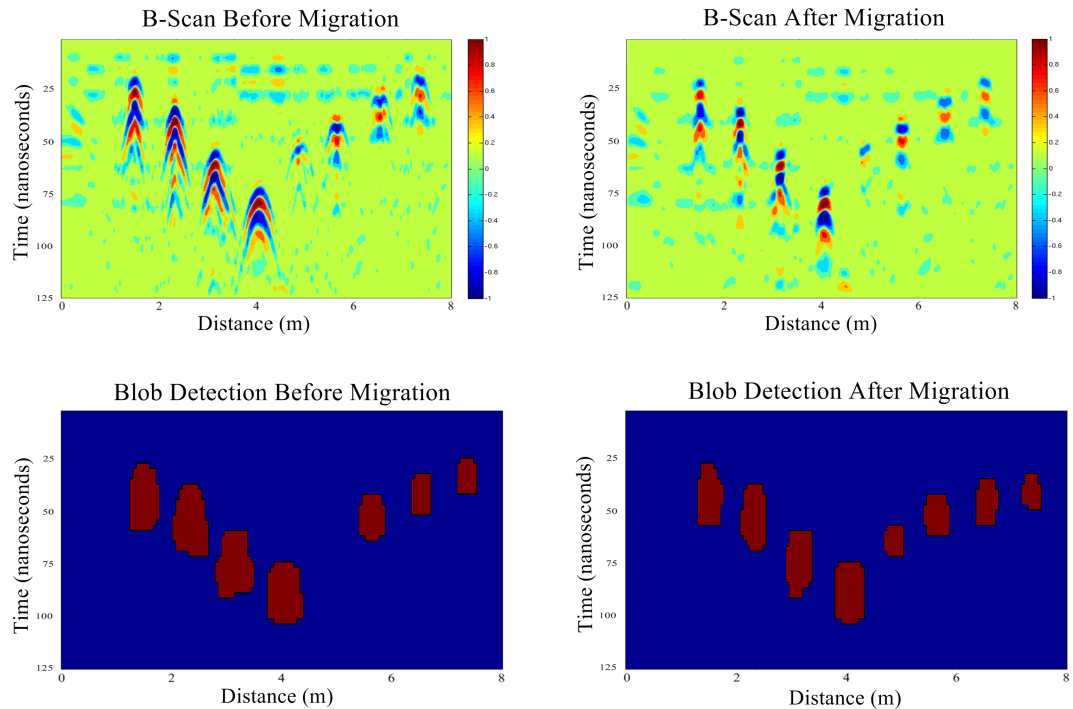


Figure 107: Target recognition performed on a B-Scan before and after migration.

15.4 Results

Having now developed two target detection methods, we now present the results to see what effect performing the multiple migration and stacking algorithm has on a B-Scan. The results of trying to detect the 528 AT mines are shown in Figures 108 and 109 for the norm of each A-Scan and target recognition respectively. For the norm of an A-Scan, we vary the cut-off to generate the table of results as shown in Figure 106. For target

recognition, we vary the threshold needed for a region to be designated as a target. This variation is done by considering how many standard deviations of difference there are from a sample piece of ground with no targets present. From looking at Figures 108 and 109, it

Cutoff Value	Without Migration		With Migration	
	Number Detected	False Alarms	Number Detected	False Alarms
0.001	528	100	528	47
0.1	528	91	528	44
0.2	528	78	527	34
0.3	528	63	521	25
0.4	527	54	514	22
0.5	516	34	509	16
0.6	505	29	502	10
0.7	477	16	488	6
0.8	440	6	459	4
0.9	403	4	433	1
1	352	4	381	1
1.1	303	3	313	0
1.2	246	2	240	0
1.3	161	1	181	0
1.4	64	0	124	0
1.5	31	0	47	0

Figure 108: The table of results for the norm of each A-Scan.

Standard Deviations of Difference from Background Average	Without Migration		With Migration	
	Number Detected	False Alarms	Number Detected	False Alarms
0.5	528	251	528	308
1	526	138	527	197
1.5	523	74	527	110
2	511	39	525	48
2.5	466	29	513	24
3	395	17	450	13
3.5	308	11	367	3
4	267	5	291	1
4.5	220	2	229	0
5	175	1	199	0

Figure 109: The table of results for target recognition.

can be seen that both methods offer a clear improvement upon performing the migration. For example, considering Figure 109 it can be seen that without migration we detected 523 out of the 528 targets with 74 false alarms. Whereas with the migration algorithm we detected 525 targets with only 48 false alarms. A similar result can be obtained from Figure 108. Hence, we can say that the multiple migration and stacking algorithm does

indeed improve the target detection rates for landmine detection.

16 Conclusion

16.1 Summary

In this chapter, numerous methods of improving target detection rate for ground penetrating radar were considered and algorithms implemented for the most promising algorithms. In the end a multiple migration and stacking algorithm based upon the idea of reverse time migration was developed with the aim of eliminating the diffraction effects present in GPR images. If we consider the norm of the A-Scans, then the multiple migration and stacking algorithm increased the probability of detection of AT landmines at a false alarm rate of 0.01 from a probability of detection of 0.6 to 0.85 with similar results from using target recognition. This demonstrates a substantial improvement from using the multiple migration and scattering algorithm. The aim of this technique is to eliminate the hyperbolic scattering present when detecting landmines in GPR images for a range of different ground conditions. The key feature of this new approach is the stacking technique which reduces the effect of fluctuations of the ground conditions and in the movement of the detector operator. This method was tested on real data to observe the effectiveness of this technique at improving the target detection rate.

16.2 Future Work

16.2.1 Short Time Fourier Transforms

Short time Fourier transforms (as discussed in §13.2) offers a time-frequency representation of the GPR signal. By using a short time Fourier transform certain differences

between targets and clutter can be observed as is demonstrated in ‘Scattering analysis using fractional Fourier with applications in mine detection’ by I.I.Jouny [34]. By using this in conjunction with the multiple migration and stacking algorithm it is hoped that some of the false positives can be eliminated.

16.2.2 Anti-Personnel Mines

One of the most important regions of future research is extending the multiple migration and stacking algorithm to anti-personnel (AP) mines as so far all the test data has been on anti-tank mines. The main differences between AP and AT mines are that AP mines are often a lot smaller and buried a lot shallower. As a result of this the signal received from these targets will often be weaker than their AT counterparts and in the case of surface laid AP mines the signal will be mixed in with the surface reflection. These differences may mean that certain changes need to be implemented in order to maintain a high probability of detection and a low false alarm rate.

16.2.3 C-Scans

A further idea is to generalise the idea of reverse time migration to a 3-D C-Scan. A C-Scan is generated from a sequence of B-Scans strung together of adjacent lines in the same way a B-Scan is adjacent A-Scans strung together. This will result in having to find the possible location of a signal response in an extra dimension which will add a new level of complexity. This will hopefully give significantly more information to the user and improve target detection rates as we will now be able to look at a 3-D representation of the object rather than being limited to a 2-D representation of the object as is the case

with B-Scans.

16.2.4 Oblique Targets

One particular concern in the field of mine detection are oblique targets which, when detected using GPR, can give a false target scattering centre due to the way the rays travel underground. This is naturally a major concern in mine detection and it is hoped that with a slight modification the multiple migration and stacking algorithm can go some ways to bring the GPR image back in alignment with the target's true target scattering centre.

16.2.5 Improvement to Metrics

In §14.3 the idea of using metrics was discussed with the hope of being able to judge the correct spreading angle needed to eliminate the effects of diffraction effectively. However, none of the metrics considered consistently performed well so this idea was discarded in place of a more stable method of overlaying various spreading angles together. However if a successful metric could be developed, possibly based on feature extraction (e.g. image curvature, active contours), then it could, potentially improve target detection.

16.2.6 Improvement to Target Detection

In §15 target detection was used to decide impartially what was and what was not a target. However, by using an understanding of the reflection process that occurs within the mine itself (due to dielectric discontinuities inside the mine the radar signal reflects internally within the mine) it may be possible to generate an improved target detection

algorithm which will improve the signal to clutter ratio. Also various other target detection algorithms exist and may again improve the signal to clutter ratio.

16.3 Acknowledgement

This section originated from work undertaken as part of a six month Knowledge Transfer Partnership (KTP) organised through the Knowledge Transfer Network (KTN) between Cobham Technical Services (CTS) and the University of East Anglia. I would like to thank the CTS staff for their help, experience, knowledge and encouragement during this project. In particular I would like to thank David Daniels, Duncan Brooks and Neil Tisdale for their input. In addition, I would also like to thank Rushen Patel, the technology translator at the KTN for his advice and support.

A Finite Difference Time Domain

This method involves solving Maxwell's equations

$$\epsilon \frac{\partial \mathbf{E}}{\partial t} = \nabla \times \mathbf{H} - \mathbf{J}, \quad (\text{A.1})$$

where $J = J(\omega, \mathbf{r}', \mathbf{r}_t)$ is the forcing term, and

$$\frac{\partial \mathbf{H}}{\partial t} = -\frac{1}{\mu_0} \nabla \times \mathbf{E}, \quad (\text{A.2})$$

where \mathbf{E} is the electric field, \mathbf{H} is the magnetic field, ϵ is the dielectric field strength and μ_0 is the magnetic permittivity of free space. Solving Maxwell's equations numerically is used in 'A Matched Filter' (§13.4) to generate the forward scattering models. This method follows the work in 'Electromagnetic Simulation Using the FDTD Method' by Sullivan [52]. Finite Difference Time Domain (FDTD) works by using the electric field to calculate the magnetic field half a time step ahead and vice versa and as such go forward in time. In the most basic case we work in one dimension. Maxwell's equations in 1-D, with no forcing term ($\mathbf{J} = 0$), are

$$\frac{\partial E_x}{\partial t} = -\frac{1}{\epsilon_0 \epsilon_r} \frac{\partial H_y}{\partial z}, \quad (\text{A.3})$$

$$\frac{\partial H_y}{\partial t} = -\frac{1}{\mu_0} \frac{\partial E_x}{\partial z}, \quad (\text{A.4})$$

where ϵ_0 is the dielectric constant of free space and ϵ_r is the relevant dielectric constant so that $\epsilon = \epsilon_0 \cdot \epsilon_r$. These are the equations of a plane wave with the electric field oriented in the x direction, the magnetic field oriented in the y direction, and travelling in the z

direction. Taking the central difference approximations for both the temporal and spatial derivatives gives

$$\frac{E_x^{n+1/2}(k) - E_x^{n-1/2}(k)}{\Delta t} = -\frac{1}{\epsilon_0 \epsilon_r} \frac{H_y^n(k+1/2) - H_y^n(k-1/2)}{\Delta x}, \quad (\text{A.5})$$

$$\frac{H_y^{n+1}(k+1/2) - H_y^n(k+1/2)}{\Delta t} = -\frac{1}{\mu_0} \frac{E_x^{n+1/2}(k+1) - E_x^{n+1/2}(k)}{\Delta x}, \quad (\text{A.6})$$

where n represents the n^{th} time step (i.e. $t = \Delta t \cdot n$) and k represents the k^{th} distance step (i.e. $z = \Delta x \cdot k$). These equations are now rearranged into an iterative form

$$E_x^{n+1/2}(k) = E_x^{n-1/2}(k) - \frac{\Delta t}{\epsilon_0 \epsilon_r \Delta x} (H_y^n(k+1/2) - H_y^n(k-1/2)), \quad (\text{A.7})$$

$$H_y^{n+1}(k+1/2) = H_y^n(k+1/2) - \frac{\Delta t}{\mu_0 \Delta x} (E_x^{n+1/2}(k+1) - E_x^{n+1/2}(k)). \quad (\text{A.8})$$

Now we are in a position to be able to implement this in an algorithm. However it is important to notice that μ_0 and ϵ_0 differ by several orders of magnitude. So in order to circumvent any problems this might cause, we introduce the following change of variables

$$\tilde{E} = \sqrt{\frac{\epsilon_0}{\mu_0}} E.$$

This reduces equations (A.7) and (A.8) to

$$\tilde{E}_x^{n+1/2}(k) = \tilde{E}_x^{n-1/2}(k) - \frac{1}{\epsilon_r \sqrt{\epsilon_0 \mu_0}} \frac{\Delta t}{\Delta x} (H_y^n(k+1/2) - H_y^n(k-1/2)), \quad (\text{A.9})$$

$$H_y^{n+1}(k+1/2) = H_y^n(k+1/2) - \frac{1}{\sqrt{\epsilon_0 \mu_0}} \frac{\Delta t}{\Delta x} (\tilde{E}_x^{n+1/2}(k+1) - \tilde{E}_x^{n+1/2}(k)). \quad (\text{A.10})$$

Now, noting that $\sqrt{\epsilon_0\mu_0} = c_0$ we set our time steps to be

$$\Delta t = \frac{\Delta x}{2c_0}.$$

Now we arrive at the final expression which is used in the FDTD algorithms

$$\tilde{E}_x^{n+1/2}(k) = \tilde{E}_x^{n-1/2}(k) - \frac{1}{2\epsilon_r} (H_y^n(k+1/2) - H_y^n(k-1/2)), \quad (\text{A.11})$$

$$H_y^{n+1}(k+1/2) = H_y^n(k+1/2) - \frac{1}{2} \left(\tilde{E}_x^{n+1/2}(k+1) - \tilde{E}_x^{n+1/2}(k) \right). \quad (\text{A.12})$$

References

- [1] David G. Andrews. *An introduction to atmospheric physics*. Cambridge University Press, 2010.
- [2] Marc Antonini, Michel Barlaud, Pierre Mathieu, and Ingrid Daubechies. Image coding using wavelet transform. *Image Processing, IEEE Transactions on*, 1(2):205–220, 1992.
- [3] G. R. Ayers and J. C. Dainty. Iterative blind deconvolution method and its applications. *Opt. Lett.*, 13(7):547–549, Jul 1988.
- [4] D. H. Ballard. Generalizing the Hough transform to detect arbitrary shapes. *Pattern recognition*, 13(2):111–122, 1981.
- [5] Reinhard Blumrich, François Coulouvrat, and Dietrich Heimann. Meteorologically induced variability of sonic-boom characteristics of supersonic aircraft in cruising flight. *The Journal of the Acoustical Society of America*, 118(2):707–722, 2005.
- [6] Dennis A. Bohn. Environmental effects on the speed of sound. *Journal of the Audio Engineering Society*, 36(4):223–231, 1988.
- [7] T. H. Chong. A variable mesh finite difference method for solving a class of parabolic differential equations in one space variable. *SIAM Journal on Numerical Analysis*, 15(4):835–857, 1978.
- [8] John Frederick Clarke and Malcolm McChesney. Dynamics of relaxing gases. *London, Butterworths and Co.(Publishers), Ltd., 1976. 587 p.*, 1, 1976.
- [9] Robin Olav Cleveland. *Propagation of sonic booms through a real, stratified atmosphere*. PhD thesis, The University of Texas at Austin, 1995.

- [10] Julian D Cole. On a quasi-linear parabolic equation occurring in aerodynamics. *Quarterly of applied mathematics*, 9(3):225–236, 1951.
- [11] Lawrence B Conyers and Dean Goodman. *Ground-penetrating radar*. AltaMira Press An Introduction for Archaeologist, 1997.
- [12] D. G. Crighton. Model equations of nonlinear acoustics. *Annual Review of Fluid Mechanics*, 11:11–33, 1979.
- [13] D. G. Crighton and J. F. Scott. Asymptotic solutions of model equations in nonlinear acoustics. *Royal Society of London Philosophical Transactions Series A*, 292:101–134, August 1979.
- [14] Mike Croll. *The History of Landmines*. Leo Cooper, Barnsley [U.K.], 1998.
- [15] Loren W. Crow. 6th weather wing pamphlet: Sonic boom. 1966.
- [16] D. J. Daniels. Surface-penetrating radar. *Electronics & Communication Engineering Journal*, 8(4):165–182, 1996.
- [17] D. J. Daniels. *Ground Penetrating Radar*, pages 247–352. Institution of Engineering and Technology., 2005.
- [18] D. J. Daniels, D. J. Gunton, and H. F. Scott. Introduction to subsurface radar. In *Radar and Signal Processing, IEE Proceedings F*, volume 135, pages 278–320. IET, 1988.
- [19] Ross W. Deming and Anthony J. Devaney. Diffraction tomography for multi-monostatic ground penetrating radar imaging. *Inverse Problems*, 13:29–45, 1997.

- [20] B. O. Enflo. On the connection between the asymptotic waveform and the fading tail of an initial N-wave in nonlinear acoustics. *Acta Acustica united with Acustica*, 84(3):401–413, 1998.
- [21] Bengt Fornberg. *A practical guide to pseudospectral methods*, volume 1. Cambridge university press, 1998.
- [22] J. Gazdag and P. Sguazzero. Migration of seismic data. *Proceedings of the IEEE*, 72(10):1302–1315, 1984.
- [23] Amara Graps. An introduction to wavelets. *Computational Science & Engineering, IEEE*, 2(2):50–61, 1995.
- [24] Willis Ray Gregg. Standard atmosphere. Technical report, NACA, 1922.
- [25] Edward A. Haering, L. J. Ehernberger, and Stephen A. Whitmore. *Preliminary airborne measurements for the SR-71 sonic boom propagation experiment*. National Aeronautics and Space Administration, Ames Research Center, Dryden Flight Research Facility, 1995.
- [26] P. W. Hammerton and D. G. Crighton. Old-age behaviour of cylindrical and spherical nonlinear waves: numerical and asymptotic results. *Proceedings of the Royal Society of London. A. Mathematical and Physical Sciences*, 422(1863):387–405, 1989.
- [27] Wallace D. Hayes, Rudolph C. Haefeli, and H. E. Kulsrud. Sonic boom propagation in a stratified atmosphere, with computer program. 1969.
- [28] Eberhard Hopf. The partial differential equation $u_t + uu_x = \mu u_{xx}$. *Communications on Pure and Applied mathematics*, 3(3):201–230, 1950.

- [29] P. V. C. Hough. Method and means for recognizing complex patterns, December 18 1962. US Patent 3,069,654.
- [30] Zhou Hui-lin, Tian Mao, and Chen Xiao-li. Feature extraction and classification of echo signal of ground penetrating radar. *Wuhan University Journal of Natural Sciences*, 10:1009–1012, 2005. 10.1007/BF02832458.
- [31] D. Ioannou, W. Huda, and A. F. Laine. Circle recognition through a 2D Hough transform and radius histogramming. *Image and vision computing*, 17(1):15–26, 1999.
- [32] M. E. Johnson. *Relaxation effects on sonic boom waveforms propagating through the atmosphere*. PhD thesis, University of East Anglia, 2003.
- [33] M. E. Johnson and P. W. Hammerton. Effect of molecular relaxation processes on travelling wave solutions of sonic boom waveforms. *Wave motion*, 38(3):229–240, 2003.
- [34] I. I. Jouny. Scattering analysis using fractional Fourier transforms with applications in mine detection. In *Geoscience and Remote Sensing Symposium, 2004. IGARSS '04. Proceedings. 2004 IEEE International*, volume 5, pages 3460–3463 vol.5, Sept 2004.
- [35] George S. Kell. Density, thermal expansivity, and compressibility of liquid water from 0 degrees to 150 degrees. *Journal of Chemical and Engineering Data*, 20(1):97–105, 1975.
- [36] Ramdas Kumaresan, Louis L. Scharf, and Arnab K. Shaw. An algorithm for pole-zero modeling and spectral analysis. *IEEE Acoustics, Speech and Signal Processing*, 34:637–640, 1996.

- [37] C. J. Leuschen and R. G. Plumb. A matched filter based reverse time migration algorithm for ground penetrating radar data. *Geoscience and Remote Sensing, IEEE Transactions on*, 39(5):929–936, May 2001.
- [38] M. J. Lighthill. Viscosity effects in sound waves of finite amplitude. *Surveys in mechanics*, pages 250–351, 1956.
- [39] J. David Logan. *An introduction to nonlinear partial differential Equations; 2nd ed.* Pure and Applied Mathematics. Wiley, Hoboken, NJ, 2008.
- [40] Francis N. Madden, Keith R. Godfrey, Michael J. Chappell, Roman Hovorka, and Ronald A. Bates. A comparison of six deconvolution techniques. *Journal of pharmacokinetics and biopharmaceutics*, 24(3):283–299, 1996.
- [41] Domenic J. Maglieri, David A. Hilton, and Norman J. McLeod. *Experiments on the effects of atmospheric refraction and airplane accelerations on sonic-boom ground-pressure patterns*, volume 3520. National Aeronautics and Space Administration, 1966.
- [42] P. Meincke. Linear gpr inversion for lossy soil and a planar air-soil interface. *Geoscience and Remote Sensing, IEEE Transactions on*, 39(12):2713–2721, Dec 2001.
- [43] Larry Morley and Jon Claerbout. Predictive deconvolution in shot-receiver space. *Geophysics*, 48(5):515–531, 1983.
- [44] Joseph W. Pawlowski, David H. Graham, Charles H. Boccadoro, Peter G. Coen, and Domenic J. Maglieri. Origins and overview of the shaped sonic boom demonstration program. *AIAA paper*, 5:2005, 2005.

- [45] Allan D Pierce et al. *Acoustics: an introduction to its physical principles and applications*, volume 20. McGraw-Hill New York, 1981.
- [46] Allan D. Pierce and Domenic J. Maglieri. Effects of atmospheric irregularities on sonic-boom propagation. *The Journal of the Acoustical Society of America*, 51(2C):702–721, 1972.
- [47] P. L. Sachdev, V. G. Tikekar, and K. R. C. Nair. Evolution and decay of spherical and cylindrical N waves. *Journal of Fluid Mechanics*, 172:347–371, 1986.
- [48] J. M. Schofield, D. J. Daniels, and P. W. Hammerton. A multiple migration and stacking algorithm designed for land mine detection. *Geoscience and Remote Sensing, IEEE Transactions on*, 52(11):6983–6988, Nov 2014.
- [49] J. M. Schofield and P. W. Hammerton. Numerical and asymptotic solutions of generalised burgers’ equation. *Wave Motion*, 51(6):919–934, 2014.
- [50] John W. Shirley. An early experimental determination of Snell’s law. *American Journal of Physics*, 19(9):507–508, 1951.
- [51] Robert H Stolt and Alvin K Benson. *Seismic migration: Theory and practice*, volume 5. Pergamon, 1986.
- [52] Dennis M. Sullivan. Electromagnetic simulation using the FDTD method. *IEEE Press series on RF and microwave technology*, page 165, 2000.
- [53] Albion D Taylor. *The TRAPS sonic boom program*. Department of Commerce, National Oceanic and Atmospheric Administration, Environmental Research Laboratories, 1980.

- [54] Andrey Tikhonov. Solution of incorrectly formulated problems and the regularization method. In *Soviet Math. Dokl.*, volume 5, pages 1035–1038, 1963.
- [55] Yilun Wang, Junfeng Yang, Wotao Yin, and Yin Zhang. A new alternating minimization algorithm for total variation image reconstruction. *SIAM Journal on Imaging Sciences*, 1(3):248–272, 2008.
- [56] H. Wechsler and J. Sklansky. *Automatic detection of rib contours in chest radiographs*. PhD thesis, Citeseer, 1975.
- [57] P. V. Yuldashev, M. V. Averiyarov, V. A. Khokhlova, S. Ollivier, and P. Blanc-Benon. Nonlinear spherically divergent shock waves propagating in a relaxing medium. *Acoustical Physics*, 54(1):32–41, 2008.